DESIGN AND DEVELOPMENT OF AN OPTICAL CHIP INTERFEROMETER FOR HIGH PRECISION ON-LINE SURFACE MEASUREMENT

PRASHANT KUMAR

A thesis submitted to the University of Huddersfield in partial fulfilment of the requirements for the degree of Doctor of Philosophy

The University of Huddersfield in collaboration with – CIP Technologies Ltd., Ipswich

June 2015

Copyright statement

i. The author of this thesis (including any appendices and/or schedules to this thesis) owns any copyright in it (the "Copyright") and s/he has given The University of Huddersfield the right to use such copyright for any administrative, promotional, educational and/or teaching purposes.

ii. Copies of this thesis, either in full or in extracts, may be made only in accordance with the regulations of the University Library. Details of these regulations may be obtained from the Librarian. This page must form part of any such copies made.

iii. The ownership of any patents, designs, trademarks and any and all other intellectual property rights except for the Copyright (the "Intellectual Property Rights") and any reproductions of copyright works, for example graphs and tables ("Reproductions"), which may be described in this thesis, may not be owned by the author and may be owned by third parties. Such Intellectual Property Rights and Reproductions cannot and must not be made available for use without the prior written permission of the owner(s) of the relevant Intellectual Property Rights and/or Reproductions

Abstract

Advances in manufacturing and with the demand of achieving faster throughput at a lower cost in any industrial setting have put forward the need for embedded metrology. Embedded metrology is the provision of metrology on the manufacturing platform, enabling measurement without the removal of the workpiece. Providing closer integration of metrology upon the manufacturing platform will improve material processing and reliability of manufacture for high added value products in ultra-high-precision engineering. Currently, almost all available metrology instrumentation is either too bulky, slow, destructive in terms of damaging the surfaces with a contacting stylus or is carried out off-line. One technology that holds promise for improving the current state-of-the-art in the online measurement of surfaces is hybrid photonic integration. This technique provides for the integration of individual optoelectronic components onto silicon daughter boards which are then incorporated on a silica motherboard containing waveguides to produce a complete photonic circuit.

This thesis presents first of its kind a novel chip interferometer sensor based on hybrid integration technology for online surface and dimensional metrology applications. The complete metrology sensor system is structured into two parts; hybrid photonic chip and optical probe. The hybrid photonic chip interferometer is based on a silica-on-silicon etched integrated-optic motherboard containing waveguide structures and evanescent couplers. Upon the motherboard, electro-optic components such as photodiodes and a semiconductor gain block are mounted and bonded to provide the required functionality. Optical probe is a separate entity attached to the integrated optic module which serves as optical stylus for surface scanning in two measurement modes a) A single-point for measuring distance and thus form/surface topography through movement of the device or workpiece, b) Profiling (lateral scanning where assessment of 2D surface parameters may be determined in a single shot. Wavelength scanning and phase shifting inteferometry implemented for the retrival of phase information eventually providing the surface height measurement. The signal analysis methodology for the two measurement modes is described as well as a theoretical and experimental appraisal of the metrology capabilities in terms of range and resolution.

The incremetal development of various hybrid photonic modules such as wavelength encoder unit, signal detection unit etc. of the chip interferometer are presented. Initial measurement results from various componets of metrology sensor and the surface measurement results in two measurement modes validate the applicability of the described sensor system as a potential metrology tool for online surface measurement applications.

.

Acknowledgements

I would like to thank all the people who have in some way contributed in the research work described in this thesis. First and foremost, I would like to express my sincere gratitude to my supervisor Professor Xiangqian Jiang for her guidance, support and encouragement during my doctoral research endavour. I appreciate all her contributions in providing me the ideas, intellectal freedom in my work, necessary facilities and funding to undertake this research and supporting my attendances at various conferences.

A special thanks to Dr. Haydn Paul Martin for his advice, assitance and technical guidance during the course of my PhD. He has helped me immensely and had been the source of technical and practical inputs whenever needed during the experiments.

The members of the EPSRC Centre for Innovative Manufacturing in Advanced Metrology including the Professor Liam Blunt have greatly contributed personally and professionally during my time at university. Thanks to all of you for making a pleasant and fun place to work.

I also wish to thank Centre for Integrated Optics, Ipswich and its technical director Dr. Graeme Maxwell for providing instruments and device support required for the project. Thanks to all other colleague for their help and support making my life easier during my stay at CIP, Ipswich.

Finally I would like to thank my family especially my parents for all their support, love and encouragement in my pirsuits. Thanks to my brother Pranav who held my family obligations with sheer patience alowing me to spend and focus time on my research work. And most of all my wife Anupam and daughter Radhika for the love, support and patience they have shown and for enduring seperation with great courage in the past two years.

Table of Contents

Contents

List of Tables

List of Figures

List of abbreviations

PIC	Photonic Integrated Circuit
EIC	Electronic Integrated Circuit
PLC	Planar Lightwave Circuit
RIE	Reactive Ion Etching
TMAH	Tetra Methyl Ammonium Hydroxide
IO	Integrated Optics
MEMS	Micro-Electro Mechanical Systems
STS	Silica-on-Terraced Silicon
UV	Ultravoilet
WDM	Wavelength Division Multiplexing
SS-LD	Spot Size converted Laser Diode
WG-PD	Waveguide Photodiode
LD	Laser Diode
PD	Photodiode
TLS	Tuneable Laser Source
SOI	Silicon-on-Insulator
TE	Transverse Electric
TM	Transverse Magnetic
FHD	Flame Hydrolysis Deposition
PECVD	Plasma Enhanced chemical Vapour Deposition
DC	Directional Coupler
PT	Power Throughput
PC	Power Coupled
MZI	Mach-Zehnder Interferometer
LO	Local Oscillator
SOP	State of Polarisation
FP	Febry-Perot
M-DCPBH	Modified-Dual Channel Planar Buried Hetrostructure

MQW	Multiple Quantum Well
ECDL	External Cavity Dode Laser
PIN	p-i-n Photodiode
APD	Avalanche Photodiode
MSM	Metal-Semiconductor-Metal
NEP	Noise Equivalent Power
CIP	Centre for Integrated Photonics
RSOA	Reflective Semiconductor Optical Amplifier
MMI	Multi-Mode interference
TFF	Thin Film Filter
AR	Anti-Reflection
TIA	Trans Impedance Amplifier
OSA	Optical Spectrum Analyser
GRIN	Graded Index
NI	National Instruments
PC	Personal Computer
PZT	Pizeo-Electric Translator
TEC	Thermo-Electric Cooling
PCB	Printed Circuit Board
USB	Universal Serial Bus
SMSR	Side Mode Supression Ratio
RIN	Relative Intensity Noise
HP	Hewlet Packard
TEC	Thermo Electric Controller

1 Introduction

1.1 Overview

Surface metrology is used in engineering to understand the creation and behaviour of surfaces topographies. As the dimensions of a product become smaller the importance of the surface and its properties become a dominant factor in the functionality of the product (X. Jiang et al., 2007b). Modern deterministic/structured surfaces are actually being specifically designed to provide certain functionality. As such it is vital to have proper understanding of the surfaces and their properties. High and ultra-precision manufactured surfaces are for a growing number of state of the art optical elements or devices; for example lenses and mirrors which are integral component to many other value added products such as mobile phone cameras, laser printers, flatbed scanners, displays, telecommunication, photonics and biomedical devices (Lee, 2005). The fundamental limiting factor in the manufacture of such ultra-precision surfaces is the lack of adequate measurement techniques or tools having both large measurement range and high resolution either in academic research or industry (X. Jiang, Lin, et al., 2006). More importantly, the overwhelming requirement within precision manufacturing is for on-line surface metrology methods for the efficient characterisation of surfaces. The online metrology measurement allows improvement of accuracy by minimizing chances of work piece damage and a reduction of machining time by eliminating repositioning operations. Currently, almost all available metrology instrumentation is either too bulky, slow, destructive in terms of damaging the surfaces with a contacting stylus or is carried out off-line (Singleton et al., 2002).

With improved embedded metrology it is possible to further enhance the material processing and reliability of high added-value critical components, ultimately leading to the manufacturing of high added value products. This will aid the transition of high tech products from research and development to the consumer market. However for manufacturing platform integration of measurement tools, it is necessary for them to be compact and flexible enough allow for the easy installation. Furthermore they must be capable of reaching the same performance as their commercial standalone equivalents (X. Jiang, 2012). Also within the precision manufacturing, the online characterization of surfaces is an important requirement in many applications as it has a direct influence on function. Optical non-contact methods are essential where these surfaces need to be verified quickly and without damage. One technology that holds promise for

improving the current state-of-the-art in the online measurement of surfaces is hybrid photonic integration. This technique provides for the integration of individual optoelectronic (OE) components onto silicon daughter boards which are then incorporated on a silica motherboard containing waveguides to produce a complete photonic circuit. Device structures can be extremely compact compared to bulk optic designed and costs may be reduced for volume production. Currently, integrated-optics finds its major application in the field of optical telecommunications. Recently in bio-sensing applications integrated optics has emerged as the most suitable technology for lab-on-chip integration due to their ability for miniaturization replacing the bulk sensor systems. Sensing devices based on integrated optics are portable, easy to use and highly sensitive and promises to have a larger impact on clinical diagnostics, chemical & biological surveillance, process control, metrology, environmental monitoring, and food industry (Estevez et al., 2012).

In surface metrology currently all the available tools are made up of large numbers of bulk optical or mechanical parts such as lenses, beam splitters, fibres, bulk lasers, detectors, mechanical stages etc. Bulk components make device configuration larger and also amounts to higher effective cost of the metrology device. For example the cost of a bulky tuneable laser used in an interferometry based measurement systems can be typically 30 thousand pounds. By leveraging the semiconductor micro- fabrication technologies miniature components similar to the bulk counterparts can be easily fabricated and integrated onto a single platform which in turn will provide high sensitivity, robustness, reliability, and potential for multiplexing and mass production at low cost. In this approach the aim is to develop a novel integrate-optic on-line surface measurement tool based on optical interferometry and a spatial light wavelength scanning method (Kuwamura et al., 1997). The developed metrology tool will have a compact configuration, much smaller size with reduced cost and provide stable and fast online surface measurement at very high precision.

1.2 Aim

The research aims to develop an optical chip interferometer system for high precision online surface measurement using advanced micro-technology and optical methodologies. The complete device architecture of a fully integrated optical chip for online surface measurement will resemble the design as shown in figure 1.1. The optical chip is composed of an optical chip interferometer and an optical dispersive probe to form a miniaturised and robust measurement

system. The function of the hybrid optical chip is based on two interferometry techniques; wavelength scanning and phase shifting. The wavelength dependent spatial scanning property of the dispersive probe is exploited to scan across the test surface.

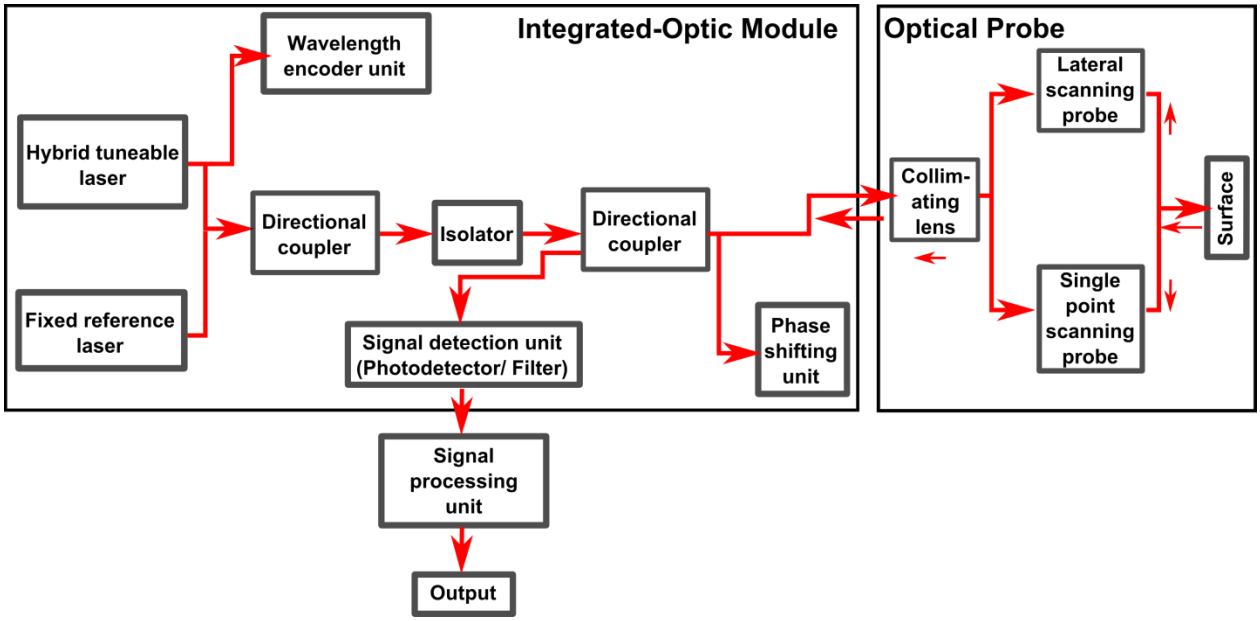

Figure 1.1 Device architecture of integrated optical chip device online surface measurement

The point of focus of the research will be the design and fabrication of various elements of an integrated optical chip device comprising; a tuneable laser source (TLS), an isolator, a directional coupler, a photo-detector (PD) and an optical probe. Furthermore, the research work will involve developing processes for the nanoscale manipulation of the components to modify the optical properties in such a way as to enable the component integration through low cost passive assembly ensuring that the process developed is reliable and suitable for manufacture. In addition to this, full device testing will be carried out in order to optimise the functionality of individual chip components. Once the components meet the desired performance target, the full integration of individual chip components will be performed on the silicon motherboard. The overall integration will produce a device that is compact, robust, fast and stable enough to provide online surface measurement at very high precision. This research work is being carried out in collaboration with Centre for Integrated Photonics, Ipswich, a pioneer UK company in the design and devopment of silica-on-silicon hybrid photonics devices. The optoelectronic device fabrication and chip integration was taken care of by the CIP, while building the chip interferometry, the design and development of scanning optical probe and verifying the feasibility of the miniaturized sensor system was done at University of Huddersfield.

1.2.1 Objectives

1. To design and fabricate various elements of integrated chip comprising; optical waveguides, tuneable laser, optical isolator, optical circulator, photo-detector etc.
2. To investigate the functionality of individual chip components and to optimise it to achieve the performance targets. Once this is achieved final integration is done using hybrid integration techniques.
3. To investigate the approaches for designing an optical probe to achieve the vertical resolution in nanometre while maximising lateral range and resolution.
4. To develop and optimise algorithms and signal processing units to effectively operate the chip interferometer system.
5. Building of a prototype metrology system combining a chip interferometer and dispersive probe.
6. The testing and performance review of the sensor system as a metrology tool proving its feasibility and reliability as an online micro/nano scale surface measurement.

1.3 Full target specification of the chip metrology sensor

The target is to develop a robust and compact metrology sensor system capable performing fast online surface measurement. The overall performance target for the chip metrology sensor system is outlined in the table 5.1.

Table 1.1 Target specifications of the device

Parameter	**Lateral scanning**		**Single point scanning**	
Measurement Time	< 1 s		< 1 s	
Vertical Uncertainty	<0.5 nm RMS		<1 um	
Vertical Range	<0.5 μm		13um – several mm	
Lateral Resolution	Diffraction Limited		Diffraction Limited	
Form factor	Hybrid unit 10×5×2 cm	Optical probe Length: 100 mm Diameter: 40 mm (size can be reduced significantly by beam folding optics)	Hybrid unit 10×5×2 cm	Optical probe Dimension: 25 mmX15 mm

1.4 Novel Contribution

- The development of a miniaturised chip metrology sensor system using hybrid integrated technology incorporating two measurement modes; single point and lateral scanning measurement modes. The operation of the sensor system is based on wavelength scanning, Fourier transform profilometry and phase shifting interferometry techniques.
- The sensor investigated presents first of its kind a novel metrology device which can do both absolute distance as well as profile measurements. The device can perform absolute distance and profile measurements (point by point scanning) using the single point probing method while measurement of suraface profile at nanoscale level can be achieved by operating the device in lateral scaning mode.
- Development of prototype spectrally encoded lateral scanning probe. The lateral resolution of the optical probe system was found to be 3.66 um which was very close to diffraction limited at central design wavelength.
- Demonstration and implementation of the device for absolute distance and surface profile measurements on real samples in both the measurement modes verifying its capability and its feasibility for online measurement applications. The axial resolution in absolute distance measurement mode is limited by the light source bandwidth while lateral scanning sub-nanometre can be achieved which is inherently due to the interferometry.
- Development of a wavelength encoder and signal detection unit. The wavelength encoder unit will provide the real time monitoring of the tuneable laser wavelengths. The signals detection unit comprised of directional coupler and Edge Filter to separate the reference and the measurement signals. The current investigations shows the individual units are operable but needs further improvements.
- Once optimised and calibrated the metrology sensor can be used on variety of platforms as embedded metrology tool.
- The development of a fully functional compact device will bring a step change in field of surface metrology and instrumentation extending the range of currently available online metrology techniques.

1.5 Thesis organisation

This research work presents the development of a hybrid photonics based chip interferometer for embedded metrology applications with the aim of producing a compact, metrology instrument capable of performing nanoscale measurements. The work is organised into nine chapters to present the overall aim of the research project.

- Chapter 2 gives a brief introduction about the surface metrology. It also covers an overview of numerous techniques and tools available for surface measurement with more focus on interferometry based online measurement instruments.
- Chapter 3 introduces devices integration technology utilized for the development of hybrid metrology tool. It underlines the importance of hybrid component integration and discusses various examples and approaches for low cost passive integration of optical components for device development.
- Chapter 4 presents various optical components of the hybrid metrology device. This chapter explains theory, working principle and fabrication processes of individual components to use for the development of the full measurement device.
- Chapter 5 describes the full metrology sensor in two operating modes; lateral scanning and absolute distance measurement. Hybrid integration of various components and its packaging are presented. This chapter also investigates the performance of the individual device components.
- Chapter 6 investigates the use of hybrid metrology device for absolute distance and surface profile measurements. The operation of the device is validated by measuring several test samples such as glass slides and standard step height samples.
- Chapter 7 presents the development of spectrally encoded lateral scanning optical probe for surface profile measurement. Optical performance of the probe is investigated by Zemax simulation and further validated empirically. This chapter finally investigates the use hybrid sensor incorporating lateral scanning probe for surface profile measurement application.
- Chapter 8 presents an appraisal of investigated hybrid metrology sensor and future works relating potential improvements in the device are discussed.
- Chapter 9 presents the final conclusion of the research work.

1.6 Publications and awards

The work in this thesis has produced two peer reviewed journal papers, and three conference papers. A full publication list may be found in the “Publications and Awards” section at the end of this thesis.

2 Surface Metrology

2.1 Introduction

The chapter gives an introduction about surface metrology and its importance in manufacturing and optimizing the performance of a work piece. Basic geometrical features such as roughness, waviness and form and methods responsible for their creation are discussed. Further in the chapter a detailed overview of the recent trends in surface metrology is presented with special emphasis on interferometric optical surface measurement techniques. In addition the need for online metrology tool is presented with some examples.

2.2 Surface metrology

Surface metrology is the science of measuring small scale geometrical features on surfaces: the topography surfaces (X. Jiang et al., 2007a). The term "topography "is derived from the Greek word "topo" which means place and "graphy" refers to a type of symbolic diagram. Topography measurement specifically covers measurements such as surface texture, surface roughness, surface shape, surface finish, form etc. Surfaces can be functional or non-functional depending on its influence on the quality of the part manufactured. High precision engineered surfaces of desired functionality are manufactured by manipulating geometrical features on surfaces. These surfaces are produced by variety of processes such as grinding, polishing, molding, diamond turning, milling etc. Functional properties directly relate to the geometrical features and hence measurements of such features are extremely important. This not only allows the assessment of functionalized product but also give valuable feedback to the manufacturing units for controlled manufacture.

2.3 Importance of surface metrology: Manufacture and Function

Surface metrology has been used in engineering to understand the creation and behaviour of surfaces topographies. As the dimensions of the product become smaller the importance of the surface and its properties become a dominant factor in the functionality of the product (X. Jiang, et al., 2007b). Manufacturing a workpiece involves, the interaction between the manufacturing process and the production technique or the tool used (Whitehouse, 1997). Any change in the manufacturing process or the technique induces change in the surface features thus pointing to the need for a high degree of control. A necessary feature of controlled manufacture is the

measure of surface geometry (Bruzzone et al., 2008). With advanced metrology techniques, there is the possibility of improving material processing, making manufacturing more efficient, reliable and economic and less environmentally sensitive while at the same time optimising performance in terms of high added-value critical components (X. J. Jiang et al., 2012).

Structured surfaces have enabled functional advancement far beyond the capability of traditional surfaces made by simple grinding and milling. Surfaces generated by micro-fabrication behave differently compared to the conventional surfaces. The change is even more marked at the nano level and has different behavioural properties from either sub-millimetre or macro (De Chiffre et al., 2003). Thus the geometrical figure of the surface is required at first hand which influences the functions such as lubrication, adhesion, wear diagnostics, friction, and so on.

2.4 Surface features

Surface features are generally characterized along the vertical direction by height parameters and along the horizontal direction by spatial (wavelength) parameters (Sherrington et al., 1988)[7]. Roughness measurement along both the direction should be obtained to properly quantify topography or the structure of the specimen surface. The structures on the surfaces are basically various components of frequency related to the manufacturing process or the production technique used (Whitehouse, 1997). Nature of different frequency components affects the performance of the work piece. These frequencies have been grouped mainly into three categories, namely roughness, waviness and form (Blunt et al., 2003).

Roughness

Roughness refers to the highest frequency components present on a surface of interest. Roughness depends on the type of manufacturing method employed rather than the machine type.

Waviness

Waviness results due machine deflections and vibration and is defined as repeating irregularities with spacing greater than roughness. In terms of frequency, the next lower order frequency components on the surface represents waviness.

Form

Form of a surface is generated due to lack of rigidity of the work piece during the machining process allowing it to flex or bend (Vorburger et al., 1990). This contains lowest frequency

components on a surface. Several factors such as material strain, temperature changes during manufacture, excessive surface residual stress can cause form error.

As different factors leads to the creation of basic forms of surface geometry, they do exhibit different relationships to the functionality of the piece part. Hence it becomes important to separate them by analysis or characterization techniques. After analysing these features on the surfaces one may conclude about the nature of process or methods responsible for creation geometrical features. One can exploit this information to control manufacturing process, functional properties and performance of a workpiece.

2.5 Ultra/high precision manufactured surfaces: Applications

The applications of Ultra/high precision manufactured surfaces are immense. Ultra precision surfaces determine the product performance. Surfaces can be designed and structured with high precision to optimize the device performance, for example lenses and mirrors which are integral component to many other value added products such as mobile phone cameras, laser printers, flatbed scanners, displays, telecommunication, photonics and biomedical devices (Lee, 2005). Their transmission and reflectance properties can be molded to give the desired functionality. Using diamond turning it is possible to achieve form accuracy of up to a fraction of light wavelength for highly precise mold inserts for high –volume plastic injection molding for production of plastic lenses to be used in consumer camera or telescopes. Smoothed lens precision structured surfaces scatter less light and have better optical qualities which enhances accuracy, effectiveness and quality of the image to be recorded. The quality of surfaces within the optical tower of a lithography wafer stepper is a fine example of ultra-precision surfaces. Lithography wafer stepper is a step and scan approach for lithographic patterning of features by projecting mask structures on to the wafers and shifting it below the optical system after each exposure precisely to the size of the image field. The extremely high quality optical system creates the small feature size of transistor on an electronic integrated circuit (IC) at a very high degree of precision providing greater packing density, ultimately reducing the size of the IC (Shore et al., 2008).

Today ultra- precision micro-grooved films are widely used as a ‘directors’ for the orientation of liquid crystal materials in LCD , organic light emitting diodes (OLED’s) flat panel displays to control the output light from the external light source. Micro-grooved light guide with focusing foil with switchable backlight generates 2-D and 3-D images and can be used for the 3-

D display technology (Shieh et al., 2005). These displays now a day are widely used in consumer products such as TV's, computers and digital cameras. The use of such precision manufactured micro-groved films has greatly enhanced the image quality, minimizing the size and cost to meet the demanding requirement of portable displays. Micro-grooved structured surface with optimum geometry are of great importance for better tribological performance (Sung et al., 2003). They help in orientation of the living cells leading to faster securing of prosthesis.

2.6 Surface measurement procedures

Surface measurement involves three basic steps; acquisition of data by an instrument, filtration and analysis by parameterisation. Sometimes fitting of the acquired data is required to remove any underlying shape due to the tilt of sample relative to the measuring instrument. Filtering is used either to remove the undesired aspects of surface topography or selects the elements which are need for analysis or evaluation. So filtering wherever employed must be carried out with utmost care so that the desired information always remains. Filtering is performed to separate the three basic form of surface geometry. Depending on the type of filtration used either of these surface geometries can be easily separated out. After filtering the data is analysed to describe the surface features in some numbers called parameterisation.

The imprints made by various machining processes such as polishing, grinding , milling etc. makes surfaces highly complex in nature. These processes are statistical in nature and hence to quantify for the surface topographies one needs statistical descriptors. Two basic kinds of descriptors are parameters such as RMS roughness (quantifies the surface statistics by a number) and surface statistical functions such as power spectral density (Bendat et al., 2011; Nayak, 1971). Large numbers of surface parameters are developed to characterize the surface topography. These surface parameters have been categorised into mainly four groups; Height parameter, shape parameter, wavelength parameter, and combination of these known as hybrid parameter. Similarly statistical function gives detailed statistical description of surface properties. Examples of statistical functions are; power spectral density function, the autocorrelation function, amplitude density function and the bearing area curve.

2.7 Probing systems in surface metrology

The probing systems are classified into mainly two categories; contact and non-contact types depending on the nature of sensing. Contact profilometer are the most basic measurement tool

for surface measurement which examines the surface by direct touching the sample whereas non-contact type measures samples without touching and is mainly light based optical systems. Stylus profilometry is the earliest form of profilometer developed to measure the surface topography of the sample. The tip of the stylus measures the height profile and is recorded via a transducer generating profile of the surface. The transducer acts as a gauge which controls and tracks the force between the stylus and the surface and gives exact height measurement outputs. Examples of the contact profilometers are linear variable differential transformer (LVDT) and scanning probe microscopes [SPM] (Tersoff et al., 1993). High resolution at angstrom level can be achieved by scanning probe microscopes. In spite of high lateral resolution and vertical range stylus based instruments have numerous deficiencies however. Stylus tips and the transducers are delicate and have chances of getting damaged if not used in clean and quiet environment. Conventional stylus instruments are very slow as they scan point by point and generate two dimensional mapping of the surfaces. This makes it unsuitable where three dimensional surface mapping or inspection of entire surface of a product is required as it covers only a fraction of area in one single scan. Slow speed, destructive nature and the size of stylus instruments also restricts its applicability to online and inline measurement applications in manufacturing.

To overcome the above limitations of contact devices, designs and constructions of devices based on optical phenomena are developed. Optical methods are non-contact in nature and obtain morphological information of surfaces without any physical contact between the sensor and the object. Hence they are non-destructive in nature and even soft and delicate samples can be easily investigated without fear of damage Also they are reasonably faster than their stylus counterparts. For the online measurement of surfaces optical methods are considered the most suitable non- contact profiling techniques. Various optical methods based on conventional imaging including video and microscopy systems, displacement measurement and ranging, interferometry, scanned imaging systems such as confocal microscopy, scattering, polarisation, structured lighting for surface profiling etc. have been described in detail in scientific literatures by several authors, e.g. Bennett's (Bennett, 1992a, 1992b), Tiziani's (Tiziani, 1989), Leonhardt's (Leonhardt et al., 1989). In recent times advancement in modern computers, software and electronics has made interferometry a preferred and most popular technique for metrological

applications. The following section will details various interferometric techniques developed for for efficient characterization of surfaces and profile measurements.

2.8 Interferometric profiling techniques

There have been many developments in the design of interferometry based metrology instruments to achieve higher measurement accuracy. With the use of interferometry the measurement of engineered surfaces can be obtained at very high precision. The most popular techniques of metrology based on interferometry are phase shifting interferometry (PSI), white light interferometry (WLI), wavelength scanning interferometry (WSI). These methods have been detailed in the following section. Interference signal is obtained by varying the path length between the test object and the reference beams. The path length variation is generally induced by either vertical scanning or phase shifting techniques which involves mechanical scanning. Path length variation also sometimes is induced by non-mechanical means such as wavelength scanning and dispersive methods. Interference microscopy which is a fusion of interferometry and microscopy provides a powerful measurement method for the roughness measurement of specular surfaces. For surface measurement at high vertical and horizontal resolution interference microscopy stands the most suitable. Vertical resolution of nano-scale level can be achieved by the interference signal while the lateral resolution is limited by the objectives used.

2.8.1 Phase shifting interferometry

2.8.1.1 Single wavelength interferometry

Single wavelength interferometric profilers were based on single wavelength phase shifting interferometry. This technique employs a monochromatic light source to characterize very smooth surfaces. Surface profile of a test surface is obtained by analyzing interference signal obtained at each point on the object by inducing phase difference in steps using PZT shifter either in the object or the reference arm (Malacara, 1990). Phase shifting interferometry techniques comes under the dynamic fringe analysis technique as a time varying phase shift is applied between the reference and test beam. The phase of the wavefront can be directly calculated from the variations of the intensity recorded in interferogram. Here a phase change is induced in a particular fashion and a number of interferograms are recorded. The recorded individual interferogram is mathematically represented by the equation,

$$I = 2I_o[1 + V\cos(\delta)] \tag{2.1}$$

In the above equation there are three unknowns Io back ground intensity, V the visibility and δ the phase. So in order to determine these three unknowns we require minimum three temporally phase shifted intensity patterns. Similarly n number of interferogram can be recorded by simultaneously shifting the phase by a known quantity (α) and unknowns can be obtained by solving these equations in some manner.

$$I_1 = 2I_o[1+\mathrm{V}\cos(\delta+\alpha_1)]$$

$$I_2 = 2I_o[1+\mathrm{V}\cos(\delta+\alpha_2)]$$

……..

……..

$$I_n = 2I_o[1+\mathrm{V}\cos(\delta+\alpha_n)]$$

Many algorithms have been developed to retrieve the resultant phase from the series of recorded interferograms; three step algorithm, four step algorithm, least square algorithm, Carre algorithm, five step algorithm, Hariharan algorithm etc. A particular algorithm is chosen depending upon the nature of reference phase variation and number of times and the rate at which the interference pattern is measured. The three step algorithm (Wyant et al., 1984) involves three interferograms recordings shifted by equal phase steps where as in the four steps algorithm (Schwider et al., 1983) required recording of four 90 degree phase shifted interferograms. Both the algorithms requires a known phase shifts between the interferograms, and hence cannot be employed for unknown or errors in phase shifts or , for e.g. phase shift provided by PZT motion remains unknown due to errors in the linearity response. For such cases Carre algorithm (Carré, 1966) is designed to recover phase from interferogram shifted by unknown yet constant phase shifts and this algorithm has been implemented this work for phase calculations.

Surface measurements with low noise and at very high resolution of the order of angstrom are obtained using this method. However this method has limited height measurement range because of the 2π phase ambiguity problems. Hence this technique can only measure height discontinuities less than λ/4 (λ being the wavelength of light). Also the use of monochromatic wavelength restricts its applicability to ranges where only continuous fringes can be obtained (Ali, 2012). The ambiguity range can be extended by either using a source of longer wavelength or high resolution detectors.

2.8.1.2 Multiple wavelength interferometry

Multiple wavelength interferometry is an extension to single wavelength interferometry which can be used to measure smooth to rough surfaces with height discontinuities up to few millimeters. The measurement range can be increased by either using longer wavelengths or shorter visible wavelength to synthesize longer effective wavelengths called as synthetic wavelength. The option of producing synthetic wavelength is a better option as it doesn't requires expensive light sources and detectors at these wavelengths. Multiple wavelengths include two, three, four or sometimes many wavelengths to produce effective wavelengths which enable accurate measurement over wider range of surfaces. Multiple wavelength for example two wavelength creates a synthetic wavelength (λs) much longer than the individual wavelengths ($\lambda 1$, $\lambda 2$). The synthetic wavelength is given by,

$$\lambda_s = \frac{\lambda_1 \times \lambda_2}{\lambda_1 - \lambda_2} \tag{2.2}$$

Several authors have discussed measurements based on two wavelengths or multiple wavelength interferometry. Two wavelengths with the phase shifting interferometry were adopted by Cheng and Wyant (1984) to test steep optical surfaces (Cheng et al., 1984) and they achieved measurement precision better than 25 A^o. Katherine Creath also performed step height measurement using two wavelength phase shifting interferometry applied to a phase measuring microscope (Creath, 1987). Suzuki et al proposed another two wavelength laser diode interferometer for step height measurement using integrated-bucket method in conjunction with time-shared sinusoidal phase modulation (Suzuki et al., 2002). Step height of 1 um was measured with an error of ~15nm and suggested possible improvements in measurement error can be achieved by using feedback control system.

2.8.2 White light interferometry

Step height measurements by interference microscopy using multiple wavelength interferometry have been performed by several authors. Depth of field of interference objective limits the height measurement range rather than effective synthetic wavelength. White light interferometry (WLI) is well established technique of optical profiling for measurement of engineering surfaces. This interferometry technique is also labeled as vertical scanning interferometry (VSI). A white light interferometry used in conjunction with interference microscope extends the measurable heights which are limited by the working distance of the

objective (Conroy et al., 2005). A broadband light source is used and the microscope objective focusses the light beam onto the test sample. The schematic of white light interferometry is shown in the figure 2.1.

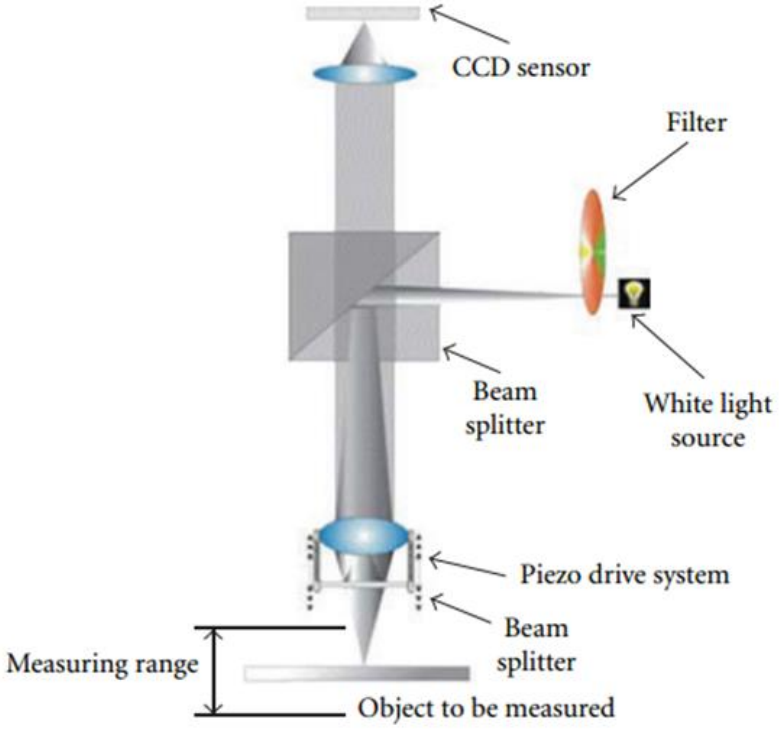

Figure 2.1 Schematic of white light interferometry [Adapted from Conroy et al., 2005]

The light beam from the source is split by the upper beam splitter and is directed towards the objective lens. The interference objective containing a beam splitter further splits the beams into the two; reference beam and the test beam. The reflected beams from the reference mirror and the sample combines to produce interference fringes which are recorded by the CCD sensor. The objective head is moved in vertical direction which changes the OPD between the two beams of the interferometer creating a series of moving fringes (shown in figure). Since a broadband source of light is used mutually incoherent wavelengths combine to produce light fringes in the form of envelope. The maximum of the envelope corresponds to the zero OPD between the reference and the measurement beams. Intensity quickly falls away from this zero OPD position and hence the fringes obtained in this case are said to be localized. The fringe maxima also called as coherence peak is tracked and processed to give the topography of the surface. Axial scanning of the surface by WLI to track the coherence peak (Figure 2.2) has been labeled under various names such as Coherence Scanning Interferometry (CSI), Low coherence interferometry,

coherence correlation interferometry (CCI). The recorded intensity images are analyzed to give the topography of the surface.

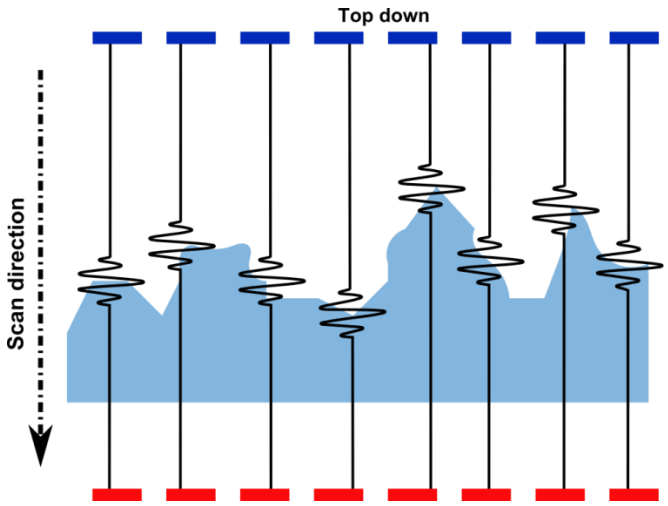

Figure 2.2Interferogram generation using the coherence scanning interferometry

As WLI can scan entire area defined by the field of view of the objective, it makes measurement process faster in comparison to other optical and stylus based instruments. One of the first practical WLI was developed by Balasubramanian (1982) for characterization of an aspheric surface. He used wavefront scanning by translating either the test or reference surfaces to record loci of points of maximum fringe contrast (Balasubramanian, 1982). Similar technique of detecting peak contrast in a fringe pattern was used employed by Davidson (1987) to measure the profile of integrated circuits (Davidson et al., 1987). One of the important factors which determine the performance of WLI is the interference objectives (S. Ma et al., 2011). The objective determines the lateral resolution of the system and is defined by the diffraction limit of the objective used. A commercial WLI developed by Zygo provides non-contact 3D measurement of variety of surfaces at sub-nanometer resolution with extended vertical range up to 20 mm. White light interferometry combined with the phase shifting interferometry is referred to as enhanced vertical scanning interferometry (Zecchino, 2005). Intensity distribution is of the interference signal maxima for the points falling in the focus of the optical system are detected by individual pixels.

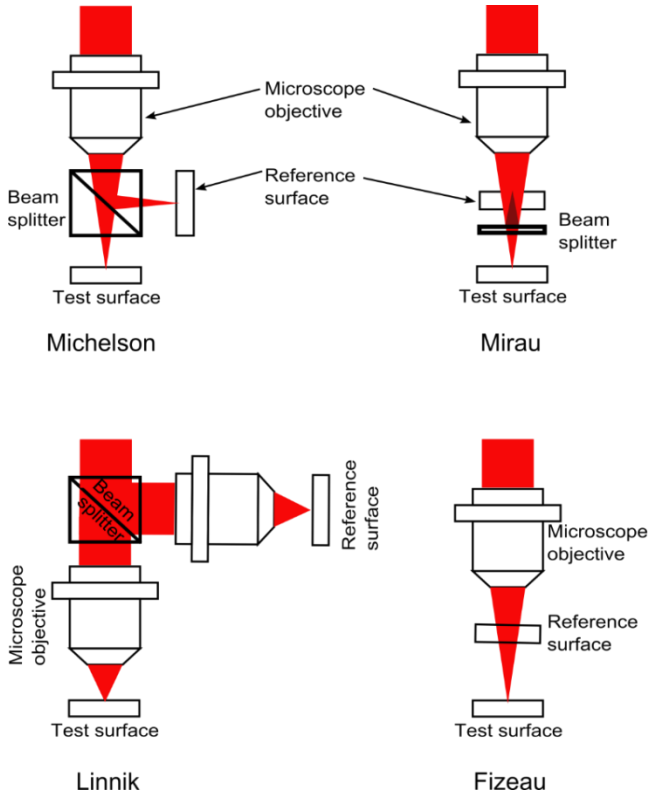

Figure 2.3 Interference objectives (a) Michelson interferometer, (b) Mirau interferometer, and (c) Linnik interferometer, (d) Fizeau interferometer.

Depending on the type of object to be measured one or other interferometer setup is preferred. In general there are four interferometric objective setups used for the measurement of surfaces; Michelson, Mirau, Linnik, Fizeau (Figure 2.3). The design of these four interferometer setup differs in the way the beam is split into reference and object beams. The figure below shows the schematics of all four types of interferometer setups. In Michelson setup the beam splitter is placed between the objective and the test surface and hence it requires a long working distance microscope. It is used for low magnification applications. The second interferometer is Mirau which is suitable for medium magnifications such as 10X, 20X. One of the disadvantage of Mirau configuration is the central obscuration present in the system due to the reference mirror or the reflective spot. So for best imaging the reference reflective spot must be larger or equal to the field of view of objective. For very high magnification applications Linnik interferometer setup is used.

It requires two matched microscope objectives to provide aberration free maximum fringe contrast. Since no optical element is placed in between the objective and the test sample this configuration provides flexibility of using large numerical aperture short working distance

microscope objectives. Large numerical aperture provides highest possible optical resolution. All the above interferometer setup mentioned are variants of Michelson interferometer having equal paths. In contrast Fizeau interferometer is an unequal path interferometer which is well suited for single wavelength interferometry.

2.8.3 Wavelength scanning interferometry

Wavelength scanning interferometry (WSI) is also known as spectral interferometer which utilizes wide range of wavelengths obtained through tuning light source to generate spectral fringes. Surface shape measurement of rough and stepped smooth surface can be easily characterized by WSI without 2pi phase ambiguities (Malacara, 2007). The system uses a Michelson interferometer setup with a light source which is wavelength tunable. The tunable light source sweeps the wavelength which in turn gives fringes of different frequencies from which the height of test surface is obtained relative to the reference surface.

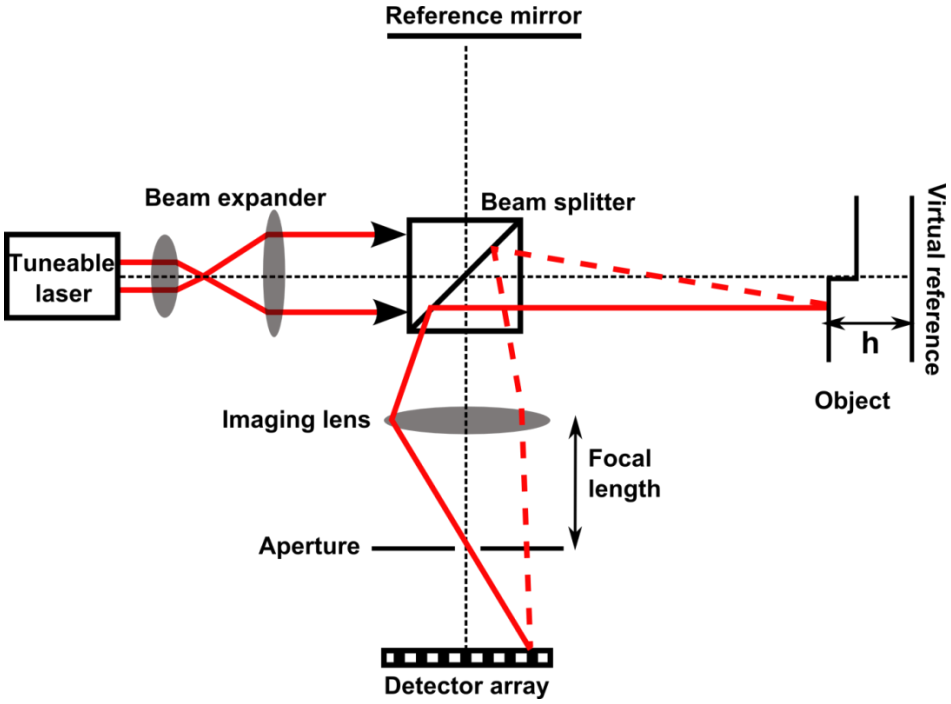

Figure 2.4 Optical setup of wavelength scanning interferometry

[Adapted from Kuwamura & Yamaguchi, 1997]

The fundamental problem is to calculate the phase information from the fringes obtained by wavelength scanning (Kuwamura & Yamaguchi, 1997). The optical setup for the wavelength scanning interferometry is shown in the figure 2.4. As the phase difference is provided by wavelength scanning of the light source this system does not requires any mechanical scanning

compared to confocal microscopy or white light interferometry. Axial resolution and maximum measurable range depends on the maximum tuning range and minimum tuning step of the light source (Yamamoto et al., 2001; Yamamoto et al., 2000)[37, 38]. The axial resolution δg of wavelength scanning interferometer is given by,

$$\delta g = \frac{\pi}{\Delta k} = \frac{\lambda_{\max}\lambda_{\min}}{\lambda_{\max} - \lambda_{\min}} \tag{2.3}$$

where λmax and λmin are the maximum and minimum wavelengths of scanning. So to achieve a high resolution, light sources with wider and quicker tenability such as external cavity laser diodes would be beneficial. The maximum measurement range (Δg) or the depth of measurement is determined by the minimum tuning step (δk) of the source used and is given by,

$$\Delta g = \frac{\pi}{\delta k} \tag{2.4}$$

If an optical imaging element (lens) is used in the measurement arm of the interferometer the depth of measurement is defined by depth of focus of the imaging system (Yamaguchi et al., 1998). For accurate and precision surface measurement linearity of the tunable light source plays an important role. Any non-linearity in the source wavelength scanning or the mode hopping behavior exhibited by the light source will lead to incorrect results (Kikuta et al., 1986; Thiel et al., 1995). Several methods have been proposed for obtaining continuous and linear wavelength scanning either by modifying the laser cavity or setting up a reference interferometer (Moore, 2011).

Several methods of phase retrieval in interferometric sensors have been developed and investigated (H. P. Martin, 2010). One of the well-establised techniques for the retrieval of absolute phase values from the interferograms is the phase shifting as discussed in section 2.8.1.1. The intensity pattern of recorded interferogram encodes the wavefront variations and phase is retrieved by simple point by point calculation (Malacara, 2007). The need of locating fringe centre is also eliminated along with the associated problems. Other benefits of PSI are its insensitivity to spatial variations of intensity, detector sensitivity and fixed pattern noise. The repeatability or the precision of PSI technique is much greater than the static interferogram analysis techniques. The optical integration technology offers feasible solutions for the integration of phase shifting unit in the reference arm for a more stable and controlled phase shifts operation. Examples of phase shifting units are; thermo-optic phase shifters or reflective

semiconductor optical amplifiers. So because of all the obvious advantages, this thesis will use PSI technique for phase calculation application.

2.9 Interferometry based on-line metrology techniques

With advances in machining technology the demand for high precision surface measurement instruments continues to grow to achieve high level of precision and accuracy in topography measurements. Currently there are many commercial profilers both; contact and non-contact types are available which can perform topography at nanometer resolution. All the available metrology instrumentation is too bulky, slow, and destructive in terms of damaging the surfaces with a contacting stylus or is carried out off-line. So the challenge is to address an innovative approach for online surface topography which can be embedded and utilized as added functionality to the manufacturing unit. Non-destructive, high speed (< 1 s), high resolution (nanometer level), automated measurement, compact size, noise insensitive, cost effective and measurement reliability are all the requisites of a metrology tool for its applicability as online measurement systems. The optical profiling method offers great possibility for high precision measurement of surfaces during manufacturing process. The online metrology measurement allows improvement of accuracy by minimizing chances of work piece damage and a reduction of machining time by eliminating repositioning operations. A light based optical probe is eternally free of friction and hence provides non-destructive easy to use instrumentation. Other advantages include speed and areal measurement capability which makes it possible to quickly measure larger surface area of products in industrial environment.

In previous years many researchers around the world have proposed methods for optical on-line and in-process surface measurement. Majority of the methods relied on the light scattering technique(Vorburger et al., 1981; Wang et al., 2003) which only provides qualitative evaluation of surface texture or detect defects with micro-level features. The major limitation of methods based on light scattering is their inability to quantitatively assess the sub-micron features of surface texture with any sort of traceability (X. Jiang, Wang, et al., 2006). Some of the recently developed metrology tools based on interferometric techniques are described below.

2.9.1 Measurement techniques

Alvarez et al used conoscopic holography, triangulation and speckle reduction method to obtain submicron online profile measurements. The developed prototype (Figure 2.5) showed

promising results and resolution of the order of < 0.08-um rms in focus and < 0.095-um rms along a depth of field were obtained with measured Ra value as small as 0.3um from working distances of 110mm (Alvarez et al., 2008).

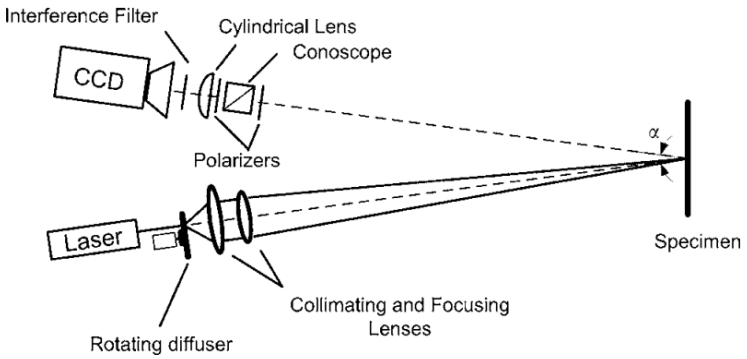

Figure 2.5 Conoscopic sensor including triangulation and a rotating diffuser for speckle reduction [Alvarez et al., 2008]

The system is quite robust against the vibrations and the harsh environmental conditions and quick enough to be used for online metrology applications. Phase information is used to obtain the profile and hence this method is limited by ambiguity range. Enguita et al further modified this setup by using Savart plate instead of a conoscope and developed a common path two wavelength interferometer for profile measurements in on-line applications using two laser sources. The two wavelengths are used to provide enhanced improvement in the measurement range of the device. The two beams are then passed through the rotating holographic diffuser to reduce the speckle effects. The laser line is then projected onto the object under inspection, and the Savart plate, sandwiched between two polarizers, divides the reflected wavefront in two (corresponding to ordinary and extraordinary rays), which interferes in the detection plane. A cylindrical lens is used to obtain the signal corresponding to the whole profile in a single frame. A 12 mm profile of a target in single frame with submicron precision and working distances larger than 100 mm is obtained by the above method (Enguita et al., 2010).

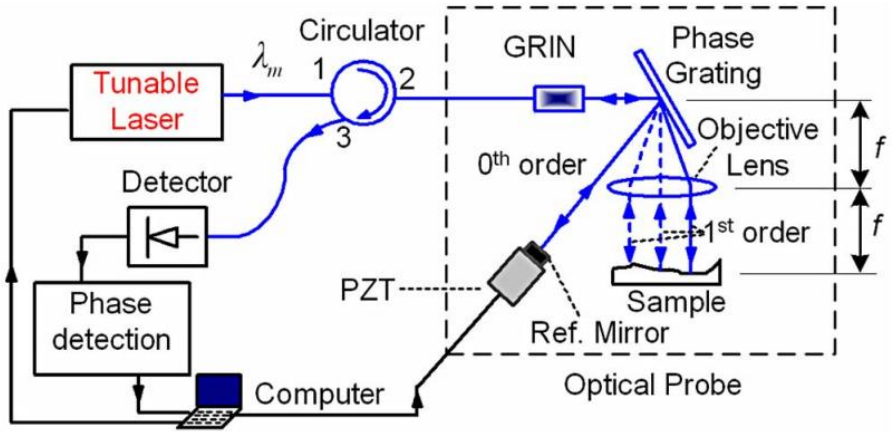

Figure 2.6 Schematic of proposed online surface measurement system

[Adapted from X. Jiang, Wang, et al., 2006]

A new common path optical fiber interferometer for potentially fast on-line micro-scale and nano-scale surface measurement was proposed by Jiang et al (X. Jiang, Wang, et al., 2006). The schematic of the fiber interferometer is shown in the figure 2.6. The proposed system replaced the traditional mechanical stylus with optical beam scanning with the help of diffraction grating to achieve fast and long range lateral profile measurements. Wavelength change by tunable laser changes the first order diffraction angle on the phase grating producing the spatial scanning of the surface. The light reflected (1st order) back from the surface interferes with the zero order diffraction beams and gives the measurement signal. Phase shifting interferometry technique was employed to retrieve the phase information and consequently the profile from the interferometer output. The phase shift is obtained by moving the reference mirror by pizeoelectric transducer (PZT). Measurement accuracy of 4.1 nm was achieved for the displacement measurement experiment. Measurement time of the probe system is 1.6s which was limited by the scanning speed of the tunable laser source.

An improved method of optical interferometry system for fast areal surface measurement at micro and nano-scale has been developed recently by Hussam et al (Muhamedsalih, 2013). The optical interferometry system is based on wavelength scanning interferometry (WSI) and is capable of providing embedded metrology solutions (Figure 2.7). A reference interferometer is multiplexed with WSI to stabilize the system against environmental disturbances. High speed measurement is achieved by parallel programming model using large number of threads processed by cores of graphic processing unit. For instance, the computing time is reduced from 32 s to 1.2 s for 256 frames of 640 x 480 pixels.

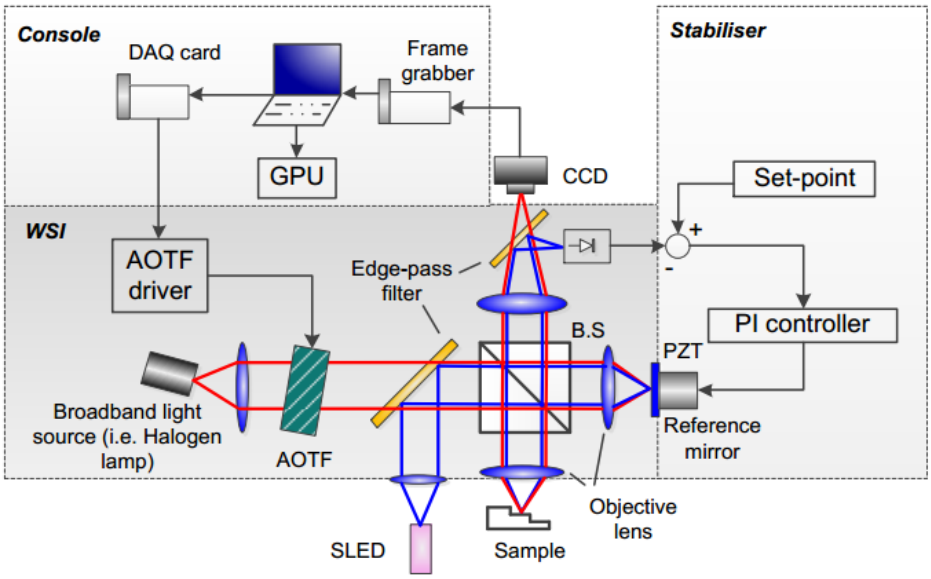

Figure 2.7 Schematic of WSI interferometry system for embedded metrology applications [Adapted from Muhamedsalih et al., 2013]

Nanometer accuracy surface measurements were obtained for step height samples. 2.970 um step height standard sample supplied by National Physical Laboratory was measured by WSI system. The measured step height obtained was 2.971 nm. Similarly other sample of 292nm step height was measured whose value was obtained as 291.1nm. So error in both the measurement obtained was < 1 nm (X. Jiang et al., 2010b).

2.10 Integrated optics based interferometric metrology sensors

Integrated optics (IO) is an attractive way to achieve optical circuits in several fields of application. This is especially true for optical sensors where IO can bring both the classical advantages of optics: insensitivity to electromagnetic noise; ability for non-contact measurements; suitability for use in harsh environment; and the advantages of integration: circuit miniaturization; better reliability; the ability for mass production and low cost (Valette et al., 1990). This section will detail various examples of integrated optical sensors developed for metrological applications. Easy implementation of compact interferometers and other functional components constructed onto integrated optical chip adds improved application flexibility providing excellent measurement resolution. One of the earliest demonstrations of integrated optic device for micro displacement sensor utilized a Michelson interferometer configuration (Izutsu et al., 1982). The experimental setup for PZT vibration measurement is shown in the

figure 2.8. The key component of the interferometer was a passive hybrid coupler fabricated onto LiNbO3 substrate and a semi-reflecting mirror. A mirror is directly attached onto the end surface of waveguide substrate which serves as the reference arm while the other arm is the sensing branch to which a PZT with mirror is attached to test transducers performance.

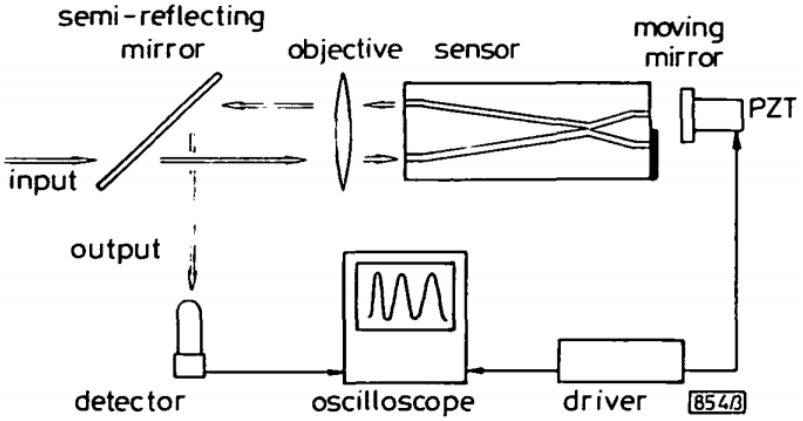

Figure 2.8 Integrated optic micro displacement sensor on Lithium Niobate

[Adapted from Izutsu et al., 1982]

In this case an external collimating lens was required for measurement over a long working range. Ura et al demonstrated a fully hybrid integrated optic position/displacement sensor (Figure) onto a silicon substrate. The device consisted of two planar interferometers; photodetector in a glass waveguide, a butt coupled single mode laser diode and the key component focusing grating coupler (FGC) (Figure 2.9).

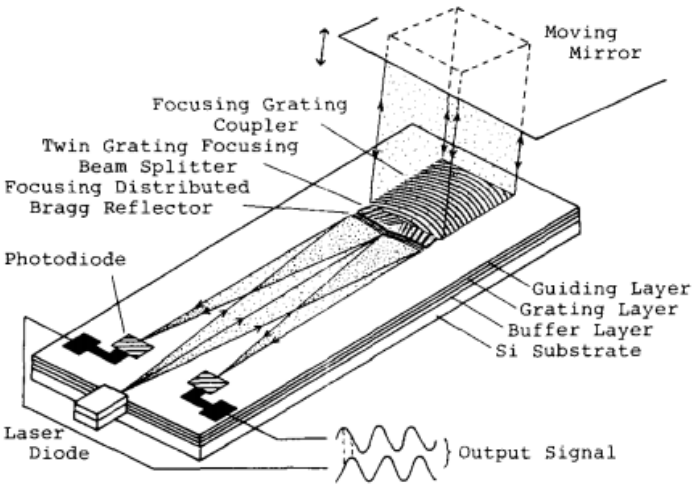

Figure 2.9 Hybrid integrated interferometric position sensor [Adapted from Ura et al., 1989]

The laser beam is transmitted through the waveguides to the focusing grating coupler (FGC). FGC out couples the beams in free space forming a collimated sensing beam making it

incident onto the moving mirror. The moving mirror reflects the beam back into the waveguide by same FGC. Another twin focusing distributed Bragg reflector gives the reference waves and also divides the reflected incoming waves into two halves allowing the beam to fall onto the two photo-detectors. Thus signal and reference wave interfere in the PD's and hence displacement is detected by recording the periodic modulation of the output photo-current. Long working range was achieved by the collimated sensing beam directly radiated from displacement sensor. Interference signals corresponding to the mirror movement were obtained experimentally over a 15-cm range with a 0.39-um modulation period (Ura et al., 1989).

The above reported device was based on hybrid integration using an external laser diode. Suhara et al used monolithic integration of all the components which provided further miniaturization, simple assembly and eliminated coupling losses. He also replaced the laser diode with single quantum well distributed- feedback laser for stable single mode operation which is crucial for metrology applications (Suhara et al., 1995).

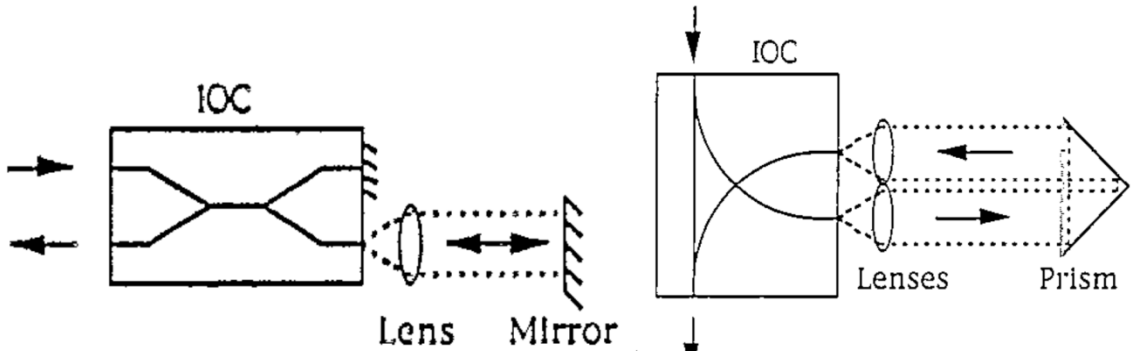

Figure 2.10 (a) A Michelson interferometer on an integrated optical circuit (L), (b) proposed Mach-Zehnder interferometer [Adapted from Hellesø et al., 1995]

Helleso et al (Figure 2.10 (a)) demonstrated another a Michelson interferometer based displacement sensor on glass using integrated optics technology. The proposed configuration consisted of integrated optic circuit (IOC) containing single mode waveguides made by potassium-sodium ion exchange on glass substrate, a lenses and a reflecting external mirror. The laser beam was injected into the single mode guide which was split between the reference mirror and an output. The output beam was collimated by a lens, reflected by a measurement mirror, focused by a lens and re-injected into the waveguide to combine and interfere. The interfered signal was detected by the photodetectors to obtain visibility over sensor-mirror distance up to 4 m (Hellesø et al., 1995). Further spectral width and coherence length of the laser diode are calculated from visibility measurements. He also proposed a Mach-Zehnder based IOC sensor

alternative to Michelson interferometer to exploit two advantages; no guided light reflected towards the source and no intrinsic losses (Figure 2.10 (b)).

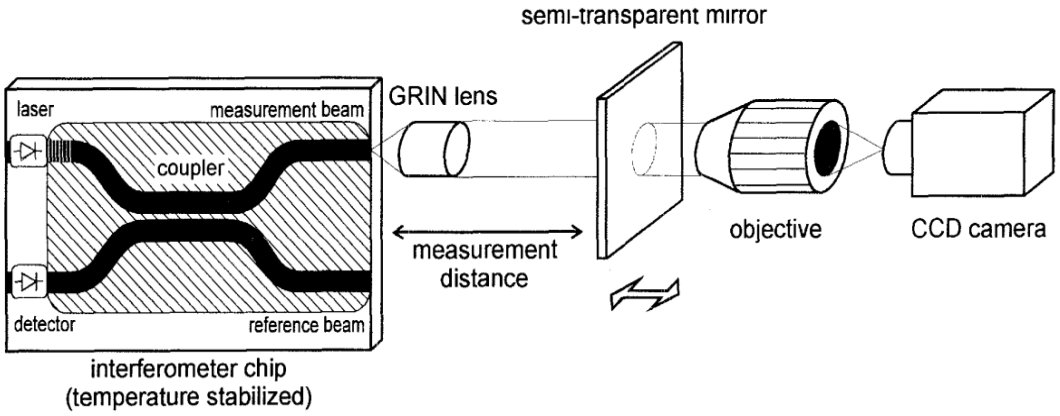

Figure 2.11 Schematic of the measurement setup for the characterization of integrated interferometer

Zappe et al presented a monothically integrated optical displacement sensor which consisted of a Michelson interferometer with an integrated DBR laser and waveguide photo-detector fabricated onto a single GaAs optical chip. The schematic of the displacement sensor is shown in the figure 2.11. Displacement measurement with sub-100 nm resolution was obtained (Zappe, 1996). Since all the interferometer components were fabricated onto a single optical chip precise alignment is automatically achieved between the various components. It was suggested that using hybrid integration of components will bring out more highly functional sensor microsystem.

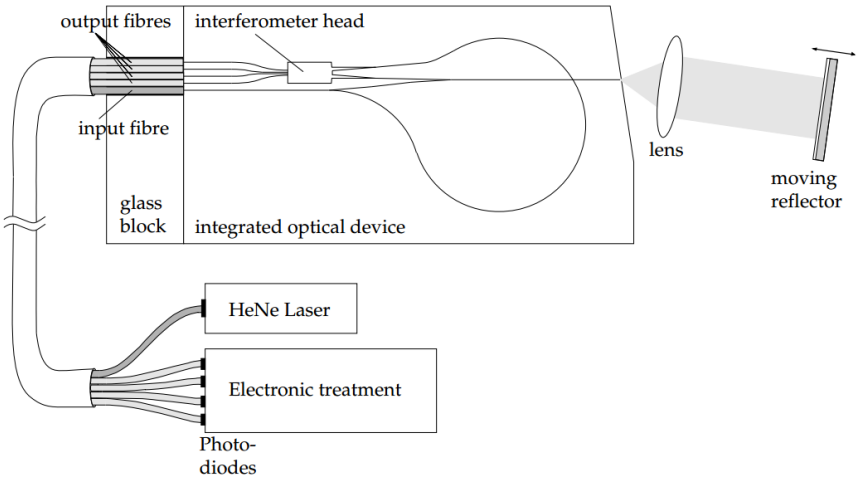

Figure 2.12 Integrated optical displacement sensor on glass with multiphase detection

[Adapted from Lang et al., 1998]

An integrated optical displacement sensor on glass with multiphase detection is shown in figure 2.12. Generally the integrated optical displacement sensors outputs two phase shifted

output signals which are minimum configuration necessary for detection of the direction of the movement. However it suffers with problems dealing with signal fluctuations and diminishing contrasts especially when an operation of displacement sensor beyond simple fringe counting or over a large measuring range is demanded (Lang et al., 1998). So a four channel pi/2 phase shifted interferometer system was designed by Lang et al to overcome the above difficulties by suitable electronic processing and allowed fringe counting with a precision of λ/8 with measurement range of several meters with an accuracy of 10^{-7} in a temperature stabilized environment.

Higurashi and Sawada developed an integrated micro- displacement sensor based on hybrid integration technique (Figure 2.13). The sensor structure had a polyamide waveguide, a distributed feedback diode laser, a two segment edge illuminated refracting-facet photodiode, a polarization beam splitter, a quarter wave plate, and a beam splitter all onto a single silicon substrate. The components formed an integrated Fizeau-type interferometric displacement sensor. Nanometer-scale positioning of the mirror was accomplished with good stability against creep phenomena of the piezoelectric transducer (E Higurashi et al., 2002).

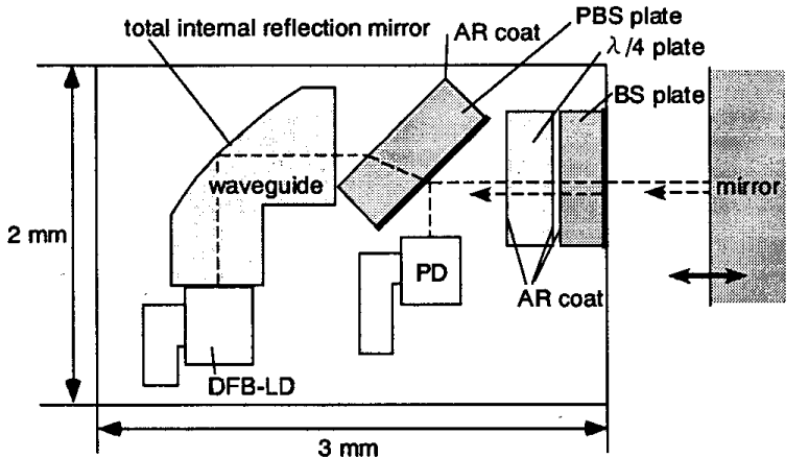

Figure 2.13 Schematic of an integrated Fizeau based displacement sensor
[Adapted from E Higurashi et al., 2002]

A monolithic integrated optical micro displacement sensor on a GaAs substrate containing laser diode photodiode and optical waveguide has been developed by Ito et al which used a divergent laser beam for displacement measurement with resolution as high as 0.01 um (Ito et al., 2003). The measurement principle was based on received light power against the displacement.

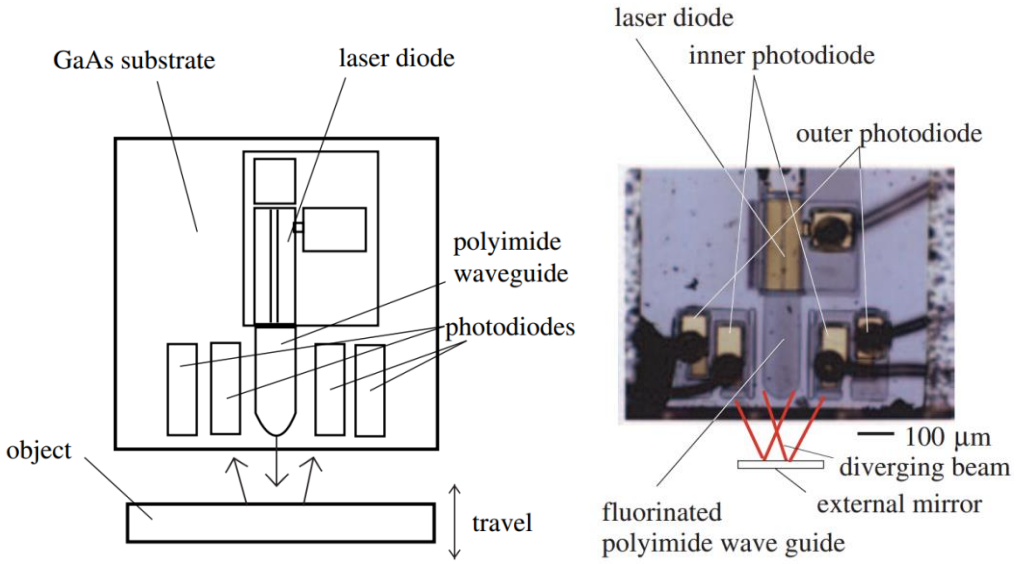

Figure 2.14 Monolithic integrated two dimensional micro displacement sensor using beam divergence [Adapted from Ito et al., 2003]

With large displacement of the object the received light power decreases as the displacement increases and vice versa because of the divergence of the laser beam. The sensor is only 0.8×0.75 mm2, and can therefore be directly attached at the place where the displacement is to be measured. Another similar micro displacement sensor based on beam divergence was developed by Inokuchi et al which was two dimensionally distributed and monolithically integrated with eight PD's and a VCSEL in the center. This sensor can measure linear motion as well as tilt angle external mirror. Use of eight PD's in two dimensional from enabled increased measurement rage of the sensor (Inokuchi et al., 2009). The size of the sensor was 1.3mm x 1.3mm x 1.3mm. Thus all the above examples suggest the feasibility of integrated optics technology for the development of miniature metrology sensor systems. With size being greatly reduced such sensors systems will facilitate easy installation onto the machining tool to provide on-line measurement of distances and surface profiles.

2.11 Optical probing using flying spot scanning systems

The integrated metrology sensor system presented in this thesis incorporates a separate optical probe structure for lateral scanning of the measurement surface. The design of the lateral scanning probe will be based on the flying spot laser scanning microscopy system. The following section will review various scanning probes developed and implemented on variety of probing systems from imaging to metrology applications.

In laser scanning microscopy the object or the sample under test is scanned point by point by a focussed laser beam using a microscope objective and the characteristic of the object is generated from the reflected radiation by electronic systems. Generally two basic schemes are prevalent in laser scanning microscopy; finite conjugate and the infinity corrected microscopes. In the finite conjugate systems an objective lens creates an intermediate image of the sample which is seen through an eye piece. This has a simple configuration as it has few optical elements but has other drawbacks. Use of optical components such as beam splitter or filters within the beam path will lead to intensity reduction and aberrations in the system.

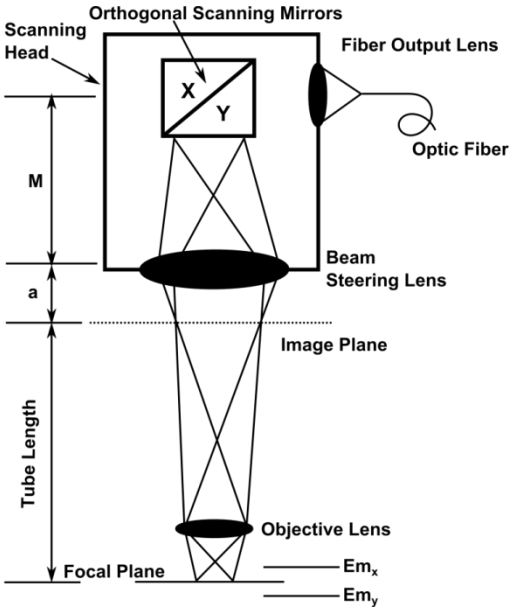

Figure 2.15 Schematic representation of the scanning head configuration of the fibre optic laser scanning confocal microscope. [Adapted from Delaney et al 1994]

One of the examples for confocal microscopy using standard finite microscope objectives and single mode fibre as both source and detection aperture is shown below (Delaney et al., 1994). This design used a standard microscope objective with a fixed tube length (160 mm, Figure 2.15) where objective forms image of the sample. The benefit of this design is that one less lens is required for beam scanning; however it is extremely difficult to find a suitable objective lens having non-infinity corrected format in the wavelength operating range of 1500 nm -1600 nm.

The above limitations of the finite conjugate objectives are overcome by the infinity corrected scheme. This configuration uses infinity corrected objective and a tube lens so as to avoid off axis rays to improve the performance of the microscope (Pawley, 2010). The infinity

corrected objective does not produce the image of the sample; instead it only gives the parallel beam. Thus it requires an additional lens (tube lens) to form image of the sample at the intermediate image plane. The distance between the objective and tube lens (tube length) needs to be optimized to provide flexibility to microscope configuration without compromising the performance of the device. Since the beam remains parallel between the objective and the tube lens so any introduction of optical components will not produce any distortion in the system. Generally the tube lens is placed at its focal length from the objective lens to obtain better angular control of the illuminated spot when operating in the confocal arrangement. If the scan element is placed at the back focal plane of the scan lens and the tube lens back focal length coincides with the intermediate focal plane formed by focussed spots of scan lens will provide larger angular movements of the beam at the scanning element to translates to a much smaller angle at the objective lens and corresponding lateral movement of the beam on the sample plane.

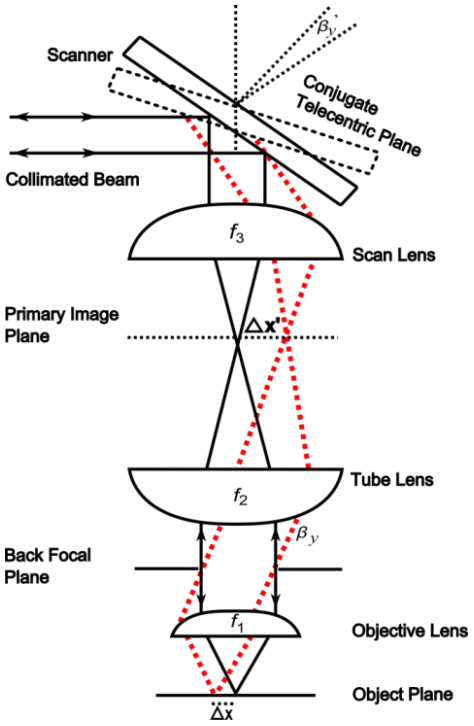

Figure 2.16 Simplified diagram of the scanning head of the confocal fluorescence microscope

[Adapted from Pawley, 1992]

The diagram above (Figure 2.16) is an altered version (to show only one degree of scan freedom) of a generic telecentric scan system as found in a typical confocal microscope system (Pawley, 2010). Several optical probes based on telecentric scanning probe systems have

reported in literatures with its applications mainly in the biomedical imaging and instrumentation.

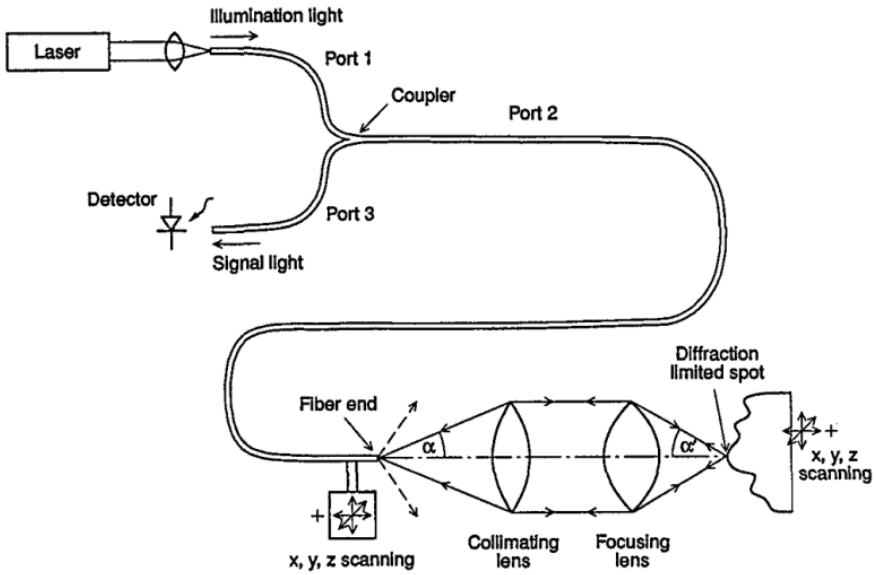

Figure 2.17 Schematic design of the FOCON design for a confocal microscope [Adapted from Dabbs et al. 1992]

Dabbs & Glass (1992) consider a system using two infinity corrected microscope lens as shown above. In order that non-confocal operation is maintained, it is necessary to ensure that NAcollimator > NAfibre (Dabbs et al., 1992; Wilson et al., 1987). This system is more compact, as it requires fewer elements (Figuire 2.17). However the scanning system here works laterally, and uses optical end fibre to rapidly scan in the x, y and z directions. Use of single mode fibre in place of conventional pin holes allows fibre optic confocal microscope (FOCON) to operate more reliably even in a dirty environment. The microscope head can also be poistioned far from the source and electronics allowing it to operate in noisy or hazardous locations.

Similar construction was employed by Kim et al to construct a near-infrared fibre optic confocal microscopy system with 3-D scanning capability for Bio-photonics applications (Kim et al., 2008). The system showed a lateral resolution as high as 1.1 um with 60X objective lens. To maximize the coupling efficiency between the collimator and the single mode fibre a high numerical aperture collimating (N.A = 0.36) lens was used. The use of high numerical aperture reduced the confocality and hence the resolution of the system had a value close to the conventional wide aperture conventional microscope.

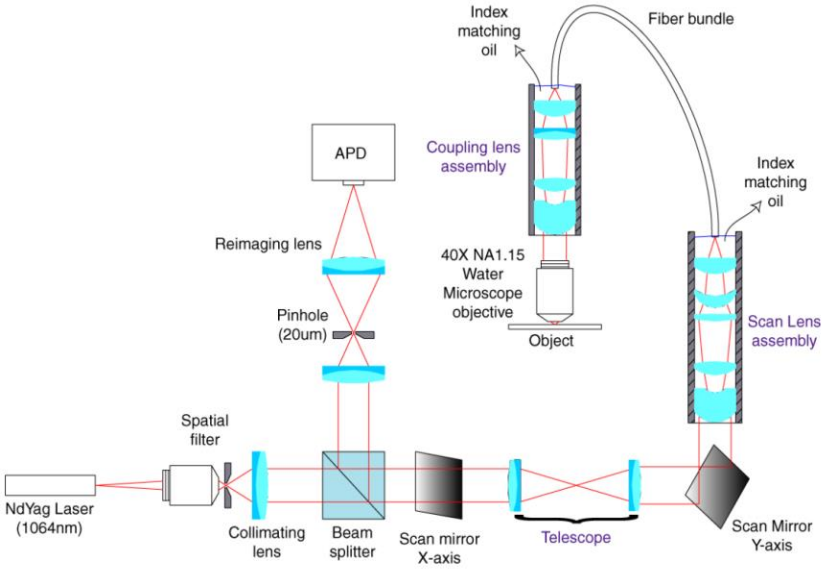

Figure 2.18 Schematic of the fiber confocal reflectance microscope

[Adapted from Liang et al., 2001]

A fiber confocal reflectance microscopy (FCRM) was developed for detecting pre-cancerous cells in the crevix by in-vivo imagaing using a coherent-fibre-bundle (Liang et al., 2001). The system consited of commerically available microscope objective, custom designed telescope, scan lens and coupling lens (Figure 2.18). The lateral resolution of the system is limited by the fibre spacing in within the fibre buldle and the magnification factor of the microscope objective and the coupling lens combination. The measured lateral and axial resolution of FCRM was 2um and 6um respectively and optical sectioning was sucessfully performed over the thick human cervical biospy tissue. Drawback associated with fiber bundles include inherent pixalation due to finite spacing between the fibres and a limitation on the system's lateral resolution imposed by sampling requirements.

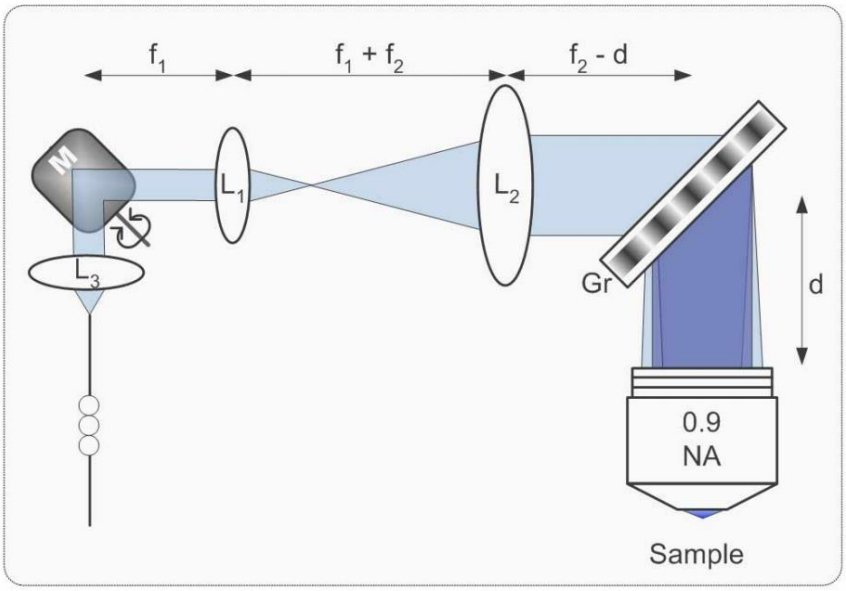

Figure 2.19 Imaging arm configuration of the spectrally encoded confocal microscopy. galvanometer mounted mirror (M), transmission grating (Gr), L1 and L2 from the afocal telescope system, L3 is the fibre beam collimator [Adapted from (Boudoux et al., 2005)]

Boudoux et al developed a spectrally encoded confocal microscopy (SECM) using the optical fiber as pinhole (Boudoux, et al., 2005). The figure of the Imaging arm of the SECM is shown in the figure 2.19. A rapid wavelength source with 70 nm spectral bandwidth and 0.1 nm line width was used to obtain large field of view. Large field of view image acquired demonstrate high lateral resolution (1.4 um) and axial resolution (6 um). Instead of fibre bundles complicated scan lens and coupling lens assemply he employed simple achromatic lenses. Light from the single mode fibre was collimated onto a galvanometer mounted mirror by a near infrared achromat and relayed to high groove density transmission holographic diffraction grating and finally incident onto the sample through the objective lens.

A galvanometer mounted mirror provided slow axis scanning of collimated light into and out of the plane of the figure while grating gives fast axis scanning by diffracting the wavelength swept light on the sample. Grating was placed between the objective lens and the tube lens and hence no distrotions occurred in the system. Rapid change in wavelength alowed fast scanning of the focussed spot across the sample and thus rapid detection of the signal using a single photodiode. As it does point by point scanning the signal as a function of time represemts the signal as a function of wavelengths and hence eleminates the need of spectral detection and makes configuration simple by the use of simple photodetectors to detect the signal.

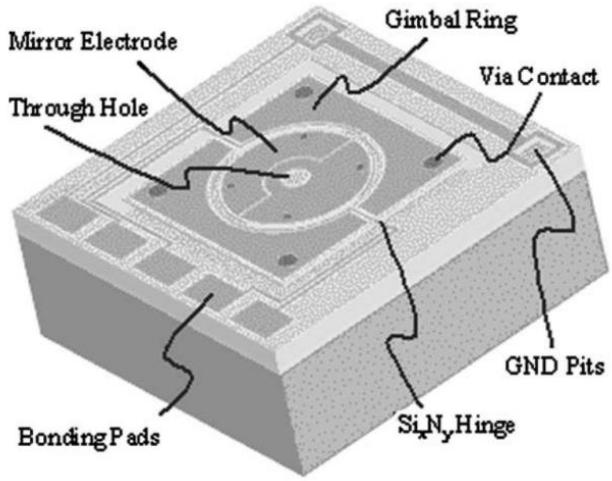

Figure 2.20 Schematic of MEMS gimbal mirror [Adapted from Miyajima et al. 2004]

Recently miniaturised scanning mirrors based on the microelectromechnical systems have have gained significant interest as it brings unique strength of miniaturization, batch fabrication and easy integration of actuators, sensors and electronics (Dickensheets et al., 1996; Maitland et al., 2006; Miyajima et al., 2004). Miyajima et al. developed a MEMS gimbal mirror for confocal laser scanning microscope shown in figure 2.20. The substrate used for mirror was silicon with a high resistivity of 3 kΩ, and was contacted with the driving electrodes by several via contacts to generate potential difference in the mirror substrate. Shin et al demonstrated a fibre-optic confocal microscope using a MEMS scanner and miniature objective lens (Shin et al., 2007)[14]. This used a miniaturised microscope which substantially reduced the size (~ 40-50 mm) of the probe. The beam scanning is provided by a MEMS scanner with electrostatic vertical comb actuators. The axial and lateral resolution reported is to be 9.55 um and 0.83 um are in good agreement with the theoretical values. The disadvantage to this MEMS scanners is its nonlinear response between the voltage and the mechanical scan angle and unstable scanning characteristics due to a significant tendency to exhibit the pull-in phenomenan and cease scanning operation (Kumar et al., 2010).

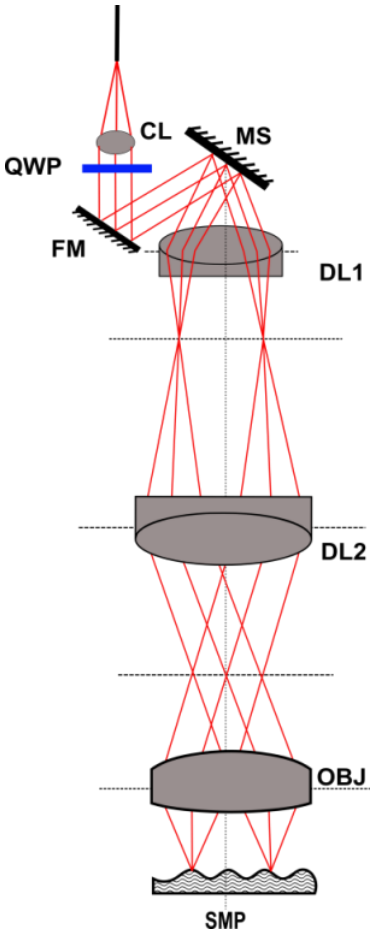

Figure 2.21 Schematic of the optical layout of the single-fibre laser-scanning confocal microscope probe CL - collimating lens; QWP – quarter wave plate; FM - folding mirror; MS - micro mirror scanner; DL1 - doublet beam expander lens 1; DL2 - doublet beam expander [Adapted from Kumar et al., 2010]

Another forward imaging laser scanning confocal micrscope for interventional imaging was demonstated by Kumar et al. The schematic of the optical probe is shown in figure 2.21. The distal forward imaging probe consisted of microelectromechanical scanner (MEMS), afocal Keplerian bem expander, and the high- NA objective lens. A 2-axis MEMS scanning mirror provided faster raster scanning ~ 2.5 kHz line scan and 3-5 frame per second for sample imaging. Lateral and axial resolution of the probe measured to be 0.49 um and 4.18 um respectively. With all the advantages there are drawbacks to the MEMS based beam scanning systems. MEMS micromirrors used in the above mentioned studies have complicated fabrication processes resulting in low wafer yield.

Several approaches of beam scanning techniques such as scanning galvo-mirrors and micro-electro-mechanical-systems mechanical systems or proximal scanning of single-mode fibre bundles have been devised and implemented as discussed in above examples to scan the beam in

orthogonal directions onto the object plane. The majority of probing systems developed so far are limited to biomedical or endoscopic imaging applications only. The major drawbacks of these spot scanning techniques is that the off axis lens aberration must be minimised and corrections are required for the off-axis light transmission reduction (Dabbs & Glass, 1992). Also because of the mass of the elements and the mechanical scanners used makes the configuration very complex leading to beam scanning fairly slow.

2.12 Summary

Majority of engineering components and devices failures are surface initiated. Thus surface metrology is becomes important for measurement and quality control of the manufactured surfaces to increase the throughput. Various metrology tools have been developed for characterization of engineering surfaces. Each instrument has its own advantages and disadvantages. Stylus instruments are contacting in nature and are relatively slow. Being non-destructive, optical profiling especially interferometric based has advantages such as high speed, resolution and measurement accuracy. Numerous examples in in open space, fiber and integrated optics suggest viability of interferometry based metrology systems for micro/ nano- scale online measurement applications.

Out of all, metrology sensors based on integrated optics technology will significantly reduce the size and cost facilitating embedding measurement on the manufacturing platform. The majority of integrated optic based metrology sensors reviewed in this chapter have been developed as either displacement or position sensors. None of the IO based sensors have been demonstrated so far which can perfrom both online surface profile and absolute distance measurements. Also these sensors are very simple as they have fewer integrated components mainly waveguides and photodiodes. So by exploiting the hybrid integrated technology it is possible to achieve multichip integration of devices of desired functionality onto a single optical chip making up a very compact interferometer sensor system encorporating a lateral scanning probe for embedded metrology applications.

3 Device Integration Technology

3.1 Introduction

This chapter describes the photonic integrated circuit technology which forms the basis of development of metrology sensor system. Benefits of component integration onto a single platform are discussed in comparison to the bulk optic systems. Various device packaging approaches with special emphasis on hybrid integration schemes and the key challenges facing the integration and packaging are presented. Finally the integration platform developed for the integration of metrology sensor are described in detail.

3.2 Photonics integrated circuit technology

A photonic integrated circuit (PIC) is an optical analogue of an electronic integrated circuit (EIC). While the latter integrates many transistors, capacitors, resistors, a PIC integrates optical components such as lasers, detectors, modulators, multiplexers, amplifiers (Infinera, 2013). Integrated optics finds extensive application in the field of sensing, microfluidics, digital and analog communications, light sources, signal processing and instrumentation. Single mode fiber systems are generally required for linking such applications. In photonics integrated circuits light is guided and manipulated through waveguide structures fabricated by microelectronic fabrication techniques on a given substrate. These waveguide structures are the fundamental building blocks of PIC's which connects various other components and devices onto a single chip. A refractive index contrast is created between the core and cladding which provides confinement to the waves propagating through it. Based on the light interaction with the matter, integrated optics components are generally classified into two groups; active and passive components (Giancarlo C. Righini, 1988). An optical component which involves dynamic interaction with light and matter are called active components, e.g. lasers, amplifiers, modulators and detectors. Light amplification, electro-optic, thermo-optic, acousto-optic, pizeo-electric and liquid–crystal based systems undergo dynamical interaction and hence they all are categorized as active components (Doerr, 2013). Contrary to these optical components which provides only light guiding and redirection are called as passive components, e.g. waveguides, directional coupler, isolators, circulators.

The integration platform includes the use of both type of integration technology; Monolithic and Hybrid similar to those of electronics. Multiple single-function optical devices are assembled

in a single consolidated package and are interconnected with each other using electronic or optical coupling.

3.3 The need for optical integration

With current technologies majority of optical components and modules are assembled separately and are optically connected using fiber pigtails as the primary method for optical interconnection (W. Hunziker et al., 1996). In recent years the demand for the high density optical interconnects and communication systems spurred interest in the optical integrated circuits leading to a more mature and developed technology for higher level of integration and more functionality on a single chip while decreasing the component size and cost. The added leverage in terms of an established technology can be employed and harnessed to develop many other devices and tools for various purposes. In this work, we will employ optical integrated circuit technology for the development of metrology tool for surface measurement.

Device packaging is the critical aspect dominating the cost of a photonics module, therefore it is desirable to have fiber free interconnects based on guided- wave components with minimal degradation in performance. Photonics integrated circuit (PIC) integrates lasers, detectors, modulators with passive array of waveguide onto a chip eliminating the need of free space fiber pigtail connection. The optical integration on a single chip offers many advantages: higher and newer functionality, reduced packaging of individual components and cost, improved performance by eliminating parasitic, and more uniform control of the environment (temperature) (Whitney, 2002).Since most integration provides shrinkage of elements and obsolescence of additional packaging levels, the size of devices is reduced. This enables smaller footprint products. Fewer interfaces and fewer separate parts normally enhance reliability and so on. Further, multiple component integration with desired functionality at a low packaging cost is the key challenge for the future optical integrated circuits.

3.4 Monolithic and Hybrid integration

Optical integration involves integration of various optical components onto a single optical chip. The methods involved in the device integration are; monolithic and hybrid integration techniques. Monolithic integration unifies all components and devices (active and passive) on the same substrate. Thus monolithic integration technique provides all photonic coupling and other functionality within the substrate providing a single physically unique device. However there are

practical difficulties in implementing active OE components such as lasing, modulation and light detection in silicon and limits this technique to the integration of passive devices only. Hybrid integration technique has the added advantage of integrating active components such as lasers, photodiodes directly onto the substrates or the motherboard containing waveguides as light guiding structures. Various sub–components and devices reaching their performance targets can be easily bonded to the motherboard so as to achieve operational requirements of the device. Thus this provides flexibility of incorporating on chip elements best suited for a particular application compared to monolithic subsystems.

3.5 Hybrid Integration

The assembly of optical components using the hybrid integration technology can be very complex as many discrete devices need to be interconnected in a package with very close degree of tolerance. Thus there are several issues must be addressed for practical hybrid integration (McDougall, 2006). While choosing a hybrid integration method as a viable alternative to discrete devices and monolithic integration, one must consider the following.

1. Optical coupling: Coupling efficiency is a critical parameter for the integration platform and the waveguide. Loss arises due to the mode mismatch and miss-alignment between the waveguide and the fibre. Difference either in the index contrast or the core size leads to mode mismatch and power loss at interfaces connecting various active and passive components (Lin et al., 1995). An alignment tolerance is another big issue and it becomes significant in the case of power coupling between the waveguides with small mode size. Alignment tolerances greater than 1 um range is required in such cases and hence this enforces the use of sophisticated alignment technologies to maintain good output coupling.
2. Packaging feasibility and tolerances: Packaging is a big challenge as different materials will have different packaging design requirements due to difference in optical, mechanical, thermal properties. For example if the two materials have different coefficient, the component will get misaligned at different operating temperatures and will require external coolers, thus compounding packaging complexity and cost. Existing assembly technology uses active alignment techniques where the components are electrically activated to precision align onto a chip while monitoring the light output in

real time. So there is need for a more versatile technology such as passive assembly to realise a cost effective assembly of multiple components both actives and passives.

3. Heat dissipation management and power consumption: Heat generation becomes a problem with the increasing density of active components on the chip operating at faster speed. So proper heat sinking or a cooling mechanism is required for reliable performance of the device. This also poses a packaging challenge.
4. Manufacturability: It has been observed and verified that an extra processing step in manufacturing a module will have increased chances of error and module failure. In addition, this compounds to the overall cost of the device. The introduction of alignment features such as registration marks, contact metallisation, with the etching in the lithography step will facilitate better alignment by relieving the required precision for placing the tool and also decreases assembly time drastically.
5. Multichip integration: Multichip integration is a challenge in terms of the alignment of each component into the assembly. Various techniques of passive assembly have to be implemented to successfully integrate the modules.
6. Electrical and optical performance and crosstalk: The optical performance of the module is entirely based on the component performance. Hybrid integration which requires very tight alignment tolerances increases the possibility of degradation and cross talk. Since the optical mode properties of individual components are different, coupling efficiency becomes very critical in the performance of the device. There can be the chances of optical cross-talk arising due to component densities and the components chosen for integration. Electrical performance depends upon electrical circuit design and the isolation between electrical lines.

3.6 Material for integrated optics devices

Optical components integration on a single chip involves integration of passive waveguides, light generation and detection, as well as signal manipulation such as amplification, modulation, regeneration and switching. To achieve the above mentioned functionalities it requires suitable material platforms called as substrates to support large scale optical integration. The choice of substrate material depends on the application required, cost and the complexity of the fabrication process. It is always desired to have a single substrate system for all the devices to be integrated but this brings limitations to the optimum device performance. Also the material which can

provide all the functionality especially light generation and detection are very limited. Indium phosphide (InP) and gallium arsenide (GaAs) are the examples of such substrate system. The major difficulty with these material systems is the complex fabrication techniques and the cost and integration limit to only few devices per chip. Because of this they are generally confined to research and laboratory demonstrations (Grattan et al., 1995). For sensor applications where cost is often very important hybridisation of separate components such as light sources, detectors and waveguides can be highly prescribed to achieve the required sensor function. There are several choices available for the substrates such as glasses, lithium niobate ($LiNbO_3$) and silicon (Si), polymers for the hybrid integration. Lithium niobate is an outstanding candidate as it offers a unique combination of excellent electro-optical, acousto-optical and non-linear properties allowing the fabrication of various functional devices except the light sources and detectors (Selvarajan, 1992). But the major difficulty is the growth of such crystals in large sizes and the cost which is an obstacle to the commercial success of components made from lithium niobate. Polymers can provide cost effective solution for hybrid integration applications but they have the disadvantage of large temperature dependence and poor shelf life. In terms of the cost and ease of processing silicon is an ideal substrate material for hybrid integration applications. The compatibility of silica based waveguides on the silicon with the optical fibres makes silicon an attractive substrate not only for passive planar lightwave circuits (PLCs) but also as integration platform (Henry et al., 1989). In addition it offers multi-chip integration (higher level of integration) and by leveraging the well-developed silicon technology in microelectronics industry mass production of hybrid integration of optoelectronic devices all on a general purpose silicon platform can be obtained at a potentially low cost (Binh, 2008).

3.7 Silicon substrate as the integration platform

Among the available material platforms silicon based PLCs are of great interest because, in addition to optical function, they have versatile electrical properties and can combine electronic control units on the same silicon platform. Also the silicon substrate guarantees high surface quality, good thermal conductivity, chemical stability, mechanically robust and low cost even for large area substrates (Jones et al., 1996). Other advantages include low toxicity, tolerance to high processing temperatures ~1500^{o}C, ease of etching and micromachining (Petersen, 1982). For hybrid integration silicon is micro-machined to facilitate assembly of electronic and optoelectronic components onto the silicon motherboard. Micromachining refers to the selective

removal of significant amount of silicon by chemical or the physical process to create small features (trenches, holes and membranes) with submicron tolerances to provide dimensional control and alignment to structures such as waveguides. Two popular techniques of micromachining are anisotropic wet etching and reactive ion etching (RIE). Wet etching relies on the fact that the different crystal planes have different etching rates based on a silicon oxidiser (H_2O_2, HNO_3) and a complexing agent (HF, H_2SO_4). Commonly used etchants are potassium hydroxide (KOH), Tetramethyl ammonium hydroxide (TMAH), NaOH, LiOH and NH_4OH. These chemicals have different etch rates in silicon and hence depending on the application one or the other solution is preferred for etching. The redox reaction takes place involving electron transfer as a part of surface reaction. Overall reaction which occurs during anisotropic chemical etching of silicon is

$$Si + 2OH^- + 2H_2O \rightarrow Si(OH)_4 + H_2 \rightarrow Si(OH)_2^{2-} + 2H_2 \tag{1.1}$$

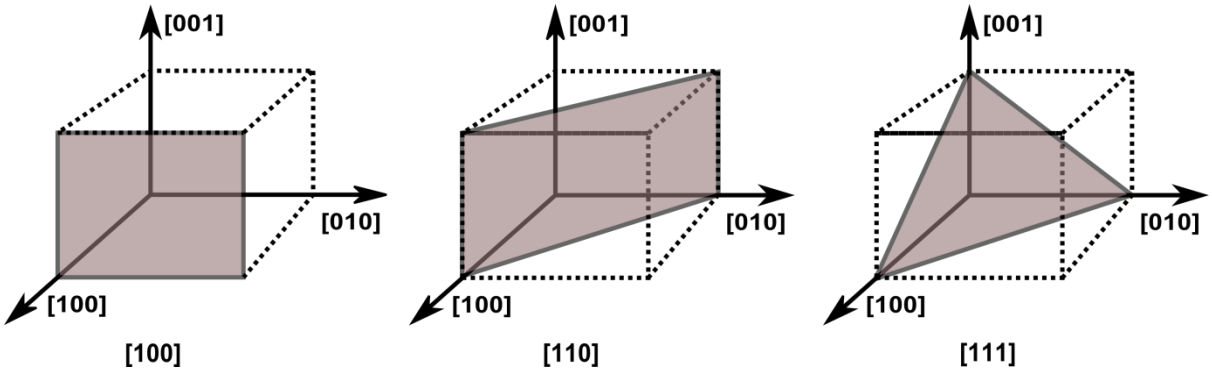

Figure 3.1 Crystal planes of monocrystalline silicon

The crystal planes of silicon is shown in figure 3.1. Etch rate of silicon (111) planes are up to 100 times slower than the (100) planes, allowing V-grooves, pits and other structures to be etched in the silicon surface (Bassous, 1978). The area which requires etching or micromachining is defined by photolithographic mask patterned onto the wafer surface in the form of photo-resist (Figure 3.2). This method of etching is low cost and very accurate for bulk micromachining of silicon wafers. The disadvantage with the chemical etching is that the waveguides have to be oriented with respect to crystal orientation of the silicon substrate. This puts some limitation on the component design corresponding to the placement of grooves.

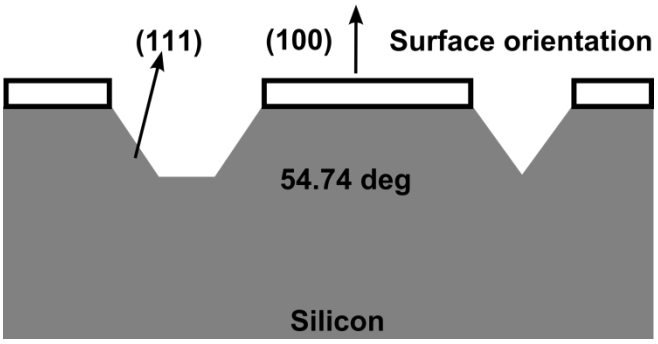

Figure 3.2 Anisotropic etching of silicon wafers using chemical method

Another technique of micromachining is RIE which uses reactive ions of plasma as etching medium (Terui et al., 1985). This is dry etch process and has the advantage of etching width and depth independent of each other on a silicon substrate. The geometric restrictions imposed by wet etching are overcome in the case of reactive ion etching. Also there is less chemical contamination compared to the wet etching. Very shallow (<100nm) and deep microstructures (>1000um) can be obtained by the RIE dry etching technique (Bryzek et al., 1994). Silicon pedestals were etched using RIE by Armiento et al. against which laser diode arrays were positioned, relative to an array of fibres held in V-grooves (Armiento et al., 1992). So depending on the application and requirement the above simple techniques are used to fabricate V grooves and pedestals to assist hybrid integration of optical components such as waveguides, optical fibres, lenses etc.

3.8 Integration platform and packaging approaches

Development of packaging technology is needed for turning the integrated optics (IO) chips into real and practical IO devices with optical fibre pigtails (H. Liu, 2005). Generally speaking, packaging technology should be modified to match different substrate materials used for IO chips. Packaging is an important aspect in the development of an integrated optics device as it dominates the cost of the module. A large proportion of the cost originates from process of achieving accurate alignment (S. Li et al., 2011). This is one of the barriers to the large scale integration and mass production of devices. Packaging of integrated optics devices includes manual coupling and alignment, V grooves, fibre array fabrication, wiring, bonding sealing and reliability test. Hybrid integrated module packaging requires high precision alignment of optical axes of waveguides and optical components for efficient coupling and optimised performance of any device. Both active and passive alignment techniques for device

integration have been developed. The active alignment is accomplished by close loop optimisation of components until optimum coupling of light is achieved (Eiji Higurashi, 2008). Low processing time and high equipment cost makes this alignment process expensive and of low throughput. Particularly in cases where there is multiple chip integration, alignment of individual components can be time consuming and costly affair leading to low yield. Hence active alignment is most appropriate for development of low-volume or prototype subsystems where cost is not a principle driver (Wada, 1994).

Passive alignment techniques on the other hand provides an easy and cost effective solution for such multichip integration as it eliminates the need of alignment of optical axes by means of micro manipulation which requires real time monitoring of optical output power (J. i. Sasaki et al., 2001). The impact of passive alignment technique becomes more profound as optoelectronic module incorporates variety of optical elements each requiring alignment, on a common platform. Passive assembly technique enables the development of such subsystems using production assembly techniques already developed in the electronics industry. Leveraging such techniques reduces cost of device development. But this alignment technique is mainly limited due the accumulation of misalignments occurred during the fabrication process (Park et al., 2002). So with greater accuracy in fabrication, high degree of component alignment can be easily achieved. Currently there are two major approaches available to obtain passive optical alignment; mechanical passive alignment in which the parts are made so precise so that they fit properly into alignment and the second is the visual alignment by a camera to guide the manipulation of parts into located positions. Common type of passive alignment techniques are:

- Index alignment using fiducial marks
- Self-alignment by solder bump technique
- Mechanical contacts using mechanical rails, pits and stand-offs
- Purely visual passive assembly
- Alignment with Micro Electro Mechanical Syatems (MEMS) or micro machines

The above mentioned techniques provide device alignment in horizontal and vertical directions (in-plane alignment) for efficient light coupling. The section below details the various integration platforms for aligning and packaging optical components onto an optical chip. Yamada et al developed a low-loss silica based waveguides on silicon substrates as an

integration platform (Y Yamada et al., 1993a). This integration platform was called as Silica on Terraced Silicon (STS, Figure 3.3).

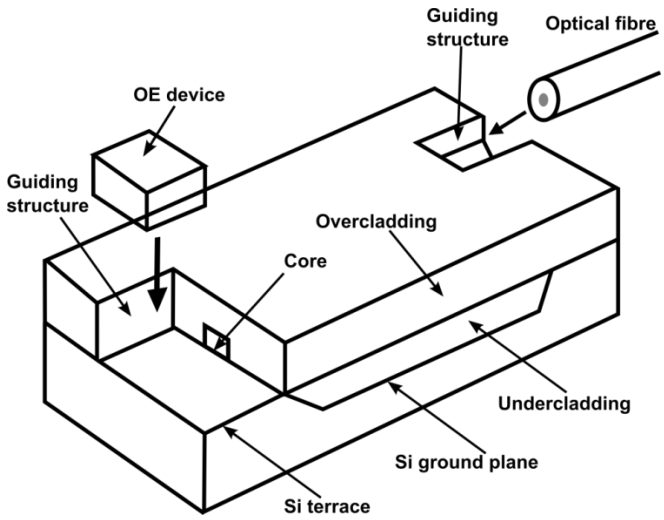

Figure 3.3 PLC platform STS for hybrid integration [Adapted from Y Yamada et al., 1993b]

A vertical etch well was made in the silicon substrate which was then filled with the thick (30 um) silica under cladding material. Further the surface of substrate was flattened by mechanical polishing. The waveguide (6 um thick) is then formed onto the silica underclad layer, the under surface of the core layer being coincident with the height of the terraced surface. Guiding structure for the OE device was formed on the silicon terrace by RIE of silica based waveguides. Because the silicon terrace acted as an etch stop layer during etching, the relative position between the core and the terrace was precisely determined. Thus silicon terrace acted as an high precision aligner and heat sink when the optoelectronic devices is flip chipped bonded onto the silicon terrace. To couple the light from the integrated optoelectronic device for external use optical fibre connections are needed. V groves are commonly used for pig tailing of integrated optical devices and connecting to planar waveguides. High precision V-groves are anisotropic etched (different etch depth depending on the crystal orientation) in silicon to place fibre at correct position for optimum coupling from the waveguide (Boyd et al., 1978).

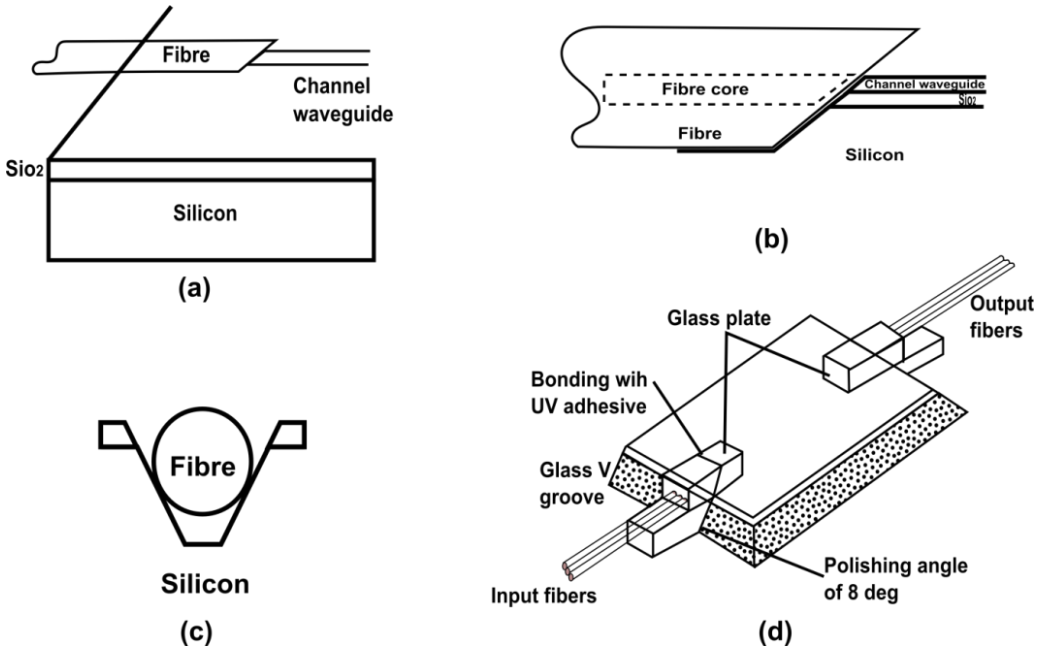

Figure 3.4 Fibre to channel waveguide coupling

(a) SiO_2/ Si substrate integration platform for fibre waveguide coupling, (b) Fibre supported on etched flattened V groove at the edge of silicon substrate, (c) cross-sectional view of the V-groove and the fibre and (d) fully integrated fibre pigtailed PLC chip [Adapted from Himeno, 1999]

Figure 3.4 shows input and output fibre arrays mounted on glass V-groves. End facets of the V-grooves and the PLC chip are polished at an angle of 8^o , and the V-grooves are connected to opposite ends of the chip by using ultra voilet (UV) curable adhesive (Himeno, 1999).

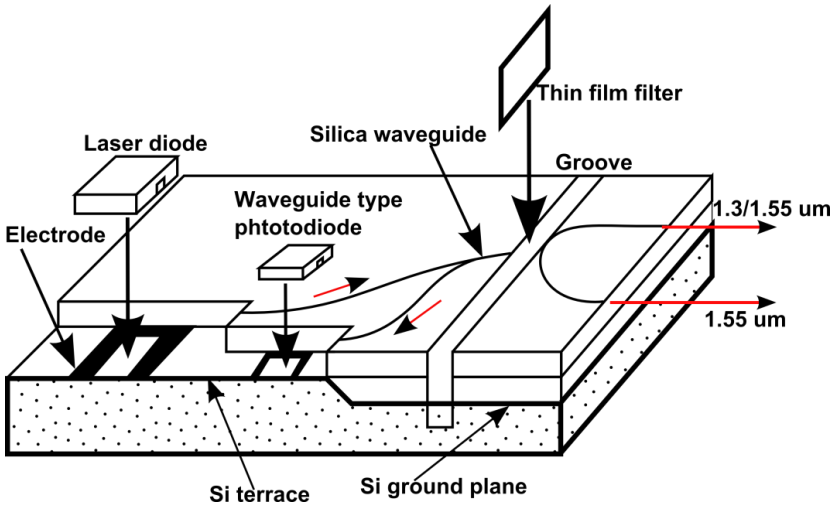

Figure 3.5 Hybrid integrated WDM trans receiver [Adapted from Y Yamada et al., 1995]

Yanmada et al developed an integration platform based on silica-on terraced silicon encorporating silica PLC which provided device assembly by simply flip-chip bonding of optical devices onto silica terrace (Y Yamada et al., 1995). The developed filter type wavelength

demultiplexing (WDM) transmitter/receiver module is shown in figure 3.5. A thin-film filter inserted into groove facing the waveguides to seperate the 1.55 um optical signals for video distribution. Flip chip bonding of spot size converted laser diode (SS-LD) and side illuminated wavguide photodiode (WG-PD) was performed to integrate it onto the substrate. No extra components such as lenses or mirrors were used in this configuration. This integration platform provided increased coupling efficiency and a much more relaxed components positioning by reducing the number of module components ans simplifying the assembly process. The edge detecting photodiode was also flip chipped integrated so as the light coupling occurs in-plane parallel to the wafer surafce (Yasufumi Yamada et al., 1989). A self-aligning technique based on the flip chip solder bump bonding was introduced by Michael and Colin for high precision chip assembly (Figure 3.6). Solder bumps were used to attach the integrated optical chip to the silicon substrate carrying optical fibres in V-groves and electrical connections on its dielectric insulated surface (Wale et al., 1990).

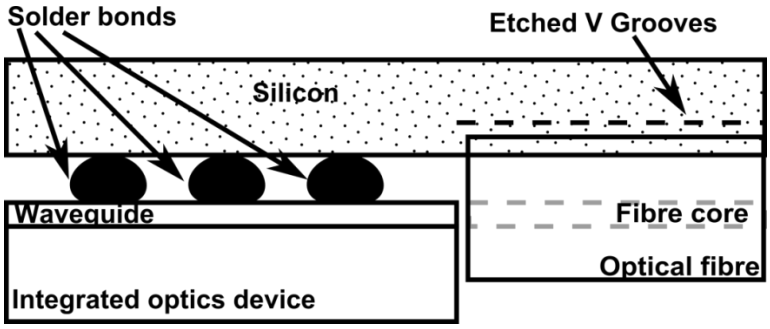

Figure 3.6 Solder bump assembly of an integrated optical device to optical fibres using silicon V-grove [Adapted from Wale et al., 1990]

Accuracy of solder bump method is determined by the photo-engraving steps used to prepare solder bumps and wettable metal pads. In this method precise volume of solder bump is placed between the wettable metals pads surrounded by non-wettable dielectric surface. When the solder is heated at the melting point, the melted solder exerts surface tension forces to achieve minimum energy configuration bringing structures to the alignment positions (Figure 3.7). The volume of the solder bumps determines the vertical alignment precision (i.e., its diameter and thickness). Alignment accuracies well within 0.5 microns variation have been reported by Edge et al and Hunziker et al (Edge et al., 1991; W Hunziker et al., 1995). Solder bump method for alignment is also used in conjunction with standoffs and stops is explained in later examples.

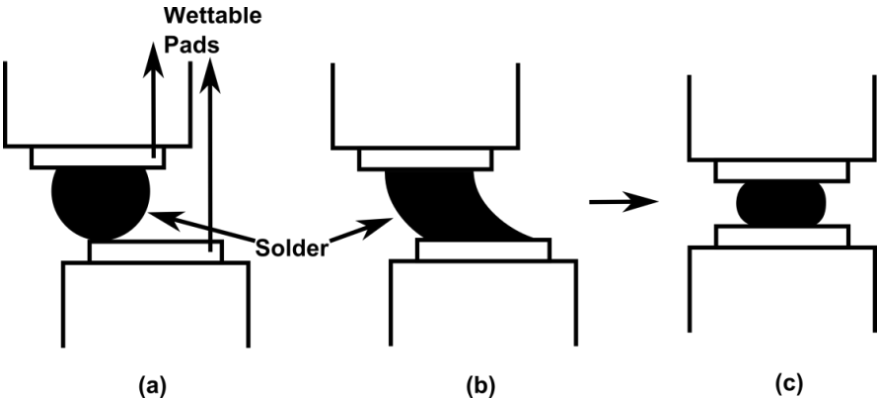

Figure 3.7 Stages of flip chip solder bump bonding process.

a) The parts are placed in contact, b) solder reflows, c) precise alignment is achieved

b) [Adapted from (Edge et al., 1991; W Hunziker et al., 1995]

In the above discussed Si-terraced PLC platforms there exists a step between the Si-Terrace and the PLC which may deteriorate the accuracy of the alignment mark position in the lateral directions and cause misalignments. A novel method of fabrication and structure of PLC platform presented by the Park et al overcomes this problem by achieving optical axis alignment using a signle mask containing PLC core, alignment keys of laser diode (LD) and V-groves for fibre alignment (Park, et al., 2002). So any misalignments due to multiple steps of photolithography is automatically eleminated. The proposed PLC platform is shown in the figure 3.8.

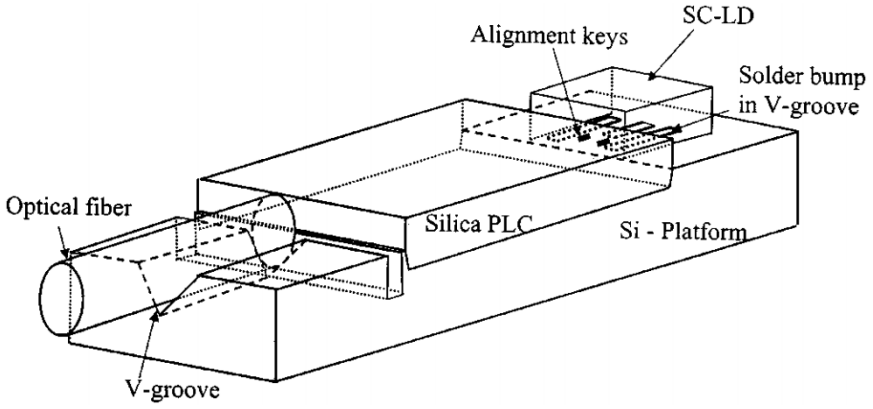

Figure 3.8 Configuration of the PLC platform developed by Park et al., 2002

High precision vertical alignment of LD core is achieved by precisely controlling the distance from the LD core and the surface. The LD is bonded with the solder bumps fromed in the V-grooves (Figure 3.9).

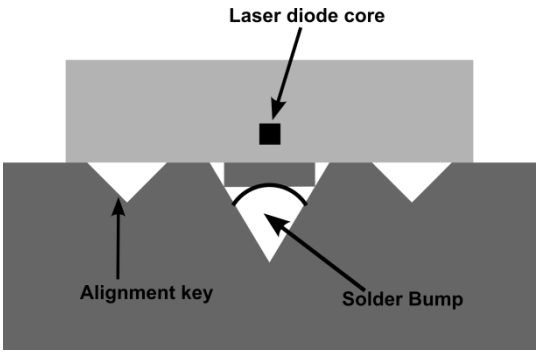

Figure 3.9 Vertical alignment of the laser diode by bonding it with the solder bump formed within the V-grove

Armiento et al proposed a silicon waferboard hybrid integration approach for combining optoelectronic, optical and electrical components. Accurate placement of the laser array is achieved through the use of alignment pedestals and standoffs fabricated on the waferboard surface (Armiento, et al., 1992). The positioning of the laser array was achieved by mating the edges of diode array to the alignment pedestals while the vertical positioning was fixed by mounting the laser array onto the standoffs whose thickness is controlled during the fabrication of waferboard. Thus this technique facilitated easier positioning of the laser emitting region just by controlling the standoffs thickness in comparison to the solder reflow method becomes easier. The cross-sectional schematic of the laser array mounted onto the waferboard is shown in the figure 3.10.

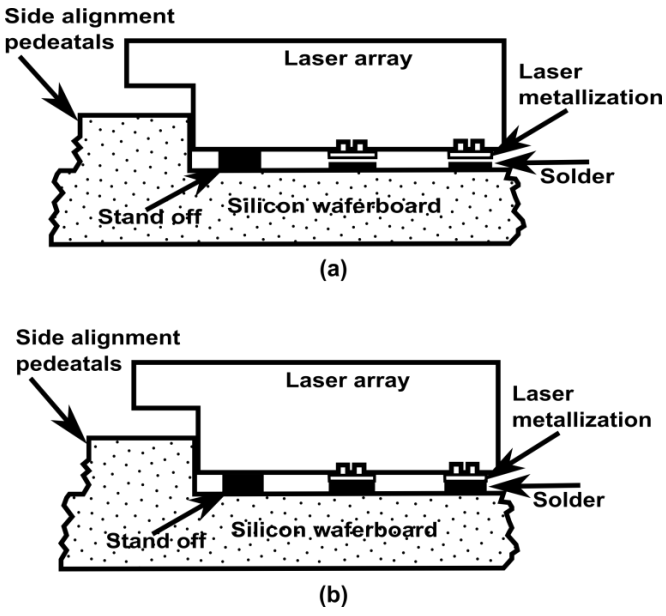

Figure 3.10 Cross-sectional schematic of a laser array mounted on a waferboard (a) before and (b) after solder reflow process [Adapted from Armiento, et al., 1992]

A similar approach was employed by Jackson et al., which used 4 mechanical standoffs at the four corners of integrated chip to place laser chip with etched notches (Figure 3.11). The standoffs are made of the same material as that of the waveguide and used as an in-plane alignment feature for the laser to butt up against. The laser chip is flipped and placed onto the standoffs with etched trenches against the alignment pedestals lowering the active so that the light is efficiently coupled to the centre of passive waveguide. Further the optoelectronic module was bonded using solder-bump technique (Sasaki et al., 1992). The use of standoffs however posed a problem as it provides frictional force in contact with the chip and nullifies the restoring force of the molten solder ball leading to misalignment. To overcome this problem, little offset to the pads are introduced.

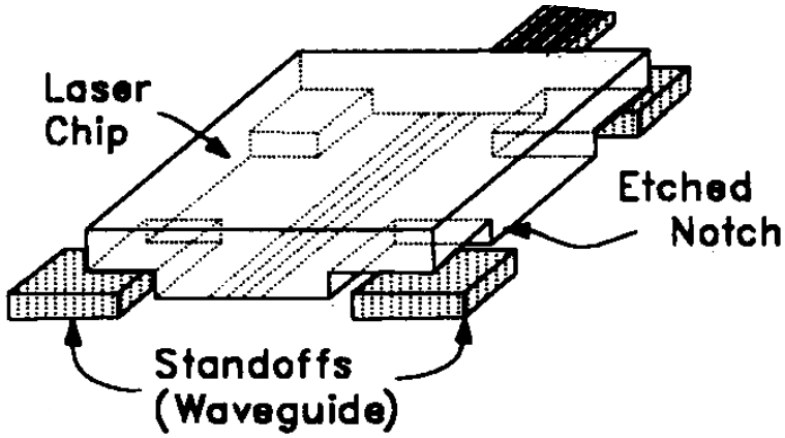

Figure 3.11 Schematic representation of laser chip integration to planar waveguides [Adapted from Jackson et al., 1994]

Depending on the etch tolerance of the waveguide and standoffs and etched trench alignment accuracy of the components can be determined. Tolerance limits of the components have been found to be well within ± 1 um which in turn in worst cases may cause misalignments in vertical and lateral directions by ± 2 um (Jackson et al., 1994). Figure 3.9 is an example of solder self-alignment with mechanical stops. The solder bump alignment is explained in the section below. Another passive alignment technique based on index alignment was first proposed by M. Cohen et al. The laser fibre alignment was achieved by a passive method based on the registration principles of the photolithography (Cohen et al., 1991). Fuducial marks and other critical features are lithographically placed onto the laser, the fibre carrier chip and the alignment plate which enabled precise placement by juxtapositioning of components such that each chip falls directly in line with the alignment registration marks (Figure 3.12).

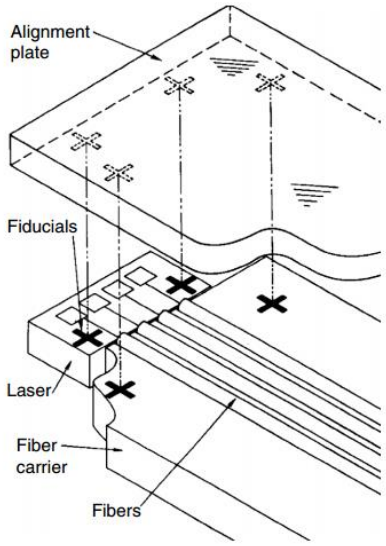

Figure 3.12 Alignment of four laser chip using the index alignment methods [Adapted from Cohen et al., 1991]

Vertical alignment alignment of both the components was automatically achieved because of their contact with the flat, smooth bottom surface alignment plate. After the alignment the components were on held by vacuum and further soldered onto a substrate to get the final module. K. Kurata et al developed another type of index alignment method which uses infrared light to observe the alignment marks (Figure 3.13).

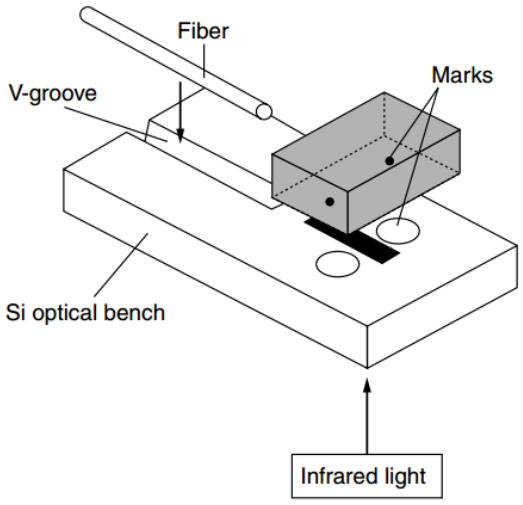

Figure 3.13 Index alignments using infrared light [Kurata et al., 1996]

Infrared light from the underside of the silicon optical bench (platform to integrate optical components and subsystems: motherboard) was projected and imaged onto an infrared video

camera to align the marks onto the optical bench and the laser diode. Further laser diode is bonded in position with the help of AuSn solder. An average alignment accuracy better than ± 1 um was achieved using this technique (Kurata et al., 1996). Index alignment methods have a clear advantage over mechanical contact alignment, as there is no etching process involved to create precise mechanical contacts. This method can applied to any type of substrate and OE devices. The various integration schemes discussed above deals only with in-plane light couplings between the waveguides and other components. Crookes et al proposed a simpler out-of-plane approach for coupling to self-aligned rear illuminated photodiode (Crookes, 1994). The alignment tolerances required for the photodiode integration significantly reduced compared to the in plane alignment technique employed by Yamada et al. The schematic of the photodiode integration platform is shown in figure 3.14. A mirror is fabricated in silica waveguides by chemical etching methods. Light propagating in the silica waveguide encountering the mirror get reflected normal to the propagation direction falling onto the rear illuminated InGaAs photodiode.

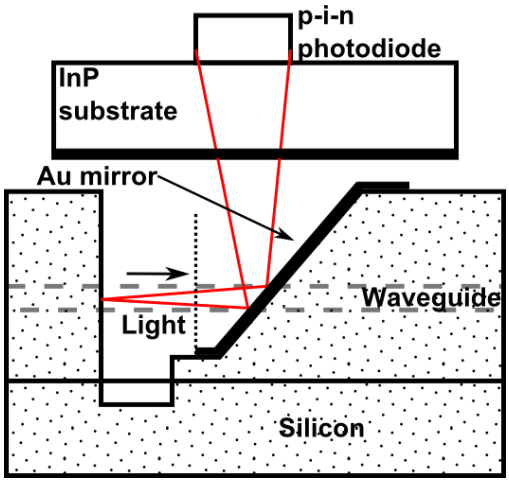

Figure 3.14 Out of plane light coupling to photo-detector using etched and metallised cavity mirror fabricated in the waveguide [Adapted from Crookes, 1994]

A multi-channel power level monitor based utilizing an upward reflector was demonstrated by Sasaki et al. A tilted narrow grove (angle: 30^{o}, width: 15 um) was fabricated to accommodate the thin film filter of thickness 11 um as a reflector (Figure 3.15) (T. Sasaki et al., 2001). A part signal of signal propagating through the PLC core was reflected upoaward, which was detected by the photodetector array.

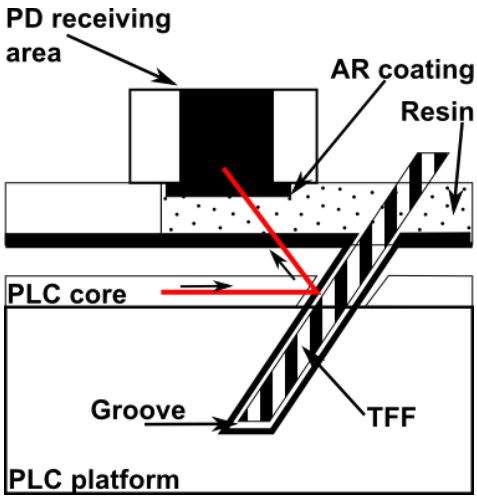

Figure 3.15 Out of plane light coupling to photo-detectors using the thin film filter [T. Sasaki et al., 2001]

In the above two examples the major challenge is the fabrication of high performmance sloping mirror which changes the direction of guided light from horizontal to vertical. Terui et al proposed a simpler method of micromirror fabrication for out of plane light coupling to photodiodes.

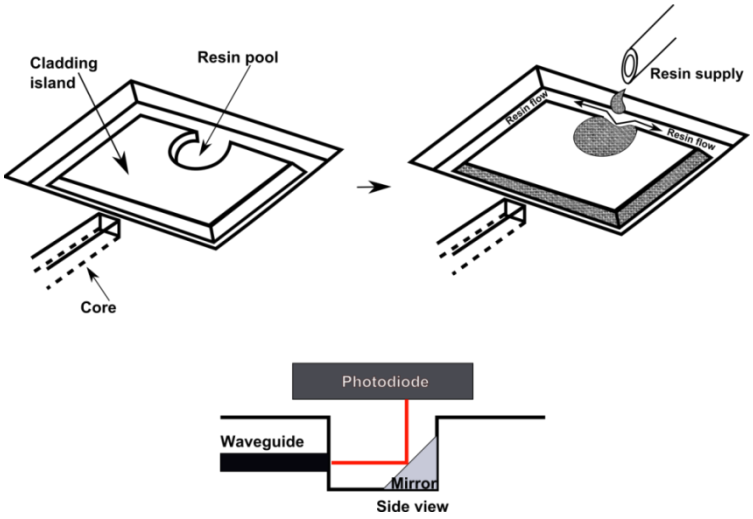

Figure 3.16 Light coupling to photo-detector by mirror fabricated into the groove using resin [Terui et al., 1996]

Figure 3.16 shows the micromirror slope fabrication process. At the end of waveguide where PD is to be mounted, a closed groove was cut by reactive ion etching technique. The close groove was then filled with resin which spread all around the side walls of cladding island because of surface tension, froming a slope structure opposite to the waveguide (Terui et al., 1996). Once the resin hardened the slope surface was coated with high reflecting gold (Au)

coating. The mirror exhibited high reflectivity (98%) and uniformity. Configuration of eight PD array integration platform is shown in the figure.

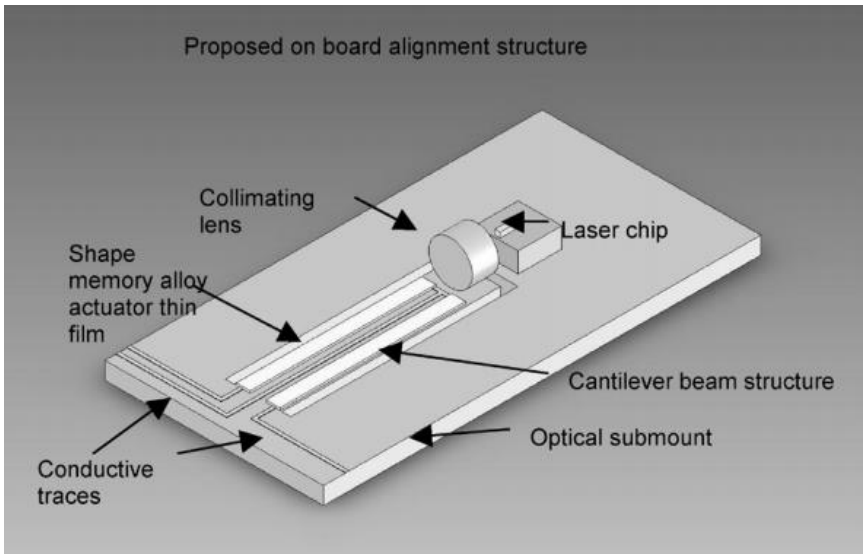

Figure 3.17 Shape memory alloys on board alignment [Adapted from Shakespeare et al., 2005]

Recently a MEMS integrated submount alignment apparatus have been developed by Shakespeare et al. The method utilizes microelectromechanical system shape memory alloy actuation technology to allow on-baord alighment using thermal and shape memory actuation (SMA) methods (Figure 3.17) (Shakespeare et al., 2005). High-precision alignment in lateral directions (x and y) were provided by a MEMS cantiliver structure. The proposed board alignment MEMS structure is shown in the figure. The MEMS thin films bi-morph actuation on the top and the bottom creates x-y motion for the alignment.

3.9 Integration approach adopted in this thesis

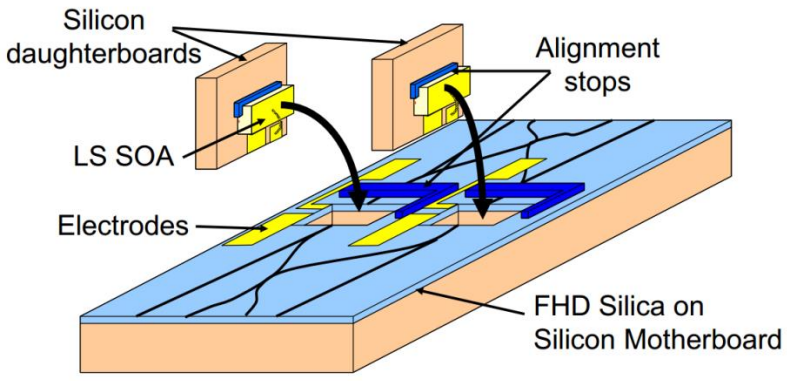

Figure 3.18 Schematic of CIP hybrid integration platform with passive assembly [Adapted from Maxwell et al., 2005; Poustie, 2008]

In this thesis hybrid integration approach similar to above discussed is utilized for the integration of different photonic components for application to surface metrology sensor. A silicon based integration platform (motherboard) will be developed to combine various optical components such as OE devices, single mode planar silica waveguides micromachined silicon submounts, isolators, thin-film filters, wavelength encoders and phase shifters together via passive assembly onto a single platform (Figure 3.18). The planar silica waveguide device acted as the optical printed circuit board (or motherboard) providing the passive waveguide interconnection fabric and incorporates the passive function required on the mother board such as interferometer, splitters, modulators etc. (Maxwell et al., 2005; Poustie, 2008). To achieve required level of integration, lithographically defined precise alignment features stops and stand-offs are fabricated onto the motherboard and submounts for the positioning of the individual components.

3.10 Summary

Photonic integration technology enables integration of various optical components on a single platform. The two main integration schemes are monolithic and hybrid integration. Monolothic integration unifies all the components onto a single substrate but is limited to the integration of passive devices only. Hybrid integration technique has the added advantage as it allows integration of various sub–components and devices (passive and active both) reaching their performance targets required for a particular application and can be easily bonded to the motherboard. Assembly of device onto the optical chip is the most costly affair and hence passive alignment technique is always given a preference over the active alignment. Several integration platforms and methods of passive alignment techniques for fibre waveguide interface, laser waveguide interface, and detector waveguide interface are reviewed and discussed to understand the pros and cons and practical challenges of available integration technologies. This will in turn help deciding the most appropriate integration technology and methods to be adopted for the development of chip interferometer sensor device. The chip interferometer system consists of a hybrid tuneable laser, fixed wavelength hybrid laser as a reference, waveguides, optical couplers, wavelength encoder unit, path spiral length compensation and a phase shifting unit. Next chapter will detail the working principle and fabrication technologies of individual components of the sensor system.

4 Device component development and its functioning

4.1 Introduction

This chapter describes the various active and passive optical components which are the building blocks of the chip interferometer system. The description includes the device designs, fabrication and working principle of individual components.

4.2 Passive devices

Passive are those devices which do not require electrical-to-optical or optical-to-electrical conversion during its operation i.e. they neither generate nor detect light. Instead they are involved in only light guiding and manipulating without adding energy to it. Passive optical components includes passive waveguides, directional couplers, isolators, fixed optical attenuators as well as more complicated electrically controlled optical devices like switches and variable optical attenuators.

4.2.1 Optical waveguides

An optical waveguide is a structure which provides light confinement utilising the spatial refractive index contrast in a material system for e.g. optical fibre. In optical fibre light launched remains confined with the core region while it propagates along the axis. The refractive index of the core is greater than the refractive index of the cladding. The light coupled into the end face of the fibre (waveguide) propagates by total internal reflection at the core clad interface. In this way optical energy can be transported from point to point long distances in fibre or in optical integrated photonic chip. Several requirements need to be fulfilled for the waveguide structures which directly relate to the material selection: low insertion loss, low propagation loss polarization-independent operation, high integration density, and the accessibility of reliable low-cost fabrication technologies (Wörhoff et al., 2007). No material is capable of fulfilling all the requirements and thus a trade-off is to be made while choosing waveguide material. Materials such as dielectrics, semiconductors and polymers are commonly used for fabricating photonic integrated circuits. Depending on the index contrast these waveguide materials have been grouped into two main classes; low-index contrast material (silica, polymers) and high-index contrast material (Si, Silicon-on- Insulator (SOI), Indium Phosphide (InP). Low index contrast materials have lower propagation losses, but offers lower integration density because of

large bend radius. In addition to this low index materials are not suitable for active photonics integrated circuits as they provide weak confinement and hence large modal volume which is contrary to the operation of number of photonic devices including on-chip light sources (Hu et al., 2007). High index contrast materials (InP) supports active as well as high density integration but suffers from high propagation and coupling losses.

In the case of photonic chips a planar or buried channel waveguides are fabricated onto a substrate where higher index core material is completely surrounded by a lower index cladding material to provide optical energy confinement and transmission along the guide. The waveguide (passive) is being made out of silica core and cladding layers (SiO_2) grown on silicon (Si) substrates generally called as 'Silica on Silicon'. The waveguide network on a passive chip is called as photonics lightwave circuit (PLC) and the complete chip is referred as a motherboard. The motherboard behaves as integration platform for various active, passive devices and other optical components to form a miniaturised integrated photonic system with improved performance over the open space optics or fibre optic counterparts. Planar optical waveguides are the basic component for the construction of an integrated optical circuit (K. Okamoto, 2010). The PLC in general defines the performance of the hybrid chip device and thus the design of PLC becomes critical.

4.2.1.1 Waveguide Theory

The wave propagation in optical waveguides can be explained two approaches; ray optic and electromagnetic approach using Maxwell's equation (Snyder et al., 1983). Both the methods are well capable of describing the mode propagation inside waveguide system giving finite modal solutions. Ray optics approach is simpler but provides a less complete description of the light propagation (Hunsperger, 1984). This approach is applicable in cases where the dimension of the core is much larger than the wavelength of light used for e.g. multimode waveguides. The electromagnetic approach using Maxwell's equation gives the complete description of the bound modes of the system. Hence it is necessary to solve Maxwell's equations to get a complete and accurate analysis of the allowed modes propagating in the system.

4.2.1.2 Electromagnetic analysis of light propagation in waveguides

Consider the simple three layer planar waveguide structure by assuming by assuming infinite structures in y and z directions and semininfinite in x direction (Figure 4.1). Light waves

are assumed to be propagating in z direction and is described by a mode which actually is the spatial distribution of optical energy in one or more diomension.

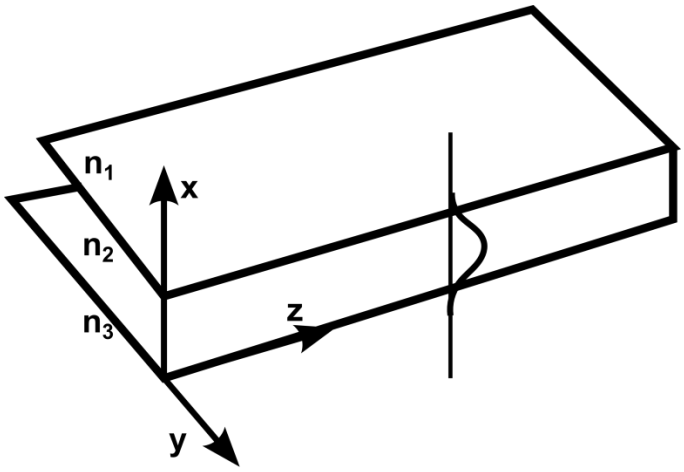

Figure 4.1 Three layer planar waveguide structure

Mathematically it can be respresented as a solution of Maxwell's wave equation,

$$\nabla^2 E(r,t) = \left[n^2(r)/c^2 \right] \partial^2 E(r,t)/\partial t^2 \tag{4.1}$$

Where E is the electric field vector , r is the radius vector, $n(r)$ is the index of refraction and c is the speed of light in vacuum. For monochtromatic waves the solution of the above equation takes the form

$$E(r,t) = E(r)e^{i\omega t} \tag{4.2}$$

Where ω is the radian frequency. Substituting the E in equation 4.1 gives

$$\nabla^2 E(r) + k^2 n^2(r) E(r) = 0 \tag{4.3}$$

Where $k \equiv \omega/c$ .For convenience assuming a uniform wave propagation in the z direction, i.e. $E(r) = E(x,y)\exp(-i\beta z)$, β being a propagation constant equation 4.3 becomes

$$\partial^2 E(x,y)/\partial x^2 + \partial^2 E(x,y)/\partial y^2 + \left[k^2 n^2(r) - \beta^2 \right] E(x,y) = 0 \tag{4.4}$$

As the waveguides is infinite in y direction separate equation for three regions in x, i.e. upper middle and bottom layers with refractive indices n_1, n_2 and n_3 respectively can be written as

$$\begin{aligned}
&\partial^2 E(x,y)/\partial x^2 + \partial^2 E(x,y)/\partial y^2 + \left[k^2 n_1^{\,2}(r) - \beta^2 \right] E(x,y) = 0 \\
&\partial^2 E(x,y)/\partial x^2 + \partial^2 E(x,y)/\partial y^2 + \left[k^2 n_2^{\,2}(r) - \beta^2 \right] E(x,y) = 0 \\
&\partial^2 E(x,y)/\partial x^2 + \partial^2 E(x,y)/\partial y^2 + \left[k^2 n_3^{\,2}(r) - \beta^2 \right] E(x,y) = 0
\end{aligned} \tag{4.5}$$

Where $E(x,y)$ is one of the cartesian components. The solution of the equation 4.6 are either sinusoidal or exponential functions of x in each region depending on wheather the quantity $k^2 n_i^2 - \beta^2, i = 1,2,3$ is grater than or less than zero. Of course, $E(x,y)$ and $\partial E(x,y)/\partial x$ must be continious at the interface between layers.

4.2.1.3 Waveguide Materials

The most common and widely used waveguide are assembled from Si-based thin films on silicon substrates (Pernas et al., 2005). This is an interesting material for the fabrication of various active and passive channel waveguides which can be easily integrated with other OE devices. Due to its abundance, low cost, appropriate material properties and mature processing technology it is widely used in microchips for device integration. Lithium niobate presents important material properties such as high electro-optic coefficients, high optical transparency in the near infrared wavelengths and high curie temperature (1100^{o}C -1180^{o}C) which makes it practical for the fabrication of low –loss optical waveguides through indiffusion of metals (Wooten et al., 2000). Techniques for the waveguide fabrication in lithium niobate are well established and the waveguides formed of lithium niobate have very low losses, typically of the order 0.01-0.2 dB/cm (Lifante, 2003). III-V semiconductor compounds (mainly InP, GaAs) are widely employed for waveguide devices due to their versatile capability of integrating various active and passive components such as lasers, photodetector (PD) operating at 1550 nm (Deri et al., 1991). These days polymers are emerging as a potential material for highly integrated optical components and circuits (H. Ma et al., 2002). Important polymer properties such as electro-optic nonlinearity, photosensitivity and thermo-optical properties bring out the possibility of building large size multifunctional integrated circuit devices for next generation OE systems (Chen et al., 2000). Also the combination of flexibility and toughness in optical polymers makes them suitable for vertical integration to realize 3D and even all-polymer integrated optics. Several promising materials (photolime gel, polyacrylates, polyimides, and polymethyl methacrylate) with acceptable optical and mechanical properties have been developed and many passive and active devices have been demonstrated. Also a well-established technology from microelectronic industry gives cost effectiveness to the fabrication of polymer waveguides. However polymer based integrated optics is still in early stage of research and development to demonstrate their full advantage in terms of size, low cost, yield, performance and commercial viability.

Another promising material is ‘Silica on Silicon’ photonics waveguides which has a high optical quality and has rendered high performance planar light-wave circuits (Y Yamada et al., 1993b). The development of optical fibre has established silica as an extremely low loss optical material. Also integrated optical components made from silica will have a matched refractive index to that of silica based optical fibre to which it coupled, resulting in a low coupling loss. Silica is highly transparent and has a well-controlled stable refractive index (Y. P. Li et al., 1996). This material system also has the advantage of sharing a facility that is used for conventional silicon IC processing, thus from the point of view of the cost of processing equipment this is a practical advantage. Propagation losses in silica based devices are 100 to 1000 times lower than silicon or III-V based semiconductor devices (Bauters et al., 2013). In this work we have used silica-based planar light wave circuits. These waveguides are fabricated using flame hydrolysis deposition (FHD) and reactive ion etching technique (Kawachi, 1990).

4.2.1.4 Wave guide parameters and properties

The waveguide parameters are used to characterise the waveguide system in terms of dimension, refractive index, and wavelength of the propagating mode. Moreover waveguide parameters also communicate the propagation characteristics of the guides (Ladouceur et al., 1996; K. Okamoto, 2010; Roychoudhuri, 2008).

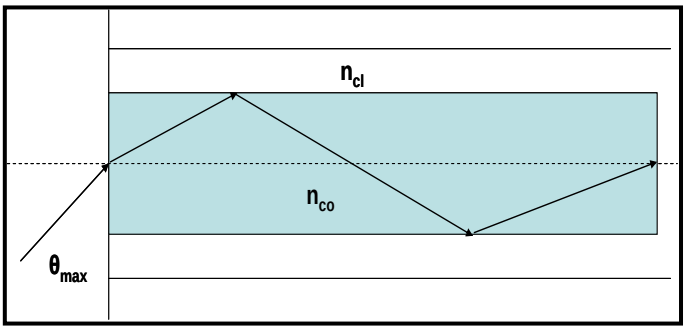

Figure 4.2 Light ray propagation inside a waveguide (Roychoudhuri, 2008)

Relative index difference

This parameter tells about the index contrast of the waveguide. This is represented as delta (Δ) and is given by

$$\Delta = \frac{n^2_{co} - n^2_{cl}}{2n^2_{co}} \tag{4.6}$$

Higher the value of Δ for a given cross section, larger is the number of bound modes that can be accommodated inside the waveguide.

Numerical aperture

Numerical aperture defines the light gathering capability of the waveguide structure. It is given by

$$NA = \theta_{\max} = \tilde{} \left(n^2_{co} - n^2_{cl} \right)^{1/2} = n_{co} \left(2\Delta \right)^{1/2} \tag{4.7}$$

Waveguide parameter

Waveguide parameter is a dimensionless quantity V, often called as degree of guidance. It is given by:

$$V = \frac{2\pi}{\lambda} \rho \left(n^2_{co} - n^2_{cl} \right)^{1/2} \tag{4.8}$$

where ρ is the waveguide ½ core cross section dimension. The quantity $\left(n^2_{co} - n^2_{cl} \right)^{1/2}$ is referred to as the numerical aperture. For the slab waveguide (step index) single mode condition is achieved when $0<V<\pi/2$ allowing only the fundamental to exist in a waveguide.

4.2.1.5 Waveguide Fabrication

Several techniques exist for the fabrication of silica or silica based compounds for integrated optics applications; thermal oxidation, sol-gel, and plasma enhanced chemical vapour deposition (PECVD), flame hydrolysis method. Each of the techniques has their own advantages and a method is preferred over other depending upon the requirement and facilities available. The choice of technology is based on ease of manufacturing, mass productivity and low production cost. Thermal oxidation method is a direct route of producing high quality silica by simply placing silicon wafers at a high temperature (~1000^{o}C) and high pressure (several atmospheres) oxygen or water vapour environment. The steam oxidises the silicon surface to turn into oxide layers which moves further into the bulk as reaction proceeds. Few micron thicknesses of silica layers can be formed using this method. Addition of dopants to control the refractive index is not straight forward and hence the formation of core and the over-cladding layers with this method is not generally employed or practised. Another technique is the sol-gel which exploits chemical reaction of main precursor, generally an organometallic compound in alcoholic solutions (Giancarlo C Righini et al., 2014). The reactions involved are the hydrolysis and condensation of

metal alkoxides. A limitation of this method is the time length of the process due to the risk of stress cracking. Generally it is impossible to deposit films of thicknesses greater than 200nm in a single step. Several cycles of deposition and heating are necessary to deposit film thicknesses suitable for optical waveguiding. In PECVD the energy to dissociate the reactants is provided by radio frequency, microwave or photon excitation (Bunshah, 1990). Since additional input energy is provided PECVD deposition can be carried out at lower temperatures and brings benefits for production techniques where temperature above few hundred degrees are not tolerated. But this technique requires high temperature (>1100^{o}C) annealing steps which is required to reduce the losses in the waveguide to a suitable level (Hoffmann et al., 1997). Because of the complexity of the process it is also not suitable for batch fabrication of waveguides. The work presented in this thesis relies on waveguide and devices fabricated using flame hydrolysis method. FHD method in conjunction with RIE technique is the most economical for the deposition of SiO_2 films which has the advantage of low loss channelled waveguide best matched to optical fibre in terms of index of refraction (Kashyap et al., 1989). In addition this technique gives a thick deposition of film over the substrate at a faster rate, with high material quality and at a low production cost. Particular attention is given to the FHD as this is the technique used to fabricate the planar waveguide used in this thesis.

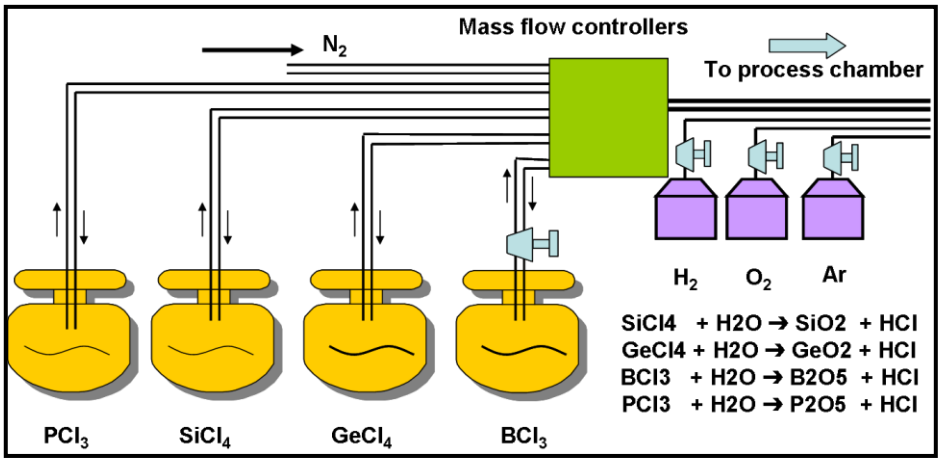

Figure 4.3 Flame Hydrolysis Deposition

FHD is essentially a planar version of the technique used to make cylindrical fibre preforms (Figure 4.3). This is the method of depositing glasses in the form of powdery 'soot'. The mixture of vapours, such as silicon tetrachloride ($SiCl_4$), titanium tetrachloride ($TiCl_4$) and germanium tetrachloride ($GeCl_4$) forms the precursor for the reaction in an oxy-hydrogen flame. In this process glass precursor particle on combustion hydrolyses to form fine glass particles. The glass

soot particles are then deposited onto the Silicon substrate. After the soot deposition, the wafer is transferred to a furnace and heated to 1300^{o}C to consolidate the porous layer into uniform solid free of bubbles or any structural defects.

Once the SiO_2 layer is formed, a photoresist is applied to the surface of the wafer. The spin coating technique is used to produce a thin uniform layer of photoresist on the wafer surface. This photoresist coating is applied to protect or remove a portion of the guide onto the wafer using suitable masks. The mask is an outline of circuitry or the pattern to be printed onto the wafer. On exposure to UV rays the sensitizer in the resist undergoes chemical change so that it becomes soluble in developer. The region of exposed resists is then removed by applying suitable developer leaving windows for the bare underlying material.

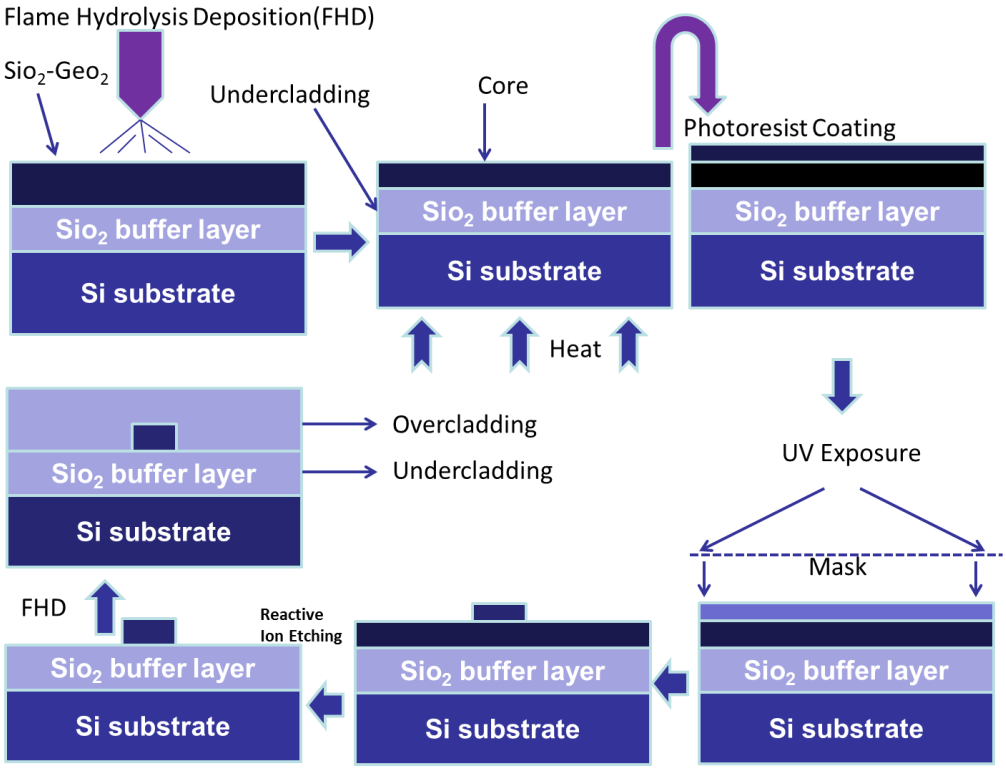

Figure 4.4 Waveguide fabrication process

The wafer is then etched using reactive ion etching technique to remove the unwanted regions of the core structure uncovered by resist. Now the resist is no longer needed and is removed using various organic chemicals such as Acetone, Dimethyl sulfoxide etc. Finally once again FHD is used to deposit overcladding layer having refractive index similar to that of the buffer layer. The step by step waveguide fabrication process is shown in the figure 4.4.

4.2.1.6 Losses in a Waveguide

Propagation losses in the waveguides are much higher than that of the optical fibre despite the waveguides made of similar composition and cross-section to that of the optical fibre. One reason is that the glass is flown much better during the fibre drawing at ~2000^{o}C than the glass in waveguide. Another factor is the manner in which fibre drawing is performed. Drawing decreases the area and increases the axial dimension by more than four orders of magnitude, demagnifying any inhomogeneity existing in the preform. In the case of waveguides smoothing process is not available and a low loss waveguide is achieved by simultaneous deposition of various layers onto the substrate, densification and etching techniques. Most of the losses in the waveguide are due to bulk in-homogeneities and surface scattering. Bulk inhomogeneity or defect in material gives Rayleigh scattering and such scattering losses can be minimised to acceptable levels proper annealing or controlling material processing methods. Scattering also arises from the roughness of the side-walls of the waveguide introduced due to imperfections in lithography or etch processes used to define the waveguides.

4.2.2 Directional coupler

Directional couplers (DC) are passive optical reciprocal component used to combine or split signal in a network. This splitting and combining of signal is achieved by optical power coupling between cores of two parallel running fibres when placed in close proximity with each other. In such case evanescent field extends into the adjacent guide providing field overlap across the coupled length. The extent of field overlap between the two waveguides in close proximity of each other determines the coupling strength. An example of 2X2 fibre coupler is shown in the figure 4.5. Couplers are also fabricated using waveguides for light coupling in the optical network patterned onto a chip called motherboard in integrated optics.

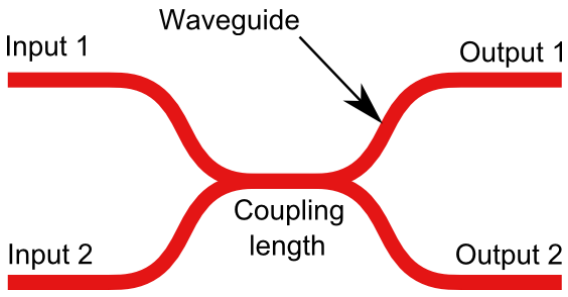

Figure 4.5 Directional coupler

4.2.2.1 Operating principle

The optical power coupling between the guides in a directional coupler is explained by the coupled mode theory (Huang, 1994). Consider the simplest situation of 2x2 waveguide directional coupler made of identical waveguides. The light is launched into one of the input of the waveguide, which stimulates a linear combination of symmetric and anti-symmetric supermodes as shown in figure 4.6.

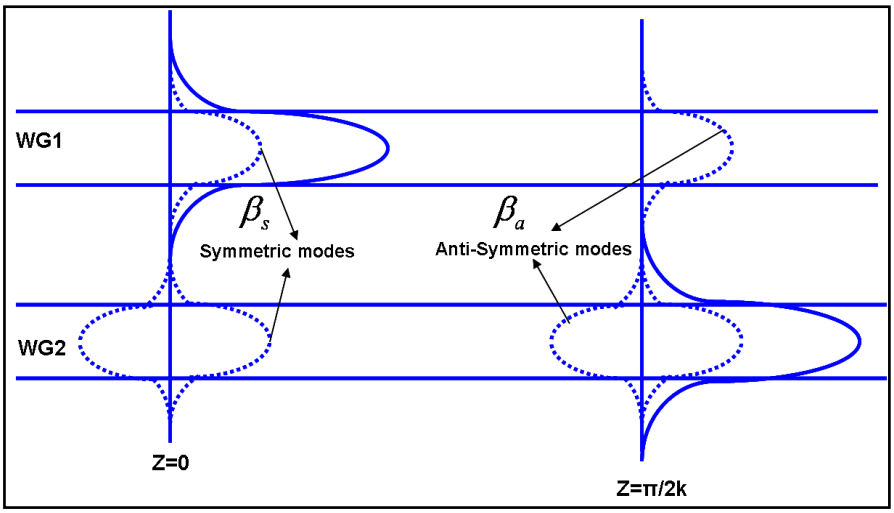

Figure 4.6 Shows complete transfer of optical power into the second waveguide after an interaction length of z= π/2k [Adapted from Payne et al., 1985]

These supermodes propagate with different propagation constant and they develop a relative phase difference while transversing a certain length inside the fibre (Payne et al., 1985). At a certain distance when the modes acquire a phase difference of π the superposition of the two modal fields results in cancellation of the field amplitudes in the input waveguide while amplitudes gets added in the second waveguide. The distance at which complete coupling of the light from input waveguide to the second waveguide occurs, is termed as the coupling length L_c of the coupler. Such a situation where there is complete transfer of optical power to the other waveguide is called is referred to as the completely coupled state. Further reverse coupling from second guide to the input guide starts when the interaction length extends beyond the coupling length of the directional coupler. Hence by choosing identical waveguides periodic transfer of optical power between the closely spaced waveguides can be achieved by varying the coupling length.

Considering 2X2 coupler (shown in figure) with a unit power launched at $z = 0$ the power distribution between the throughput (PT) and coupled waveguide (PC) by at any z is given by (Ghatak et al., 1998),

$$P_T(z) = 1 - \frac{k^2}{\gamma^2}\sin^2 \gamma z \tag{4.9}$$

$$P_C(z) = \frac{k^2}{\gamma^2}\sin^2 \gamma z \tag{4.10}$$

$$\text{where } \gamma^2 = k^2 + \frac{(\Delta\beta)^2}{4} \tag{4.11}$$

$$\Delta\beta = \beta_1 - \beta_2 \tag{4.12}$$

β_1 , β_2 are the propagation constant of the fundamental modes of the individual waveguides and k is the coupling coefficient. Coupling coefficient gives the measure of strength of coupling and is a function of the width of the waveguide, the refractive indices of the waveguide region and proximity of the two waveguides. Thus for two identical waveguides $(\Delta\beta = 0)$ the above equations reduces to

$$P_T(z) = \cos^2 kz \tag{4.13}$$

$$P_C(z) = \sin^2 kz \tag{4.14}$$

Now it is obvious from the equations that the complete transfer of optical power from the input waveguide to coupled will take place at an interaction length of $z = \pi / 2k$. A 50% distribution of optical power between the waveguides requires an interaction length of $z = \pi / 4k$ which follows in the case the 3dB directional coupler. This property of 3 dB coupler thus can be harnessed as splitters and combiners.

4.2.3 Mach-Zehnder Interferometer

Mach- Zehnder interferometer (MZI) is a device based on light interference by division of amplitude (Figure 4.7). The device is generally used to determine the relative phase shifts between the two collimated beams from a coherent light source. A light beam is first split into two by a beam splitter, which then follows the different arms of the interferometer and each beams are reflected by a mirror to combine again at a second beamsplitter. Depending upon the optical path length covered by the two beams which in turn induces a relative phase difference,

the second beam splitter reflects the beam with efficiency between 0 and 100% (Zetie et al., 2000). MZIs are used for phase measurements, refractive index measurement, wavelength conversion, optical switches, wavelength filters, as multiplexers and de-multiplexers. In integrated optics MZIs are constructed using two 3 dB directional couplers interconnected through two paths of differing wavelengths, as shown in figure. MZI is fabricated on a substrate usually silicon, and the waveguide and cladding is made of silica.

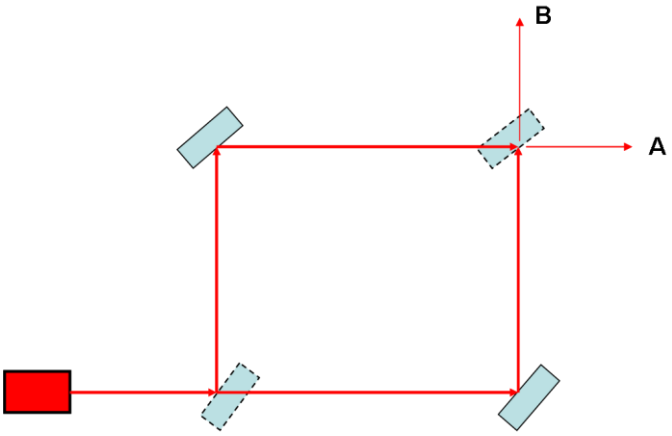

Figure 4.7 Mach-Zehnder interferometer

4.2.2.2 Mach-Zehnder Interferometer as a de-multiplexer

Suppose a signal (S1) consisting of several wavelengths ($\lambda_1, \lambda_2, \lambda_3, \lambda_4$ etc) is fed into one of the input port of the MZI (Figure 4.8). The first directional coupler divides the input signal equally between the two arms of the MZI with a phase difference of $\pi/2$ between the signals (Ramaswami et al., 2009). In particular the signal in the lower arm or the opposite arm lags the one in the upper arm by a phase $\pi/2$. Further there is a length difference ΔL in between the two arms giving additional phase lag of $\beta\Delta L$ in the lower arm. In the second directional coupler the signal from the lower arm undergoes another phase lag of $\pi/2$ in going to the first output relative to the signal from the upper arm.

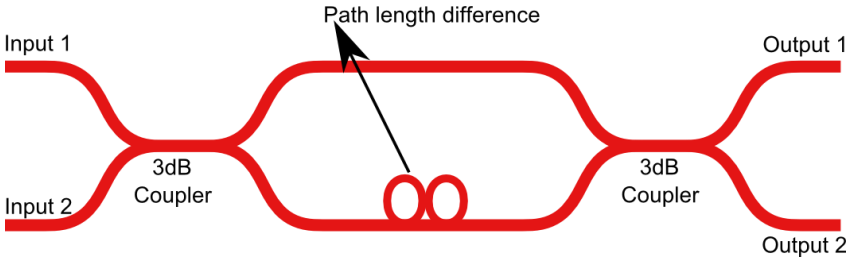

Figure 4.8 Phase shifts in different sections of an MZI de-multiplexer

Table 4.1 Mach-Zehnder interferometer as a de-multiplexer

Phase		Coupler 1	Coupler 2	Output 1	Output 2
Signal (S)	S11	0	0	0	$-\pi/2$
	S12	$-\pi/2$	$-\pi/2-\beta\Delta L$	$-\pi/2-\beta\Delta L-\pi/2$	$-\pi/2-\beta\Delta L$

The table 4.1 above shows the phase values of the signals in the two arms at different sections in the interferometer. Thus the total relative phase difference at the lower output between the two signals is $-\pi/2-\left(-\pi/2-\beta\Delta L\right)=\beta\Delta L$. If $\beta\Delta L=k\pi$ and k is odd, the signals at the second output add with opposite phase and thus cancel each other. Thus the wavelengths passed through the first input to the first output are those wavelengths for which $\beta\Delta L=k\pi$ and k is odd. Similarly the wavelengths passed through the first input to the second output are those wavelengths which satisfy $\beta\Delta L=k\pi$ for k is even.

4.2.3 90° optical hybrids for wavelength monitoring

An optical hybrid is a multi-port device used for coherent signal demodulation in detection. Optical hybrids mix the incoming optical signal with the local oscillator (LO) into a pair of balanced detectors to measure the amplitude and phase of the signal (Dong et al., 2014). These hybrids have been realized in all fibre (Kazovsky et al., 1987), planar waveguide (Jeong et al., 2010; Zimmermann et al., 2009) and with free space bulk optics (Zhou et al., 2009). Free optics and fibre based systems are inherently bulky and sensitive to the environmental noise and vibrations. Several configurations of optical hybrids are available; the simplest of all configurations is 3dB coupler also known as 50/50 beam splitter or 180^o hybrid. The 180^o hybrid is shown in the figure 4.9.

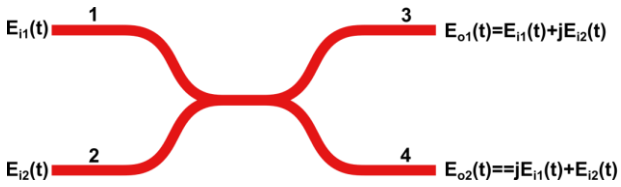

Figure 4.9 180° optical hybrid made of 3-dB couplers. A phase shift of 180degrees is obtained at one of the output ports.

A 90° optical hybrid is a six port device with two input and 4 output ports commonly used for coherent signal demodulation and phase sensitive detections. Balance of power in and accuracy in phase shifts are the important features of 90 degree optical hybrids. 90° optical hybrids along with the digital signal processing provide high efficiency cost effective spectral

systems for coherent optical detections and monitoring. Optical hybrids based on photonic integrated circuits offers compactness, low cost, and stable noise insensitive features.

4.2.3.1 Implementation of optical hybrid

90° optical hybrid is generally constructed using two 50/50-beam splitters (de-multiplexer) and two beam combiners, plus one 90° phase shifter (Figure 4.10). For 2×4 90° optical hybrids there are two inputs and four outputs as shown in the figure below. In between the two 3 dB couplers the first arm waveguide of the first and second de-multiplexers are connected to the first and second input ports of the first combiner each having the same length. Similarly the second arm waveguide of the first and second de-multiplexer is connected to the first and second input ports of second combiner. A 90° phase shift is inserted into one of the arm waveguides between the de-miltiplexer and the combiner. Light input to the hybrid is fed through the first and fourth input port or into the second and third input port.

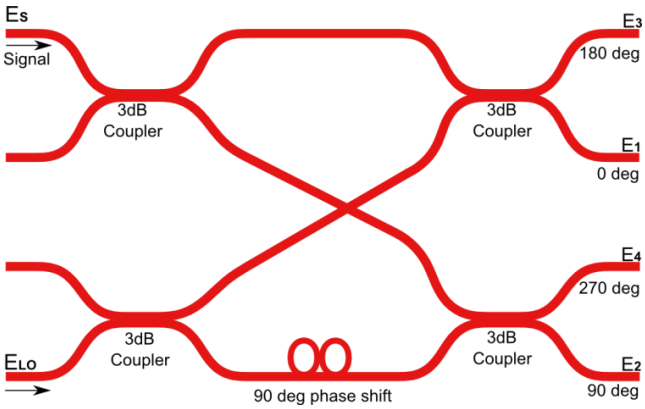

Figure 4.10 2x 4 90° optical hybrid made of 3-dB couplers and a phase delay
[Adapted from Seimetz et al., 2006]

4.2.3.2 Theory of operation

In a 2×4 90° optical hybrids, the light of the incoming optical signal is mixed with the local oscillator. The field equation for the laser beam and the LO can be represented in complex notation as,

$$E_S = \sqrt{P_S}\times e^{j(\omega_S t+\varphi_S)} \tag{4.15}$$

$$E_{LO} = \sqrt{P_{LO}}\times e^{j(\omega_{LO} t+\varphi_{LO})} \tag{4.16}$$

The P_S and the P_{LO} represents the input optical powers into the two input channels of the hybrid coupler and ω_S ,φ_{LO} and the ω_{LO} ,φ_{LO} are angular frequencies and phase of the signal and the LO respectively. An interfering light beam of the inputted signal light beam and local oscillation light beam gives out an in-phase component and a quadrature components which can be separately detected by optical receiver. The signal and the local oscillator after combining will generate output fields E1, E2, E3, E4 which is given by (Seimetz et al., 2006),

$$\begin{bmatrix} E_1 \\ E_2 \\ E_3 \\ E_4 \end{bmatrix} = \frac{1}{2} \cdot \begin{bmatrix} 1 & 1 \\ 1 & j \\ 1 & -1 \\ 1 & -j \end{bmatrix} \cdot \begin{bmatrix} E_S \\ E_{LO} \end{bmatrix} = \begin{bmatrix} \frac{E_S}{2} + \frac{E_{LO}}{2} \\ \frac{E_S}{2} + j\frac{E_{LO}}{2} \\ \frac{E_S}{2} - \frac{E_{LO}}{2} \\ \frac{E_S}{2} - j\frac{E_{LO}}{2} \end{bmatrix} \tag{4.17}$$

Using a balanced detection scheme using array of photo-diodes, the photocurrent outputs from E_3, E_1 and E_4, E_1 is obtained as

$$I_I(\mathrm{t}) = I_{I1} - I_{I2} = R\sqrt{\mathrm{P}_S\ \mathrm{P}_{LO}}\cos\left((\omega_S - \omega_{LO})t + (\theta_S - \theta_{LO})\right) \tag{4.18}$$

$$I_Q(\mathrm{t}) = I_{Q1} - I_{Q2} = R\sqrt{\mathrm{P}_S\ \mathrm{P}_{LO}}\sin\left((\omega_S - \omega_{LO})t + (\theta_S - \theta_{LO})\right) \tag{4.19}$$

Where I_{I1}, I_{I2}, I_{Q1}, I_{Q2} are the individual photo-detector currents and R is the responsivity of individual detectors. For homodyne detection the frequencies of the signal and the LO are same $\left(\omega_S = \omega_{LO}\right)$. The signal demodulation which is basically extracting the accurate phase information to relate it to the wavelengths is performed by arctangent computation and is given by,

$$\theta_{fine} = \tan^{-1}\left(\frac{V_I}{V_Q}\right) \tag{4.20}$$

Important requirements of the 90° optical hybrids are the power balance of the output ports and accuracy of the 90° phase shifts. Fabrication variations will also result in power imbalance at the outputs. The other factor that will induce the power variation is the variable gain of the photo-detector.

4.2.4 Optical Isolators

Optical isolators are optical analogue of the electronic diodes which allows light to propagate in only one direction. This is a non-reciprocal device two port device and is used in systems such as optical amplifiers and lasers primarily to prevent reflections from entering these devices which would otherwise degrade the performance of the system. The operation of device is based on Faraday rotation (Figure 4.11) (Schulz, 1989). The main components of isolator are: an input linear polarizer, a magnetic rotator based on the Faraday effect, and an output linear polarizer whose pass axis is rotated 45^o relative to the input polarizer.

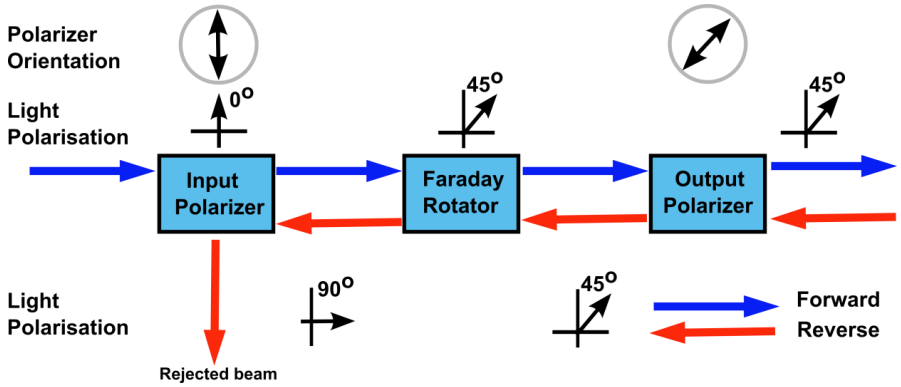

Figure 4.11 Principle of operation of an isolator for a particular state of polarization

A Faraday rotator is a non-reciprocal device made of a crystal that rotates the initial state of polarisation (SOP) in a particular direction regardless of the propagation direction. The magnetic field is applied so that the plane of polarization is rotated by 45^o into the output polarizer's pass direction. Thus the light propagates from left to right without any loss. On the other hand light entering the device from right to left via reflection with the same 45^o SOP is rotated by another 45^o after passing through the faraday rotator. In total the back reflected light is rotated by 90^o degrees relative to the initial SOP while passing through the rotator and thus the light is completely blocked at the input linear polariser. The above operation of isolator is explained considering a particular SOP for the input light signal. Practically it is very tough to control the SOP of the input light and hence an isolator must work irrespective of the input SOP. For an isolator to work for an arbitrary SOP a more complicated design constituting other optical components is required.

The Faraday effect is dependent on the wavelength of the light, the magneto-optic constant, the magnetic field and the length of the crystal. A fibre optic isolator is thus made for a specific wavelength range. If the length of the rotator changes or the magneto-optic constant changes, the

isolator would change operation wavelength range. Both the length of the crystal and the magneto-optic constant will be temperature dependent. There is thus a fundamental temperature dependence of the fibre optic isolator which limits the operating temperature range. The insertion loss and the backward loss may still be approximately the same, but the wavelength range has changed. A fibre optic isolator is usually made from miniature versions of bulk optical components. The alignment of the different components will be critical and thus vulnerable to mechanical and environmental loads. The operation of the device is dependent on the magnetic field. The device should therefore be completely shielded from external magnetic field.

4.3 Active components

Active components are those devices which require electrical-to-optical or optical-to-electrical conversion during its operation i.e. they involve light generation and detection. Examples of active components are semiconductor optical amplifier, photo-detectors, light emitting diodes, lasers etc. These devices are responsible for converting both analogue and digital signals to and from optical pulses transported over the waveguide or fibre network.

4.3.1 Semiconductor Laser

The very first suggestion in public about the semiconductor lasers was put forward by Pierre Aigrain (Dupuis, 1987) but the actual feasibility of stimulated emission in semiconductor was introduced by Basov et al in 1961 (Chow et al., 1999). He suggested that by impact ionisation electron hole pairs can be generated in a p-n junction which then recombines to give stimulated radiation. A p-n junction provides the active region containing excited electrons and holes present together. The recombination produces radiation that may interact with valance electrons and get absorbed or interact with electrons in the conduction band producing further photons of the same frequency. When the injected carrier concentration become large enough i.e. population inversion is achieved the stimulated emission exceeds absorption giving steep increase in the light output.

Because of the very low observed efficiency and hazy details and poor understanding of the underlying light emission concepts of semiconductors led to the slow progress of semiconductor lasers diodes in the beginning. Only after the successful demonstration of radiation emission using Zn-diffused GaAs p-n junction by a group from MIT Lincoln labs it sparked interest among the scientific community (Hall et al., 1962). There are several reasons to note for the

slow progress: need for the development of new semiconductor technology, problem involving high threshold currents for lasing which limited laser operation at cryogenic temperatures only etc. Unless the semiconductor laser could work at room temperature, its potential would be very limited. Further a breakthrough by the Bell laboratory research team in 1970 which led the introduction of hetrostructures replacing a simple P-N junction with multiple semiconductor layers of different composition made possible the laser operation at room temperature (Z. Alferov, 2000).

Miniaturised, low cost, fast and reliable optoelectronic devices are important requirements to the current technological applications in many areas of research and industry. A semiconductor laser naturally becomes technology of the choice for various applications due to its small size, low cost, high reliability performance and spectral and modulation characteristics (Mulet, 2002). The most important application is found in telecommunications where signals are propagated over several kilometres along the fibre. This replaced the use of electric wires for long distance signal transmission which was relatively slow and inefficient. The signal transmission through electric wires was of poor quality, and they required a relay device called repeaters every kilometre. Too many relay devices produced time lags, background noise, and caused lines to be cut-off. Now with the use of semiconductor laser and fibre noise free gigahertz transmission rate are possible with only few repeaters are required over a long haul fibre transmission system. Further the applications of semiconductor laser are in consumer electronics such as bar code readers in supermarkets, laser printers, laser pointers, in compact disc read/write etc.

4.3.1.1 Semiconductor laser: Working principle

The energy states are different in semiconductors compared to that of the discrete energy states in atomic systems. When several atoms comes closer to form solid, the behaviour of the interaction between the atoms and its neighbours changes leading to the formation wide bands instead of sharply defined energy states. The energy states of the outermost electrons of the atoms combine to produce a band of filled energy states called the valance band. Similarly excited energy states of atoms combines to produce an energy band which is empty at absolute zero. This lowest energy empty band is called conduction band. There also is a small gap (~ 1ev) in between the valance and conduction band called the 'band gap' E_g (Figure 4.12). At thermodynamic equilibrium the distribution of charge carriers are defined by Fermi-Dirac

statistics. So at T=0 K any carrier from donor or acceptor are bound to their atoms and hence there is no conduction. For non-zero temperature, the sites can be thermally agitated releasing charge carriers in the respective bands leading to conduction. Thus the electrons occupy the bottom of the conduction band and the holes occupy the top of the valance band. Further on radiative recombination of charge carriers photons are generated. It has been observed that direct band gap materials has high probability of combining radiatively as the electron wavenumber 'k' is conserved. While in the case of indirect band gap materials the transition is indirect and is mediated by generation of a phonon leading to inefficient recombination. The photons generated may then be absorbed by the electrons in the conduction band or stimulate electrons in the conduction band to undergo recombination producing further photons of the same frequency. When the concentration of the injected charge carrier at a localized spatial region called the 'active region' becomes large enough, the stimulated emission exceeds absorption i.e. gain exceeds the loss in the active region laser light is obtained.

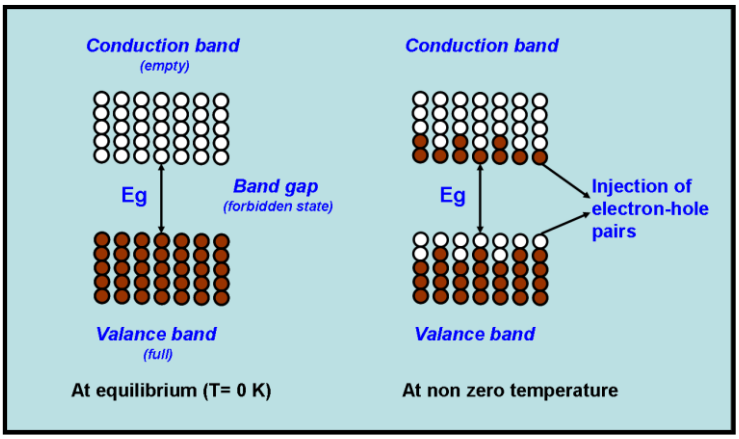

Figure 4.12 Band diagram in a semiconductor

The most important semiconductor materials in photonics are III-V binary materials such as InP, GaAs, InSb. By using different levels of doping semiconductor materials different semiconductor junctions can be formed. Adjoining semiconductors of opposite charge carriers (p-type and n-type) forms a p-n junction where excess of charge carriers is injected to achieve so called inverted state of filling of energy levels at the edges of conduction band necessary for obtaining amplification in stimulated interband radiative transition (Basov et al., 1986). This inverted state forms the basis of operation of semiconductor lasers. The simplest form of laser diode is homo-junction laser which uses a single junction and is made of same material with different doping concentrations on both sides. Improved performance is achieved by using

hetrostructure configuration by sandwiching active medium between the two semiconductors of wider band gap material. This provided better confinement of injected carriers well within the active region forming a potential well for them. Coincidently this structure also provided intra-cavity lateral beam confinement in the dielectric waveguide structure made of higher refractive index semiconductor material itself. The figure 4.13 shows the sketch of n-n--p hetrostructure. The most important class of semiconductor material are based on III-V compounds for e.g. GaAlAs/GaAs and InGaAsP. The emission wavelength in InP/InGaAsP hetrostructure system varies in the range 1- 1.7 um depending on the dopants, size of the active region and the composition of active and cladding layers (Olsen, 1981). This quaternary hetrosystems provided longer wavelength laser to cover the communication window to minimize the loss of optical signal in the fibre.

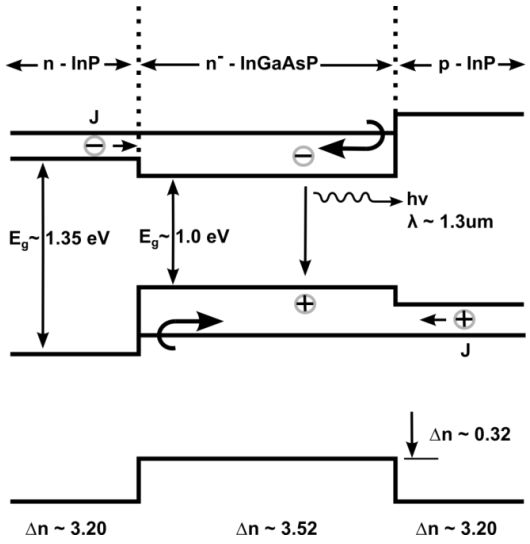

Figure 4.13 Double hetrojunction semiconductor laser [Adapted from Olsen, 1981]

In InGaAsP/InP double-hetrojunction semiconductor laser, active medium is undoped InGaAsP surrounded by higher bandgap n and p type InP cladding layers. When a bias voltage is applied in forward direction the charge carriers (electrons fron n-InP and holes from p-InP) are injected into the active region. Since the band gap energy is higher in the cladding layers which behave as a potential barrier restricts the diffusion of holes and electrons across the junctions. Thus the excess accumulation of electrons and holes in the active region generates the state of population inversion allowing the amplification by stimulated radiation (Yariv, 1989). Any photon generated within the cavity is capable of stimulating the recombination emitting photon of same wavelength and phase. As the injection is increased active region will exhibit higher gain than the absorption losses of the cavity; the device serves as an amplifier with increased

intensity of optical modes. Certain select optical modes oscillates back and forth in the cavity and experience much greater amplification than others and narrowing of emitted spectrum together with abrupt increase in emitted optical power occurs. The device is now said to lase. The condition for lasing inside the cavity satisfying the threshold condition is given as,

$$(R_1R_2)^{1/2} exp(gL) \geq 1 \tag{4.21}$$

Where R_1 and R_2 are the mirror reflectivities and the 'g' is the gain of the material and 'L' is the length of the cavity or the active medium. In semiconductors round trip gain via optical feedback is provided by the cleaved polished partially reflecting facets perpendicular to the junction forming a Febry-Perot cavity (Figure 4.14). Since the mirrors are partially reflecting a part of beam is thrown out after every round trip as a usable laser beam.

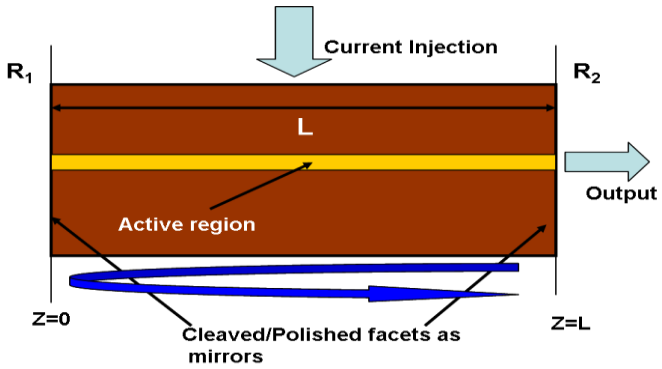

Figure 4.14 Semiconductor laser cavity

The beam propagates back and forth in the Febry- Perot (FP) etalon form a standing wave pattern, thus allowing only discrete set of frequencies to oscillate in the cavity. For a given wavelength λ and a corresponding effective index n_{eff} the number of allowed modes in the cavity is given by

$$N = \frac{2n_{eff}L}{\lambda} \tag{4.22}$$

Also the difference in wavelength between the two nearby longitudinal modes is given by

$$\Delta\lambda = 2Ln_{eff}\left(\frac{1}{N} - \frac{1}{N+1}\right) \cong \frac{\lambda_1^{\,2}}{2Ln_{eff}} \tag{4.23}$$

Thus wavelength spacing decreases with the increase in cavity length and there is greater change that more than one mode will oscillate at a time. This also induces cross talk of signal in

fibre communication. Hence in order to have single mode lasers it is required to enhance the wavelength spacing by selectively choosing a cavity of shorter length.

Advances in physics and technology of semiconductor led the development of newer low threshold high power lasers system suitable for broader range of applications and has remarkably changed or everyday life. Owing to the electron confinement, double hetrostructure laser became an important precursor for the quantum well laser structure: when middle layer had a thickness of some angstrom, the electron levels would split due to quantum size effects (Z. I. Alferov, 2000). The characteristic step like behaviour in the absorption spectra of GaAs-AlGaAs and energy shifts with the thickness of ultra thin layer was first observed by Raymond Dingle et al (McWhan, 2012). Discrete energy level provides means of tuning the resulting wavelength of the material. Thus by changing the quantum well dimension or thickness desired spacing between the energy levels can be created to achieve required tenability. Also compared to the bulk semiconductor lasers, quantum well lasers offers the advantages of considerably low threshold current density for lasing, narrower gain spectrum, smaller line-width of laser modes and much higher modulation frequencies at which lasing can be modulated electrically. For generating high optical output power from quantum wells multiple quantum well structures can be used as an amplifying medium. Further reduction in the dimensionality led to the emergence of quantum wire and quantum dot laser. In quantum wire the localization of charge carriers is in two directions and is allowed to move freely along the wire only where as in quantum dots the confinement is in all three direction. These lasers have shown superior properties than those of quantum well laser. High differential gain, ultra low threshold current density and high temperature stability of threshold current, higher modulation bandwidth, narrower line-width, and wider tunability are important characteristic of such quantum dimension lasers (Coleman et al., 2011; Kapon et al., 1989). Apart from all these advantages over quantum well lasers, the major challenges with quantum wire lasers is the fabrication of nanoscale quantum wires with good crystalline characteristics and precise growth control in lateral dimension and cross-section to minimize the homogenous broadening of emission. Similar is the case with quantum dot lasers which requires the optimisation of growth parameters to achieve a dense and uniform array of quantum wire and dots, identical in shape and size (Bhattacharya et al., 1999; Goronkin et al., 1999) to maintain efficient optical emission by avoiding any non-radiative defect channels. The phonon bottleneck phenomenon due to confinement degrades the stimulated emission leading to

reduced performance of the laser (Benisty et al., 1991). Hence it requires complex mechanism to suppress the effect.

4.3.1.2 Semiconductor optical amplifier

Semiconductor optical amplifier (SOA) is the modified form of laser diode in which the mirror end facts are transparent to prevent laser oscillation in the amplification dynamic range (Eliseev et al., 1995). To make the end of very low reflectivity it is coated with anti-reflection coating film (Figure 4.15(a)) and reflectivity as low as 7x10-5 have been achieved in the case of Modified Dual Channel Planar Buried Hetero-structure (M-DCPBH) (Stubkjær et al., 1992). Other methods of reduction of facet reflectivity are angling of the waveguide to the facet normal (Figure 4.15(b)) and creating window structures where active waveguide is terminated (Figure 4.15(c)) in semiconductor material with a matching refractive index (Cha et al., 1989).

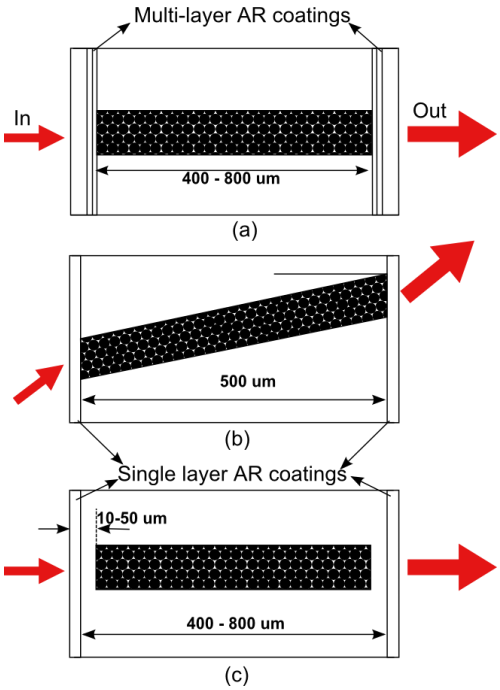

Figure 4.15 Methods for reduction of the reflectivity

a) Straight facet amplifier with multilayer AR-coatings, b) Angle facet amplifier with single layer AR-coatings, and c) buried facet amplifier with single layer AR-coating. [Adapted from Stubkjær et al., 1992]

SOAs incorporating multiple quantum well (MQW) structures exhibit high optical gain and band-width typically larger than 100 nm (Bagley et al., 1990; Ding et al., 2007). One of the disadvantages of MQW-SOA's is its high sensitivity to polarization effects. Configurations based on tensile-strained barrier MQW structures have shown insensitivity to the polarization at a working wavelength of 1.55 um. Another polarisation insensitive SOA structure was proposed

by Kelly et al which have integrated mode expanders to reduce the effective facet reflectivity when used in conjunction with the angled facets (Figure 4.16) (Kelly et al., 1996).

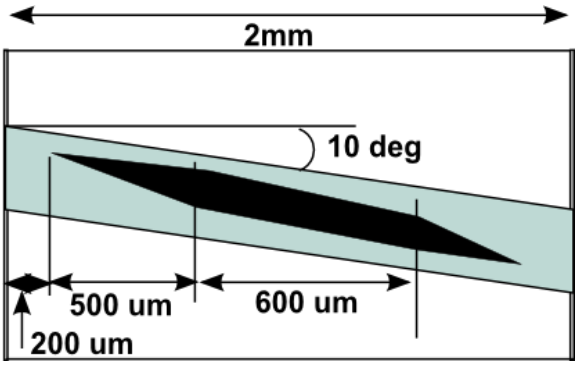

Figure 4.16 Schematic of large spot-semiconductor laser amplifier (LS-SLA)

[Adapted from Kelly et al., 1996]

SOA is a multifunctional active device and can be used for applications in high power emission sources, photo-detectors, optical modulations, switching etc. Because of the very short life time of the injected carriers it can be used fast signal processing (Last). Materials used for fabrication of SOA's are similar to the laser diodes and the choice of material depends on the required wavelength range of laser operation.

4.3.1.3 Tuning mechanism

Common technique of tuning such laser diodes are by changing injection currents or the operating temperatures. But these methods allows output beam to be tuned discontinuously and limits its application because of poor wavelength stability (Hail). Also changing current and temperature severely impacts the life time of the laser diode. The line-width of the laser beam output is relatively wider which indicates impure spectral composition and the poor cavity quality. Hence to improve the spectral composition and wavelength stability external cavity diode laser (ECDL) configurations are developed.

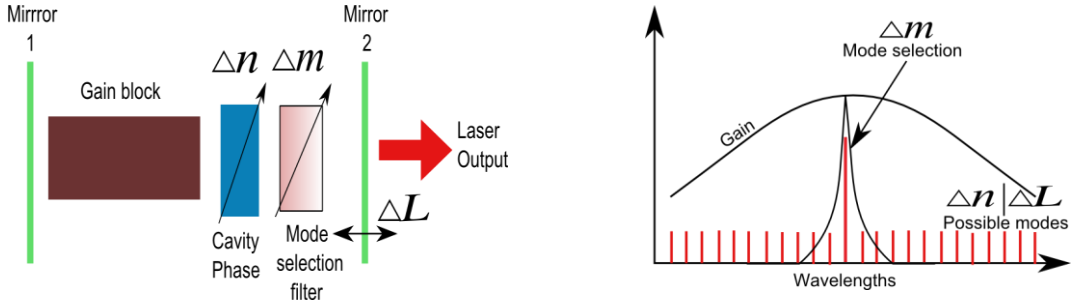

Figure 4.17 Schematic of generic external cavity tuneable laser (L), Mode selection inside the external cavity laser (R)

External cavity configuration adds versatility to the device combining features of extremely narrow line-widths, broader tenability, comparatively high output power and ease of use (Fleming et al., 1981). ECDL supplements the benefits of a cost effective laser diodes themselves; small size, low cost, high reliability. The figure 4.17 (a) is the schematic of external laser cavity consisting of mode selection filter, gain element and mirrors. This is an extension to the basic FP laser which has the gain block and two mirrors producing single frequency. The rearrangement and alignment of cavity modes using optical elements such as filters and phase shifters creates unique structures to generate tuneable single frequency lasers (Figure 4.17 (b)). Below equation gives the relationship between the effective cavity length (L), lasing wavelength (λ), effective index (n_{eff}) and the cavity mode number (N). It is evident from the relation that by changing λ, n_{eff} or the cavity length L, output wavelength can be easily changed. So the relative change in wavelength can be obtained from mode equation.

$$\frac{\Delta\lambda}{\lambda} = \frac{\Delta n_{eff}}{n_{eff}} + \frac{\Delta L}{L} - \frac{\Delta m}{m} \tag{4.24}$$

Any change either in the length, index or the mode number will result in proportional change in the wavelength.

4.3.1.4 Tuneable semiconductor lasers cavity configurations

In this section some examples of a widely tuneable external cavity semiconductor lasers based on its cavity configurations or wavelength selectors are described. Insertion of wavelength selective elements allows external control and thus provides wavelength selection and tenability of the emitted wavelength without complications of variations in current or system temperature (Mroziewicz, 2008).

Majority of tuneable lasers suffer from low tuning speed of wavelength tenability. Figure 4.18 (a) is the most basic external cavity configuration consisting of gain block, reflectors and a lens. The gain block is SOA which acts as a laser diode chip with rear and front fact coated with high and very low reflective films respectively. The lens provides light collection and collimation after the beam is diverged from the SOA. So in order to capture all the light from SOA the lens should be of large aperture.

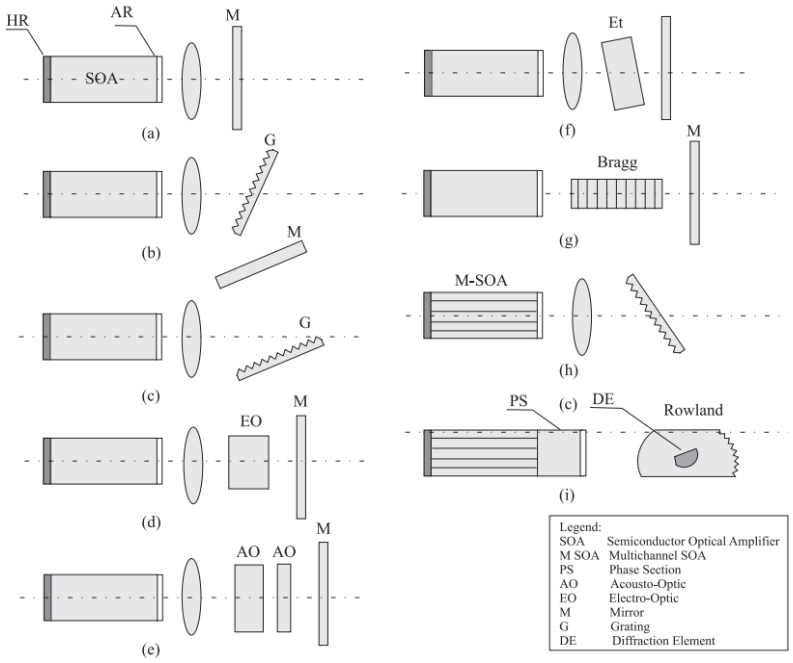

Figure 4.18 Schematic of various external cavity laser configurations [Adapted from Mroziewicz, 2008]

(a) elementary ECL consisting of a gain medium (SOA), collimating optics, and two mirrors – one of which formed by a high reflectivity coating (HR) on the SOA's rear facet, (b) Littrow (c) Littman(d) electro-optic filter (e) acousto-optic filters (AO), (f) etalon plus wavelength selective mirror (g) Bragg waveguide, (h) multichannel SOA, and (i) multichannel SOA with phase shift section (PS), and Rowland grating

In general the external cavity designs are based on two configurations; Littrow and Littman-Metcalf configurations. Littrow configuration (Figure 4.18(b)) is simple and uses a grating to directly reflect (diffract) the beam into the cavity (Hänsch, 1972). This configuration provides higher power efficiency as it used first order reflections from the grating. The main problem with this configuration is the mode hopping and thus causes limited continuous tuning of the laser. The grating provides the wavelength tenability but does changes the cavity length when it is tuned. The other design configuration is Littman Metcalf in which grating remains fixed while the mirror is tuned to get better and wider range continuous wavelength tenability but at the cost of reduced power (Figure 4.18(c)) (Littman, 1978). Since both the configurations rely on the mechanical movement of the component (grating or mirror) it leads to wear and fundamentally restricts the tuning to sub kilohertz rate. Other configurations includes electro-optic filter (Figure 4.18(d)) (Ménager et al., 2000), acousto-optic filter (Figure 4.18(e)) (Coquin et al., 1988), etalon plus wavelength selective mirror (Figure 4.18 (f)) (De Merlier et al., 2005), Bragg waveguide (Figure 4.18(g)) (Sato et al., 2002), multichannel SOA (Figure 4.18(h)) (White, 1991), and multichannel SOA with phase shift and Rowland grating (Figure 4.18(i)) (Kwon et al., 2005). Recent developments in micromechanical systems (MEMS) technology has attracted much

attention and has put forward possibilities of miniaturising of external cavity tuneable lasers (A. Liu et al., 2007). MEMS technology makes use of photolithography to fabricate structures which are able to perform complicated, fast and accurate mechanical movements at very high stability. So any such structures used for external cavity lasers will enable highly repeatable fine tuning of laser wavelengths. Moreover, MEMS structures will significantly reduce the size of the external cavity (< 100 um) which cannot be realized using bulky components. Zhang et al have investigated a compact and ultra-narrow line width tuneable laser with an external cavity based on a simple single-axis-MEMS mirror (Zhang et al., 2012). The layout of the proposed MEMS external cavity laser is shown in the figure 4.19.

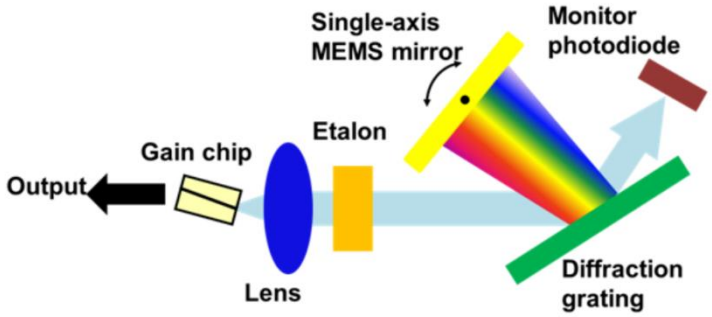

Figure 4.19 MEMS based external cavity laser layout (Adapted from Zhang et al., 2012)

A wide wavelength tuning range about 40nm in C-band with a narrow line-width of less than 50 kHz and a high wavelength accuracy of ± 1GHz over the entire tuning range was obtained. Apart from the obvious advantages of MEMS structures there are certain challenges, for example the optical system and MEMS packaging. Optical qualities of currently developed MEMS structures are not comparable to that of conventional ones. Also the fabrication of 3-D optical systems using MEMS process is very complex and requires additional assembly processes for alignment and attachment of movable structures. With the development of thin film optics the configuration based on thin film filter became popular replacing the air-spaced etalon which was not good enough as it required synchronous tuning with the external cavity longitudinal mode (Baillard et al., 2006). Thin film based Febry-Perot etalon manufactured with the coating technology provided high performance wavelength tenability just by changing the angle of the etalon inside the laser cavity. In this thesis a thin film based Febry- Perot etalon will be used inside the external cavity hybrid laser for synchronous wavelength tuning.

4.3.2 Photodetector

A photodetector is a solid state sensor for light sensing applications which operates by converting the absorbed light energy into electrical energy and the signal is processed to deliver information in useful format (Schinke et al., 1982). The photodiode is essentially a p-n junction with different doping concentrations on either side of the junction The doping creates the depletion layer and the light absorption with energy greater than the bandgap causes the charge carrier generation in the this region. Photodetection broadly involves three processes: 1) Absorption of light energy and generation of carriers, 2) Transportation of generated charge carriers, 3) carrier collection and generation of photocurrent (Bhattacharya et al., 1994). Absorption varies with the material type. Based on the bandgap structure it is classified into two category; Direct and Indirect bandgap material. The absorption in the indirect bandgap material involves the phonon generation which is basically the generation of thermal vibrations in the crystal lattice and thus it is weaker compared to direct bandgap materials. As a result these indirect bandgap materials requires thicker absorption layers leading to higher transit time and lower bandwidths. Thus direct bandgap materials are more suitable candidates for the high speed light detection. In spite of poor optical performance of the indirect bandgap materials such as Silicon (Si) and Germanium (Ge) they are detectors of the choice at optical wavelengths 0.8-0.9μm for the first generation optical fibre communication systems. The choice of material was primarily because of the absorption characteristics of the semiconductor material in the wavelength range of the interest. However with the shift in transmission at the longer wavelength for lower attenuation and dispersion in fibres and waveguides these indirect bandgap materials were no longer suitable for photo-detectors. The III-V group direct bandgap semiconductor InP with its lattice-matched compound semiconductors (GaInAsP, GaInAlAs) is currently thought to be the most appropriate material system for high performance optoelectronic device at longer wavelengths (Beling et al., 2009). Various compositions of InGaAsP lattice matched alloy system allow detection in the spectral range .92 μm to 1.65 μm (Smith et al., 1980). Based on the application various types of photodetector are possible such as p-i-n photodiode (PIN), avalanche photodiode (APD), metal-semiconductor-metal (MSM) etc. MSM photodetector are simple but are of low quantum efficiency for high speed operation. APD offers better sensitivity due to high gain but has limited bandwidth. PIN diodes have excellent bandwidth with good linearity, noise performance, and sensitivity (Bowers et al., 1987).

4.3.2.1 Principle of operation of PIN photodiodes

A p-i-n photodiode is a p-n junction diode having an intrinsic semiconductor region (lightly n doped) sandwiched between a p-doped and n-doped region (Figure 4.20). In this configuration the width of the depletion region is widened which results in better carrier collection efficiency. A large bias voltage is applied to fully separate the intrinsic charge carriers from the depletion region. These intrinsic n and p carrier concentration are negligibly small compared to the impurity concentration in the region. The incident photon with energy greater than the bandgap energy of the semiconductor generates charge pairs by exciting the electron from valance band to conduction band. These charge pairs are electron-hole pairs and are generated mainly in the depletion region where most of the light is absorbed. The bias voltage separates the charge in opposite direction giving rise to the current, known as photocurrent.

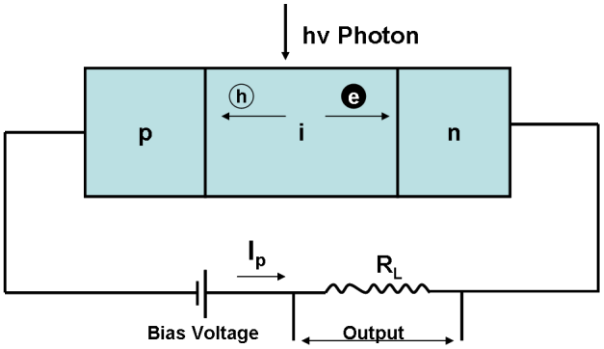

Figure 4.20 Schematic representation of a p-i-n photodiode with suitable bias voltage

The light absorption in the semiconductor material depends on the absorption coefficient and the thickness of the absorbing material. Assuming no reflection from the surface optical radiation absorbed in semiconductor material is given by,

$$P(x) = P_{inc}(1 - e^{-\alpha_\lambda x}) \tag{4.25}$$

where α is the absorption coefficient in cm-1 at a particular wavelength, P_{inc} is the incident power, P_x is the optical power absorbed at a distance x in the material. The primary photocurrent generated on absorption of the incident power P_{inc} is given by,

$$I_p = \frac{q}{h\nu} P_{inc}(1 - e^{-\alpha_\lambda x}) \tag{4.26}$$

where q is the electron charge and hν is the photon energy. Absorption coefficient has strong dependence of wavelength and its value drops to zero if photons do not have sufficient energy to excite an electron to the conduction band. Thus a particular semiconductor material

can be used only in the limited wavelength range. The upper cut-off wavelength λ_c is determined by the bandgap E_g of the material. If E_g is expressed in electron volts (eV) then the cut-off wavelength λ_c is given by,

$$\lambda_c[\mu m] = \frac{1.24}{E_g(eV)} \tag{4.27}$$

The cut-off wavelength for Si and Ge are 1.06 μm and 1.6μm respectively. So for longer wavelengths the photon energy is not sufficient to excite electrons to conduction band and hence Si and Ge cannot be used for light detection having wavelengths longer than the cut-off wavelength.

4.3.2.2 Performance metrics of a Photodetector

The performance of a photodetector is characterized by various figure of merit. These include the quantum efficiency, responsivity, response time, gain and the noise added to the signal by the detector. The paragraph below explains each performance metrics in detail.

1) Quantum Efficiency (η): Quantum efficiency (η) is defined as number of carriers generated per incident photon by a detector. This is categorised into internal (η_{int}) and external quantum efficiencies (η_{ext}). The internal quantum efficiency is defined as number of charge carrier pairs created divided by total number of photons absorbed. This is usually high in defect free materials which are not the case in general. Material defect causes absorption which lessens the amount of photo-generated charge carriers for actual signal generation. Thus external quantum efficiency is a more relevant parameter to explain the efficiency of the detector since it accounts for only those charge carrier pairs which contribute to signal creation. In equations it is written as,

$$n = \frac{i_{ph}}{q} \Big/ \frac{P_{inc}}{h\nu} \tag{4.28}$$

where i_{ph} is the current generated in response to the incident light, P_{inc} having power in watts, q the charge of the electron. The quantity $h\nu$ is the energy per photon in joules, where h the plank's constant and ν is the frequency of the light incident. There are several factors which influences the external quantum efficiency of the photodetector such as material absorption, material active area thickness, presence of passivation layers, band structure of semiconductor

material etc. Reflection of light from the surface of the material also contributes to signal loss. Approximately 30-40% of light flux falling onto the semiconductor air interface is gets reflected (Yotter et al., 2003). Suitable antireflection coating can be used to allow total light flux falling onto the surface and minimise loss. Because of various losses in the material no device can have 100% quantum efficiency. Depending upon the material, photon wavelength and sensing mechanism quantum efficiency can vary between 20%-90%. A direct bandgap material will have higher quantum efficiency compared to indirect bandgap material as it there is no loss of charge carriers for phonon generation, for e.g. Gallium arsenide (70%) has much higher quantum efficiency compared to Silicon (20-40%) (Schinke, et al., 1982).

2) Responsivity: This is a measure of sensitivity of the device to the incident light. It varies with the wavelength of the incident light as well as applied reverse bias and temperature. Responsivity increases with the applied reverse bias due to improved charge collection efficiency in photodiode. Mathematically it is defined as output current (i_{ph}) divided by the incident optical power (P_{inc}) in watts, or

$$R = \frac{i_{ph}}{P_{inc}} \tag{4.29}$$

A high responsivity improves signal-to-noise ratio of the receiver system. Higher gain due to photo-multiplication such as in the case of Avalanche Photodiode (APD) can lead to high values of responsivity but at the expense of lower bandwidth and higher noise value (Pal, 1992).

3) Noise Equivalent Power (NEP): This is the amount of light required to collect a signal equivalent in power to that of the noise in a photodetecting device. It is defined as the RMS noise current divided by the responsivity and has units in W/(Hz)1/2 .

4) Gain: Gain depicts the signal amplification in a photodetector. It is defined as the ratio of total current that flows in response to the incoming light to the current that flows in direct response to

impinging photons, where G is the Gain, I_{out} is the output current, i_{ph} is the photo-generated current.

$$G = \frac{I_{out}}{i_{ph}} \tag{4.30}$$

In normal detector such as p-i-n detector there is no multiplication of charge carriers and hence the maximum possible gain is 1. But in the case of PMT and APD, the inherent carrier multiplication results very high.

5) Dark current: The current generation under no light conditions is called as the dark current. Materials imperfections or operating temperatures above absolute zero leads to the generation of charge carriers in photodetector under an applied bias. Although charge carriers generation is in small amount, it limits the ability of detector to detect small signal from the photodetector. The dark current increases with increase in the bias current as well as with the increase of temperature.

6) Response time: This is time in which the response of the detector reaches from 10% to 90% of its final response. This is also called as the rise time. In other way it is defined as the electron transit time to the external circuit or device. So with a shorter response time, the detector can resolve events more clearly. The response time of the detector depends either on the active area or the RC constant of the circuit. The RC time constant is the capacitance C of the photodiode junction multiplied by the load resistance R. It is represented as $\tau = RC$. The larger is the active area; longer will be the response time.

4.3.3 Thermo-optic switches

Thermo-optic (TO) phase shifters are important optical elements in silica based integrated optical circuits which provides light modulation and switching characteristics. Refractive index dependence on temperature called as thermo-optic effect which manipulates the light by tuning the effective index (Okuno et al., 1995).

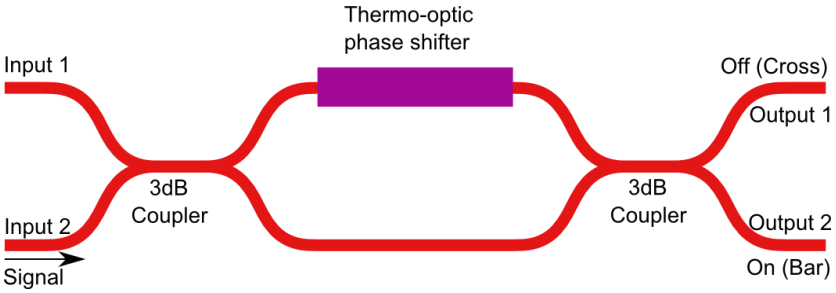

Figure 4.21 Schematic of thermo-optic switches in a Mach-Zehnder interferometer setup

The basic configuration of 2x2 TO switching unit is shown in the figure 4.21. It consists of two 3-dB directional couplers forming a Mach-Zehnder interferometer setup with two input and two output ports. Either both or one of the waveguide arms is equipped with the thin-film heater

which acts as TO phase shifter on application of suitable voltage (Himeno, 1999). Usually a metal such as chrome is deposited on the top of the cladding of a waveguide. When no voltage is applied the unit is in cross state (output 1). Adjusting the supply voltage to the thin-film heater increases the path length for light propagation ultimately lowering the speed in that waveguide and the two lights are out of phase when they are merged in the second coupler, so the light is output from port 2. Negligible insertion loss, ease of fabrication and robustness are the main advantages of thermo-optic phase shifters. On the other side TO phase shifters however consumes significant power, is relatively slow (typically ~ 2 ms) and also exhibits some polarisation dependence and cross talks between the adjacent waveguides. Loaded stripe line geometry have been implemented by Mdler et al to lower the power consumption and less lateral heat diffusion compared to the buried waveguide (Moller et al., 1993).

4.4 Summary

In this section several essential passive and active components required for metrology sensor device such as waveguides, directional coupler, wavelength encoder unit, an optical isolator, a laser, photo-detector etc. are discussed. This includes the working, design and fabrication technologies adopted for the fabrication of individual components and device development as a whole. Silica based waveguide system is chosen for low propagation loss and better mode coupling with single mode fibres. Similar material system and fabrication methodologies were used for the other passive components such as directional couplers, MMI couplers and wavelength encoder unit. For light generation and detection GaAs and InP material systems are chosen for lasers and photo-detectors. External cavity laser configurations are recognised to offer high optical power, wide tuning range and narrow line-width. Semiconductor optical amplifier based on multiple quantum well structures is coupled with external cavity configurations enables tuneable single longitudinal mode laser operation at appropriate wavelength of interest. Wavelength selection inside the cavity is based on fast rotating multi-layered thin film filter. An integrated 90^{o} optical hybrid is incorporated in the device that would provide real time fast monitoring of the laser wavelength tuning. Thermo-optic phase shifter is applied in the detection unit to couple all the reflected reference beams from the filter to reference detector. Next chapter will detail the working mechanism of the metrology sensor device. In addition it will also cover various aspects such as assembly, test and measurement of individual components and system as a whole.

5 Metrology sensor system

5.1 Introduction

This chapter presents the development of the chip interferometer system for online surface measurement. Several metrology tools have been developed using interferometric techniques for high precision surface measurements. All the current available interferometer based metrology tool options are bulky to be incorporated onto machine tools for online surface measurements. Optical integration techniques offers the possibility of integrating various passive and active components integration onto a single optical chip, thereby significantly reducing the overall form factor of the device to be used for an embedded metrology applications. Several examples of component integration and techniques are illustrated in chapter 3 (Integration technology) to support the idea of developing such a chip interferometer for online surface measurement applications. The chapter will detail the concept, developmental strategy and experimental results of the individual components and system as a whole.

5.2 The concept of metrology sensor system

Figure 5.1 show the concept metrology sensor system which comprises of two distinct elements: An integrated-optic module containing the photonic circuit, and separate optical probe structures (lateral scanning and single point probes). The integrated optic module contains essential components of the interferometer sensor: hybrid tunable laser, fixed wavelength hybrid laser (as a reference), optical couplers, wavelength monitoring system, phase shifters and photodetectors. All these elements are contained on a single silicon chip forming the interferometer system for the precise surface measurement application. In the setup the arms of the coupler forms Michelson interferometer with one arm going to the measurement probe and other to the reference containing spiral waveguide and phase shifters. The spiral waveguide is used as a path length compensator to balance the reference and measurement arms of the interferometer. On the chip there is real time wavelength monitoring system based on coherent signal detection and demodulation. This will provide faster wavelength measurements while the tunable laser is rapidly tuned. Separate signal detection units are integrated onto the optic module for the detection of signals from the two

probe types. Signal detection unit for probe1 has a coupler, a pair of TO phase shifters, thin film filter and array of PDs while probe2 has two detectors only. The probe part consists of a collimating lens, a grating element and a focusing lens. The design replaces mechanical stylus scanning as well as the bulky free space and fiber interferometers in many applications and represents a miniaturized optical tool for surface measurement. The basic principle of operation of the proposed metrology tool is based on two interferometric techniques; wavelength scanning and phase shifting. There are two possible probe types which are dependent on one of two possible measurement modes: a) the lateral scanning probe and the b) single point absolute distance probe. The working and design of two basic probe types to be employed for surface profiling and absolute distance measurements will be discussed in detail in the next chapter. With the given probe types the device can operate in one or the other measurement mode depending on the measurement requirement.

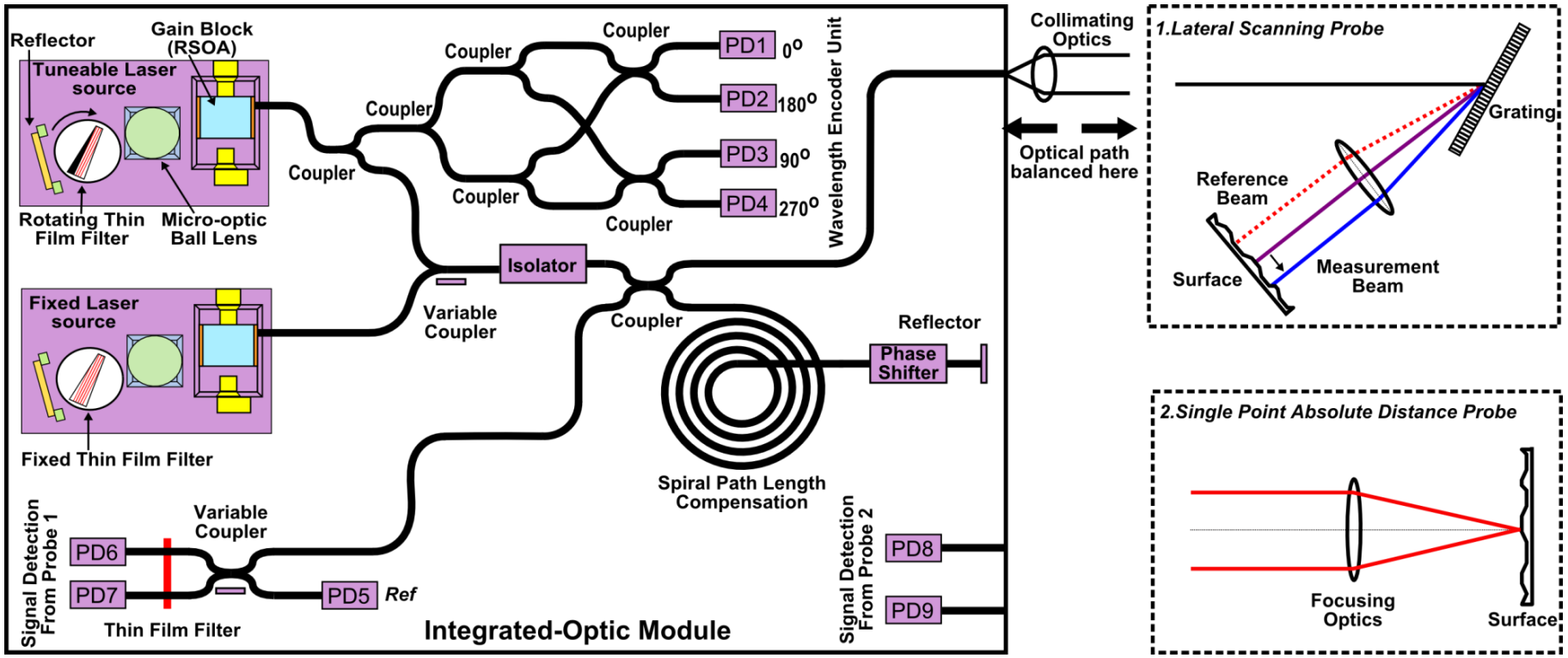

Figure 5.1 Schematic of the full integrated optical metrology chip device

5.2.1 Lateral scanning surface profile measurement mode

In lateral scanning mode the surface profile is obtained by scanning the wavelength tuned source onto the test sample using a dispersive grating (Figure 5.2). In this configuration the light from the tunable laser source is coupled with the fixed laser and passed through an optical isolator after which it is split by a coupler to form the arms of a Michelson interferometer. On the chip there is another fixed wavelength laser which acts as a reference wavelength source and is multiplexed into the chip interferometer system to track unwanted phase variations caused by vibrations or external disturbances. The reference arm has a path length compensation spiral, phase shifting unit and integrated reflector. The measurement arm light is coupled into free space by the collimating lens where it is incident on a dispersive grating. A scan lens system then focuses the beam onto the surface where it may be swept across in the manner of an "optical stylus".

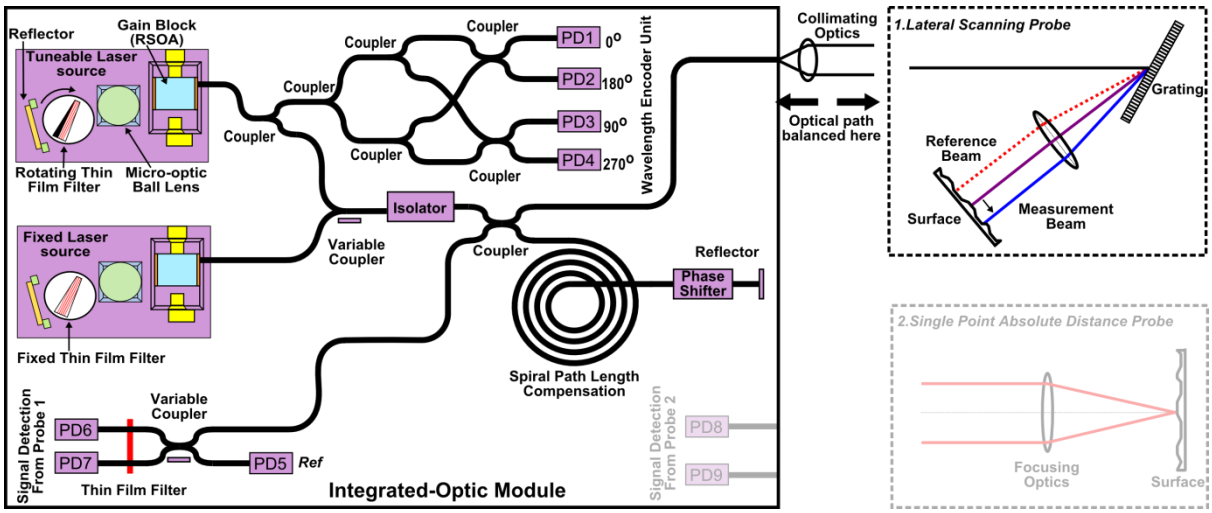

Figure 5.2 System configurations in the lateral scanning measurement mode (unshaded part)

The 1st order reflected beams from the grating forms the measurement beam. Variations in surface height changes the distance travelled by 1st order beam and hence changes the phase at the recombination point. The changing phase introduces intensity variation of the interfered light beam and is given by,

$$I(x) = A(x) + B(x)\cos\left[\frac{2\pi}{\lambda(x)}\left(2h(x) + l\right)\right] \tag{5.1}$$

where $A(x)$ and $B(x)$ are the bias intensity and the fringe visibility at a point x respectively and $h(x)$ is the height variation at that point, l is the optical path length difference between the arms of the interferometer. The surface profile is thus inferred from the interference intensity signal. There are various methods of obtaining phase from the output of an interferometer. Phase shifting interferometry is one of the popular techniques for determining the phase information from recorded interferogram (Creath, 1988). A time varying phase shift is applied between the reference and test beam and a number of interferogram are recorded. Further a suitable algorithm is then applied to retrieve the phase information from the set of interferogram.

A Carre algorithm (Carré, 1966) is used for phase calculation as it doesn't requires a known phase shift to be performed. This brings obvious advantage in implementing precise phase shifting just by ensuring the distance moved by mirror is identical with each phase step. If $\phi(x)$ is the original phase at a sampled point x on the surface and the phase is altered by four equal steps $-3\alpha, -\alpha, +\alpha, 3\alpha$ around this point then four intensity values are obtained. The four intensity values are $I_1(x), I_2(x), I_3(x)$ and $I_4(x)$ respectively. These intensities can be solved using Carre algorithm to obtain the phase value.

$$\phi(x) = \tan^{-1}\sqrt{\frac{\left(3I_2(x) - 3I_3(x) - I_1(x) + I_4(x)\right)\left(I_1(x) + I_2(x) - I_3(x) - I_4(x)\right)}{\left(I_1(x) - I_2(x) - I_3(x) + I_4(x)\right)^2}} \tag{5.2}$$

5.2.2 Single point absolute distance measurement mode

The absolute distance probe consists of a lens system to focus the beam onto the surface under test (Figure 5.3). Here the light from the tunable laser source is passed through an optical isolator after which it is directly fed into the focusing lens system and a single point on the test sample is scanned and measured at a time using wavelength scanning interferometry (X. Jiang, et al., 2010b; Yamamoto, et al., 2001).

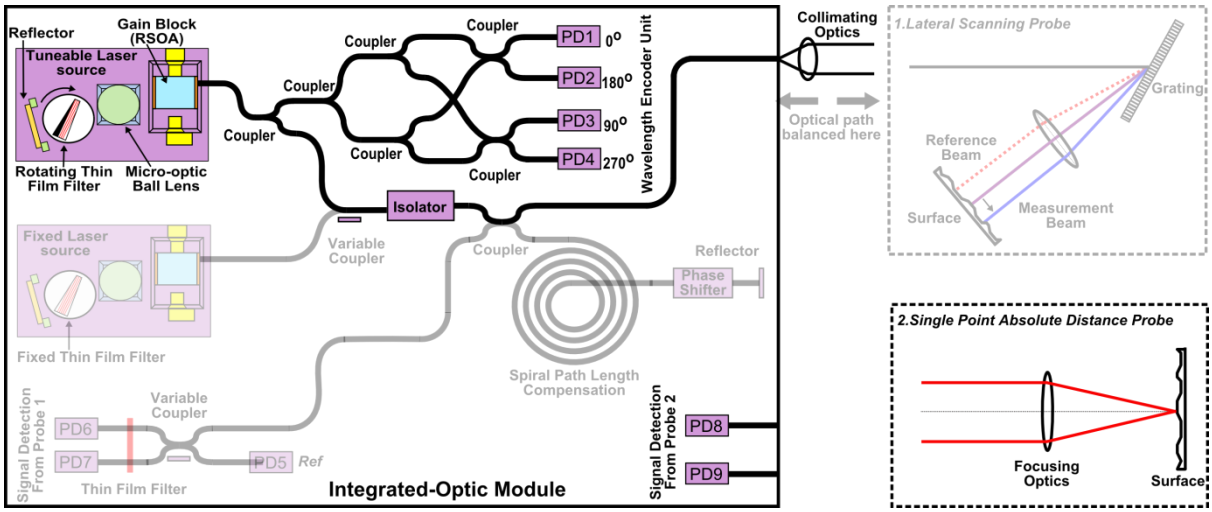

Figure 5.3 System configurations in the absolute distance measurement mode (unshaded part)

The wavelength scanning introduces a phase change, the rate of which depends on the optical path difference. Thus by calculating the actual phase change of the interference signal, it is possible to calculate the absolute distance. The phase of an interference signal $\varphi(x, y; k)$ is given by

$$\varphi(x, y; k) = 2\pi k h(x, y) \tag{5.3}$$

The phase shift owing to the wave number shift as the laser scans from start to stop wavelength is

$$\varphi(x, y; \Delta k) = 2\pi \Delta k h(x, y) \tag{5.4}$$

Finally the optical path difference (OPD) can be calculated as,

$$h(x, y) = \frac{\varphi(x, y; \Delta k)}{2\pi \Delta k} \tag{5.5}$$

The recorded interference intensity due to wavelength tuning shows periodical modulation whose frequency is proportional to the optical path difference of the interferometer. Fourier transform technique is used to determine the modulation frequency to extract phase from the interferogram. Once the phase value is obtained height or distance can be calculated using the above relation in equation 4. This measurement mode is capable of measuring over several millimeters with sub-micron resolution.

5.3 Device component integration

The present work is a continuation and extension of earlier work on rapid phase-shifting fiber interferometer with optical stylus (H. Martin et al., 2010). The fiber interferometer had a

simple fiber configuration but it required a very expensive and large-scale tunable laser. In addition it requires a complex active stabilization technique to deal with the random optical path length variation and polarization evolution inherent with optical fiber. Replacing optical fiber with integrated optics technology can provide the required compactness while also increasing the stability of the apparatus substantially over the optical fiber equivalent and will represent a miniaturized optical tool for surface measurement. To make the system usable for online surface measurement, it needs to be compact and flexible enough to be mounted on a machine tool. Hybrid integration is the technology that holds promise for improving the current state-of-the-art in in the online measurement of surfaces (Maxwell, 2008). In this approach silica based PLC is used which enables the construction of highly functional components by combining the passive function of a PLC with the active function of various photonics components assembled on silicon motherboards. An example of hybrid integration of semiconductor optical amplifier (SOA) onto silicon motherboard is illustrated in figure 5.4.

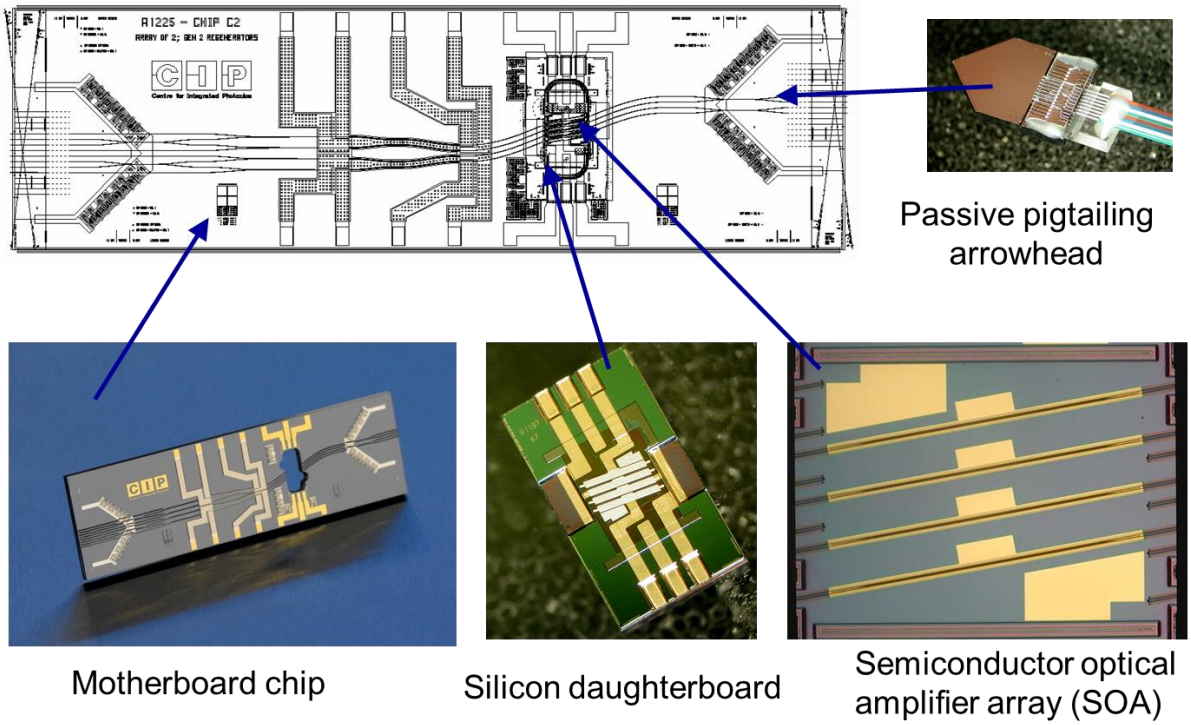

Figure 5.4 Hybrid design showing SOA array in place (CIP Device)

Similar to the above example a silica based PLC is used for the development of integrated optical metrology chip device to enable the construction of highly functional optical systems.

Horizontal alignment on the daughterboards and motherboards are obtained by lithographically defined mechanical end stops created using the SU8 polymers (a negative epoxy based photoresist). These end stops are fabricated by spinning the drop of SU8 polymers and prebaking so that it becomes hard. Further a mask is defined photolithographically onto the hardened polymer and UV light is exposed. Unwanted materials are removed after washing the substrate in the developer solution. Since the stops are photolithographically defined, accurate and precise structures can be obtained on waveguide overcladding to sucessfully align various integrating optical components. The vertical reference frame is the top of the cladding of the silica motherbaord. Alignment in vertical direction is obtained by silicon upstands. The difference in vertical heights between the active and the passive motherboard are compensated for by micromachining a terrace onto the silicon motherboard to the appropriate depth.

The motherboard used in this thesis is silica-on-silicon with precise micro-machined terrace to accommodate active components. The various components to be integrated onto silica-on-silicon etched integrated optic motherboard are waveguides, optical coupler, and hybrid tunable laser, and fixed reference laser, wavelength monitoring system, phase shifter and photodetectors. The SOA array is first bonded to the silicon daughterboard and is flipped onto the slot made on motherboard chip. Light output coupling for external application is brought out by passive pigtailing of array of fibres.

5.3.1 Waveguide

The PLC is fabricated using FHD and RIE method (Kawachi, 1990). The refractive index contrast used in the fabrication of the waveguide is 0.75% which is provided by doping the silica with Germanium (Ge) in the core of the waveguides to be fabricated. Ge is most common used dopant, both for planar waveguides and fibers, due to its chemical similarity with silicon that makes it possible to keep the material losses on low level. The fabricated waveguides cross-sectional dimensions are of 6 μm x 6 μm shown in figure 5.5. The device was manufactured in collaboration with the Centre for Integrated Photonics (CIP), UK.

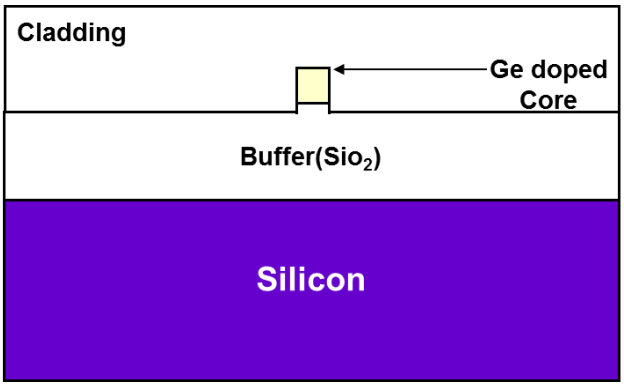

Figure 5.5 Waveguide cross-section

5.3.2 Semiconductor Optical Amplifier

InGaAs/InP material system is used for fabricating SOA gain chip to cover the required wavelength band around 1550 nm. The laser gain chip is made up of a single polarization reflective semiconductor optical amplifier (RSOA) (Lealman et al., 1998). The RSOA is a mode expanded tilted semiconductor optical amplifier array angled at 10^{o} to the external facet of the chip, which is anti-reflection coated (Figure 5.6). The active layer of the gain chip is a multiple (four) quantum well buried hetero-structure device with an active width of 3 microns designed to provide the required bandwidth. The front facet of RSOA gain chip is uniformly cleaved and structured to provide the optimum gain to the propagating mode functioning as one of the mirrors (~ 30% reflectivity).

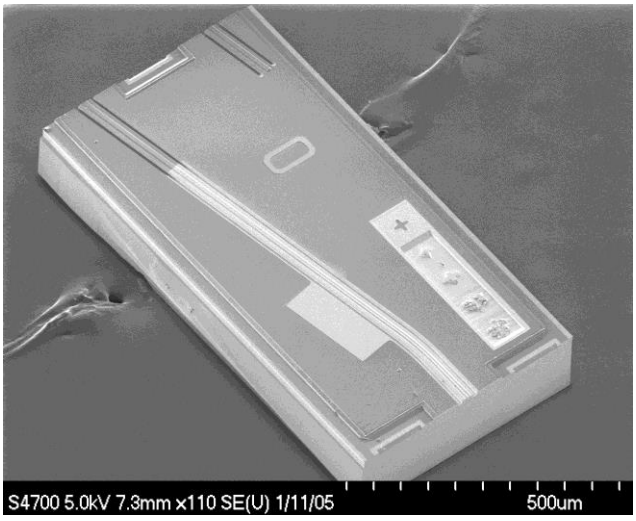

Figure 5.6 SEM image of RSOA chip showing angled facet output on the left and normal incidence facet at the right

For integration of SOA onto the daughterboard, SOA is pushed against the SU8 alignment features and stops etched in the daughterboard surface and bonded sequentially. Gold solder pads

rectangular in shape are deposited onto the chip to facilitate the bonding. The chip is held in place against the mechanical stops while the solder solidifies to ensure precise alignment of parts. A commercial Finetech thermo-compressing flip chip bonder was used for bonding between the SOA chip and the Si daughterboard. Electrical connections is provided to the SOA through the metal pads lithographically defined onto the daughterboard which is flipped and bonded to metal tracks of motherboard. The n-side of the SOA is wire bonded to another metal pad on the daughterboard as shown in figure 5.7.

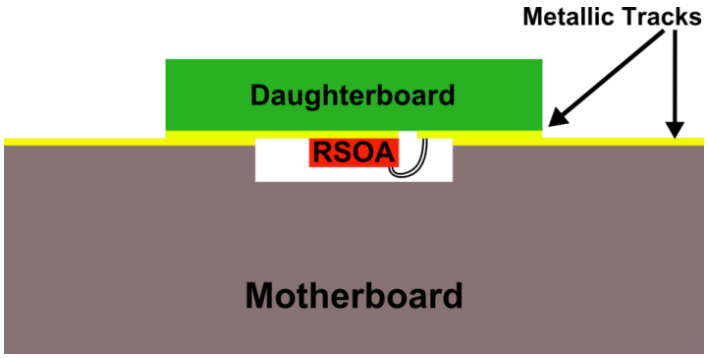

Figure 5.7 Cross-sectional view of daughterboard-motherboard integration

Further to integrate the tunable laser module on the PLC, the daughterboard with laser gain chip is flipped and bonded between the gold pads deposited on both the motherboard and the daughterboard. The output from the gain chip is horizontally and vertically aligned to the input wave guide of the PLC automatically through the integration of suitable etched passive alignment features deposited onto the motherboard and daughterboard. Such passive alignment technology is well developed for silica based PLC devices (T. Okamoto et al., 2009; Wale & Edge, 1990).

5.3.3 Phase shifter integration

The SOA's will replace the mechnical PZT as a phase shifting unit in the refernce arm. This unit is still under development stage. The SOA's forms the phase shifting unit in the reference arm of the interferometer as shown in the figure 5.8. At the end of the reference arm in the interferometer is a 1x5 MMI splitter, of which each output arm goes to a different element in an array of five RSOAs. Small increments to the path length have been included in the different output arms so that the total round trip phase delay, comprised of the phase differences between output ports of the MMI splitter plus the added path length increments, will vary by increments of $\pi/2$ between different paths.

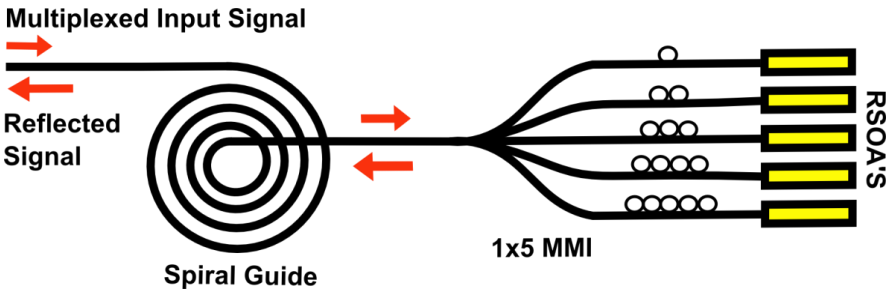

Figure 5.8 Phase shifting unit containing RSOA's

The use of SOA's as a phase shifter can provide fast switching with signal amplification as well as at the same time alleviated the need of a mechanical phase shifter making the overall chip simpler having compact configuration. The integration of SOA array followed same method employed for the development of laser gain block onto the daughterboard. Here an array of RSOA's are integrated onto the silicon daughter board which is then flipped onto the motherboard containing machined terrace to accommodate the component.

5.3.4 Optical fibre integration

For coupling the light out of chip to the fiber for external use the fibre is positioned in line with the prefabricated machined structures called as sub-mounts or the daughterboards (Figure 5.9). The silicon sub-mount has an arrow head shape which is flip-chipped onto the end of the motherboard such that the fibre V-grooves falls in line with the waveguides for coupling. The V-grooves for passive pigtailing of single mode optical fibres are achieved by etching grooves in the substrate. The etching is done using KOH solution and water. Windows are defined photolighographically such that V shaped grooves and arrow heads are obtained. Etching arrow head vertical faces into this submount and subsquent alignment to features patterned on the cladding of the motherboard provides lateral registration.

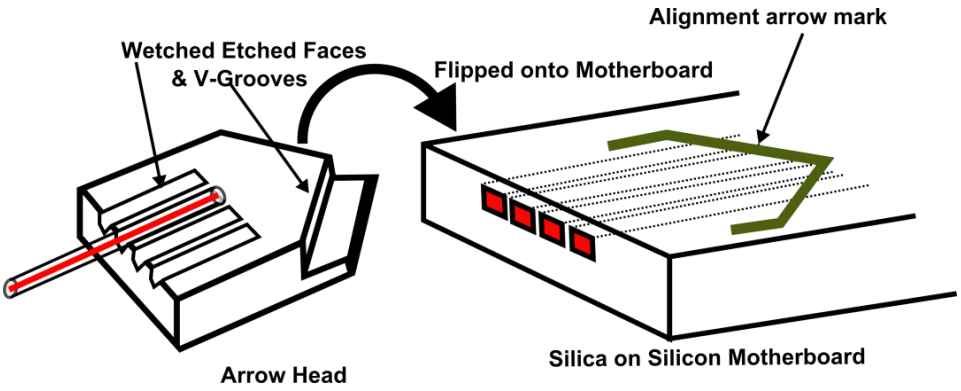

Figure 5.9 Passive pigtailing of the fibre array onto the Silicon V-groves

5.3.5 Detector Integration

The out of plane coupling to surface mounted detector have much better performance and hence this designs approach will be employed for the detector integration. The schematic of detector integration is shown in the figure 5.10.

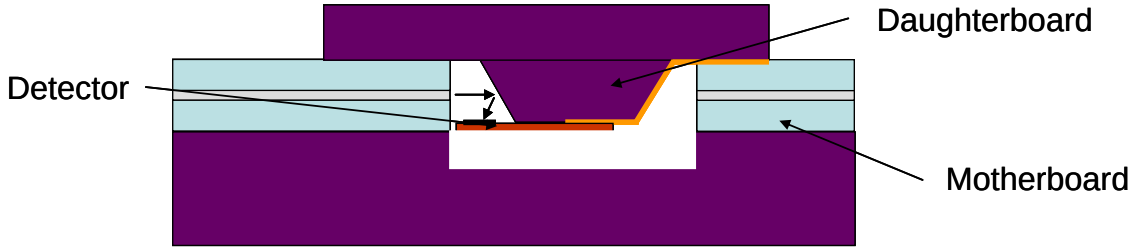

Figure 5.10 Schematic of surface coupled detector arrangement

5.3.6 Hybrid integrated devices

5.3.6.1 Tuneable Laser

The hybrid tunable laser is the most critical component of the chip metrology device. The schematic of the developed tunable laser module is shown in figure 5.11. The tunable laser has an external cavity configuration consisting of main elements as: gain block (RSOA), gain block submount, ball lens, tuning filter, rear reflector, tuning motor and optical element submount. Rear reflector made up of silicon with a high reflective coating (~ 98%) forms one end while at the other end front facet of RSOA serves as mirror completing the external cavity configuration. In the cavity a thin film filter (TFF) is placed in the path of a collimated beam coming out of RSOA through the micro-optic ball lens.

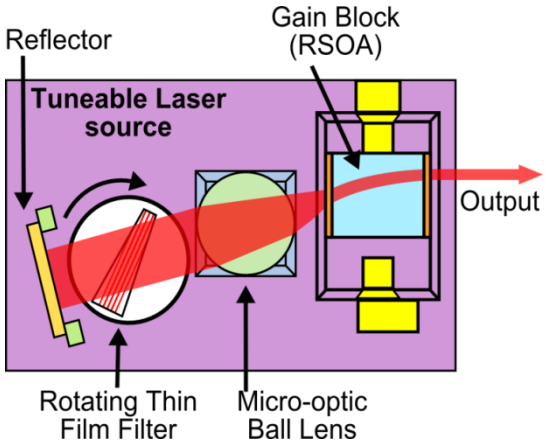

Figure 5.11 Schematic of tuneable laser configuration

Thin film filter (TFF) used in the module is a multilayer stack of dielectrics over the fused silica substrate. The TFF rotation provides the wavelength selectivity, by allowing only one

longitudinal cavity mode to oscillate at any one time. The resulting spectral shift due to rotation is described by,

$$\lambda(\theta) = \lambda(0)\sqrt{1 - \frac{\sin^2(\theta)}{n_{eff}^2}} \tag{5.6}$$

where θ is the angle of incidence and n_{eff} is the effective index of refraction. The effective thickness of the TFF changes with rotation and thus produces the wavelength selection effect. As the TFF rotates, entire bandwidth of the laser is swept and the beam is finally coupled to the waveguide drawn onto the integrated chip through the front facet of the gain block. The hybridized laser is butt-coupled to the exit of the waveguide to the fiber for the beam delivery. A thermistor is mounted on the silicon substrate to monitor the temperature of the integrated laser chip. The temperature is further controlled by thermoelectric cooler system placed underneath the chip. The target specification of the chip tunable laser is shown in the table 5.1. Several version of chip tunable laser have been developed with added improvements and modifications in the successive modules necessary to improve performance to the level that meets specifications. Section below will detail each developed versions of chip tunable laser.

Table 5.1Summary of the operating performance requirements of tuneable laser

Chip tunable laser specifications	
Parameter	**Target specifications**
Output power	+10 dBm
Tuning range	~100 nm
Tuning speed	< 1 s
Laser threshold current	<90 mA
Side mode suppression ratio	≥ 45dB
Relative intensity noise	<-160 dBc/Hz
Package dimension	10 X5 X2 cm

5.3.6.2 Versions of chip tuneable laser

Figure 5.12 is a photograph of the first version of packaged device with the dimensions of 100 x 50 x 20 mm. The device could tune over ~ 60 nm with an output power up to -4 dBm. The laser threshold current was ~200mA. This version confirmed the viability of the adopted device design. The tuning of the TFF was actuated using a pizeo- electric motor.

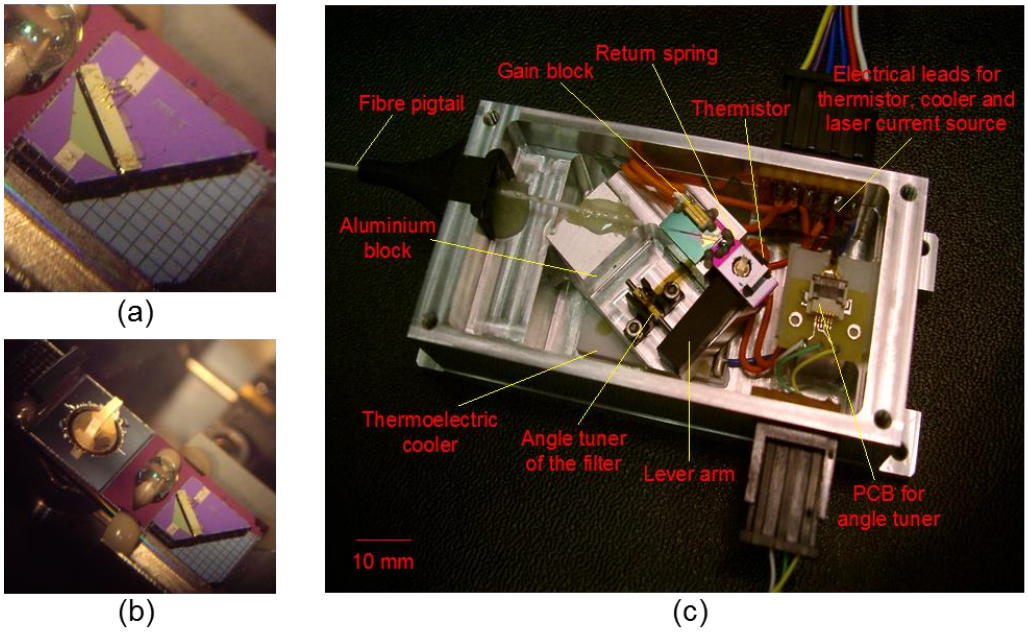

Figure 5.12 Hybrid integration of the first version of tuneable laser module

a) RSOA bonded onto the silicon daughterboard connected with the wire bonding, b) Assembled sub-mounts containing the components of chip tuneable laser, c) First version of the packaged chip tuneable laser

The device didn't have had a PLC and the light output from the gain block was directly coupled to the fiber for external use as can be seen in the figure. The output power was too low suggesting a high cavity loss. Also it had a very limited wavelength tuning range. Lasing threshold of the device was very high. These all issues were overcome in the second version of the chip tunable laser. The second version of chip device contained tuneable laser, coupler and a photodetector on the board. The filter tuning element was refined and modified to obtain extended tuning range and improved single mode operation. The second version had a tenability of ~80 nm (1510 nm - 1590 nm). With better alignment losses were minimized inside the cavity which brought the lasing threshold down to ~100 mA. The output power increased to 0 dBm measured at 250 mA. The third version (Figure 5.13) had modification with micro-optic ball lens. A machined micro-optic ball lens in the form of cylinder called as drum lens was used in this version. An anti-reflection (AR) coating was applied to both the faces of the lens to reduce

cavity losses and back reflection. The AR coating had a wider bandwidth to fully accommodate the entire wavelength range. The high quality AR coating allowed much lower reflectivity than obtainable from commercially coated lenses. The lower refractive index also improves the tuning range towards the short wavelength part of gain spectrum. Also center wavelength of the tuning filter was modified to shift towards longer wavelengths (1610 nm – 1620 nm). This extended tuning range at long wavelength end of the spectrum and achieved >90nm of wavelength tuning.

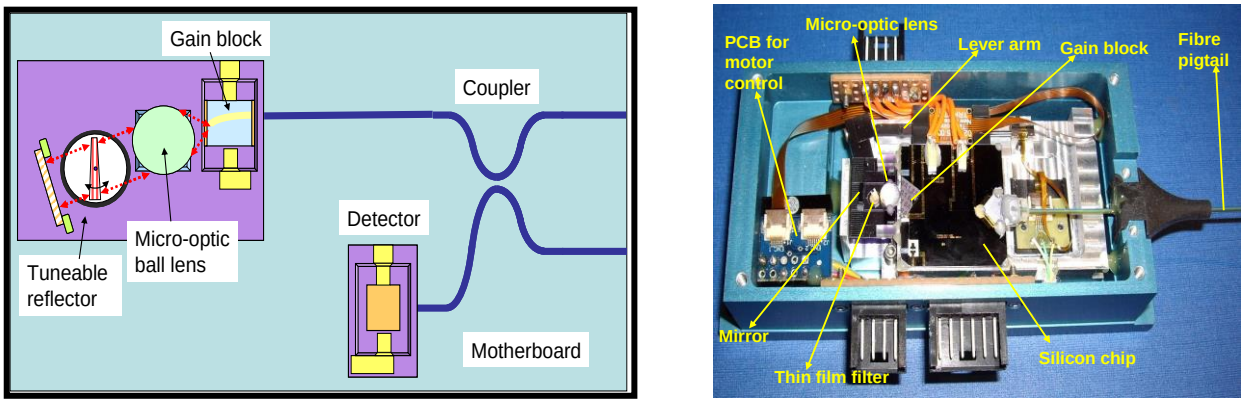

Figure 5.13 Schematic of the second version tuneable laser (L) and the fully packaged integrated chip tuneable laser(R)

5.3.6.3 Fixed Wavelength Laser:

The sensor has a fixed wavelength reference laser whose output is multiplexed into the interferometer with the help of 3 dB couplers. The configuration of fixed wavelength laser is similar to that of the tunable laser but with a fixed thin film filter for single wavelength operation (figure 5.14).

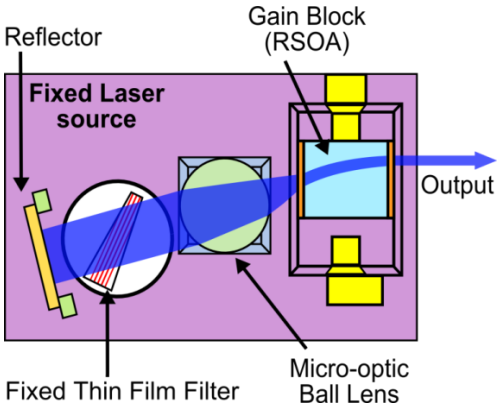

Figure 5.14 External cavity fixed laser working

This reference laser will source a static reference interferometer which will share a near common path with the measurement interferometer. So any unwanted phase disturbance due

vibrations and environmental noises can be easily tracked and compensated through feedback close loop operation. Thus the stability of reference laser is critically important as any drift beyond tolerance limit will induce error. Hence it is required to investigate the performance of reference laser and to perform error analysis to define tolerance limit. The table 5.2 gives the summary of the operating performance requirements the fixed wavelength reference laser .

Table 5.2 Summary of the operating performance requirements of fixed wavelength laser

Fixed wavelength laser operating requirements	
Parameter	**Specification**
Output power	+10dBm
Operating wavelength	1490±5 nm
Wavelength stability	0.1 nm
Relative Intensity Noise (RIN)	< -160 dB/Hz
SMSR	≥ 45dB

5.3.6.4 Wavelength encoder unit

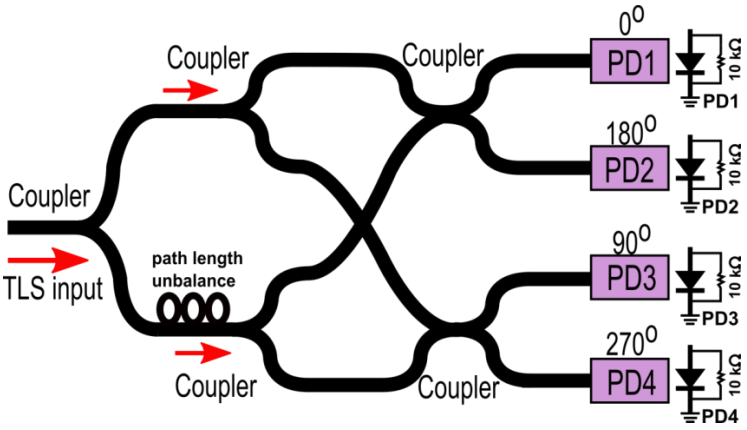

Figure 5.15 Wavelength encoder unit

Wavelength encoder unit is basically a 90° hybrid consisting of a delay interferometer and a MZI configuration for high speed real time wavelength monitoring of the tuneable laser (Figure 5.15). The hybrid is made of silica waveguides and PD arrays each consisting of four individual InGsAs/InP PIN photodiodes. Components are hybrid integrated and packaged with four linear transimpedance amplifiers. A tap coupler to the chip tuneable laser output takes a part of main signal to an unbalanced and balanced detection circuit for monitoring the tuneable laser wavelength. The unbalance in the interferometer has a physical path length of 253.5µm. The unit outputs four quadrature signals which are detected by the four photodetectors.

5.3.6.5 Signal detection unit

The signal detection unit contains a coupler, a pair of thermo-optic phase shifters, thin film filter and array of PDs (Figure 5.16). As the output of the interferometer contained multiplexed signal, a thin film filter is used to reflect back the fixed wavelength laser output and the phase shifter is adjusted to cross-couple the signal to one of a detector of the PD array. The filter is an edge filter designed to reflect the reference laser and pass the entire tuning band of the tuneable laser. Light from the tuneable laser directly passes to two other detectors, whose signal can then be summed to give the total power in the signal beam.

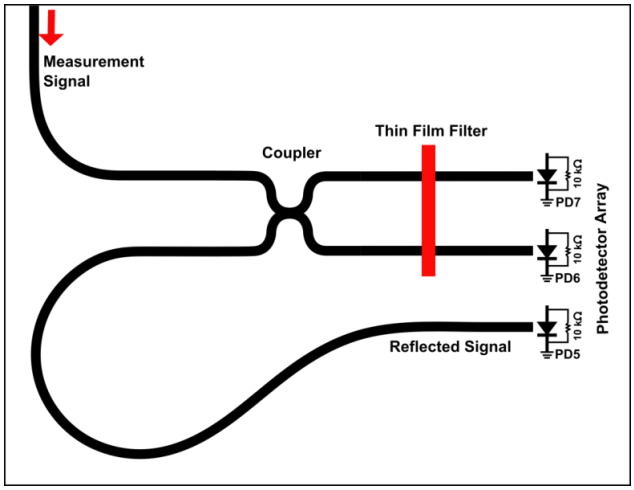

Figure 5.16 Signal detection units

The waveguides is made of silica and the filter and photodetectors are hybrid integrated onto the optical chip. Similar p-i-n photodiodes as in the case of wavelength encoder unit is used to detect the signal. The photodiodes are bonded directly across to the output without using transimpedance amplifiers (TIAs). A 10k resistor is placed in parallel with each photodiode, to provide a load for the photocurrent and reduce the risk of static damage

5.4 Test and measurement results

This section will present the test and measurement results of individual components of the chip interferometer system. This includes assessment of wavelength encoder unit and the signal detection unit and 3rd version of chip tuneable laser.

5.4.1 Wavelength encoder unit testing

The input to the wavelength encoder unit was fed through the fibre port attached to the waveguide chip (Figure 5.15). The chip tuneable laser was used as a source. The wavelength

scan along with will allow evaluation of the filter functions of 90^{o} hybrids. The wavelength of the chip laser was scanned from 1506nm to 1596 nm (~ 90nm) showing the expected cyclical response and phase shift between the various outputs of the photo-detector array as shown in figure 5.17. The output was detected at the photo-detector array on a four channel oscilloscope. The signals obtained from the photo-detectors PD1 & PD4 observed to noisy compared to the signals obtained from other two detectors. So for initial investigations signals from PD2 and PD3 can be chosen to decode and calibrate the corresponding wavelength measurements.

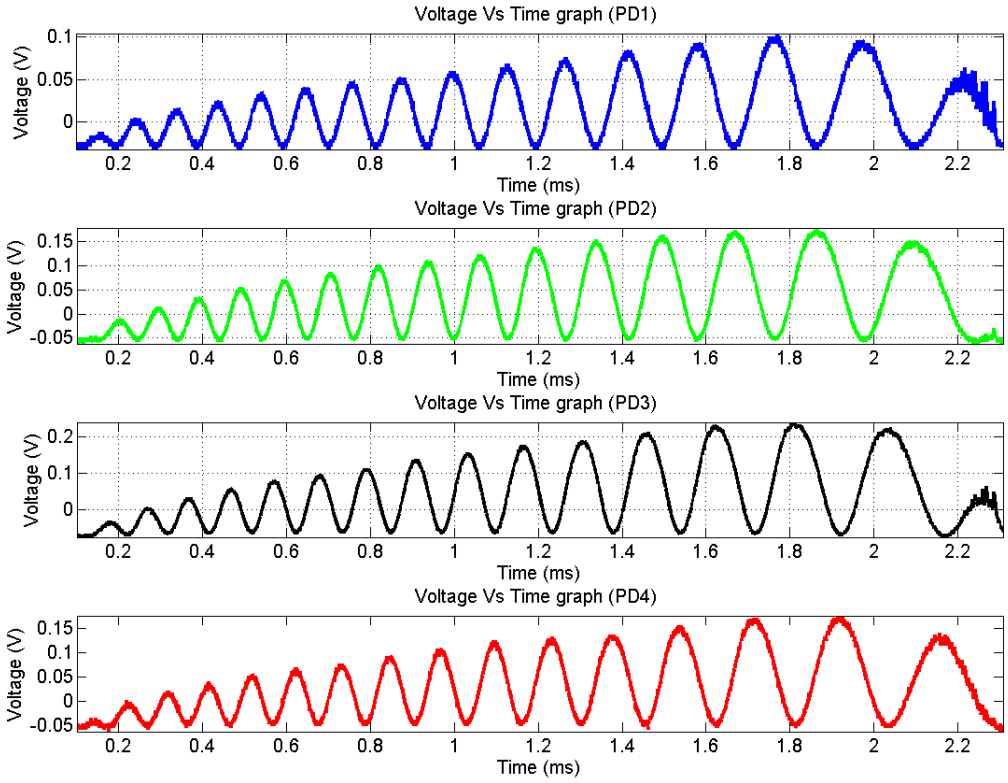

Figure 5.17 Response from the individual photo-detectors (PD1, PD2 PD3 & PD4)

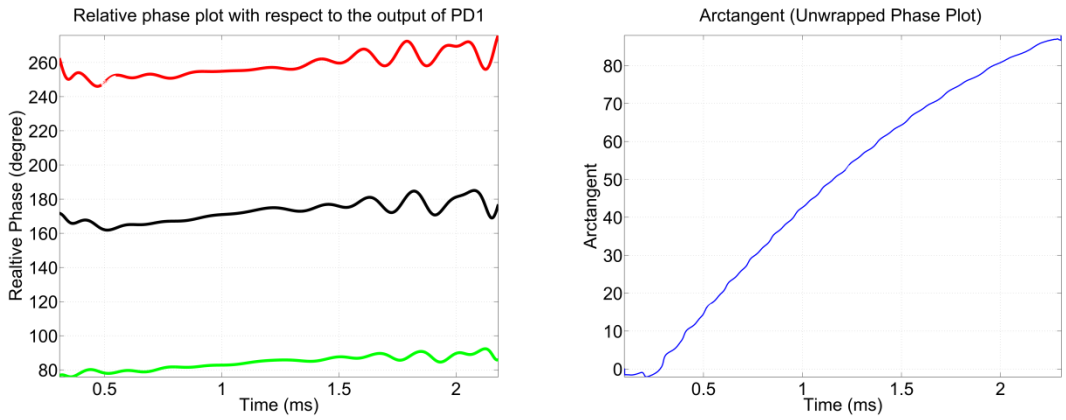

Figure 5.18 (a) Relative phases at the output ports of the wavelength encoder with respect to the PD1, (b) Unwrapped phase obtained from balanced detection

Table 5.3Relative phase difference between the output ports of the wavelength encoder

	Relative phase difference with respect to PD1(Degree)	**Ideal relativephase (Degree)**	**Error**
PD2	172.618	180	7.382
PD3	258.239	270	11.761
PD4	84.3021	90	5.697

The phase value was calculated using Fourier fringe analysis technique. The table 5.3 shows the mean value of relative phase shifts for the three signals (Figure 5.18(a)). The phase shift error was observed to vary up to $\pm 12^{o}$. The possible reason of such a variation can be due to core reproducibility and homogeneity. So by improving it a good correlation with the ideal relative phase shift can be easily achieved. The figure 5.18 (b) shows the unwrapped phase obtained following balanced detection scheme as explained in chapter 4, section 4.2.3.2. In order to correlate wavelength to the corresponding phase, a further calibration is needed using an accurate external tuneable laser. Once calibrated the high speed wavelength monitoring can be achieved based on the change of phase with scanning.

5.4.2 Signal detection unit response

An external HP tuneable laser was used for this test. The HP laser was manually tuned from 1480 nm to 1580 nm. The output from the laser (measurement signal) was fed into the signal

detection unit from the fibre port attached to the waveguide onto the signal detection chip (Figure 5.19). The photo-detector array was used to detect the signal.

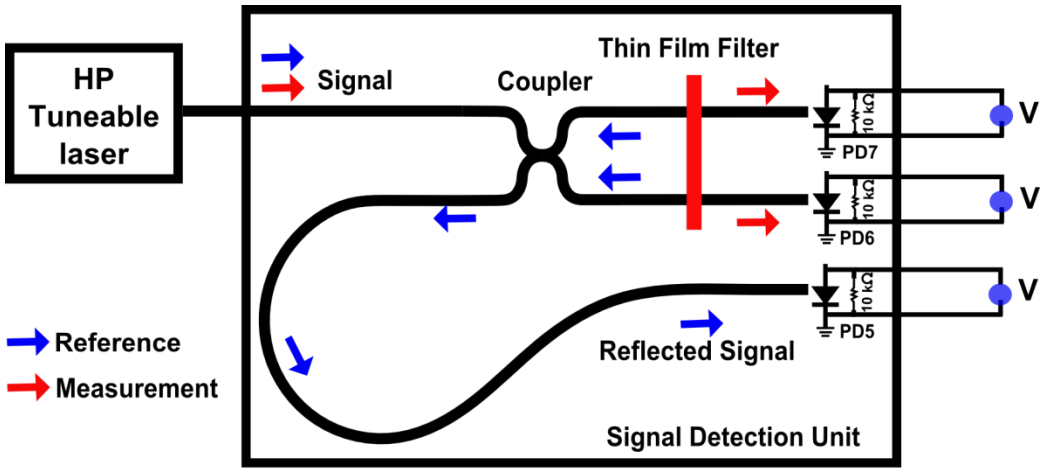

Figure 5.19 Measurement setup for the signal detection unit

Of three PDs in the array, one is used to detect the reflected signal from the filter; the other two detects the transmitted signal. The response of the detectors was measured using a voltmeter across the 10kΩ resistor. The response of the PD at high and low input powers is shown in the figure 5.20 & 5.21 respectively.

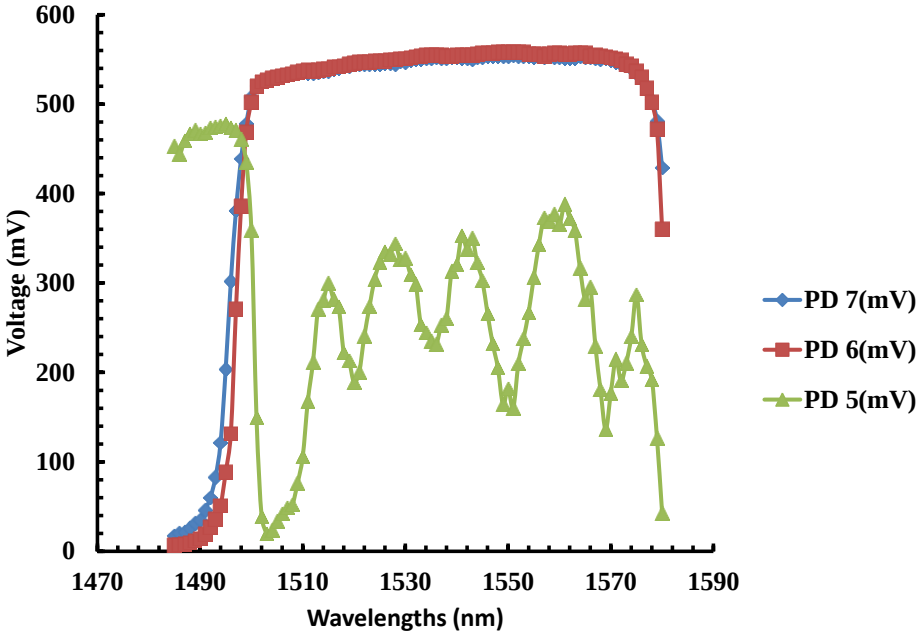

Figure 5.20 PD responses at high input power (Maximum of ~6mW)

At high input power (~ 6 mW) the PD 5 showed unexpected response (see Figure 5.20) at longer wavelengths. This was due to detector saturation because of the high input power. PD 6

and PD 7 appear to be working well with a clean cut-off below 1490 nm and a flat response above that. The test was repeated at a much lower input laser power (about 0.5 mW).

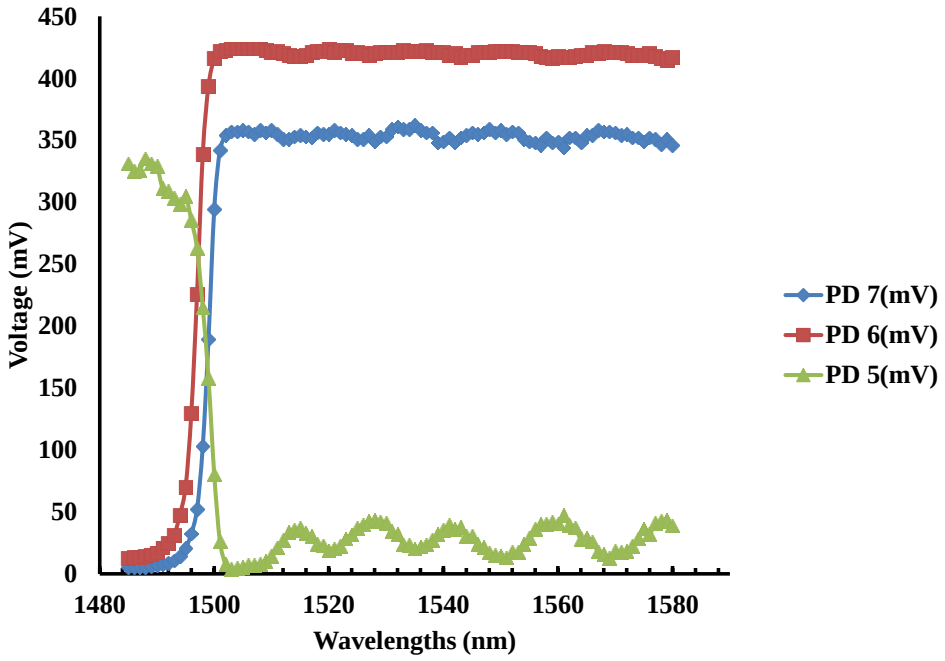

Figure 5.21 PD responses at low input power (Maximum of ~0.5mW)

The response of the PD 5 improved, but there is still some leakage is observed at longer wavelengths of the scan (Figure 5.21). The reference path, which is that reflected from the filter and incident on PD5 appear a good response in the pass band region below 1490 nm. However there is substantial ripple present in the stop band amounting to almost 10 % power at the peaks.

5.4.3 Investigations on laser tuning behaviour with squiggle motor

A laser interferometer system's accuracy is fundamentally based on the laser's wavelength accuracy. Any instability in laser will induce phase instability which consequently will lead to a measurement error. This study aims to investigate the tuning behaviour of the 3rd version of chip tuneable laser with New Scale squiggle motor. The crucial advantage of the Fizeau interferometer used is the common path construction. A Fizeau interferometer setup is used to investigate the performance of the CIP chip tuneable laser. The common path construction is an interferometer design where the reference beam and test beam share a common path. There are several advantages of using a common path interferometer. A common path interferometer is easy to align- when the position of an optic in the one arm is moved there is no compensating adjustment in the other arm.The shared optical path increases the interferometer

stability and reduces the sensitivity to vibrations because the beam overlap is automatically maintained.A variation in the surface causes change in the phase of the beam at the recombination point. In this case the path imbalance is the absolute optical path difference induced by the glass slide thickness. The changing phase results in a in the variation of the light intensity of the interfered beam and is given by,

$$I = A + B\cos\left(\frac{4\pi nd}{\lambda}\right) \tag{5.7}$$

where A and B are the bias intensity and the fringe visibility at a particular point respectively, d is the thickness of the glass slide, n is the refractive index and λ the wavelength of light.

5.4.3.1 Experimental setup

The experimental setup for tuneable laser performance testing is shown in the figure 5.22. The laser enclosure temperature and injection current were controlled using a Thorlabs temperature controller and precision current source respectively. The light beam from the laser is split into the two arms of coupler. The coupler feeds the beam to an isolator followed by a circulator which is then finally projected onto the uncoated glass slide (cavity) using a GRIN collimator. A portion of beam (interferometer output) is reflected back into the collimator which is then circulated to port 3 connecting to both the optical spectrum analyser (OSA) and photodetector by the way of a 3dB splitter. The reflected beam from the uncoated glass slide was collected by a 125 MHz New Focus PIN photodiode. A control unit linked to a PC and a NI PCI6221 data acquisition device allows the laser to be scanned over its tuning range and the reflected interferometer output was recorded using the photodiode. Optical feedback was minimized by using the minimum number of connectors and high quality optical isolators so that the back reflections from the laser beam cannot re-enter the laser causing optical instability. The recorded intensity was then analysed using Matlab to study the operational behaviour.

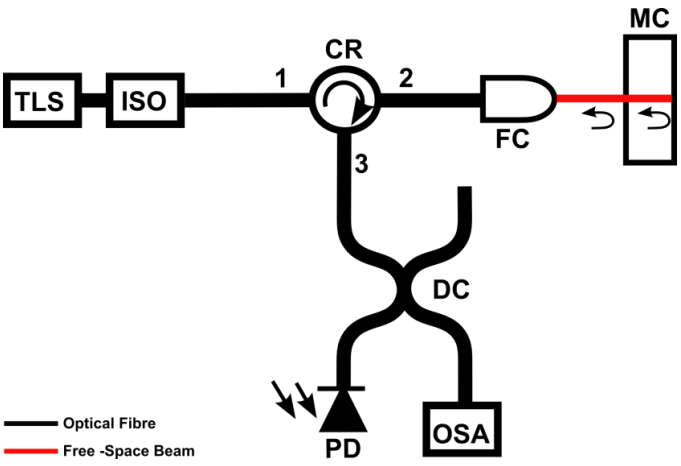

Figure 5.22 Experimental Apparatus

5.4.3.2 Normalising the interferometer output to laser power

The first requirement was for the scanned data to be normalised to the laser output power to cancel any amplitude fluctuations of the laser source obtaining good intensity stability. This throws up a few difficulties as the nature of the interferometer system means as there are some losses in the optical circuit. In addition the power output is not constant over the tuning range. It is relatively straightforward to determine the interferometer output power however. The conversion gain of the photodiode and transimpedance amplifier was calculated as 15.21 x 103 V/W. The interferometer was set to a wavelength that produced a fringe maxima (λ=1546.423, Ij=200.23 mA, Rt=10.286 kΩ). The power output direct from the laser was measured at 1.038 mW, while from the interferometer it was 26.5 µW. This is a 15.93 dB loss which is approximately as expected given the 4% Fresnel reflectivity of the glass slide, near unity fringe contrast in this type of apparatus and the total insertion losses of the various components.

5.4.3.3 Measurement of stray light on the detector

With the output of the GRIN collimating lens blocked off it is possible to measure any parasitic light reflected back through the system. At Ij = 300 mA and λ = 1579.174 nm, the output power measured directly from the laser output was 2.70 mW. The light measured at the interferometer output was 8.967 nW or 50.47 dB down when the free space beam was blocked between the grin lens and glass slide (see figure 5.17). This is about as low as can be realistically expected in the current apparatus given the specified reflection losses from the circulator and GRIN lens. Taking into account the actual returning interfered power from the Fizeau cavity (which is ≈10 dB lower than the source power) the ratio is approximately 44.7 dB.

5.4.3.4 Measurement results

With the apparatus now calibrated it is now possible to scale the fringe intensity to the interferometer output power. The following results show a wavelength scan from approximately 1504.88 to 1586.12 nm (Figure 5.23). This range represents almost the full useable tuning range of the laser and the intensity variation over the scan range is quite apparent. The output sinusoid seems to be inconsistent (chirp) throughout the scan suggesting nonlinear tuning behaviour of the laser. Also there is increase in the intensity at the longer wavelengths. Frequency change at the start and end of the scan can be clearly seen from the diagram and is attributed to occurrence of motor transients.

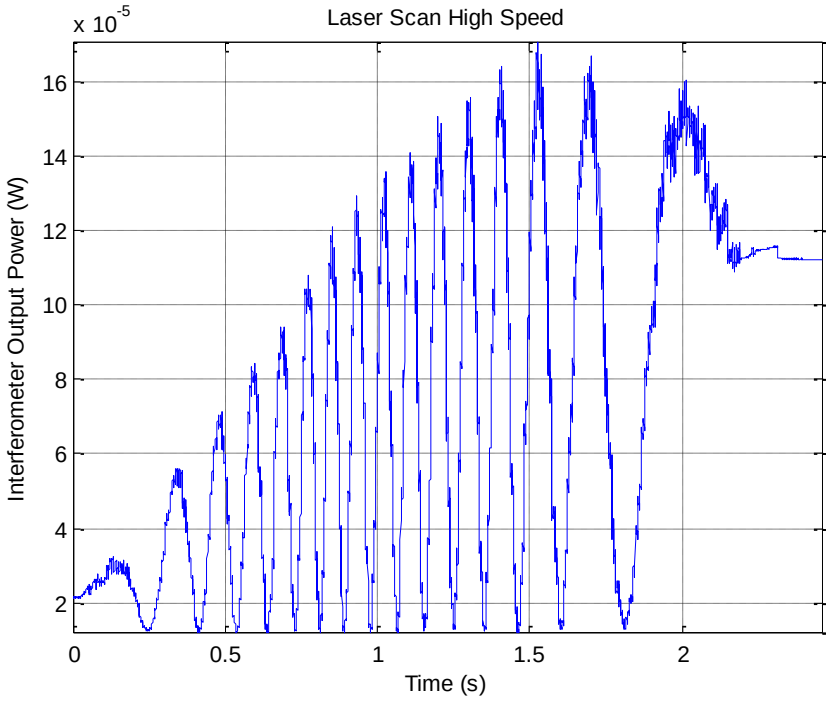

Figure 5.23 Fizeau output from wavelength scan

In order to see if the motor speed had any effect on the tuning and secondary structure, 3 scans were performed, at motor tuning speeds of 100, 1000 and 4000 µm/s while the interferometer output was sampled at 20 kHz. The results are shown in figure 5.24.

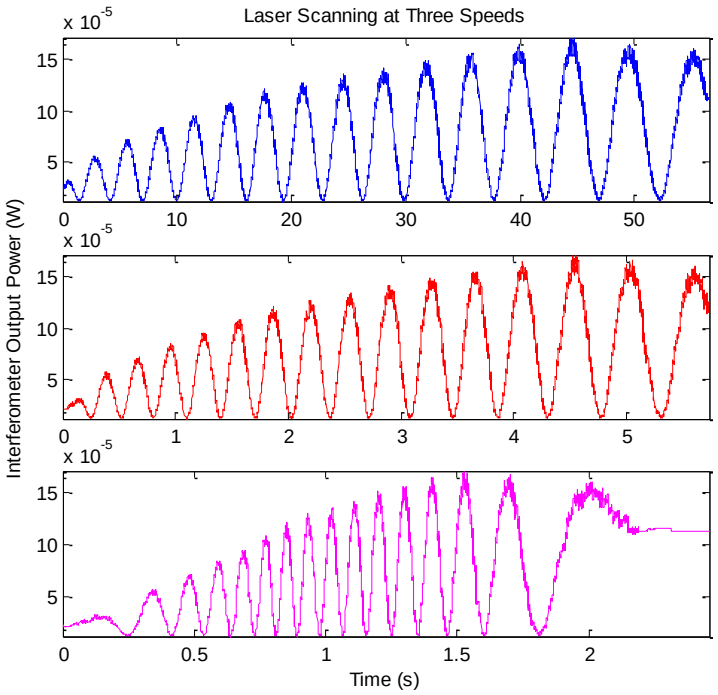

Figure 5.24 Results from various wavelength scanning speeds

A better comparison of the tuning activity can be carried out if a zoomed portion of the scan is examined. In figures 5.25 to 5.27 the area around the tenth trough in the response is examined for each scan speed.

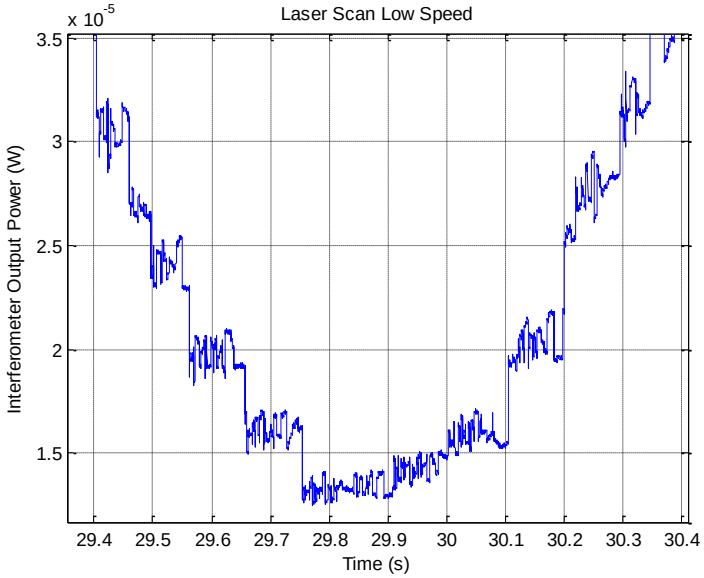

Figure 5.25 Zoomed portion of trough 10 at 100 µm/s

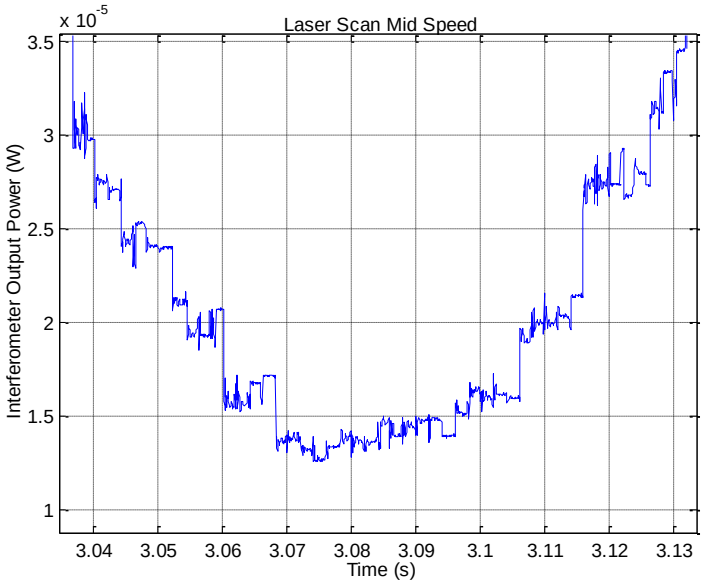

Figure 5.26 Zoomed portion of trough 10 at 1000 µm/s

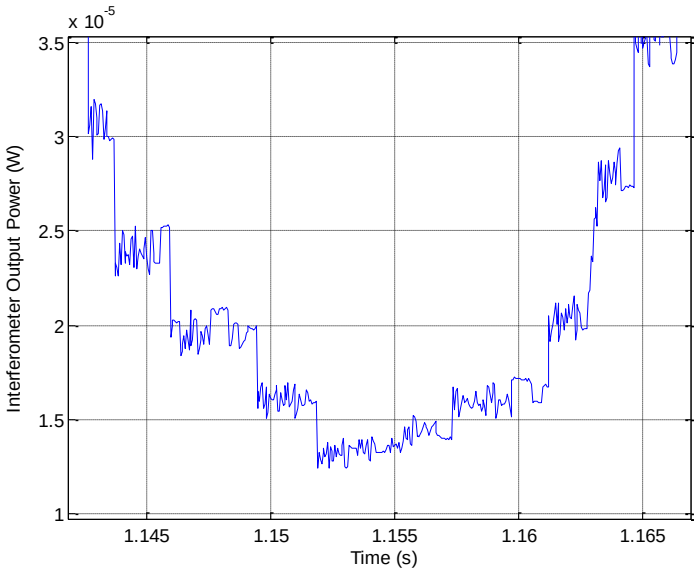

Figure 5.27 Zoomed portion of trough 10 at 4000 µm/s

Confirmation that the larger steps in the output are indeed mode hops can be indirectly established by measuring the interval in the above graphs. Table 5.4 confirms the motor step size to be 8-10 µm for each mode, which has already been established as the case (Figure 5.26).

Table 5.4Encoder step size for a mode hop

Step Duration (ms)	Tuning Speed (µm/s)	Step Size (µm)
100	100	10
8	1000	8
2.5	4000	10

More general observations are that the secondary structure is more pronounced at the slower motor speeds. The secondary structures are irregular spikes present in the in the output sinusoid waveform. These are due to secondary interference occurring in the system as a result of parasitic back reflections. The low to mid speeds appear to show good correlation, the high speed less so. The main mode hops are visible in each scan, but there appears to be little correlation in secondary structure for varying scan speeds.

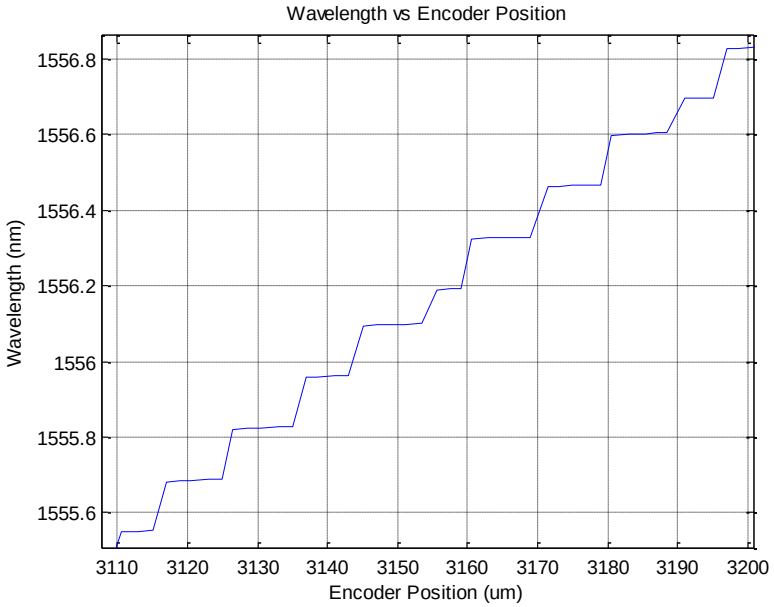

Figure 5.28 Laser wavelengths with encoder position (2 µm steps)

Figure 5.28 shows that the mode hopping occurs across a range of encoder intervals (encoder step = 2 µm) in approximately the same on the scan as the data shown in figures 5.20 to 5.22. Generally modes hope at intervals of about 8-10 µm but on occasions, approximately half of that. On thing to note is that there is a slight rising wavelength change between mode hops observable (OSA resolution = 0.01 nm).

5.4.4 Investigation of multimode behaviour during laser tuning

In order determine whether the instabilities on the interferometer output were due to multimode effects from the laser tuning, an automated test routine was set up to step the laser

drive motor at 2 µm increments and measure the laser output with the OSA after each step. The laser wavelength and line-width were recorded for each step of the drive motor. In addition the number of peaks of >30dB above the main peak in the laser output was recorded. If this figure was more than one, it was logged as a multimode event. A full run took approximately 2 hours to complete. The results of one full tuning run are shown in figure 5.29.

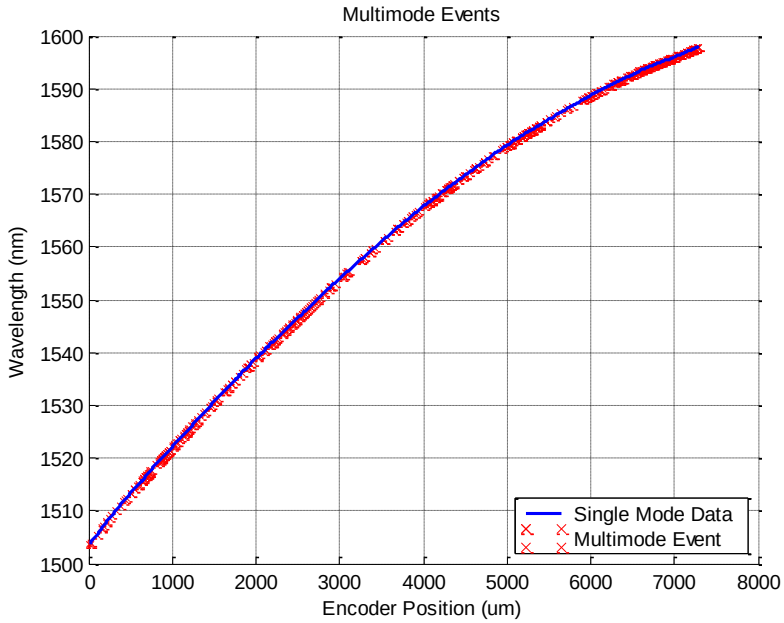

Figure 5.29 Multimode events occurring during Run 1

Multimode events clearly make up a fairly large proportion (~ 17%) of the total number of tuning steps. Qualitative observations during the experiment suggest that the laser tends to go multimode just prior to a mode hop occurring, i.e. toward the end of a wavelength step. A rough fitting using second and third degree polynomials suggest that a better method needs to be established characterising the tuning behaviour as the residuals are still far above the mode spacing (0.04 nm), see figure 5.30. Options are the investigation of a more complex fitting method or a brute force approach of a lookup table.

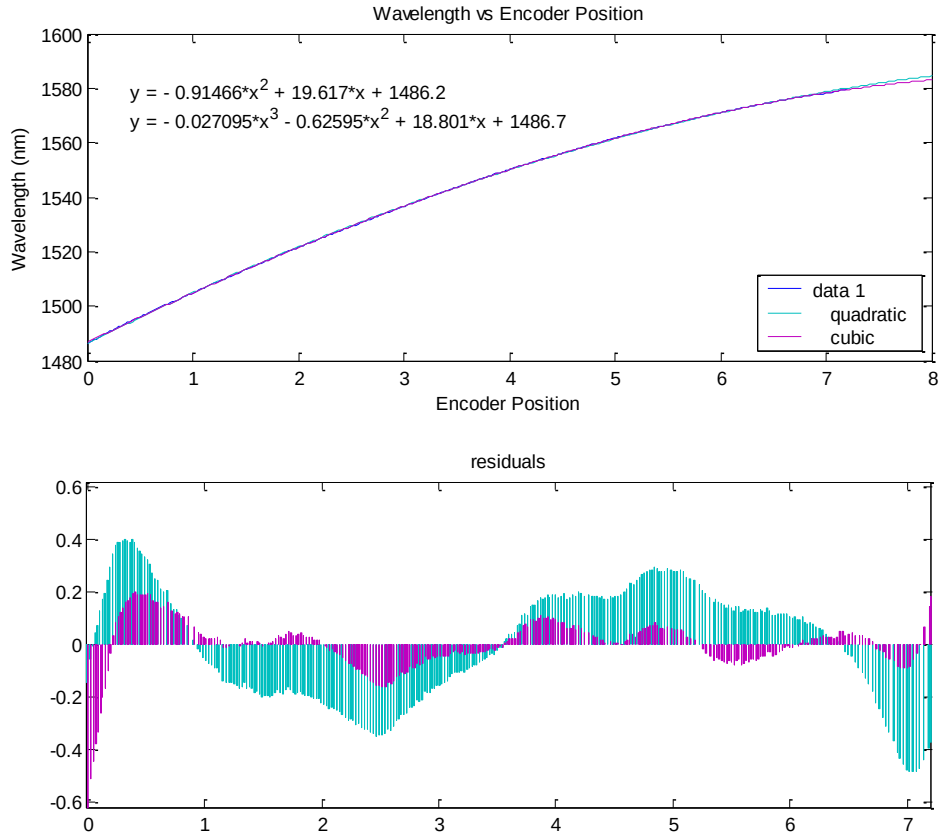

Figure 5.30 Polynomial fits to laser wavelength

Having established multimode events are occurring during the tuning cycle it is of interest to determine the nature of the events in terms of their distribution with tuned wavelength and repeatability between scans. In order to do this, the wavelength stepping routine was performed six times over across most of the useable laser tuning range. Runs were carried out consecutively, taking approximately 2 hours per run. The laser was kept temperature stable at Rt=10.286 kΩ and the injection current was fed throughout this time. The total time for the whole experiment was 12 hours. The distribution of multimode events occurring during the wavelength scan is shown across runs in figure 5.31.

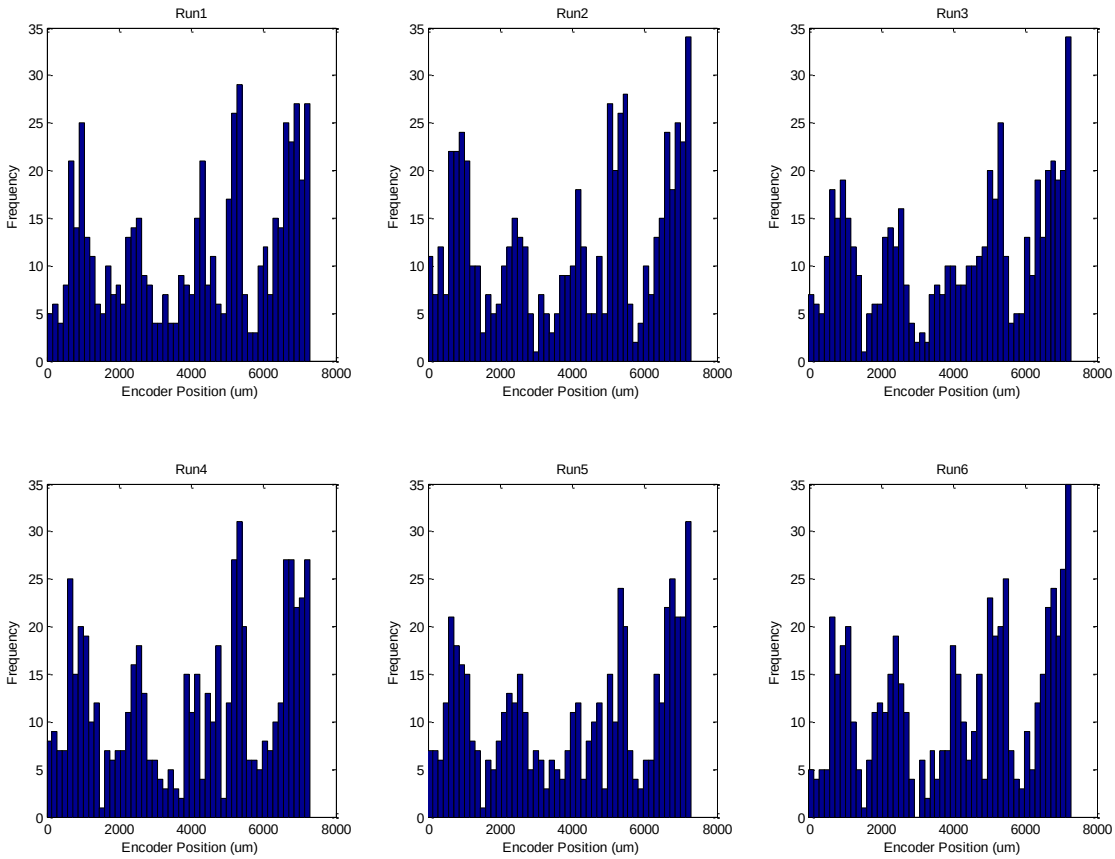

Figure 5.31 Distribution of multimode events for all 6 runs

The distribution of the multimode events shows definite patterns over the tuning range suggesting the likelihood of some multimode events being repeatable. However the variation is such that substantial numbers of multimode events are not, as illustrated by the variation table 5.5 below. Multimode events clearly make up a fairly large proportion of the total number of tuning steps.

Table 5.5Analysis of multimode tuning events over six laser tuning runs

Run	No. Tuning Steps	No. Multimode Events	% Multimode Events
1	3647	585	16.0
2	3647	621	17.0
3	3647	565	15.5
4	3650	605	16.6
5	3648	544	14.9
6	3647	590	16.2

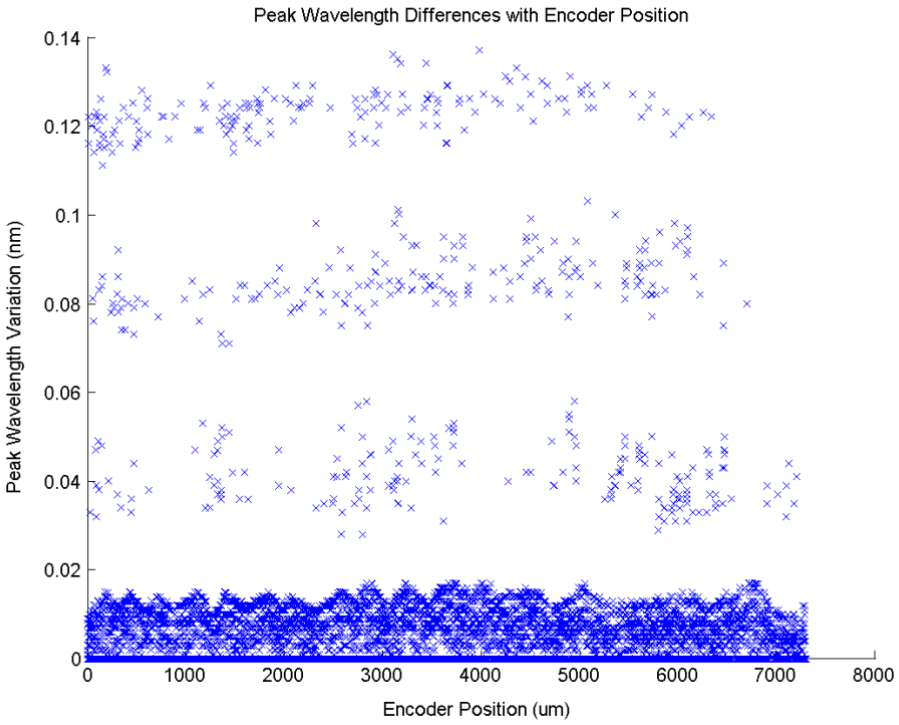

Figure 5.32 Peak variation in wavelength for encoder position

Figure 5.32 show the maximum difference in wavelength measured from the laser for different encoder values across the full useable range over the 6 runs. The differences are clearly clustered due to the mode spacing of the laser (0.04 nm). The majority of the laser output appears to be repeatable within one mode for any given encoder output. However there are clear excursions away from this, occasionally the wavelength difference is up to 3 modes. A single mode of excursion could be explained by the uncertainty of the encoder (2 µm repeatability) causing the recorded mode hop to appear to occur at a different point. However, this cannot explain the larger differences of 2 and 3 modes. One possible explanation could be the time delay between runs; with 2 hours between each run, the total test time being 12 hours. This presents environmental issues as being a possible contributor, although the operating parameters were kept constant within the specifications supplied by the current and thermo electric controller (TEC) drivers. Table 5.6 summarises the ratio of wavelength differences in terms of modes away from the ideal result.

Table 5.6 Wavelength repeatability in terms of longitudinal modes

Wavelength Variation	Percentage of Total Events
Same Mode	93.21
1 Mode Away	2.44
2 Modes Away	2.21
3 Modes Away	2.14

Modal analysis exhibited substantial amount of multimode events over the full laser scan. This can be due to inefficient tuning provided by PZT based Newscale squiggle linear motor in the earlier versions of developed chip tuneable laser. Also reliability issue were identified which translates to reduced performance and limited lifetime of the linear motor. In addition, the PZT motor is slow as it takes ~2 seconds for full scan.

5.4.5 Improved TFF tuning mechanism: Penny Motor actuator

The reported 3rd version of the miniaturised integrated optic tuneable laser requires substantial performance improvement in terms of linear tuning and single mode operation during the wavelength scan. So in order to improve the laser tuning behaviour a better method of tuning thin film filter is needs to be investigated. Brushless flat DC penny motor would be a suitable tuning alternative which will offer a better, faster and cost effective method of tuning chip tuneable laser. In this application a Brushless Flat DC-Micromotors penny-motor technology (1202 H 004B H series, Figure 5.33) is used as a rotor to tune thin film filter (TFF). The penny shaped electromagnetic motor consists of diametrically magnetized rare- earth permanent magnet (high power neodymium magnets, NdFeB) rotor surrounded by a coil system (Janocha, 2000). The motor coil system is lithographically traced onto the printed circuit board (PCB) to provide ultra-flat design making it a miniature motor of diameter 12 mm with a height of 2mm (excl. shaft).

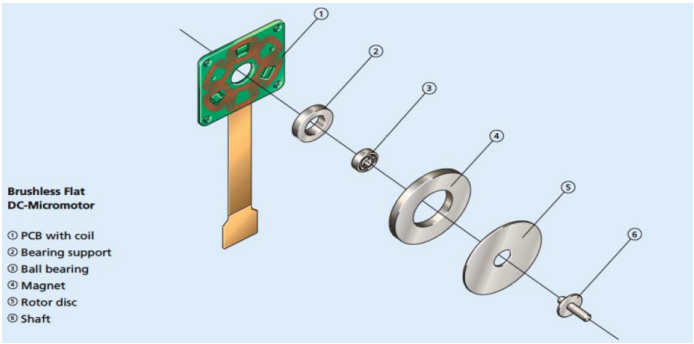

Figure 5.33 Brushless Flat DC-Micromotor: Penny Motor (Faulhaber GMBH &CO.KG)

Current flows into the coil system on connection to the power supply, generates magneto motive force which interacts with the magnetic field produced by the permanent magnet to give electromagnetic torque (Duan et al., 2014). This torque across very small radii produces extremely high accelerations and rotation velocities up to 60000 rpm to achieve a continuous operation.

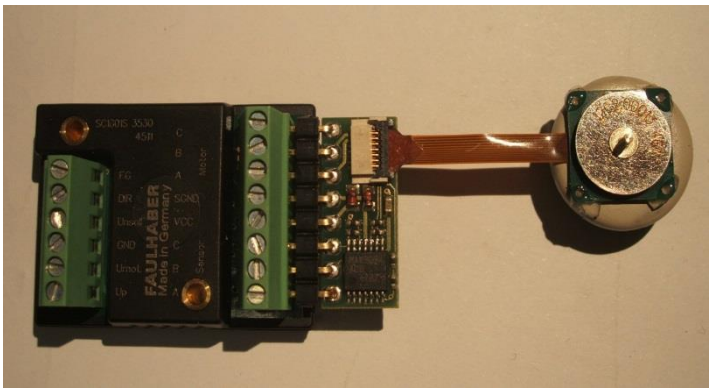

Figure 5.34 Penny motor with digital controller unit

The 1202 H 004B H penny motor generates torque up to 222µNm with a maximum no-load speed of 41740 rpm as specified. The motor is driven by a digital controller circuit SC 1801 S which provides optimum voltage for smoother operation. Further with the use of a USB Programming Adapter 6501.00097 the motor is set to operate at a particular speed within the limit. The benefits of DC penny motor are: long operational life time, no cogging, extremely low current consumption, light and compact. It is anticipated that the newer approach will provide continuous and much smoother tuning and will improve the laser performance in terms of increased scan speed. The motor is capable of performing a much faster rotation (up to 41740 rpm), which will suit large scale manufacturing requirements.

5.4.5.1 Current state of the hybrid photonic chip unit: 4th version

The current state of development of the hybrid photonic unit is shown in figure 5.35. At present it consists of a tunable laser module, mounted upon a PLC which acts as a ‘motherboard’ containing a waveguide structure to couple the light out to an optical fiber. Other components such as wavelength encoder and detection unit are developed separately for initial test and measurements which further will be integrated onto the mother board once optimized.

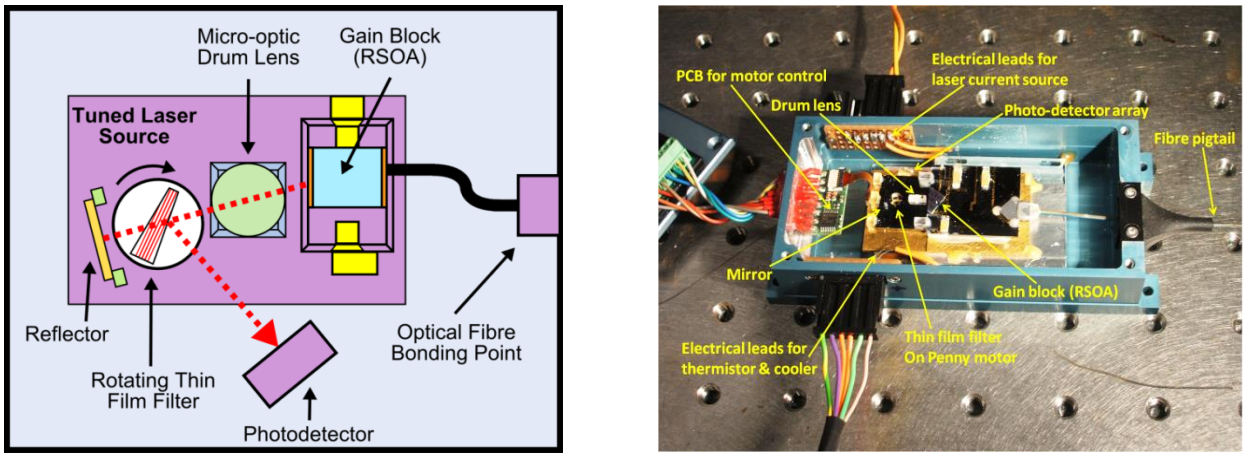

Figure 5.35 Schematic of an external cavity chip tunable laser, b) photograph showing the internals of the final packaged tunable laser module

5.4.5.2 Performance of 4th version of chip tuneable laser

This section describes the results of some initial testing of the TLS which confirms the output is suitable for use in a wavelength scanning interferometer. For these measurements it was necessary for the TFF to be held stationary at various rotations and monitor the laser output on an optical spectrum analyzer. The lasing wavelength range and the output power of the laser for various injection currents are shown in figure 5.36. The laser output power more than 7 dBm at an injection current of 300 mA over the full tuning range of 1506.12 to 1596.68 nm. SMSR (side mode suppression ratio) is over 45 dB when measured using OSA, with the TFF in stationary position. Figure 5.37 shows the relative intensity noise (RIN) of the laser output when coupled to a PIN photodiode using single mode optical fibre. The measurement was taken on an optical spectrum analyzer. A RIN value of -150 dBc/Hz is obtained over the range 0-5 GHz and is reasonably flat lying well within the limits of the device operating frequency range which is 100's of MHz. The concept metrology sensor system will have a maximum operating frequency of less than 200 MHz.

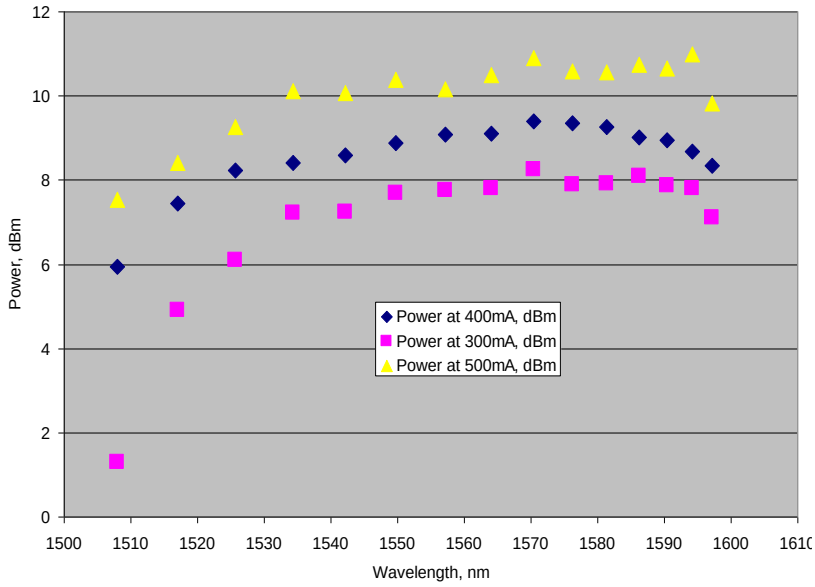

Figure 5.36 Power output across the wavelength tuning range at three injection currents

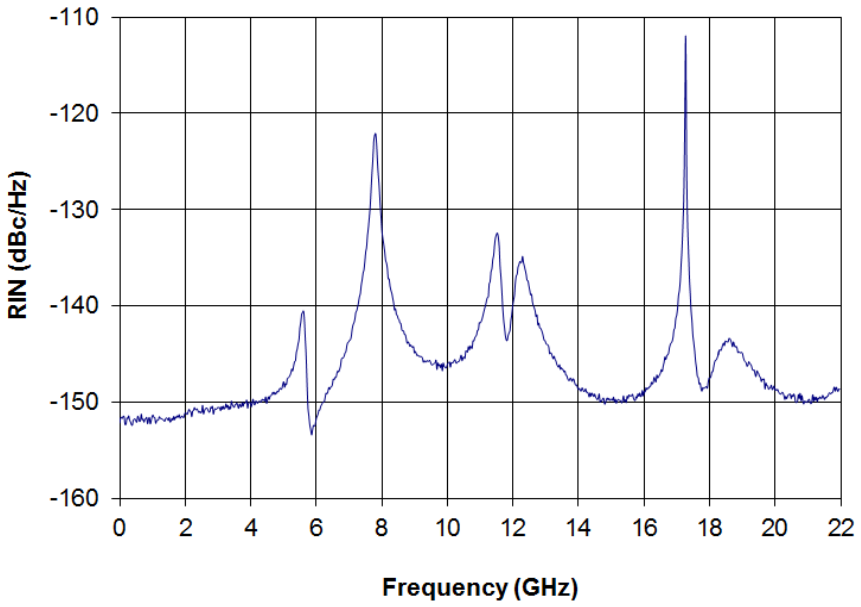

Figure 5.37 Relative intensity noise (RIN) measurement

With the TLS module confirmed as operating to a standard required for use in a wavelength scanning interferometry setup the unit was integrated into a test apparatus in order to confirm the performance in terms of measuring physical lengths.

5.5 Summary

The concept of a chip interferometer device for online surface measurement is presented along with its two measurement mode types. Chip interferometer device contains individual sub-modules such as tuneable laser, fixed wavelength laser for reference, couplers, optical wavelength encoder, unbalanced Mach-Zender Interferometer (MZI), detectors, and reflective semiconductor amplifiers (RSOA) all connected through the imprinted waveguides wiring across the chip. Hybrid integration scheme is employed to provide compactness and common integration platform for various components with optimized performance. Individual devices such as tuneable laser, wavelength encoder unit, and signal detection unit are developed separately and tested. Wavelength scanning Fizeau interferometry was applied to test the performance of the developed chip tuneable laser. The test results of the chip tuneable laser with the squiggle motor shows issues with the laser tuning behaviour. The laser behaves in a multimode fashion which is substantial over the entire scan. Even more problematic is that it is apparent that not all of these multimode events are strictly repeatable. The issue with the secondary structures present during the wavelength scanning are concerning. These issues can be due to inefficient tuning provided by the Newscale squiggle motor. Also reliability issues were identified which translates to reduced performance and limited lifetime. In addition, the PZT motor is slow as it takes ~2 seconds for full scan. An improved tuning mechanism is proposed using penny motor to provide smoother and continuous operation of thin film rotation. The wavelength encoder unit appears operable and but there is significant amount of relative phase error observed between the output signal and should be addressed in later versions. The signal detection unit is operational and the measurement signal path is working well except some ripples observed in reflected reference signal in the stop band amounting to almost 10 % power at the peaks. Next chapter will follow the development and validation of single point absolute distance metrology for thickness and profile measurements using hybrid tuneable laser with improved tuning mechanism.

6 Single point absolute distance measurement using wavelength scanning interferometry

6.1 Introduction

The chapter presents a hybrid photonics based single point measurement sensor. Wavelength scanning interferometry in conjunction with a Fourier fringe analysis technique is utilized to obtain absolute distance metrology. The sensor system incorporates a hybrid chip and an optical probe for point by point scanning of the sample. Hybrid optical chip contains tunable laser, wavelength encoder unit and photodetectors. This method can also be extended to surface profile measurements either by translating the sample or the probe head across the full measurement range. The measurement results will also examine the performance of the hybrid laser and its applicability as a miniaturized integrated device for sensor system. The complete configuration of integrated optical chip interferometer device with absolute distance measurement probe is shown in the figure 6.1. The probe system has an additional interferometer (reference) for tracking wavelength tuning non-linearity inherently present in the system due to the nature of chip tunable laser design. This reference interferometer will overcome uncertainties in measurement due to non-linearity of the tune and intensity noise.

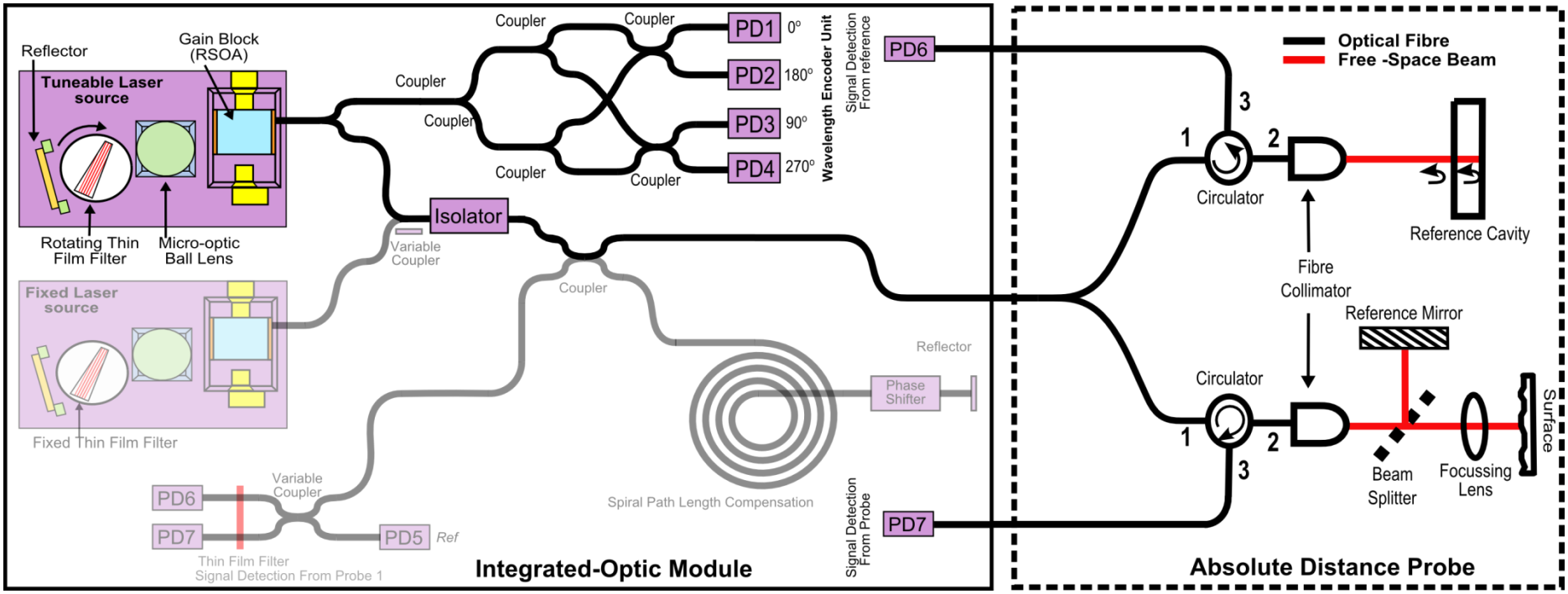

Figure 6.1 Schematic of integrated optical metrology device with absolute distance probe (Unshaded part)

6.2 Single point scanning probe

The absolute distance probe consists of a lens system to focus the beam onto the surface under test. The measurement is performed using wavelength scanning interferometry (Yamaguchi et al., 2000). The aim is to have an optical probe with large working distance and a large depth of field maintaining small optical probe diameter and small beam spot size. The best optical performance is obtained when light impinges on a sample that is located within the depth of field of the lens. This ensures that any light back reflected from the sample will be efficiently directed back into the single mode fiber.

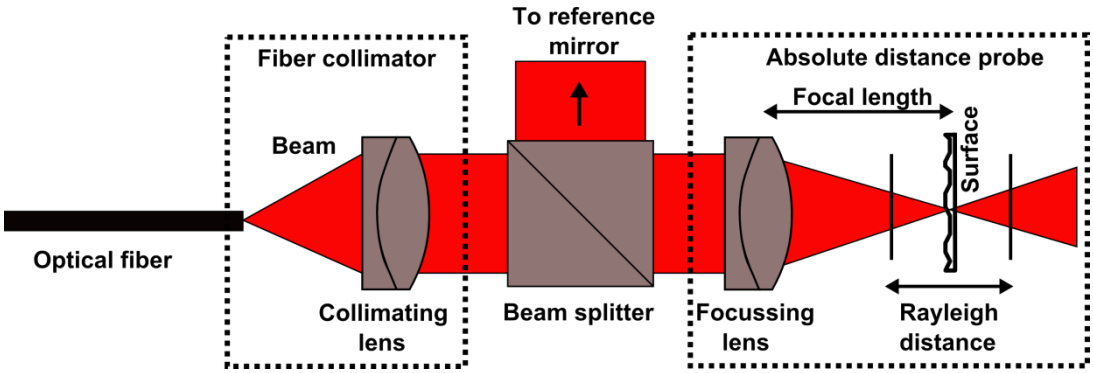

Figure 6.2 Single point scanning probe

The collimating lens in the configuration will be a fiber collimator giving out beam of desired width to full fill the entrance pupil diameter of the focusing lens. The focusing lens is a Thorlabs, Inc., AC080-016-C-ML doublet lens for scanning the beam onto the test sample. For the measurement of a transparent slide (Fizeau cavity) a fiber collimator and a focusing lens is sufficient while for measuring the profile Michelson configuration would be required. The final probe system configuration is shown in the figure 6.2 which will facilitate both kinds of measurements by just putting a shutter in the reference arm of the setup. The measurement range of wavelength scanning interferometry depends on the tuning range of the laser. Larger the wavelength tuning range smaller the cavity thickness or distance can be measured.

6.2.1 Gaussian beam optics: Theory

The single point probe follows the Gaussian beam imagery theory. The fundamental mode emitted from the collimator has a perfect plane wave at its beam waist position. The transverse irradiance profile takes the Gaussian profile whose field distribution is given by:

$$E_s = E_o \exp(-\frac{-r^2}{\omega^2_o}) \tag{6.1}$$

Where E_o is the axial field, r is the radius at any point in the beam and ω_o is the beam waist usually called as the Gaussian beam radius. The irradiance profile is given by,

$$I(\mathrm{r}) = I_o \exp(-\frac{r^2}{r_o^{\,2}}) \tag{6.2}$$

Where I_o is the axial irradiance of the beam, r is the radius at a particular point in the beam and ro is the radius of the beam where irradiance falls to $1/e^2 I_o$. The Gaussian beam while it transverses through the optical system retains its beam characteristics and remains Gaussian at every point along its path of propagation if not vignetted by the system. This is advantageous as it allows the determination of field distribution at any point in the optical system. While propagating through the optical system only the spot size and the radius of curvature of the wave front changes, the beam profile remains Gaussian. The optical system with finite aperture and diffraction effects within the system causes the beam to diverge or converge while propagating through it. Thus the beam size and the wave front curvature will vary with propagation distance (z) and is explained by the diffraction theory (figure 6.3). The beam radius at any position z is given by,

$$\omega^2(\mathrm{z}) = \omega_o^{\,2}\left[1+\left(\frac{\lambda z}{\pi\omega_o^{\,2}}\right)\right] \tag{6.3}$$

Where ω_o the beam size at minimum radius, λ is the wavelength and $\omega(z)$ being the beam radius at any point z and z is the distance propagated from the plane where the wave front is flat. Similarly the wave front radius of curvature is given by,

$$R(\mathrm{z}) = \mathrm{x}\left[1+\left(\frac{\pi\omega_o^{\,2}}{\lambda z}\right)^2\right] \tag{6.4}$$

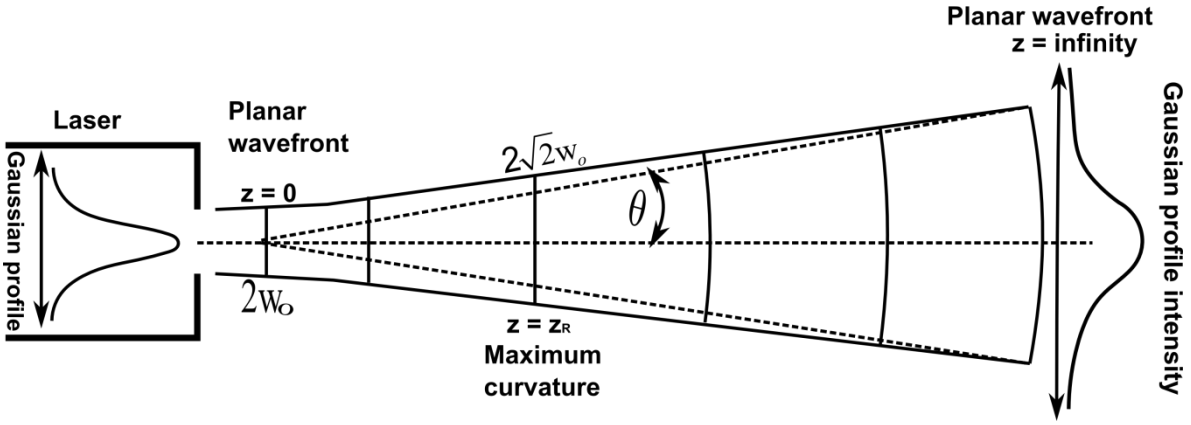

Figure 6.3 Gaussian beam propagation

The laser beam converges to a point with minimum radius (at infinite $R(z)$ for z =0) called the beam waist and further it diverges slowly first and faster with full angular beam divergence proportional to z. Also $R(z)$ approaches z for very large value of z and consequently the spot size asymptotically approaches a value given by,

$$\omega_z = \frac{\lambda z}{\pi \omega_o} \tag{6.5}$$

The z is assumed to be much larger than the $\pi\omega_o / \lambda$ and hence the $1/e^2$ irradiance approaches cone of angular radius,

$$\theta = \frac{\omega_z}{z} = \frac{4\lambda}{\pi \omega_o} \tag{6.6}$$

The product of the beam divergence and the beam waist diameter is always constant throughout the beam propagation. The wave front radius is at beam waist location is infinite and gets minimum at some finite distance away from the beam waist after which it increases to a value of z as z approaches infinity. The minimum value of the wavefront radius occurs at the position where beam waist radius takes the value $\sqrt{2}\omega_o$ and is called as the Rayleigh range. The Rayleigh range is determines the depth of focus (DOF) of the imaging optics.

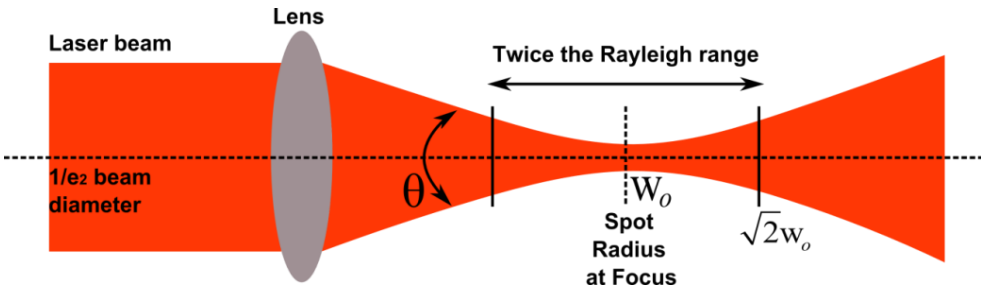

Figure 6.4Divergence of laser beam in far field

When the laser beam is focused through a lens as shown in the figure 6.4, considering the beam focused to a point, θ can be described by the geometrical optics as the diameter of the beam illumination at the entrance aperture of the lens divided by its focal length.

$$\theta \approx \frac{D}{F} = \left(\frac{F}{\#}\right)^{-1} \quad \left(F/\#\ is\ the\ f-number\ of\ the\ lens\right) \tag{6.7}$$

Inserting the θ from previous equation gives the relation of beam radius in terms of input beam parameters.

$$2\omega_o = \left(\frac{4\lambda}{\pi}\right)\left(\frac{F}{D}\right) \tag{6.8}$$

The above formulae can be extended to define the depth of focus. This is depth of focus equivalent to the twice the Rayleigh range i.e. the distance from the beam waist where the beam size becomes $\sqrt{2}\omega_o$.Thus using the equation of the beam radius at any position z, depth of focus (DOF) can be calculated as,

$$DOF = \left(\frac{8\lambda}{\pi}\right)\left(\frac{F}{D}\right)^2 \tag{6.9}$$

For our application a very small spot size is highly desirable, thus a high numerical aperture focusing lens is required for beam concentration into a very small spot size beam. The DOF is proportional to the square of focal spot size and using very high numerical aperture objective will limit the range in with the subject remains focused and can produce sharp images.

6.2.2 Resolution of single point probe

The measurement method for absolute distance is based on Fourier transform technique of wavelength scanning interferometry, so the minimum measurable sample thickness will depend on the resolvability of the first order frequency in the interference frequency spectrum (Ghim et

al., 2010; Yamamoto & Yamaguchi, 2000). Thus the axial resolution of the system is given by the minimum measurable sample thickness which follows the relation

$$\delta z = \frac{\lambda^2}{n\Delta\lambda} \tag{6.10}$$

Where $\Delta\lambda$ is the wavelength tuning range and n is the group refractive index. The resolution of the single point probe using wavelength scanning interferometry is determined by shortest synthetic wavelength which relates to the maximum tuning range $\Delta\lambda$. Assuming $\lambda_n = 1505$ nm and $\lambda_{n+1} = 1596$ nm, the start and end of wavelength scan range, the resolution of the system is calculated to be 13.06 um. This resolution can further be bettered with other approaches of measurement. The lateral resolution of the system is dependent on the type of objective lens used. Thus the lateral resolution of a conventional microscope assuming the above criteria is given by,

$$d_{\min} \approx \frac{1.22\lambda}{2NA} = \frac{0.6\lambda}{NA} \tag{6.11}$$

where λ is the wavelength of light and NA is the numerical aperture of the microscope objective.

6.2.2.1 Optical probe resolution: Foucalt's Knife edge experiment

The knife edge beam profiling technique provides easy, quick, inexpensive and accurate determination of beam parameters and has been used as a standard method for the characterization of Gaussian laser beam (Wright et al., 1992). Accurate measurement of the waist of laser beam will determine the lateral resolution of the optical probe. In this technique a knife edge or blade is positioned at the focus point of the lens and moved perpendicularly to the direction of propagation of the laser beam (figure 6.5).

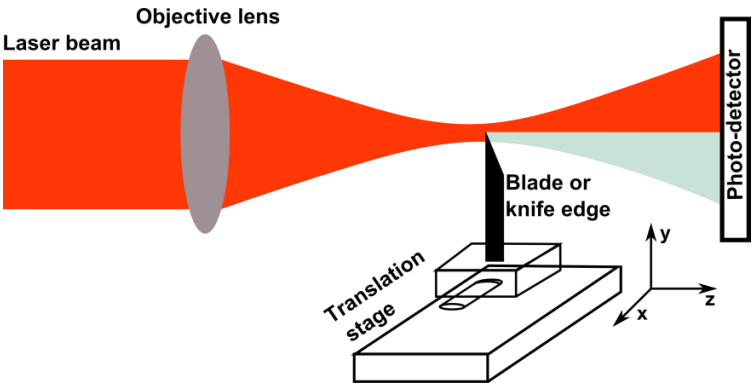

Figure 6.5 Schematic for the spot size measurement of the laser beam using the knife edge experiment. The light grey area shows the blocked rays by the knife edge

The Gaussian beam is radially symmetric and is described by equation 6.2. So a measurement of beam radius is obtained in either of orthogonal directions perpendicular to the beam propagation will be sufficient to evaluate the spot size of the beam. The total transmitted power as a function of knife edge position is measured by placing a photo detector on the other side as shown in the figure 6.6. For a Gaussian beam, the lateral resolution is defined as its $1/e^2$ radius and can be calculated from the 0.78 * 10-90% edge width of the transmission profile (shown in dashed line in the figure above) obtained at detector by laterally moving the knife edge in the focal plane across the beam (Rajadhyaksha et al., 1999).

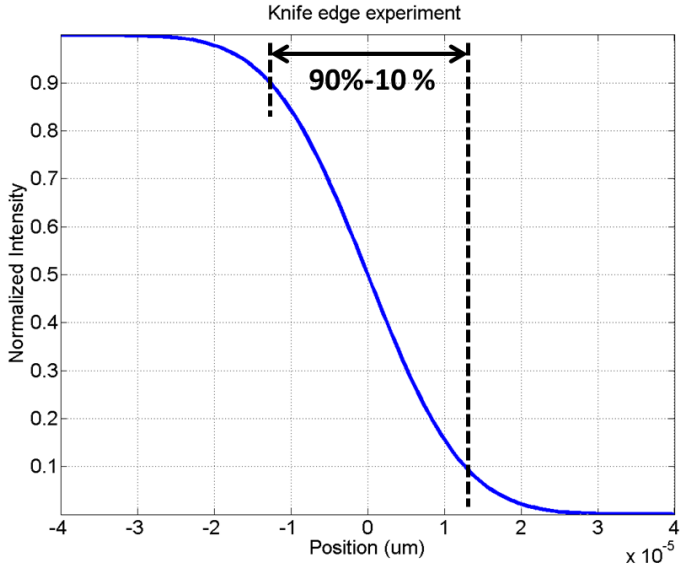

Figure 6.6 Normalized intensity vs knife edge position (Simulated)

The area of the photodiode is considered to be larger than the area of laser beam cross section at the detection position; therefore diffraction effects may be neglected (de Araújo et al., 2009).

6.2.3 Measurement range

In multi wavelength interferometry the step discontinuities are measured by performing measurements at slightly different wavelengths and subtracting the phase. Use of different wavelengths (suppose λ_1 and λ_2) extends the dynamic measurement range appearing as if the measurements were performed at a longer synthetic wavelength λ_s given by,

$$\lambda_s = \frac{\lambda_1 \times \lambda_2}{\lambda_1 - \lambda_2} \tag{6.12}$$

So the measurement range of the device based on multiple wavelengths is limited by longest synthetic wavelength (Yamamoto et al., 2002). Considering the Nyquist sampling theorem requirement of two samples per phase period, ($\lambda_n = 1550nm$, 40 pm mode spacing of the tunable laser) the maximum length measured for a phase shift of 2π is given by the equation,

$$2\pi = 4\pi\left(\frac{1}{\lambda_n} - \frac{1}{\lambda_{n+1}}\right) \tag{6.13}$$

So using the maximum measurement range of the single point probe is calculated to be 15mm. However the depth of measurement is also limited by the depth of focus of the imaging system used (Yamaguchi, et al., 1998). The depth of focus of an aberration free imaging system is given by its $F-number$,

$$D = 8\lambda F^2 \tag{6.14}$$

6.2.4 Maximum measurable slope

The maximum measurable slope of a test sample is defined by the NA of the lens or objective. This also depends on the nature of reflection (specular or diffuse) from the surface which in turn depends on the surface topography and material. Considering specular reflection from the surface maximum measurable slope is given by the equation below.

$$\alpha^{specular}{}_{\max} = \sin^{-1} NA \tag{6.15}$$

In the aforementioned probe design Thorlabs, Inc., AC080-016-C-ML doublet lens is used. The focal length of the lens is 12.3 mm and the entrance pupil diameter (EPD) is 7.2 mm. The NA of the doublet lens is calculated as,

$$NA = \frac{EPD}{2f} = \frac{7.2}{2\times 12.3} \sim 0.29 \tag{6.16}$$

So the maximum slope of the test sample measured with the doublet lens would be ~17^{o}.

6.3 Measurement principle for absolute distance

This section will describe the measurement techniques adopted for absolute distance measurement; wavelength scanning interferometry and Fourier transform fringe analysis technique.

6.3.1 Wavelength scanning interferometry

The chip interferometry system based on wavelength scanning can be extended to absolute distance measurement applications. A transparent glass slide of given refractive index (n) and thickness (d) was taken for absolute distance measurements. The transparent glass slide forms a Fizeau cavity or the interferometer which is implemented for absolute distance measurements. The light from the tunable laser (TLS) source is directed into the circulator (CR) passing through the fiber collimator (FC) making it incident on to the transparent cavity or glass slide (figure 6.7). The beam goes multiple reflections inside the cavity and finally combines to produce interference fringes. For simplicity higher order reflections are neglected and only reflections from surface A (front) and AB (back face) is taken for presenting the theory of wavelength scanning interferometry. The reflected beam into the collimator is coupled back into the optical fiber and via the circulator is made incident on a photo-detector (PD) allowing the intensity to be monitored.

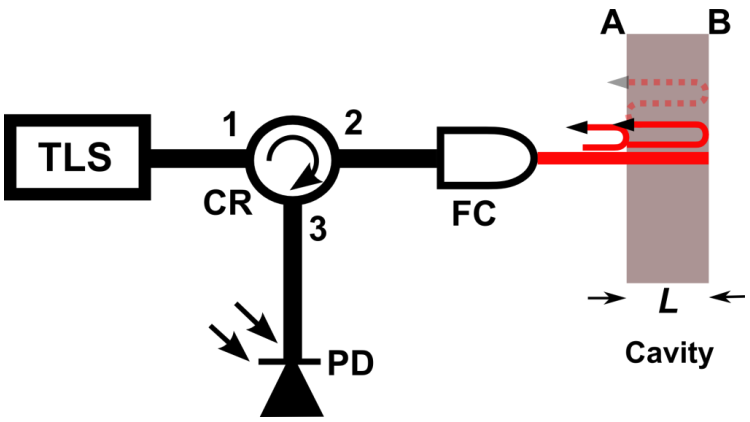

Figure 6.7 Fizeau setup for absolute distance measurement using wavelength scanning interferometry

When the TLS wavelength is scanned there is a phase change induced in the interferometer, the rate of which depends on the optical path difference. Light with optical frequency ν when incident on the glass slide (cavity) gets reflected off the two parallel surface separated by the

optical path difference produces interference. The total intensity signal varying in time with the wavelength scan and hence the reflected intensity from the glass slide can be written as,

$$i(t) = a(t) + b(t) \times \cos\left[\phi(t)\right] \tag{6.17}$$

Where $i(t)$ is the total intensity, a(t) is the intensity sum of the two beams, $b(t)$ is the fringe visibility and $\phi(t)$ is the phase difference. The phase term $\phi(t)$ on the sample can be represented by,

$$\phi(t) = 2mn(t)L(t)\frac{2\pi\nu(t)}{c} + \phi_o(t) \tag{6.18}$$

Where ν is the source optical frequency, m is order of interference (m = 1 for single reflection and m = 2 for double reflection and so on), c is the speed of light in a vacuum, n is the refractive index of the cavity, and L is the cavity physical length, ϕ_o is an initial phase constant that depends on the cavity length and starting source optical frequency and reflection between the surfaces. As the phase is tuned with time the rate of change of phase can be obtained as,

$$\frac{\partial\phi(t)}{\partial t} = \frac{4\pi mn(t)L}{c}\frac{\partial\nu(t)}{\partial t}\left[1+\left(\frac{\nu}{n}\right)\left(\frac{\partial n}{\partial\nu}\right)\right] + \frac{\partial\phi_o(t)}{\partial t} \tag{6.19}$$

The last term $\partial\phi_o(t)/\partial t$ is discarded as there is negligible phase change on reflection over the entire wavelength tuning range. The term $\left(\frac{\nu}{n}\right)\left(\frac{\partial n}{\partial\nu}\right)$ accounts for chromatic dispersion which is very small and is constant across the sample under test and hence this too can be ignored in the above equation. So for a particular optical frequency tuning rate the first order cavity interference will therefore vary at a frequency ω_s given by,

$$\omega_s = \frac{\mathrm{d}\phi(t)}{\mathrm{d}t} = \frac{4\pi nL}{c}\cdot\frac{\partial\nu}{\partial t} \tag{6.20}$$

Where $\partial\nu/\partial t$ is the optical frequency scanning rate. If $\partial\nu/\partial t$ is constant then it can be seen that the interferometer output will be modulated by a constant 'carrier frequency', ω_s and the equation (6.17) may re-written as

$$i(t) = a(t) + b(t)\cos(\omega_s t) \quad \text{where} \quad \omega_s = \frac{2nL}{c}\cdot\frac{\partial\nu}{\partial t} \tag{6.21}$$

It can be seen from equation (6.21) that if the angular carrier frequency, ω_s can be determined then, with knowledge of the optical frequency tuning rate and index of the cavity, the cavity length can be derived with no requirement to know the starting phase.

6.3.2 Fourier fringe analysis technique

It is however necessary to extract the phase term from the recorded interferogram to calculate the carrier frequency. So an approach based on Fourier fringe analysis method described by Takeda et al. is employed to extract the phase information from the interference signal. Fourier transform fringe analysis method which fast, accurate and insensitive to intensity noise (X. Jiang et al., 2010a; Takeda et al., 1994). The first stage in Fourier fringe analysis technique is to apply the Fourier transform to the interference signal. Figure 6.8 shows step by step implementation of Fourier fringe analysis technique phase retrieval. Equation (6.17) ca be represented in a complex exponential format, and * denotes the complex conjugate term.

$$i(t) = a(t) + u\exp(j\omega_s t) + u*\exp(-j\omega_s t) \quad \text{where} \quad u = \tfrac{1}{2}b(t) \tag{6.22}$$

The Fourier transform of the intensity $i(t)$ for a sample rate of f is then,

$$\Im\{i(t)\} = A(\omega) + U(\omega - \omega_s) + U^*[-(\omega + \omega_s)] \quad \text{where} \quad \omega = 2\pi f \tag{6.23}$$

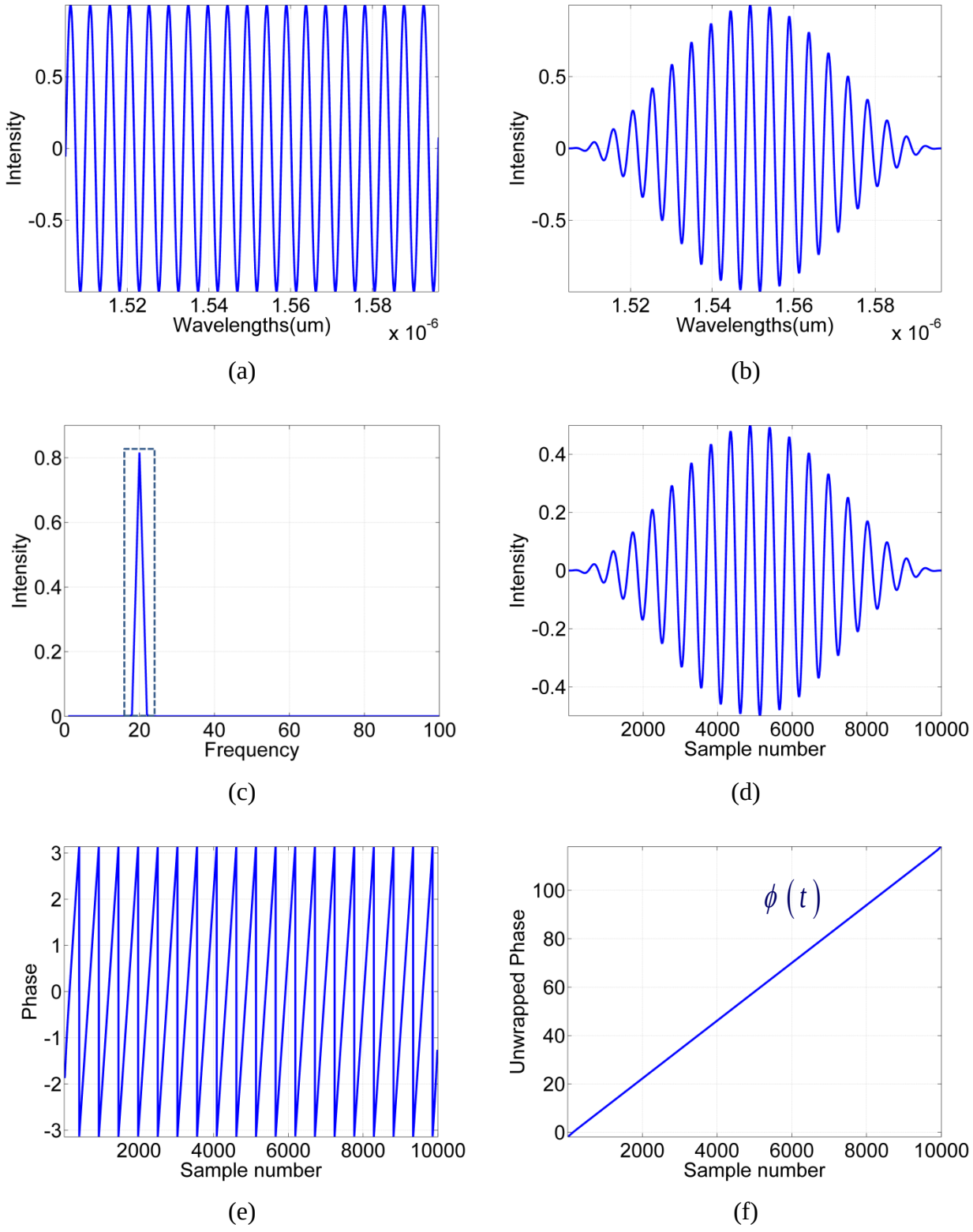

Figure 6.8Various steps involved in extracting phase using Fourier transform technique;

a) Simulated intensity signal, b) Hanning window applied signal, c) Fourier spectra of the signal, d) Real part of inverse Fourier transform signal, e) Phase value, f) Unwrapped phase

The term spectra associated with $U(\omega-\omega_s)$ contains the required phase information, so by isolating this term it is possible to retain the phase information but remove the contribution of background intensity variation represented by $a(t)$. This is done easily in the frequency domain using a suitable band-pass filter centered at the frequency $\omega-\omega_s$ .Once isolated; the inverse Fourier transforms of $U(\omega-\omega_s)$ is taken to obtain the following analytic signal,

$$\Im^{-1}\{U(\omega-\omega_s)\} = u\exp(j2\pi\omega_s t) \tag{6.24}$$

Now phase can be extracted using complex logarithm,

$$\log[u\exp(2\pi\omega_s t)] = \log[u] + j2\pi\omega_s t \tag{6.25}$$

This operation effectively removes the contribution of the fringe visibility variation represented by $b(t)$ isolating the angular carrier frequency, ω_s in the imaginary term. It is clear that the analysis above relies on a constant change of optical frequency with time; any deviation away from this will result in distortion of the spectra and inaccurate determination of the carrier frequency and introduce time dependence to ω_s (Suematsu et al., 1991).

6.4 Correction for non-linear TLS tuning

Figure 6.9 (a) shows the simulated signal over the entire wavelength scan range equivalent to chip tunable laser. The scan is assumed to be linear and is clearly visible in the signal, while Figure 6.9 (b) is simulated as a nonlinear scan of tunable source which causes frequency chirp in the signal. The above method of Fourier fringe analysis is highly sensitive to linearity of frequency tuning and in any case if the optical frequency tune departs from the linearity, the frequency peaks obtained from the spectrum will be both shifted and distorted leading to incorrect carrier frequency determination as shown in figure 6.9(c). Several methods have been proposed to overcome the problem of nonlinear laser tuning. One way is to focus the design and execution of a tunable laser source with a tuning curve that is linear in time (Glombitza et al., 1993; Iiyama et al., 1996; Yu et al., 2013). In general this technique is little difficult and less convenient. Another approach is the use of an auxiliary interferometer to measure the laser tuning rate as it changes over the wavelength sweep. As mentioned previously in this thesis section 5.4.1, the ECDL design consists of a thin film filter wavelength tuning element made up

of multilayer dielectric which on rotation, results in a non-linear change of wavelength with time over the entire tuning range.

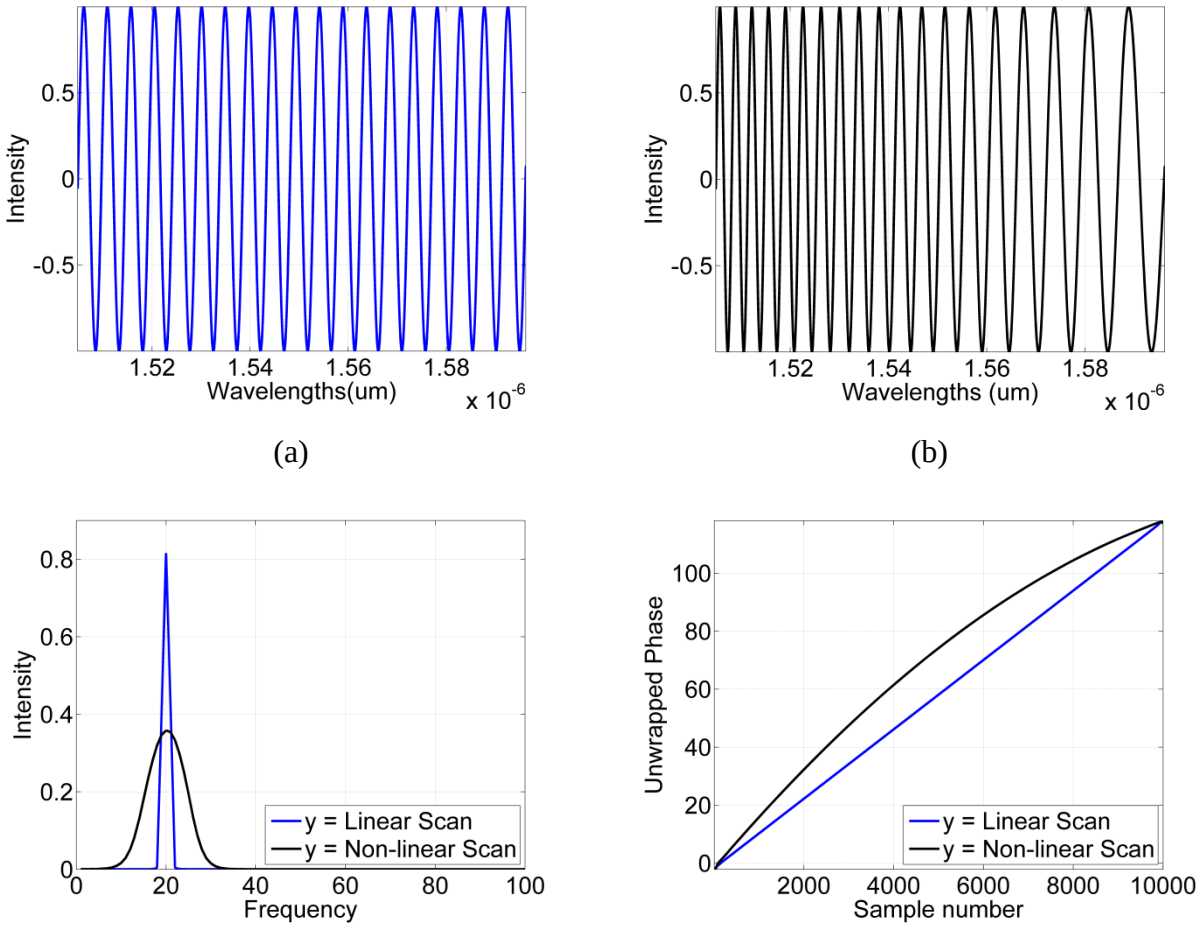

Figure 6.9 Simulated intensity signal for a given optical path length

a) Linear wavelength scan, b) Non- linear wavelength scan, c) Fourier spectra of non-linear scan showing peak shift and broadening with respect to linear scan, d) Unwrapped phase obtained using Fourier transform technique for linear and non-linear scans

Here the nonlinearity in the laser source is inherent due to the nature of ECDL design and correction method based on former (linearizing the laser sweep) would just complicate the overall measurement system. So rather than linearizing the laser it is however possible to use an auxiliary reference interferometer to null these uncertainties and the effects of non-linear tuning and as long a priori knowledge of the index and cavity length is available. Such an interferometer will generate a reference angular carrier frequency,

$$\omega_R = \frac{2n_R L_R}{c} \cdot \frac{\partial \nu}{\partial t} \tag{6.26}$$

The reference angular carrier frequency can be extracted from the reference interferogram in the same manner outlined above. The ratio of the measurement and reference angular carrier frequencies results in the cancellation of $\partial\nu / \partial t$ term to yield,

$$L = \frac{n_R L_R}{n}\left(\frac{\omega_s}{\omega_r}\right) \tag{6.27}$$

Thus the cavity length can be effectively extracted in the face of non-linear wavelength tuning, background intensity variation and fringe visibility modulation.

6.5 Experimental results

This section details experimental measurements and results using wavelength scanning interferometry (WSI) for determining absolute distance which enables the measurement of surface profiles as well as thicknesses. The tunable laser module has a wide tuning range of 1550±46 nm and can be used to measure distances, surface profiles and cavity lengths between microns to millimeter range. The fundamental principle of calculating the glass slide thickness is based on wavelength scanning and phase retrieval using Fourier domain analysis.

6.5.1 Apparatus

Figure 6.10 is a schematic representation of the apparatus which comprises two interferometers. Optical fiber is used to transport the light into the apparatus, through a 50/50 fiber coupler (CP) which splits the light into two and further propagates via circulators (CR1 & CR2) and fiber collimators (FC1 & FC2), to source two Fizeau interferometers formed by glass slides. The upper interferometer is the measurement cavity (MC) where the free space beam is incident on the cavity to be measured. The lower interferometer is the reference cavity (RC) where the free space beam is incident on an uncoated glass slide of known refractive index and thickness.

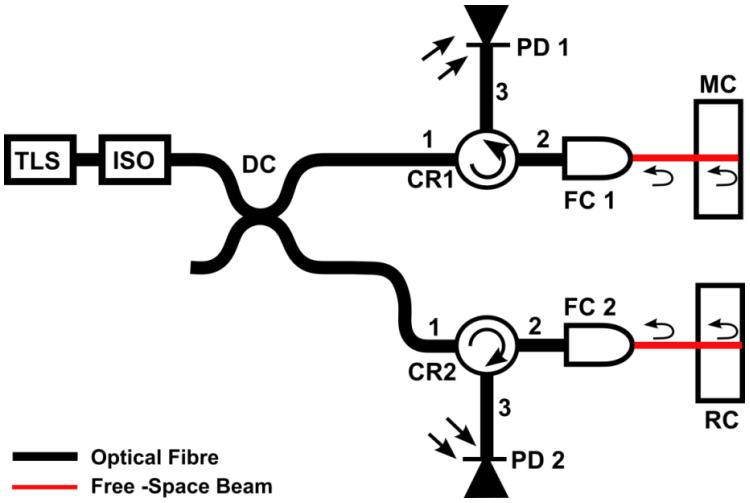

Figure 6.10 Apparatus for investigating single point measurement

This reference interferometer is used to provide correction of the inherent non-linearity in wavelength scanning produced by the TLS because of the action of the rotating TFF used to provide laser mode selection. In both interferometers, the two interfering beams are created from Fresnel reflection taking place from the front and back face of the glass slide. The beams are coupled back into the optical fiber and via the circulator are then incident on a photo-detector (PD1 & PD2) allowing the intensity to be monitored.

6.5.2 Cavity thickness measurement

In this section the operation of the experimental apparatus is described and the resulting test data analyzed according to the principle outlined in the previous section. The Penny motor was operated at 2000 rpm which provided a wavelength scanning duration of 2.2 ms across a sampled range of approximately 1505 to 1597 nm. The sample rate for electrical data acquisition was 10 MHz. The output light power from the reference and measurement interferometers was was recorded using their respective photodiodes (200 MHz Melno Systems PIN photodiode).

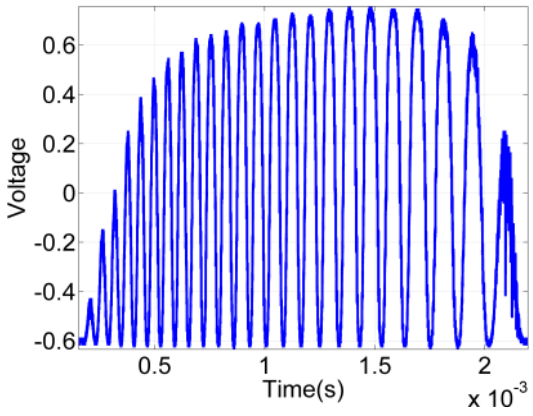
Voltage
Time(s)
x 10^-3

(a)

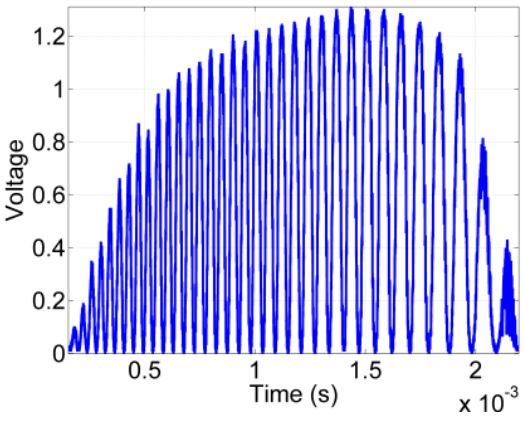
Voltage
Time (s)
x 10^-3

(d)

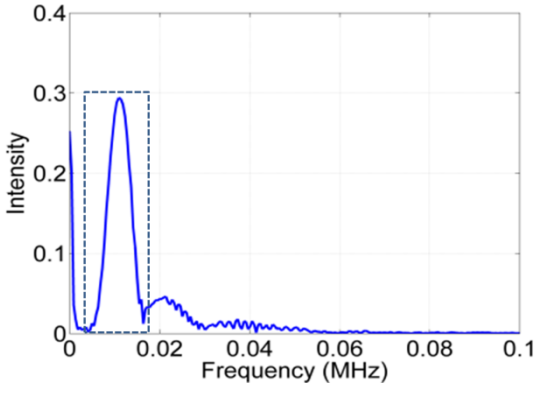
Intensity
Frequency (MHz)

(b)

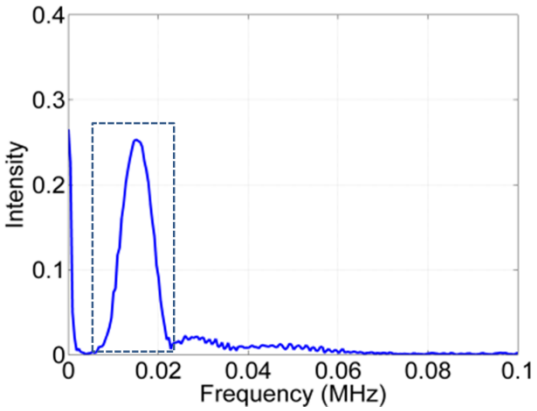
Intensity
Frequency (MHz)

(e)

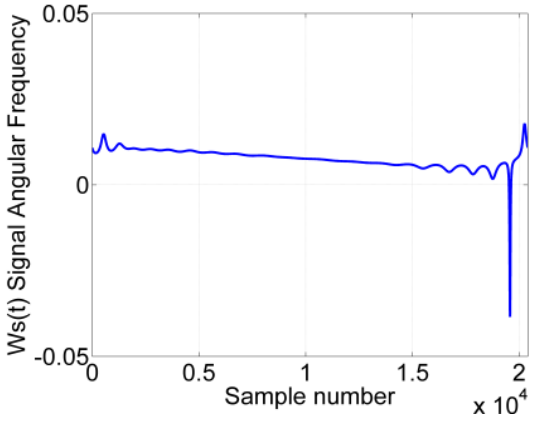
Ws(t) Signal Angular Frequency
Sample number
x 10^4

(c)

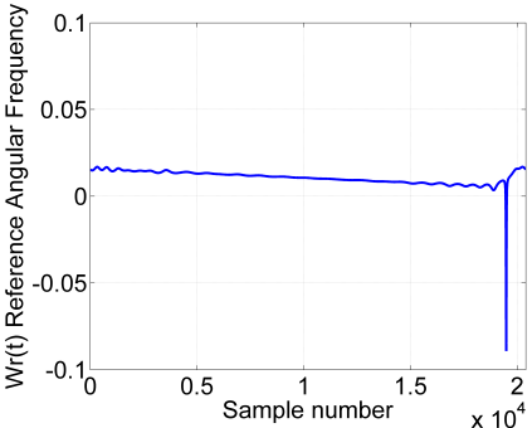
Wr(t) Reference Angular Frequency
Sample number
x 10^4

(f)

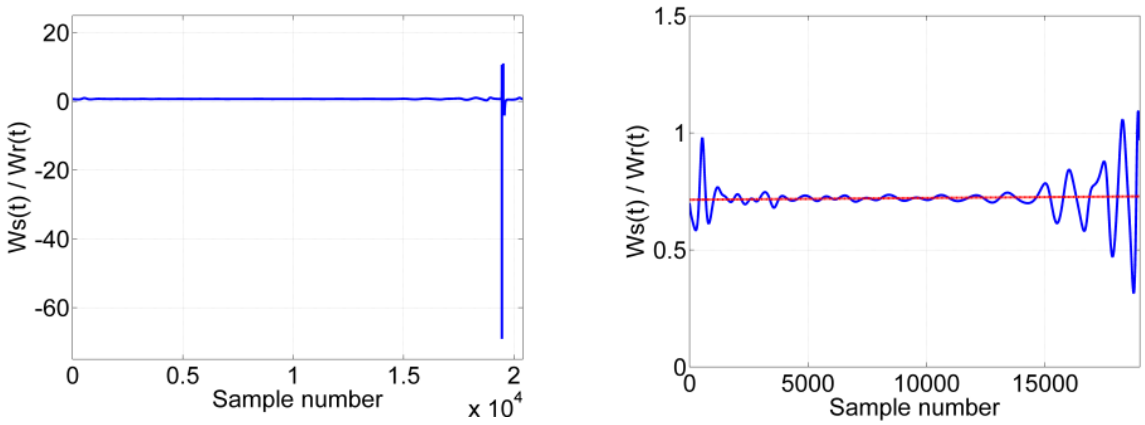

(g) (h)

Figure 6.11 Cavity thickness measurement

Measurement interferometer power; (b) Fourier spectra of measurement signal, (c) Signal angular frequencies ωS ; (d) Reference interferometer power; (e) Fourier spectra of reference signal; (f) Reference angular frequency ωR, (g) Ratio of angular frequencies; (h) Mean value of the ratio of angular frequencies

The reference interferometer was formed from a glass slide (F7) of known thickness (0.275 mm) and refractive index (1.599 at 1550 nm). Several glass slides of varying thickness and glass type where measured to assess the performance of the apparatus to measure absolute distance. Figure 6.11(a) shows the recorded interferogram from the measurement interferometer with a 0.198 mm thick F7 glass slide as the wavelength was tuned. There is a clear frequency chirp due to the non-linear tuning of the TLS module. Figure 6.11(d) shows an equivalent interferogram for the reference cavity, with the same frequency chirp being evident. The interferograms from the measurement and reference cavities where acquired simultaneously using an oscilloscope imported in to Matlab to carry out the signal processing.

The Fourier spectra computed for measurement and reference interferometer are shown in figure 6.11(b) and (e) respectively. Frequency domain filtering was used to select only the dominant peak, thus eliminating the effect of background intensity. Thereafter the phase of the signal is extracted on conversion back to the time domain according to equations (6.23) to (6.24). Figures 6.11(c) and (e) show the calculated instantaneous angular frequencies of measurement and reference signals respectively. The angular frequency is obtained by differentiating the extracted phase signal according to equation (6.20). The ratio of the individual angular frequencies is then taken to remove the effects of non-linear tuning according to equation, the result of which is shown in figure 6.11(g). Figure 6.11(h) shows the same dataset cropped to

remove the large noise spikes present and with a mean line shown. This mean value is used as the ratio ω_s / ω_R to calculate the cavity length using equation 6.26.

6.5.3 Glass side measurement results

In total 3 glass slides of varying thicknesses and index were measured using the apparatus and the signal processing methodology outline in the previous section. The results are summarized in table 6.1 where the reference slide parameters are also shown. The glass slides were measure a total of 20 times each to assess the repeatability of the measurement apparatus. The distributions are shown in figure 6.12 and 6.13 with the calculated standard deviations in table 6.1. The results shows good agreement with respect to the nominal glass slide thickness values (at least within the stated tolerance limits). Note that a tolerance was not given for the 0.198 mm Sydor slide used. It would appear that the repeatability may scale with the cavity thickness measured, but further investigation will be required to confirm this.

Table 6.1Measurement results of glass slides of different thicknesses

Slide	Thickness (mm)	Refractive index (at 1550nm)	Calculated thickness (mm)	Standard deviation (μm)
Reference Slide	0.275	1.599	-	-
Sydor Optics glass (F7)	0.198	1.599	0.19857	0.295
Edmund Optics (BK7)	0.2 ± 0.025	1.501	0.205005	0.157
Edmund Optics (BK7)	2 ± 0.2	1.501	2.004644	12.15

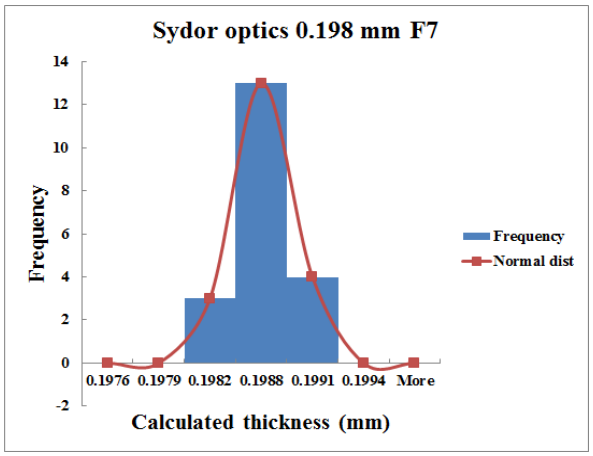

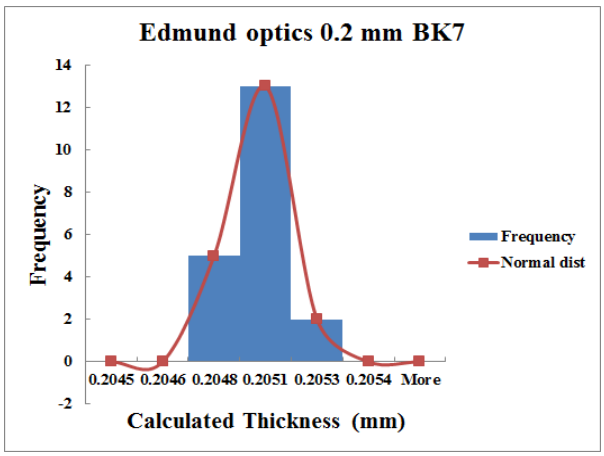

Figure 6.12 Histogram plots of twenty measurements taken with a) Sydor optics 0.198mm b) Edmund optics 0.2mm

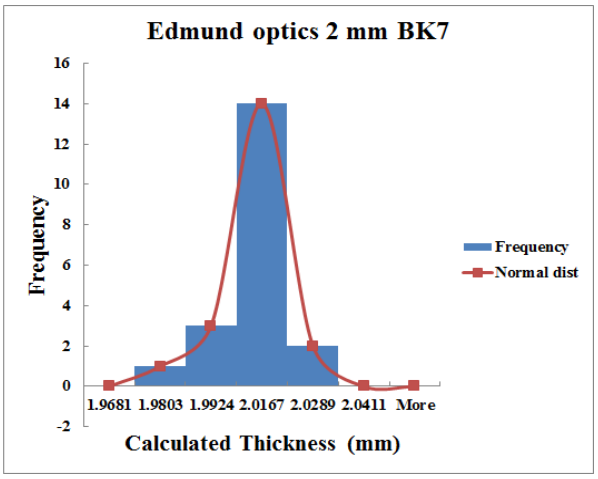

Figure 6.13 Histogram plots of twenty measurements taken with Edmund optics 2mm glass slide

Wavelength encoder unit is a 90 degree hybrid fabricated onto the optical chip for real time wavelength monitoring of the hybrid tunable laser. The working of such optical hybrid is explained in section 4.2.4 and 5.4.4 of the thesis. A tap coupler takes a part of laser beam into the encoder for wavelength monitoring. The wavelength encoder unit has an unbalanced Mach-Zehnder interferometer configuration with physical path length unbalance of 253.5 um. The refractive index of the core of the waveguide fabricated for 90 degree hybrid is 1.4673 $\pm$ 0.0003. So the total optical path length imbalance in the interferometer is 371.960 um. This path length imbalance in optical encoder unit results in-phase and quadrature signals due to interference which are separately detected by an optical receiver.

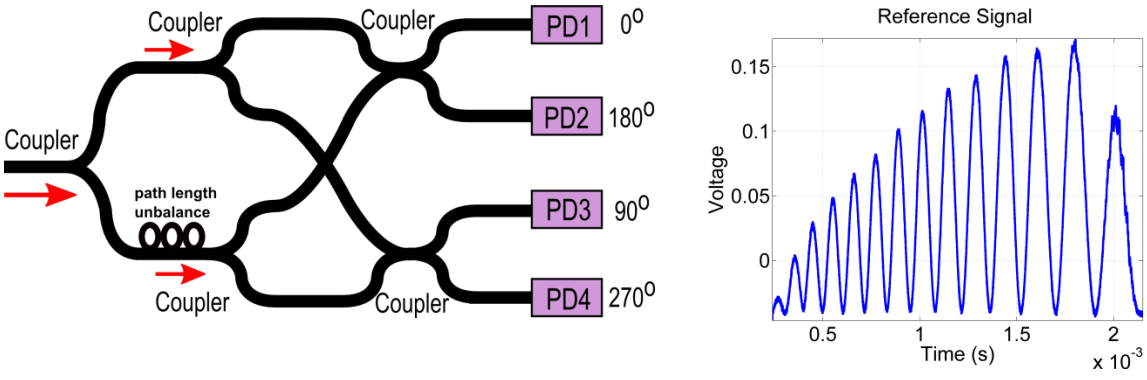

(a) (b)

Figure 6.14 a) wavelength encoder as a reference interferometer, b) Reference signal from PD1

Either of the signals obtained from unbalanced MZI (encoder) can be used as reference signal (figure 6.14) which would alleviate the need of setting up any external reference interferometer (glass slides) for non-linearity compensation as performed in previous situations. This will significantly ease the measurement setup and will provide very precise measurements as the waveguide index and length is reasonably controlled and accurate.

Table 6.2Measurement results of glass slides of different thicknesses

Slide	Thickness (mm)	Refractive index (at 1550nm)	Calculated thickness(mm)	Standard deviation(µm)
Reference unbalanced MZI	0.2535	1.4673	-	-
Sydor Optics glass (F7)	0.198	1.599	0.1977	0.00096
Edmund Optics (BK7)	0.2 ± 0.025	1.501	0.2049	0.00856
Sydor Optics glass (F7)	0.275	1.501	0.2762	0.000577

The same glass slide thickness measurement experiment performed in section 6.5 is repeated assuming the signal from the encoder as a reference signal to validate its suitability. The measurement results obtained in shown in the table 6.2. The measurement results shows good agreement with the actual value of glass slides.

6.5.4 Surface profile measurement.

6.5.4.1 Sample

A Rubert 513 reference step height specimen conforming to ISO 5436 Part 1:2000 was used to evaluate the capability of the experimental apparatus to measure a surface height profile. The

specimen features four grooves having depths of: 1 mm, 500 µm, 200 µm (C), and 30 µm (D). Only the first three of the step heights where investigated because the latter is too close to the theoretical height resolution limit of the apparatus to yield meaningful data. Figure 6.15 shows the structure of the step height specimen in the area measured.

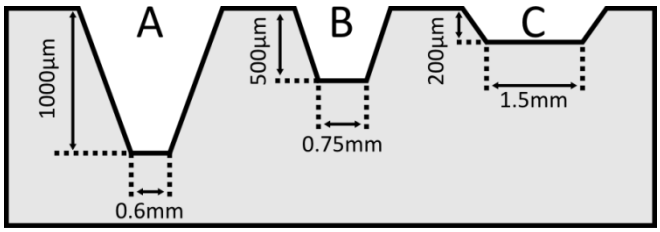

Figure 6.15 Schematic representation of the Rubert 513 reference step specimen showing the measured step features.

In order to measure the specimen an apparatus similar to those described in figure 6.11 was used with some modifications. In place of the measurement cavity a Michelson interferometer (Figure 6.16, upper part) configuration was setup with a beam splitter separating the beam into two parts for reference mirror (RM) and the sample (S). A lens (Thorlabs, Inc., AC080-016-C-ML) was used in the measurement arm to focus the beam onto the sample for the measurement. A tracking interferometer (Figure 6.16, lower) which is simply an uncoated glass slide of thickness 198 um formed a Fizeau configuration formed by reference cavity (RC).

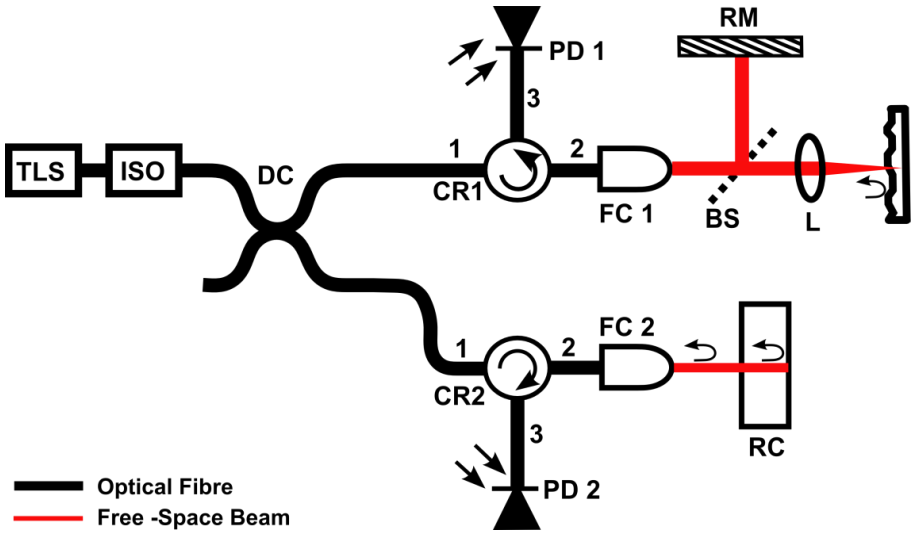

Figure 6.16 Apparatus for surface profile measurement

The TLS supplies via an isolator (ISO) a 50/50 fibre coupler (CP) which split the light into two separate free space interferometers via their respective circulators (CR1, CR1) and fibre collimators (FC1, FC2). The measurement interferometer output is coupled from port 2 to 3 of CR1 where it is monitored by a photo-detector (PD1). Similarly two beams obtained by the Fresnel reflection from the faces of the glass slide produces an interfered beam which is coupled from port 2 to 3 of CR2 where they are incident on a photo-detector (PD2).

The specimen was mounted on a translation stage with a micrometer drive and aligned such that the nominal upper plane was normal to the measurement beam. The stage was then translated step-wise in intervals of approximately 50 µm while the reference and measurement interferometer fringes were captured. These data were then processed using the method outlined in section 6.3 in order to retrieve the height information. The spot size of the beam was calculated to be approximately 14 µm for the objective lens used. The reference cavity was a glass slide of 0.198 in thickness with a refractive index of 1.599.

6.5.4.2 Probe lateral resolution

In the experiment the knife edge was translated with the step of 5 um using the micrometer stage at a set wavelength of 1550nm. Thorlabs, Inc., AC080-016-C-ML doublet lens having back focal length 12.3 mm was used as a focusing lens for scanning. Intensity was recorded using a photo-detector placed close to the knife edge. Lateral resolution deduced from the measurement curve 6.17 using the knife edge experiment was found to be 14.4 microns and shows close agreement with theoretical value calculated using the equation 6.11 is 10.842 microns.

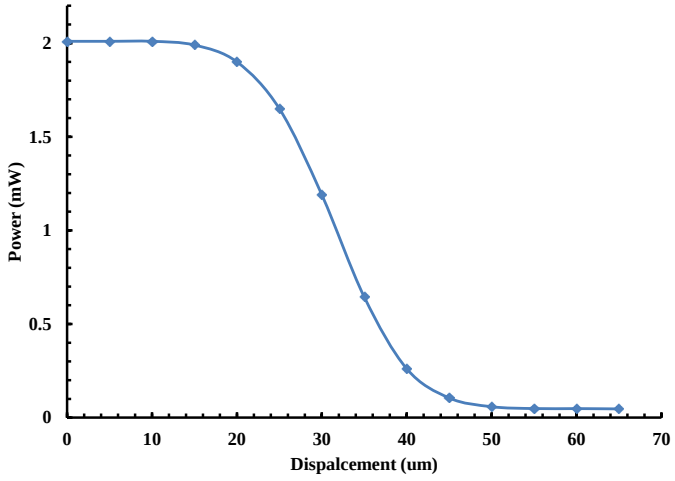

Figure 6.17 Experimental photo-detector intensity vs knife edge position

6.5.4.3 Profile measurement of Rubert 513 sample

Figure 6.18 shows captured fringe intensity data (normalized) from the reference cavity and the measurement interferometer. The total sweep time was approximately 2.3 milliseconds. The chirp of the fringe oscillation is quite clear in both the measurement and reference interferometer fringes and is due to the non-linear tuning described in the section 6.4. Similar method to that of cavity thickness measurement was adopted for the profile measurement of the sample.

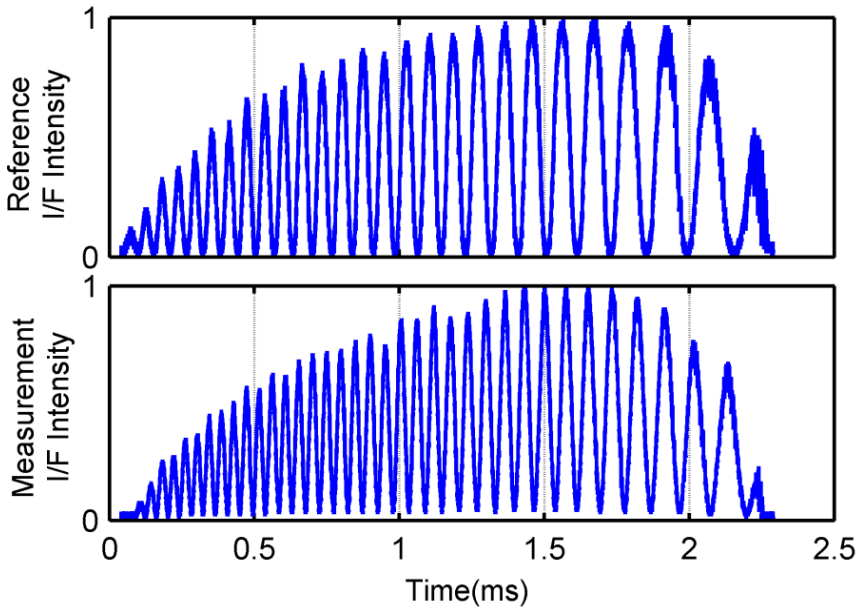

Figure 6.18 Captured intensity outputs during wavelength sweep from the reference (upper) and measurement (lower) interferometers.

Figure 6.19(a) shows the spectra resulting from a Fourier transformation of the raw data for the reference (solid) and measurement (dashed) interferometer outputs. The spectra associated with the fringe oscillation due to the changing phase, is clearly distinct from the lower frequency contributions from background intensity variation in both traces.

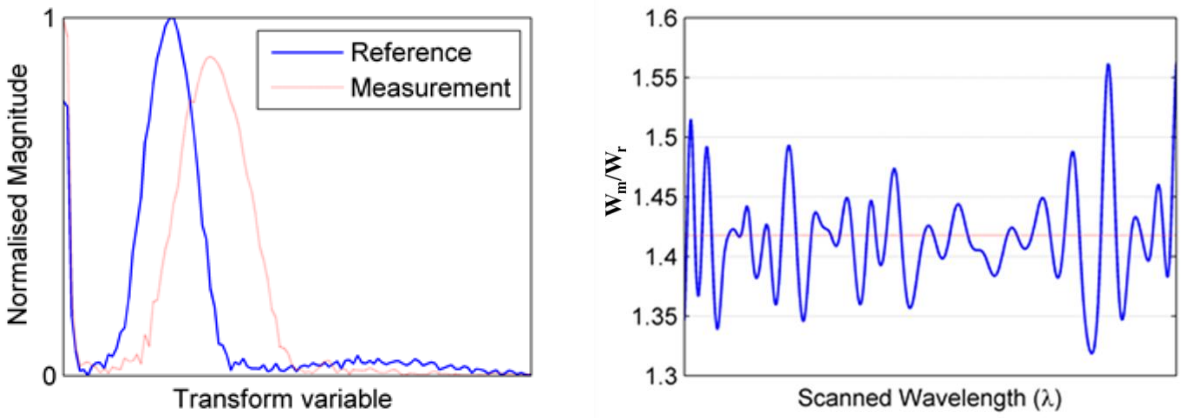

(a) (b)

Figure 6.19 a) Fourier transform of the reference (solid) and measurement (dashed) interferometer intensity data, b) Ratio of the instantaneous angular frequencies from the reference and measurement interferometers

Figure 6.19(b) shows the final ratio of the calculated instantaneous frequencies and the mean value of this were taken to extract the height using equation 6.27. The trace is cropped slightly to remove noise which is apparent at the edges of this because this adversely affects the quality of the linear fit operation. Figure 6.20 shows the surface height profiles retrieved for steps A, B and C. Note that the steep slopes evident on the sidewalls of each groove mean data could not be retrieved in those areas as returning light is outside the acceptance angle of the objective lens at this point. As such these invalid data points have been removed in the traces shown in figure 6.20. The step heights were calculated as the difference between mean lines taken from the top surface and the bottom of the respective groove. The points used for determining the mean lines are indicated by crosses on figure 6.20. It can be seen that the results suggest good agreement with the nominal values of the step heights for the Rubert 513 step height reference specimen.

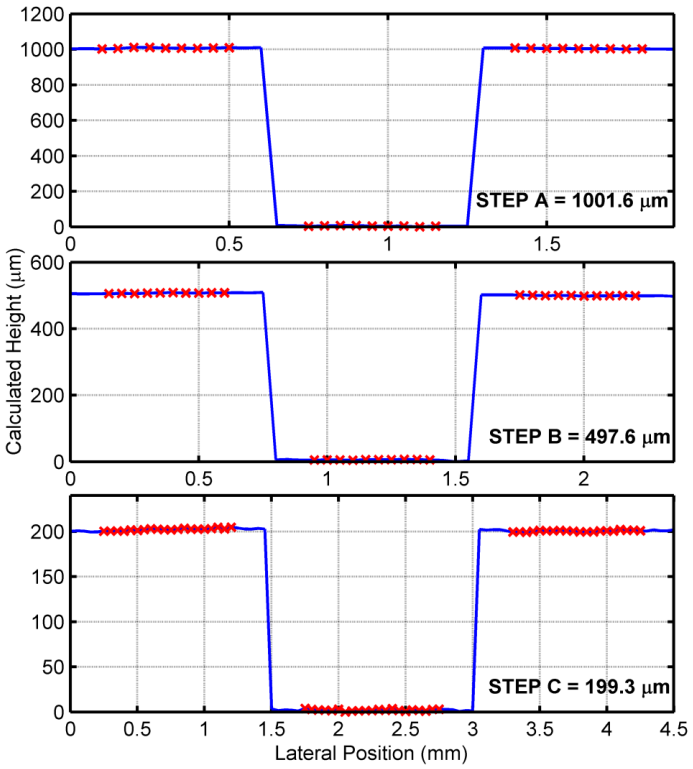

Figure 6.20 Surface height profiles calculated for steps A, B and C

6.6 Summary

In this chapter the concept of single point absolute distance measurement sensor based on hybrid photonics for embedded metrology applications is introduced. The single point measurement was performed by wavelength scanning interferometer based on Fourier domain analysis combined with a reference interferometer to overcome contributions from the systematic non-linearity in the tuning of chip tunable laser. Initially the measurement principle was validated by measuring standard glass slides of different thickness. Measurements of several glass sides were taken to analyze the performance of the apparatus. The accuracy of measurements obtained also indicated the performance of the tunable laser source. Further the sensor system was employed to measure the surface profile of standard step height specimens to verify the potential of this method for practical application. The next chapter will follow the design of a lateral scanning probe and development of a miniaturized metrology sensor on a whole to produce measurement device capable of performing high resolution profile measurements.

7 Spectrally Encoded Lateral Scanning Probe for Surface Profile Measurements

7.1 Introduction

This chapter presents the development of a miniaturized surface profilometer based on hybrid photonic integration, incorporating spectrally encoded lateral scanning optical probe to provide non-contact, fast surface measurement with high axial resolution. The complete configuration of the hybrid metrology sensor device is shown in figure 7.1. The metrology sensor system comprises of two distinct elements: An integrated-optic module containing the photonic circuit, and a separate optical probe structure. The basic principle of operation of the proposed metrology tool is based on two interferometric techniques; wavelength scanning with phase shifting. The optical probe critically determines the overall performance of the metrology sensor device. Various types of scanning probe systems implemented in metrology and imaging have been discussed in deatil in section 2.11. In this thesis a probe design is based on spectrally encoded laser scanning microscopy has been implemented using a dispersive grating which provides rapid raster scanning of the focused beam at the sample under investigation. The sensor system will have the leverage of high axial resolution provided by the interferometry. Finally the hybrid device along with the probe system is implemented for the actual measurement of the surface to assess the performance of the metrology device.

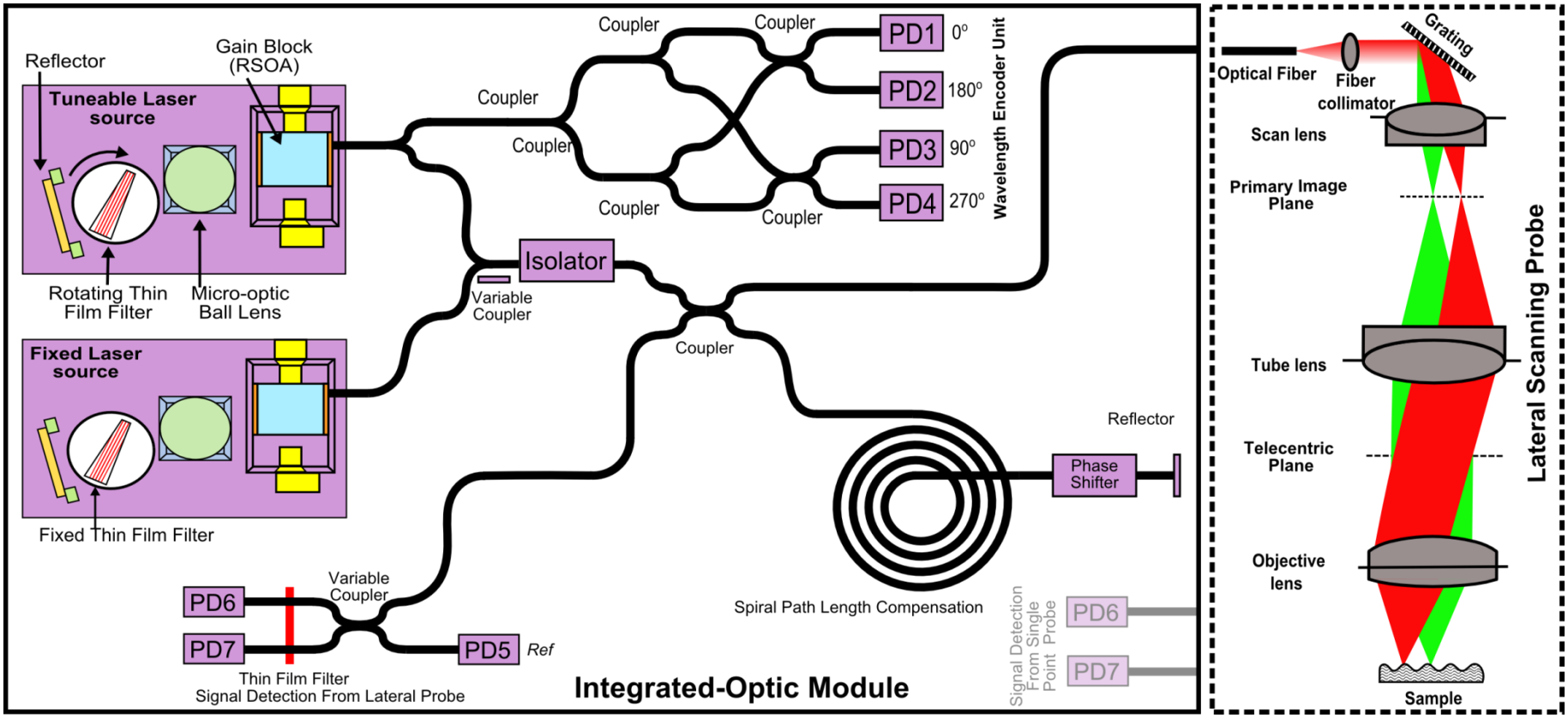

Figure 7.1 Schematic of the metrology sensor system incorporating lateral scanning probe

7.2 Spectrally encoded lateral scanning probe

Spectrally encoded lateral scanning optical probe presented in this thesis utilizes a rapid wavelength scanning source and optical probe consisting of dispersive optical element and objective lense to provide high resolution measurements for embedded sensor. The probe follows the Gaussian beam imaging theory which is explained in detail in the previous chapter 6. The fundamental working of the probe is based on wavelength division multiplexing where each focussed point along the scan line is encoded by a different wavelength using the dispersive grating and objective lens. The use of grating alleviates the need of any mechanical scanners, which significantly simplifies the probe design and construction. No additional drive circuitry is required as in the case of resonant galvo or MEMS scanners for controlling mirror positions for beam scanning. Hence in terms of durability, the performance of diffraction a grating based scanner is naturally much higher compared to mechanical ones. The scan speed of the lateral scanning probe is only limited by the tuning speed of the chip tuneable laser. With the penny motor operating at its full operational speed of 40000 rpm a scan speed ~ 330Hz can easily be achieved. Currently it is operated at 2000 rpm for initial investigations and measurements.

7.2.1 Grating as a beam scanner

Grating is an optical element consisting of number of equally parallel grooves or structures made on an optical material called a substrate. It is used to disperse different wavelengths spatially, i.e. each wavelength is directed at a particular angle in space after reflection from the grating surface. When a bundle of rays falls onto the grating, these rays or wavefront forms orthogonal set such that wavefronts are perpendicular to the rays and parallel to the grating. Every point on a wavefront acts as a point source (Huygens' Principle) and further wavefront hitting the slits forms another source of secondary wavelets spreading out cylindrical wavefront from each point in all directions. These secondary wavefront interferes either constructively or destructively to give an irradiance pattern which is basically the superposition of all the waves in phase. The basic principle of operation of phase grating is given by the equation,

$$d\ (sin\alpha + sin\beta) = m\ \lambda \qquad m = 0, \pm 1, \pm 2....., \tag{7.1}$$

where λ is the wavelength of light, d is the grating pitch or groove spacing, α is the incident angle, β is the diffraction angle, m is the diffraction order. All the angles are measured from the grating normal shown in dashed line in the figure 7.2.

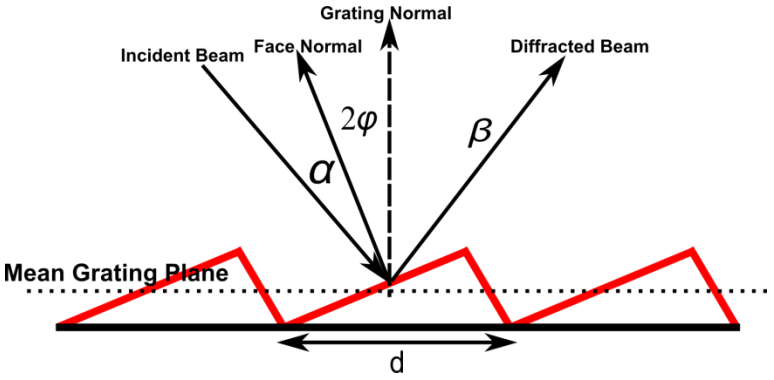

Figure 7.2Basic principle of operation of a phase grating

Equation 1 can be rearranged as in diffraction angle β_i corresponding to the wavelength λ_i is given by,

$$\sin\beta_i = \frac{m\lambda_i}{d} - \sin\alpha \tag{7.2}$$

For a source with finite bandwidth given by $\Delta\lambda$ the angular deviation $\Delta\beta$ is given by,

$$\Delta\beta = \frac{m}{\cos(\alpha)\times d}\Delta\lambda \tag{7.3}$$

Resolving power (R) of a grating is defined as its ability to separate adjacent spectral lines of average wavelength λ. It is a dimensionless quantity and is represented as,

$$R = \frac{\lambda}{(\Delta\lambda)_{\min}} \tag{7.4}$$

where $\Delta\lambda_{\min}$ is the limit of resolution; the difference in wavelength between two lines of equal intensity which is easily distinguishable. In general a Rayleigh criterion is used to determine the limit of resolution. The theoretical resolving power of a diffraction grating is given by,

$$R = mN \tag{7.5}$$

Where m is the diffraction order and N is the number of illuminated groves onto the grating surface. In order to maximize the power to a particular diffraction order gratings are blazed to some angle γ. This is called as the blaze angle of the grating. The grating (Edmund Optics, 46079, 830 Grooves) used in this thesis for the probe design had the blaze angle of 29°52’ to maximize power in the first diffraction order.

7.2.2 Optical probe system design

The optical probe consists of fibre collimator, grating element, scan lens, tube lens and infinity corrected objective lens. A configuration of the spectrally encoded lateral scanning probe is shown in figure 7.3.

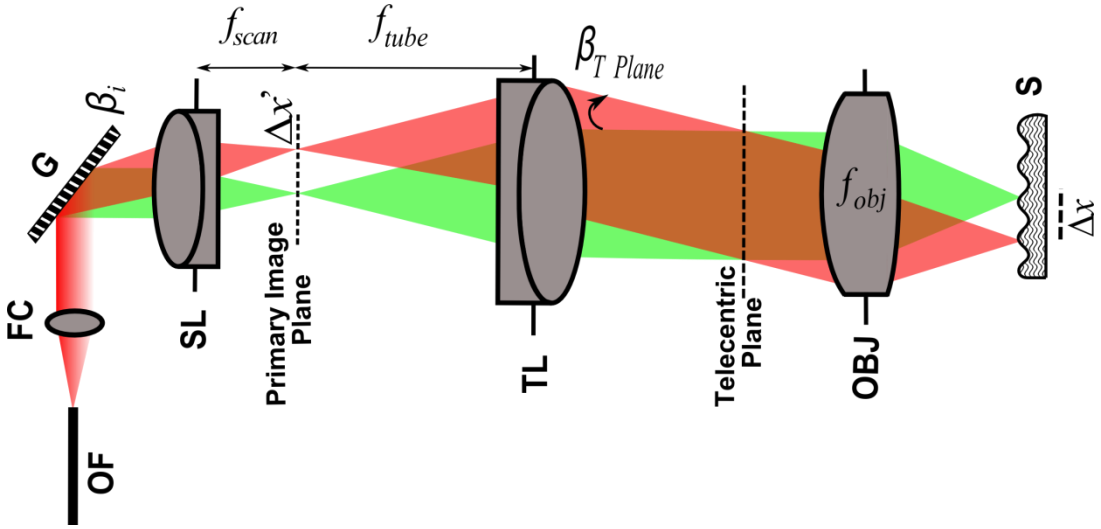

Figure 7.3 Schematic of proposed lateral scanning probe. (OF - optical fibre, FC - Fibre collimator, G - Grating, SL - Scan lens, TL - Tube lens, OBJ - Objective lens, S - Sample)

By tuning the wavelength of the light source and by suitably selecting a grating, it is possible to steer the beam of light over a desired angular range. The semiconductor tuneable laser module (chip tuneable laser) launches light into single mode fibre of core diameter ~4um. It must be noted here that the core of single mode fibre acts as the source and the detector pinholes. A high numerical aperture collimator lens maximized the coupling between the fibre and the collimator lens. This will in turn minimize the confocality providing access to full depth of focus of the microscope objective. This will also provide a simple approach for pinhole alignment to the image of point on the sample created by objective system. In bulk optics systems a slight misalignment in the input laser-pinhole assembly can induce significant attenuation and aberration. Fibre as a pinhole gives a simple approach for pinhole alignment to the image of point on the sample created by objective system (Kimura et al., 1991; Xiao et al., 1988). Also it has been observed earlier that optical fibres in place of pinholes have resulted better spatial resolution and efficiency (Hebden et al., 1993; Ilev et al., 2000). The output beam from the single mode fibre was collimated using the fibre collimator (Thorlabs, Inc., TC06APC-1550, 0.28 NA) which finally collides with the dispersive grating (Edmund Optics, 46079, 830

Grooves). The dispersed beam travels through the scan lens, through the tube lens and finally into the microscope objective to hit the sample target.

This collimator has an AR coating in the spectral range 1050-1650, focal length = 6 mm. The beam spot position in the object plane depends on the beam angle in the telecentric plane which is achieved by placing a diffraction grating at the centre of the conjugate telecentric plane of the microscope objective which is actually at a distance equal to the back focal length of the scan lens (Thorlabs, Inc., AC080-016-C-ML). The grating deflects the beam across its entrance aperture in a raster fashion. The scan lens is a part of an afocal Keplerian beam expander system acting in conjunction with the doublet lens (Thorlabs, Inc., AC254-050-C-ML). The position of front focal plane of the scan lens and the back focal plane of the doublet lens are matched to from an intermediate focal plane which contains the focussed spots formed by scan lens on beam deflection from grating. The doublet lens reconverts the linear scan into angular scan about a pivot point located at the point on the optical axis intersecting with the front focal plane of the same doublet. In effect the beam expander increases the full-width at half maximum (FWHM) diameter of the laser beam by a factor of 2 to fill the back aperture of the objective lens, there by maximizing the object-space numerical aperture (NA) of the optical system consequently achieving diffraction limited spot for maximal resolution. The intermediate optical system forms the image of diffraction grating onto the objective lens. In addition to increasing the object space NA, the beam expander also translates the real pivot point, i.e., the diffraction grating to a virtual pivot point located at the back focal plane of the objective lens. This action results in the objective lens converting the angular scan about the virtual pivot point into linear scan across the sample and is given by,

$$\Delta x = f_{obj} \times \tan \beta_{T\ Plane} \tag{7.6}$$

An infinity corrected microscope objective (Mitutoyo M Plano NIR 10X/0.26) is used for the probe design because of its obvious advantage. The rays coming from the focussed points in the sample plane is bundled to collimated beams at the rear aperture of the microscope objective. In this configuration a tube lens is used in conjunction with the objective to avoid off axis rays to improve the performance of the microscope. The magnification of the microscope objective is given by,

$$M = \frac{f_{tube}}{f_{obj}} \tag{7.7}$$

The tube lens is placed very close to the objective to capture all the peripheral light waves to avoid vignetting. This tube lens replicates the point by point scan of the sample to an intermediate image plane. The image size in the primary object plane is given by,

$$\Delta x' = \Delta x \times M \tag{7.8}$$

Also relay lens configuration adds greater flexibility in housing other components such as mirrors, polarisers; prism etc. can be conveniently placed in between the objective and tube lens without disturbing spherical aberration or change in objective working distance. In the lateral scanning probe design use of fold mirrors and prism in between the objective and tube lens will help to fold up the beam path and significantly reduce the overall size of the probe. The retro-reflected light from the sample retraces its path through the optical probe system and is collected at the optical fibre pin hole which is further detected by the photo-detector. The detected light intensity is analysed using the phase shifting technique to obtain the optical phase which relates directly to the surface shape.

7.3 Optical system performance

7.3.1 Resolution

In a surface profile measurement application resolution (vertical and lateral) is one of the most basic performance characteristics parameter of the non-contact optical probe. The use of wavelength scanning interferometry with the phase shifting techniques in the aforementioned device enables sub-nanometer vertical resolution. This gives an obvious advantage by allowing the use of lower magnification objectives while maintaining the high vertical resolution and desired FOV, enabling higher throughput with maximum accuracy. The lateral resolution of the confocal scanning probe also depends upon the instantaneous line width of the laser and resolving power of the diffraction grating which spatially separates individual wavelength allowing the line scanning of the beam onto the test surface.

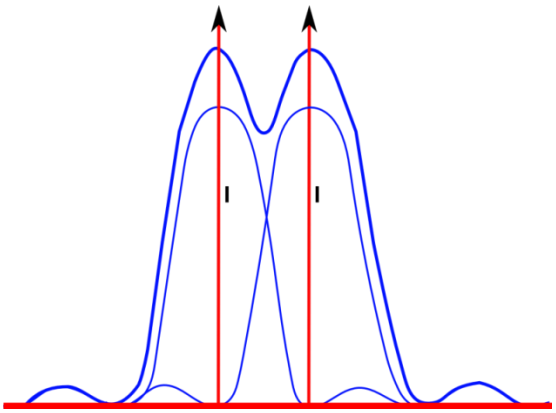

Figure 7.4 Rayleigh criteria: Airy disks overlap where central maxima coincides with first minima of other

The Rayleigh criteria for conventional microscope system to define minimum resolvable separation between two points depicts overlapping of respective Airy disk, where each point is defined by a point spread function (PSF) whose central maxima coincides with the first minima of the other (Figure 7.4). This explains that a minimum contrast of 26% is required to clearly resolve to nearby points. Thus the lateral resolution of a conventional microscope assuming the above criteria is given by,

$$d_{\min} \approx \frac{1.22\lambda}{2NA} = \frac{0.6\lambda}{NA} \tag{7.9}$$

where λ is the wavelength of light and NA is the numerical aperture of the microscope objective. Thus the scanning probe system with illumination wavelength of 1.55 µm and 0.26 NA microscope objectives the system would achieve theoretical resolution of 3.576 µm. The lateral scan is provided by the spatially deflecting the beam using a diffraction grating and hence the spectral resolution of the device will also depend on the mode spacing of the laser used. The chip tuneable laser which has a mode spacing of 0.04nm and a bandwidth of 90 nm would resolve 2250 points. The resolving power of the grating is given by equation 7.5, which can be rewritten as,

$$R = \frac{\lambda}{\Delta\lambda} = \frac{mD}{\Lambda}, \quad m \text{ being the order} \tag{7.10}$$

The resolving power of the grating is directly proportional to the incident beam diameter on the grating, and inversely proportional to the grating frequency Λ [20]. A beam of diameter (D) $1.2mm/\cos\left(63^{o}\right) = 1.2e-3/0.4539 = 2.64mm$ is made incident onto 830 line/mm grating will have first order spectral resolution of

$$\Delta\lambda = \frac{\Lambda \times \lambda_{1550nm}}{D} = \frac{1.204\times10^{-6}\times1.5510^{-6}}{2.64\times10^{-3}} = 0.706nm \qquad (7.11)$$

This corresponds to approximately 130 resolved points. Thus the resolution of the system is limited by optical resolution as long as the field of view is less than approaximately 130*3.57 um= 464.1 um.

7.3.2 Lateral scan range

The hybrid tuneable laser provides $\sim \pm 45nm$ bandwidth wavelength scan on either side of the central wavelength. The scan angle ($\Delta\beta_R$) provided by the diffraction grating corresponds to the angle difference between the central wavelength (λ_c) and at any other wavelength (λ_i). The maximum scan angle can thus be given by ($\Delta\beta_R^{\max}$),

$$\Delta\beta_R^{\max} = \beta_{\lambda_c} - \beta_{\lambda_{i(\text{end/start})}} \qquad (7.12)$$

This in turn provides a maximum tilt angle $\beta_{TPlane}^{\max}$ to the beam in the telecentric plane given by equation 3. The position of the scanned spot in the object plane is defined by the tilt angle β_{TPlane} (equation 2). Thus considering the linear dispersion of grating with the source tunable bandwidth the lateral scan range or the field of view in the object plane is given by,

$$FOV = 2\times\Delta x = 2\times f_{obj}\times\tan\beta^{\max}_{T\ Plane} \qquad (7.13)$$

7.3.3 Maximum measurable surface slope

Thus the numerical aperture of the objective lens is the limiting factor in the maximum allowable slope onto the test surface that can be me measured. If the surface is tilted the reflected cone of light tilts twice the surface tilt which leads to an offset of the returning beam (can be seen in the figure 7.5).

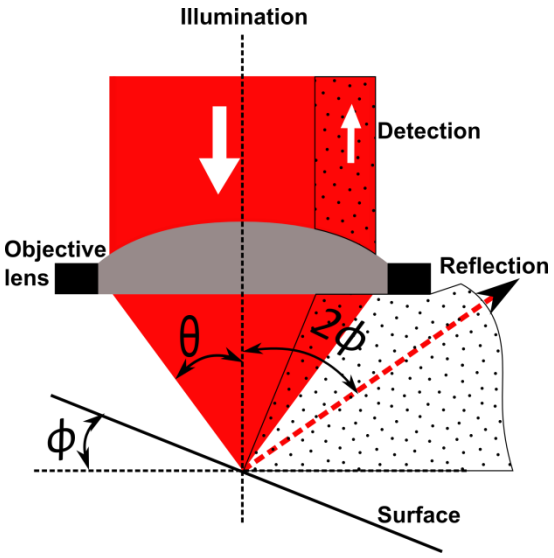

Figure 7.5 Specular reflection from the surface under investigation

For a smooth and mirror like surface ϕ creates specular reflection deviating the reflected beam by 2ϕ. This shift of returning beam leads to Tilt Dependent Error (TDE). The error can be in the form of beam vignetting. Beam vignetting is the reduction in the image brightness and saturation of the edge compared to the centre. As long as $\phi < \theta$, a part of the reflected beam can be easily captured by lens for detection. But closer the ϕ approaches θ lower will be the signal-to-noise ratio as the amount of detectable light will decrease with increasing surface slope. The maximum measurable slope of a surface in the case of specular reflection is given by,

$$\phi^{specular}_{\max} = \sin^{-1} NA \qquad (7.14)$$

The plot of the maximum measurable surface slope corresponding to the NA of the objective is shown in figure 7.6. The plot shows that higher surface slopes can be measured with the use of high NA objectives. If the surface element is rough within the spot size of the beam, the surface will exhibit diffuse reflection leading to scattering of light ultimately increasing the aperture angle. As a result the maximum measurable slope angle increases dramatically.

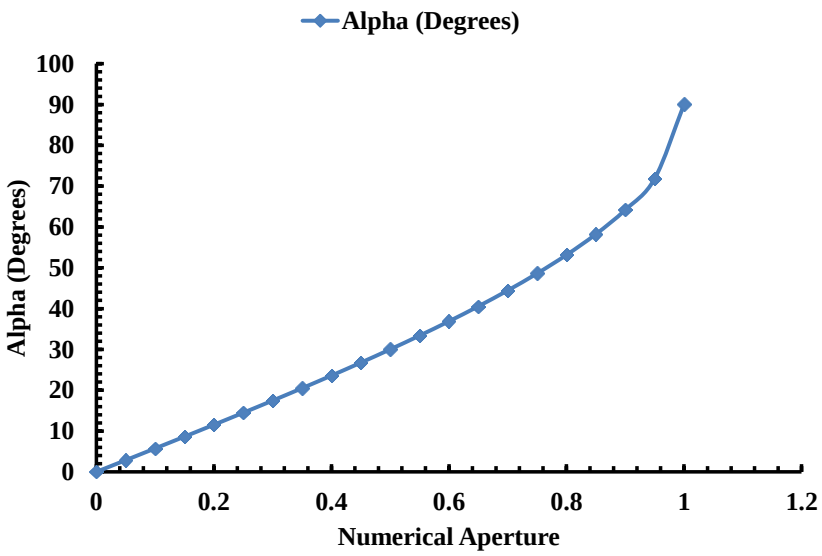

Figure 7.6 Maximum measurable surface slope corresponding to the NA of the objective (Simulated)

7.4 System characterization

This section details about the characterization methods used to study the ability and performance of the designed optical probe system. Zemax design optical software was initially used to model the system and determine approaches for reducing probe dimension. Further Foucault's knife edge and the USAF resolution target tests were performed to characterize the performance of the optical probe empirically.

7.4.1 Zemax optical design simulation

The aim is to design a compact optical probe to compliment the development of a fully miniaturised metrology sensor system for embedded metrology applications. So in order to investigate, the Zemax Optical Design simulation was performed to determine the various approaches of reducing probe dimension without compromising its performance.

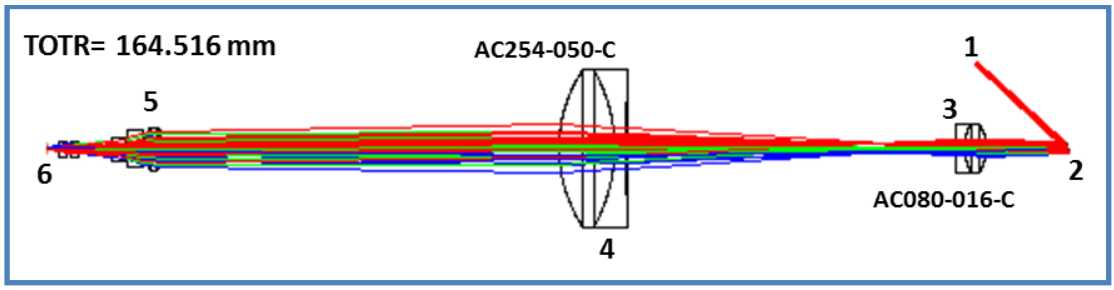

Figure 7.7 Optical layout of the probe in Zemax. The blue green and the red lines represent the scanned laser beam at the design wavelength

A sequential ray tracing technique was implemented to model the lateral scanning optical probe. Figure 7.7 shows the optical layout design of the optical probe simulated in Zemax. The system consists of (1) input beam, (2) diffraction grating, (3) and (4) relay lenses, (5) microscope objective and (6) the object. The initial parameters such as wavelengths, field angle, and entrance pupil diameter of the beam are inserted into the software. The entrance pupil diameter of the source beam is taken as 0.8 mm corresponding to the effective aperture of the microscope objective to avoid any beam vignetting. The field angle is set at zero as the beam scan is provided by the grating scanner.

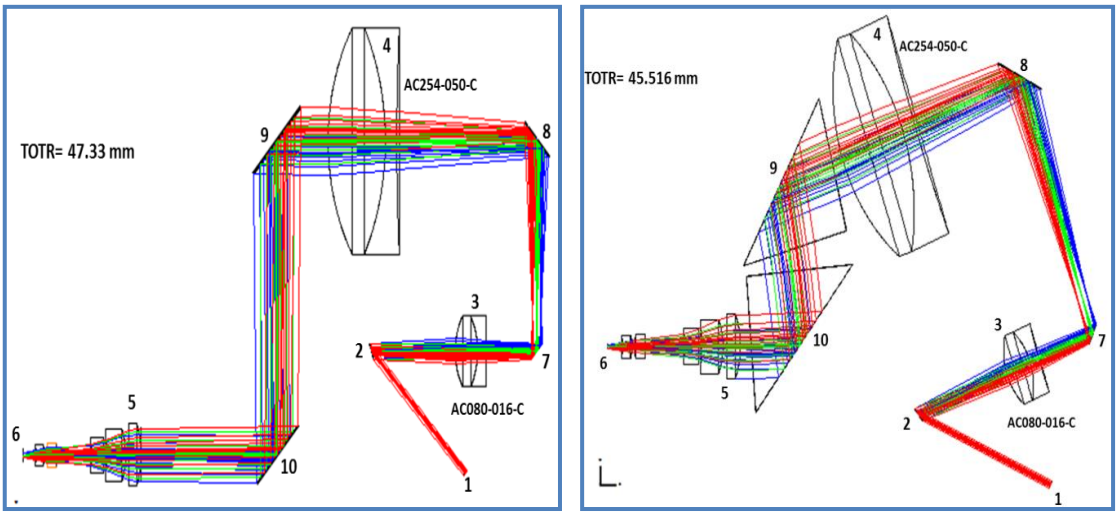

Figure 7.8 Optical layout of the compact probe in Zemax using the (a) Design 2: mirror pair (7-8, 9-10) and (b) Design 3 mirror (7-8) and prism pair (9-10) combinations

The ray tracing is performed at three wavelengths (1505nm, 1550nm, 1580 nm) in the infrared region. In order to obtain estimated lateral resolution a microscope objective close to the specifications of the Mituyoto M Plan Apo 10X NIR series was chosen. The microscope objective was selected from which had an NA of 0.26 and a magnification of 10 X. For the relay system (scan lens + tube lens) commercially available Achromatic lenses (AC080-016-C and

AC254-050-C Thorlabs) were used. The spatial frequency of the diffraction grating used had 800lines/mm. Four mirror combinations (7-8, 9-10) have been used in design 2 while in design 3 contains two mirrors (7-8) and two prism (9-10) combinations as shown in figure 7.8 (a) and 7.8 (b) respectively. The mirror and prism combinations and two mirrors have been used in the design to give a compact configuration to the probe design. The prism pair in design 3 is tilted (~5 deg) to avoid any reflections from the cavity formed by the prism pair or the lens prism combination. The glass material for the prism used is BK7. The telescope system which consists of scan and tube lens is optimised making it purely an afocal system. The axis of all the optical components are perfectly aligned relative to the central wavelength (1550nm) using the tilt and decentre elements. The grating is placed at the back focal plane of the scan lens. The grating to scan lens distance is further optimised for better beam collimation. The objective lens is then inserted. A slider tool is used to optimise the distance between the tube lens and the microscope objective. The optimum distance between the tube lens and the objective is obtained to avoid any beam vignetting. Further analysis is performed to evaluate the performance of the system. The Huygens point spread function (PSF) and the PSF cross-section are drawn at three design wavelengths and analysed. The field of view (FOV) over the full illumination spectrum (design wavelengths) is calculated using equation 4 is approximately 0.4 mm. Figure 7.9 plots the Huygens PSF at all three design wavelengths. The PSF gives the Strehl ratio which is the measure of optical image quality for very high quality imaging system.

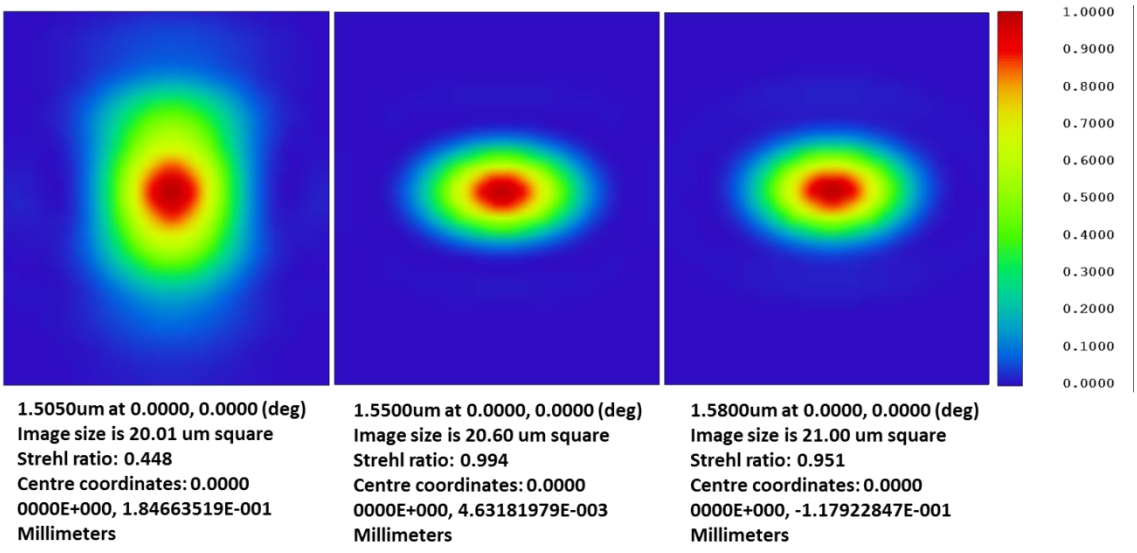

Figure 7.9 Huygens Point spread function at (a) 1505 nm (b) at 1550 nm (c) 1580 nm

The Strehl ratio is defined as the peak intensity of the diffraction PSF divided by the peak intensity of the diffraction PSF in the absence of aberrations. Strehl ratio takes the value between 0 and 1 with a perfect optical system having the value unity. Strehl ratio at wavelength 1505nm is 0.5 while at other two wavelengths the value is close to unity. This suggests that the probe system is aberration free except for minor degradation at 1505 nm. The lateral resolution of the system is observed to indicate the performance of the system. Since the grating induces astigmatism in the system the spot size of the beam will have different values in orthogonal directions. Hence a PSF cross-section (Figure 7.10) was used to determine the spot size values which will give an assessment of the lateral resolution of the system over the entire wavelength range.

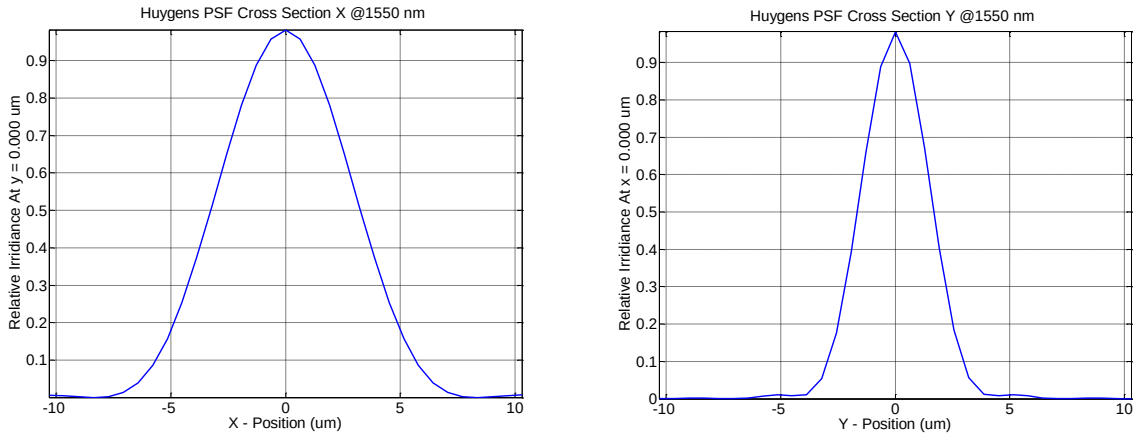

Figure 7.10 Huygens Point spread function cross-section at 1550 nm along X (L) and Y (R) directions

The result of the simulation at 1550 nm is shown in the figure 5 spot size diagram. The spot size is calculated at 1/e2 value of the maximum irradiance curve obtained from the Huygens PSF cross- section along the orthogonal direction X and Y. A minimum spot size of 2.575 µm is obtained along Y for 1550 nm while it degrades at the other two wavelengths on either sides of central position of FOV.

Table 7.1Spot sizes in orthogonal directions at different wavelengths

Wavelengths	Spot size along X (um)	Spot size along Y (um)
1505 nm	4.376	5.313
1550 nm	5.150	2.575
1580 nm	5.250	2.625

The table 7.1 below shows the values of spot sizes obtained at three different wavelengths of the scan range. The spot size along lateral direction (X) is more or less at all the wavelength

while in transverse direction (Y) the spot size varies as expected with minimum at design wavelength 1550 nm aligned to optical axis. Similar performances have been observed in the case of design 2 (mirror pair) and design 3(mirror prism pair) which provides the device a compact and portable configuration.

7.4.2 Knife edge experiment

The knife edge beam profiling technique (figure 7.11) provides easy, quick, inexpensive and accurate determination of beam parameters and has been used as a standard method for the characterization of Gaussian laser beam. The Gaussian beam here is this case is not radially symmetric because of the astigmatism provided by the grating element. So a measurement of beam radius is obtained in orthogonal directions perpendicular to the beam propagation which was aligned with the major and minor axes. The spot size of the beam was measured at different set wavelengths of the tuneable laser within the tuneable range.

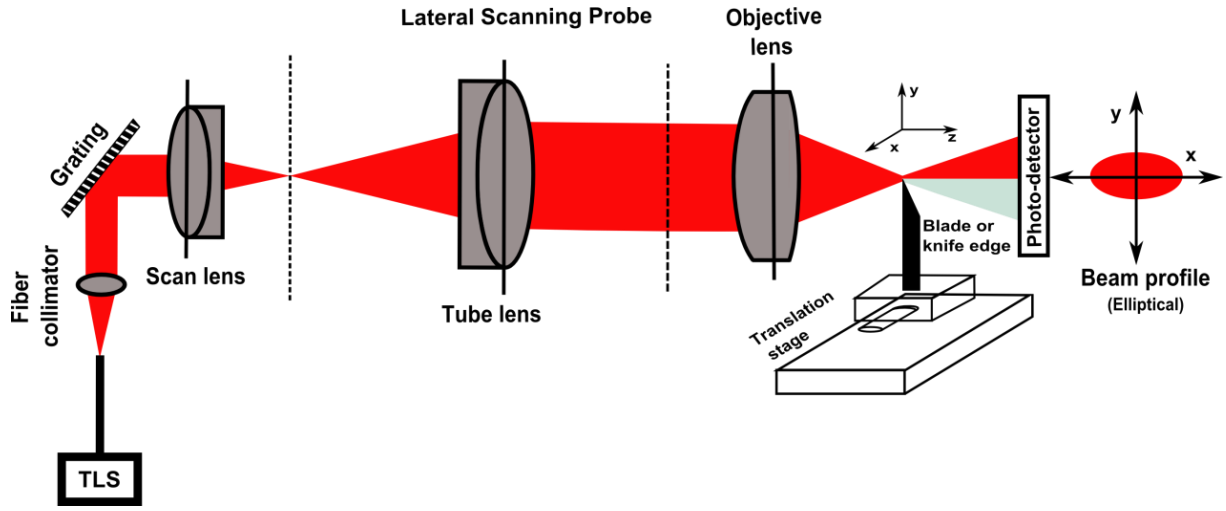

Figure 7.11 Schematic for the spot size measurement of the laser beam using the knife edge experiment. The light grey area shows the blocked rays by the knife edge

The knife edge was translated with the step of 2.5 um at each set wavelength using the high resolution Newport linear motor. Intensity was recorded using a photo-detector placed close to the knife edge. For a Gaussian beam, the lateral resolution is defined as its $1/e^2$ radius and can be calculated from the 0.78 * 10-90% edge width of the transmission profile (Chapter 6, Section 6.2.2.1) obtained at detector by laterally moving the knife edge in the focal plane across the beam.

Table 7.2 Spot size measured along lateral direction at different wavelengths using knife edge experiment

Wavelengths (nm)	Spot size (um) along Y
1505	6.864
1520	4.524
1535	4.056
1550	3.666
1565	3.900
1580	4.056

The calculated spot sizes of the beam at focus are given in the table 7.2 above. The minimum spot size is obtained at the centre wavelength 1550nm which is aligned to the optical axis of the system (Figure 7.12). The spot size slowly increases on the either side of the wavelength scan. Figure 7.13 & 7.14 shows the plots of spot sizes obtained from Zemax simulation and knife edge experiment along transverse and lateral direction at different wavelengths of the scan. The calculated spot size using knife edge experiment shows good correlation with the simulated one.

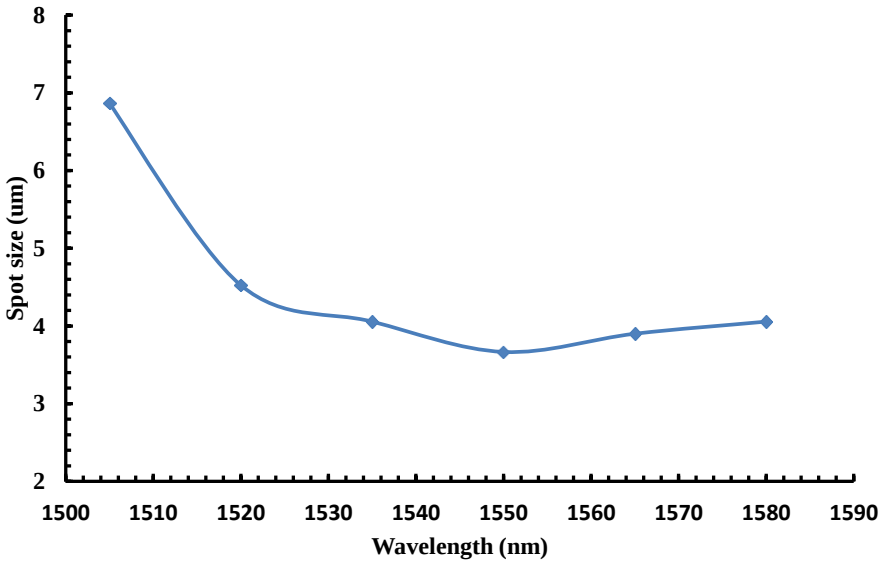

Figure 7.12 Plot of spot size measured along transverse direction (Y) at different wavelengths using knife edge experiment

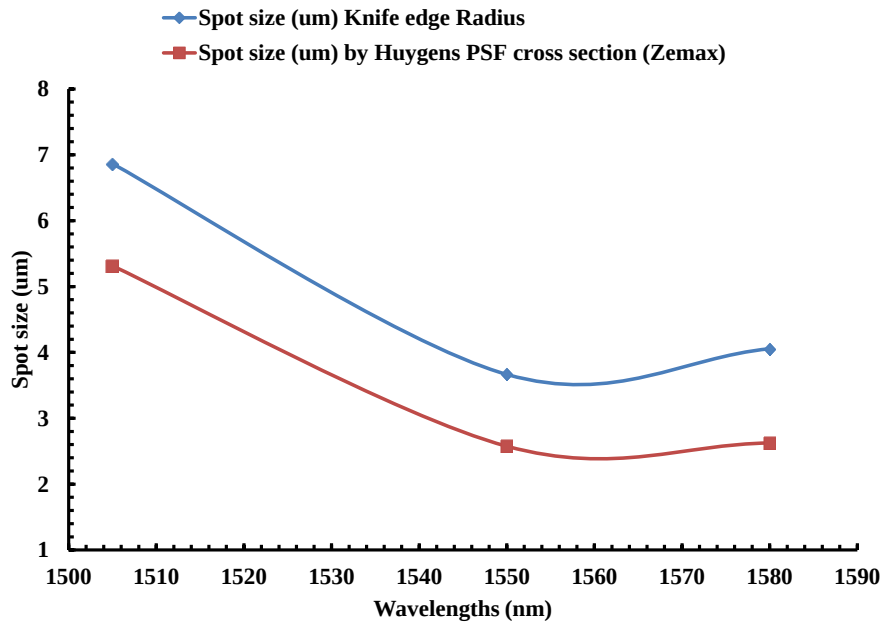

Figure 7.13 Plot of the spot sizes along transverse direction (Y) using knife edge experiment and Zemax simulation

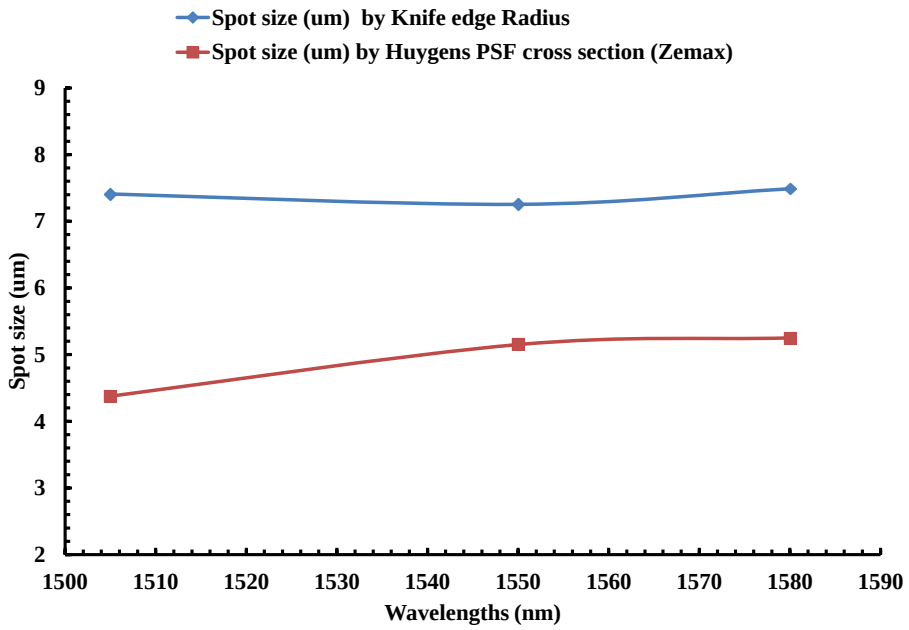

Figure 7.14 Plot of the spot sizes along lateral direction (X) using knife edge experiment and Zemax simulation

7.4.3 UASF target resolution test

USAF target resolution test provides another method of characterizing the optical resolution of the probe system. The target consists of black bars of precisely defined width and spacings

from big to small defined in groups on the resolution target (Figure 7.15(a)). The smallest of these elements for which the microscope probe can just differentiate between two bars, for which the intervening space is thus barely still detectable, is an indicative of the usable resolution of the probe. The usable resolution can be determined by analysing the intensity modulation obatined by scanning the laser beam onto the lithographically imprinted structures on the test target.

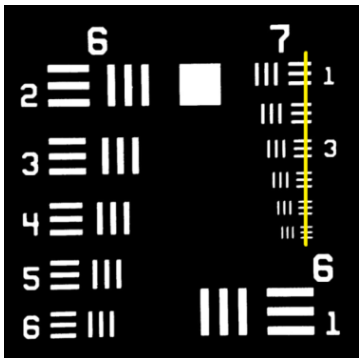

USAF 1951 Resolution Target (Elements)	Group 6 Size (um)	Group 7 Size (um)
1	7.81	3.90
2	6.96	3.47
3	6.20	3.11
4	5.52	2.76
5	4.90	2.46
6	4.39	2.19

Figure 7.15 (a) The image of the USAF test target (L), (b) Size chart of group 6 and 7(R)

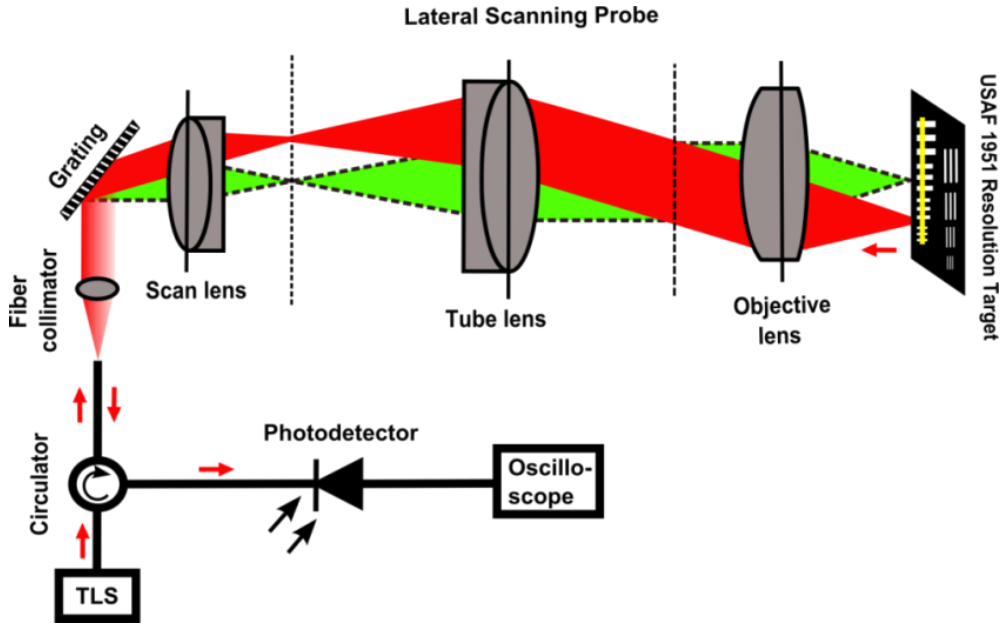

Figure 7.16 Optical setup for intensity modulation measurement with the USAF 1951 resolution target

The light output from the tuneable laser was coupled into the input end of the circulator. The output from the circulator was collimated using the fibre collimator (Throlabs TC06APC-1550) and transmitted into the lateral scanning probe system (Figure 7.16). The resolution test target was placed at the focus plane of the objective and aligned properly such that the reflected rays off the target is coupled back into the probe system through the collimator and directed into third output port of the collimator. A high speed photo-detector was used to detect the reflected

intensity modulation signal from the test target and displayed using the Tektronix DPO 2014 oscilloscope. Data acquisition was done by the USB interface of the oscilloscope.

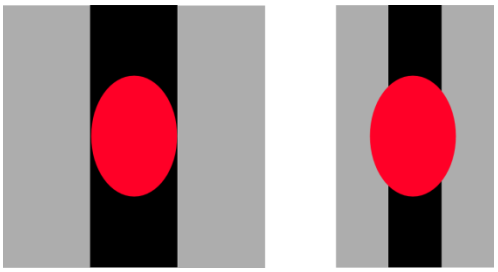

Figure 7.17 Beam spot size overlap on the imprinted lines on the USAF target

The intensity change was measured along the vertical lines of a group 6 and 7. Figure 7.17 shows the beam spot size overlap onto the line of different widths. The black region is the reflective region while the other is transparent. If the beam size is smaller than the structure width, all of the intensity will be reflected back into the system and the signal will reach the maximum value while in tranparent region all the light bypasses and hence a minima is reached.

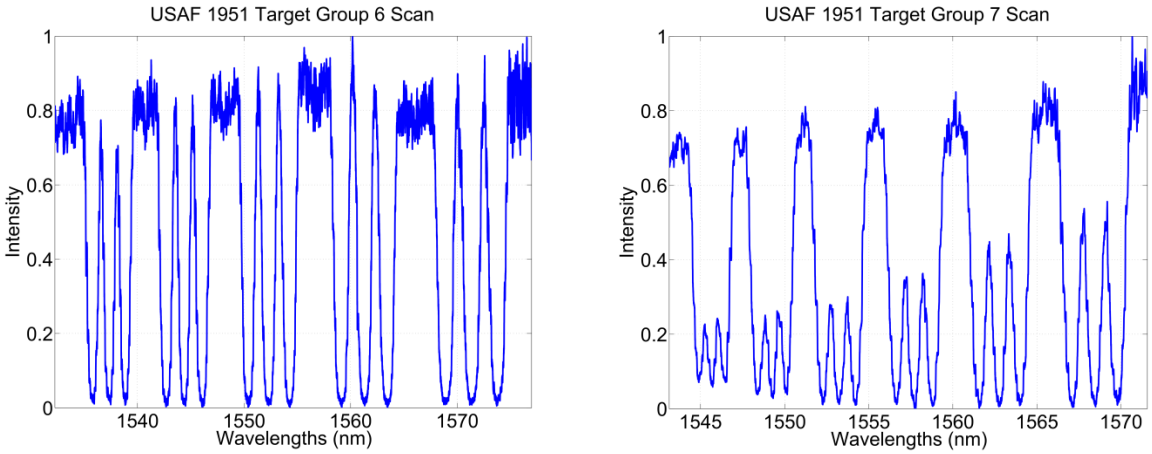

Figure 7.18 Intensity change measured along the vertical line passing through elements of group 6 (L), and group 7 (R)

Figure 7.18 is an intensity modulation plot of the group 6 and 7 scan. In figure 7.18 (a) the reflected intensity reaches maximum level which suggests that the spot size of the beam lies well within the width of the imprinted structure and implies well resolvable points. Figure 7.18 (b) shows the group 7 scan where the width of line gets smaller from right to left down to 2.19 um. The 1st peak from right end has the line width of 3.9 um where intensity of the reflected beam falls to almost half of maximimum intensity. This means the beam now is bigger than the the line width and overlaps on either side in the transparent region leading to intensity loss. Although other structures are detectable and can be seen in the plot but 50% intensity loss will be a

reasonable assumption for well resolved nearby points. Considering this element 1 of group 7 is easily resolvable which confirms and validates the theoretical resolution and resolution estimated by knife edge test.

7.5 Surface profile measurement

This section details the perfromance evaluation of the lateral scanning probe by its implementation to the measurement of a standard step height sample.

7.5.1 Apparatus

The current state of development of the hybrid photonic unit is shown in Fig. 7.19. At present it consists of a tunable laser module, mounted upon a photonic light wave circuit (PLC) which acts as a 'motherboard' containing a waveguide structure to couple the light out to an optical fibre and a photodetector to provide trigger signal for the acquisition of interference signal.

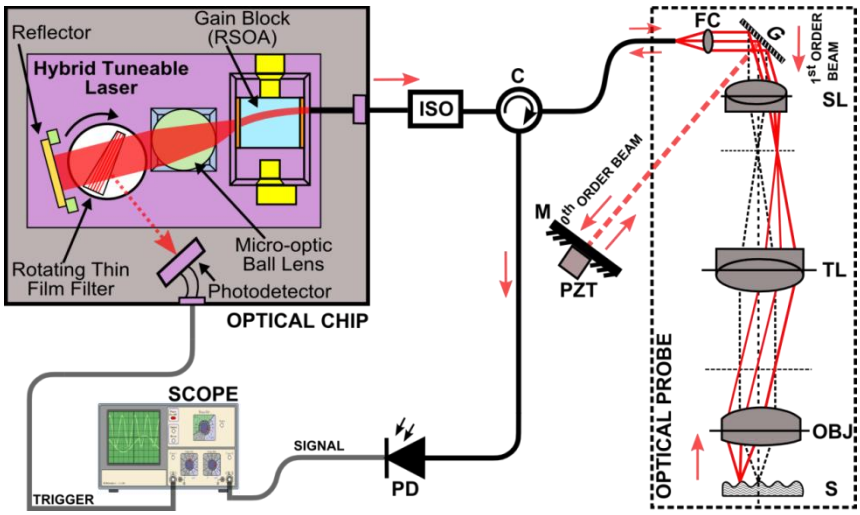

Figure 7.19 Schematic of the scanning probe system with hybrid tuneable laser. Black line – Fibre/Waveguide, Brown – Electrical line.(ISO -Isolator, C - Circulator, FC - Fibre collimator, G - Grating, SL - Scan lens, TL - Tube lens, OBJ - Objective lens, S - Sample, M - Mirror, PD – Photodetector)

In this system the light from the tunable laser source is passed through an optical isolator after which it is coupled into the optical probe of the system through a fibre optic circulator and a collimator. The 0^{th} order beam reflected off the grating was taken as the reference beam. The 1^{st} order beam forms the measurement arm and propagates through the lateral scanning probe to the sample. The two beams are coupled back into the fibre and via a circulator is made incident on a photodetector . Variations in surface height changes the distance travelled by 1st order beam and

hence changes the phase at the recombination point. The changing phase introduces intensity variation of the interfered light beam and is given by,

$$I = 2I_o[1+\mathrm{V}\cos(\delta)] \tag{7.15}$$

The surface profile is thus inferred from the interference intensity signal. A Carre algorithm will be implement for phase calculations and hence requires four phase shifted interferenmce signal. If $\phi(x)$ is the original phase at a sampled point x on the surface and the phase is altered by four equal steps $-3\alpha,-\alpha,+\alpha,3\alpha$ around this point then four intensity values are obtained. The four intensity values are $I_1(x), I_2(x), I_3(x)$ and $I_4(x)$ respectively. These intensities can be solved using Carre algorithm to obtain the phase value.

$$\phi(x) = \tan^{-1}\sqrt{\frac{\left(3I_2(x)-3I_3(x)-I_1(x)+I_4(x)\right)\left(I_1(x)+I_2(x)-I_3(x)-I_4(x)\right)}{\left(I_1(x)-I_2(x)-I_3(x)+I_4(x)\right)^2}} \tag{7.16}$$

For synchronous data acquisition a photodiode is mounted onto the optical chip to pick a portion of reflected beam from the TFF to be used for trigger signal. The data is acquired through the oscilloscope and post processed into Matlab to obtain the measurement results.

7.5.2 Measurement result

To attest the feasibility of the developed optical scanning probe for surface profilometry a measurement experiment was performed on a standard calibrated NPL artefact step height sample. Fig. 7.20 shows the 2-D crossectional profile of the step height sample measured by Taylor Hobson CCI instrument (5x Objective lens). The measured step height of the sample was found to be ~107nm.

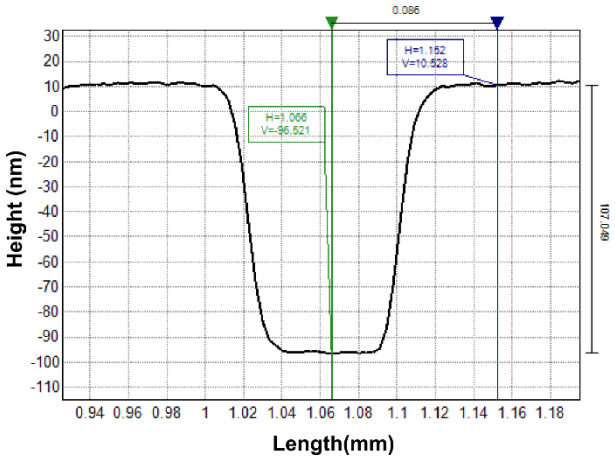

Figure 7.20 Standard NPL artefact sample cross-section profile

The lateral scanning probe was implemented for the measuremnt of the above sample in combination to the hybrid tuneable laser. Four phase shifted interferograms were recorded and is shown in figure 7.21. In order to shift the phase a piezoelectric transducer (PZT P-840, Physik Instrumente) was attached to the mirror in the reference arm and was controlled by computer to provide sufficient voltage required for the phase shifts. Phase shifting interferometry was implemented to retrieve the phase information from the recorded set of interferograms. Phase ambiguity corrections were done to obtain phase over the full 2π range by examining the sign of the quantities proportional to $\sin\varphi$ and $\cos\varphi$ ensuring calculated phase is placed in correct quadrants.

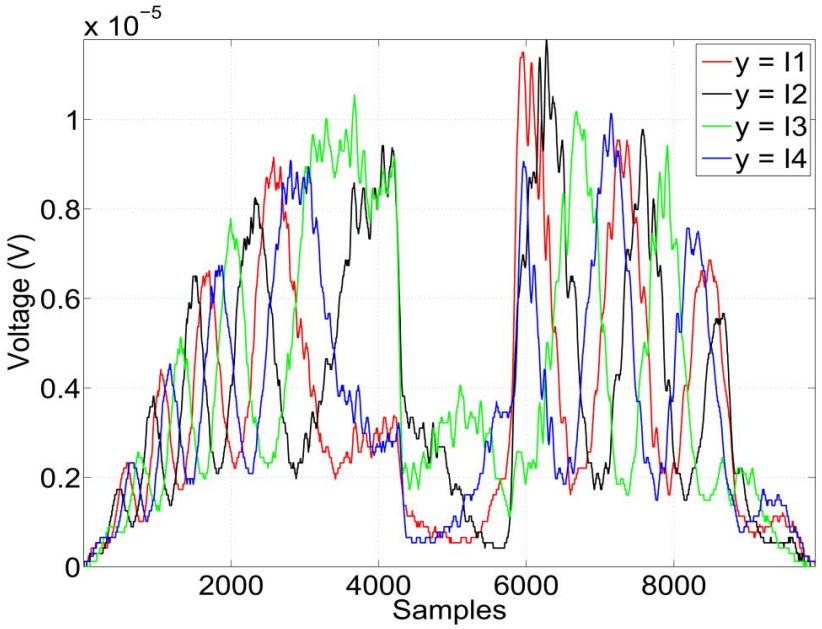

Fig. 7.21 Four phase shifted interferogram signals

The obtained phase is then unwrapped to get the final phase value which was used for the calculation of the height. Figure 7.22 shows the the profile of the same step height measured using the lateral scanning scanning probe. The step height obtained is ~108.49nm. Although higher level of noise is observed in scanning probe measurement output but it shows overall good correlation with the values obtained with the commercial Taylor Hobson profilometer.

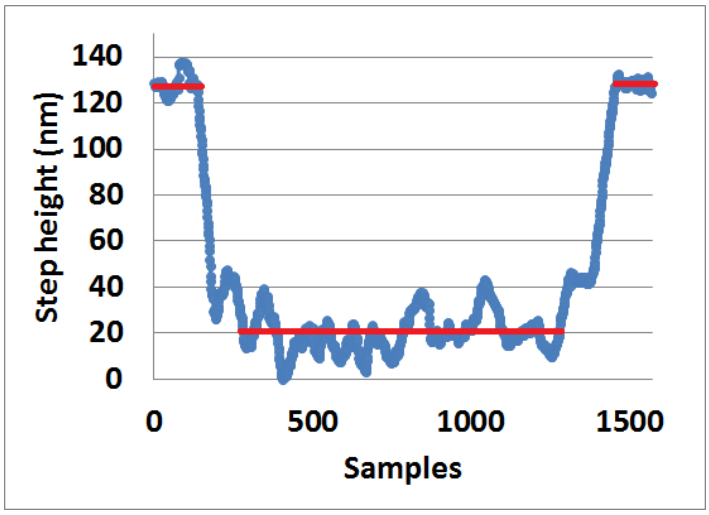

Figure 7.22 Step height measured by lateral scanning probe

7.6 Summary

In summary, spectrally encoded lateral scanning probe for the metrology sensor system is presented. Various types of bulk optic and fibre based laser beam scanning confocal probing system for beam scanning in orthogonal directions onto the object plane has been reviewed. Most of the approaches used mechanical scanners and because of the mass and configuration of the elements beam scanning becomes very complex and fairly slow. Lateral scanning optical probe for embedded metrology sensor utilizeses a rapid wavelength scanning source and optical probe consisting of dispersive optical element. The use of dispersive element alleviates the need of mechanical scanners making it simpler and faster in operation.

Further the Zemax optical design software was used to simulate a compact design and beam profile characterization of a lateral scanning optical probe. Investigation on beam folding techniques using mirror or prism pair combinations was performed to obtain a compact probe size. The beam profile characteristics show that the diffraction limited imaging performance can be achieved in all the designs covering the entire illumination spectrum. The design used a wide aperture collimating lens minimize the fibre pinhole effect which reduces the depth of focus allowing maximum light reflected collection from the test surface. A bench top prototype design is obtained using a suitable optical cage mounting system. Initial characterization of the lateral scanning probe was performed using the knife edge experiment and the USAF resolution test target. Experimental investigations were performed to evaluate the actual capability of the optical probe system for surface measurement applications by measurment of a calibrated standard step height sample.

8 Discussion and Conclusion and Future Work

8.1 Discussion

In manufacturing proper quality management and process control is highly required for the manufacture of high quality products. To support this, manufacturing metrology must be developed to keep pace with the demands of modern manufacturing. Ongoing evolution in high precision manufacturing and miniaturization of components is driving more towards adopting metrology in the manufacturing environment. Metrology in manufacturing environment will provide holistic measurement with economic benefits by improving speed and cost of measurements. But these systems must be versatile, reliable and easy to setup and must be capable of providing online measuremnt in difficult conditions in the production line. Also the small size of the metrology will provide greater autonomy in performing online measurements. One potential technology that the holds promise for improving the current state-of-the-art in the online measurement of surfaces is hybrid photonic integration. This technique provides the integration of individual optoelectronic components onto silicon daughter boards which are then incorporated on a silica motherboard containing waveguides to produce a complete photonic circuit to make up the extremely compact and robust measurement system. Several micro-displacements sensors have been demonstrated by miniaturizing interferometric functions on an integrated optical chip confirming the applicability of such a technology for the development of online metrology sensors. This brought up the idea of developing a miniaturised non-contact metrology sensor system capable of providing quantitative assesment of surfaces enabling the creation of manufacturing environment based measurement technology.

The sensor system consists of two parts; optical chip and an optical probe. The optical chip integrates interferometric function with other essential components such as tuneable laser, reference laser, directional coupler, phase shifting unit, wavelength encoder unit and a spiral waveguide for path length compensation. For device integration onto the chip two common integration schemes are monolithic and hybrid integration. Monolothic integration uses a single substrate material for all devices and hence the performance trade off is met integrating devices onto the same wafer. Hybrid integration technique has the added advantage as it allows integration of various sub–components and devices (passive and active both) reaching their

performance targets required for a particular application and can be easily bonded to the motherboard. Device packaging and assembly onto the optical chip is the most costly affair in the develoment of a device and hence proper techniques are required to be implemented to achieve cost effective assembly of components. The developmental strategy of the metrology sensor system adopted hybrid integration technology combined with passive alignment assembly techniques for integration and packing of individual components onto the optical chip. The material system used was silica-on-silicon to obtain low propagation loss in the photonic circuit. The waveguide was fabricated using FHD and RIE techniques. Integration of active components such as tuneable laser, photodiodes etc was very challenging as it involved multiple integration steps. The developed tuneable laser has a external cavity configuration containing a multi-layer thin film filter within the cavity which is rotated to select the longitudinal mode at which the laser operates and provides wavelength scanning. The TFF was rotated using a penny size rotary motor incorporating an encoder in the package. The tuneable laser is a critical component and determines the overall perfromance of the device. The hybrid chip contains a wavelength encoder and real time wavelength monitoring can be obtained by tapping a portion of tuneable laser beam into this unit . There is a reference fixed wavelength laser whose output is multiplexed with the tuneable laser into the interferometer system to track and compensate any unwanted phase disturbance experienced by the system. Wavelength encoder unit is actually an unbalanced MZI 90 degree hybrid which outputs four phase shifted signals and was demodulated to retrieve the wavelength information. The measurement principle of the metrology sensor device is based on wavelength scanning and phase shifting interferometry. RSOA's in conjunction with 1X5 MMI's can be used to obtain high speed phase shifting in the chip interferometer system. Spiral wavegide is fabricated for optical path length compensation to operate the interferometer system in balanced configuration. The signal detection unit seperates the measurement signal and the reference signal using a optical filter integrated onto the chip. These signlas are detected by array of p-i-n photodetectors attached to the optical chip.

There are two possible probe types which are dependent on one of two possible measurement modes: a) single point absolute distance probe b) the lateral scanning probe. Being a separate entity, optical probes together with the optical chip will determine the overall size of the metrology sensor system. The optical probe is attached to the measurement arm of the interferometer system. There is a possibility of significantly reducing the size of the probe using

beam folding techniques. Also significant size reduction can be achieved by a more customised design of grating and lenses for both the probe types. The single point scanning probe has a simple configuration. It consists of a single lens system. The lateral scanning probe consists of grating element and lens system which determines the lateral resolution of the measurement system. The design of the probe was based on the laser scanning microscopy to create an optical stylus to scan surfaces under test.

Investigations were performed on hybrid metrology sensor in two measurement modes; absolute distance and lateral scanning. Absolute distance measurement mode was based on wavelength scanning onto a single point via optical probe. Two interferometer configurations were used depending upon the nature of measurement. For transparent glass slides thickness measurements, the slides itself formed Fizeau interferometer while for surface profile measurements a Michelson interferometer was required. By scanning the wavelength absolute distances was determined using Fourier Transform interferometry. The major issue with the Fourier transform technique was its susceptibility to the non-linearity of the wavelength scan leading inaccurate phase measurement results. This was overcome by the use of a reference cavity which cancelled out the effect of non-linear tuning. Initially an external glass slide was chosen as a reference cavity but later investigations were performed to leverage the use of signal output from integrated wavelength encoder unit. This measurement mode can provide measurement from tens of microns to several millimetres with greater repeatability. Surface profile measurements were also performed on standard step height specimens to verify the potential of this method for practical application.

A second lateral scanning measurement mode was investigated using a dispersive optical probe based on laser scanning microscopy to create an optical stylus to scan the surface profile. Zemax optical design software was used to simulate a compact design and beam profile characterization of a lateral scanning optical probe. Two other probe design using mirror and prism pair combinations are investigated to provide probe a compact configuration to compliment the miniaturised metrology sensor system. A bench top prototype was obtained using a suitable optical cage mounting system. Initial characterization of the lateral scanning probe was performed using the knife edge experiment and the USAF resolution test target. Once the probe design was optimised the optical stylus was scanned onto the test sample and height information was determined using phase shifting interferometry. The lateral resolution of the

system was diffraction limited where as the axial resolution is sub-nanometer and is inherently due to the interferometry. The maximum measurement range of the sensor system in this measurement mode is λ/4~400 nm and is limited by the phase shifting interferometry. The outcome of the research work carried out in this thesis is to validate the feasibility of a hybrid photonics based non-contact metrology device for embedded metrology applications. But like anything there is always room for improvement that can be made to the metrology device to improve the existing devices and its performance and are discussed in the following section.

8.2 Future work

This section discusses various things needs to be carried out for further improvement in the metrology sensor device making it suitable for nano-scale online surface measurement.

- The prototype tuneable laser has not fully reached the performance target in terms of its tuning range. By the optimising TFF design and the shifting the central wavelength maxima to little longer wavelength a full bandwidth of ~100 nm can be easily achieved. The penny motor tuning needs optimisation in terms of motor control parameters. Also the optical encoder unit is to be investigated to evaluate its performance of the in terms of bandwidth and wavelength uncertainty.
- Phase shifting unit comprising of 1X5 MMI's and an array of RSOA is to be investigated in terms of gain profiles, power loss and noise characteristics. Once optimised this phase shifting unit is implemented for the surface profile measurement using phase shifting interferometry.
- Investigate methods of supressing ripples in the reference path of signal detection unit to obtain a flat photodetector response with clean cut-off over the entire wavelength scanning range of hybrid tuneable laser.
- Build and evaluate bench top optical probe prototypes using folding mirrors or prism pair using a suitable optical cage mounting to give lateral scanning probe a compact configuration. Similarly for the single point probes more optimal designs in terms of lateral resolution overall probe size needs to be performed. It would also be beneficial to look out for possible miniature probe design alternatives with the Gradient Index Optics technology. This will substantially reduce the single point probe from size.

- Suitable artefacts to be acquired and/or manufactured to test the key aspects of the two measurement modes in terms of vertical range/resolution, uncertainty, repeatability, slope angle, speed etc. A suite of measurements to be taken and evaluated on a variety of artefacts to indicate the potential of the finalised hybrid photonic device and probe combination for real world application.

Long term plan:

- Current version of the hybrid external cavity laser has alignment complexities and is also labour intensive. Different components are either glued by epoxy or soldered. All these bring up issues with device reliability and its performance. So tuneable laser design based on monolithically integrated fast and digitally tuned wavelength tuneable semiconductor ring laser would be a potential alternative. Investigations are needed to confirm its suitability to for the development of next generation chip interferometer device.
- Current version of the hybrid chip has an external bulk isolator. To make the system more compact the isolator requires on chip integration. The integrated isolator design to achieve desired functionality has to be investigated.

9 Conclusion

A novel hybrid photonic interferometer device for embedded metrology applications has been investigated. The aim was develop a miniaturised non-contact online metrology sensor system capable of executing absolute distance and surface profile measurements at micro and nano-scale level respectively.

The two operating modes of the metrology sensor system; single point and lateral scanning are based on wavelength scanning interferometry. In single point the entired wavelength of a broadly tuneable laser is scanned onto a single point onto the sample. This doesnot requires any mechanical movement and interference signals are produced by wavelength scan of tuneable laser which is further porcessed using Fourier transform technique to obtain the absolute distance measurements. In the lateral scanning mode wavlength scanning combined with dispersive optical stylus sweeps the beam across the sample. A set of interferene fringes are obtained for each wavelength scan with incermental phase shifts and the height information is determined using phase shifting interferometry using suitable algorithm.

The sensor system and individual devices such as wavelength encoder unit, signal detection unit and tuneable laser, which are developed separately and tested. The wavelength encoder unit appears operable and but there is significant amount of relative phase error observed between the output signal and should be addressed in later versions. The signal detection unit is operational and the measurement signal path is working well except some ripples observed in reflected reference signal in the stop band. The older version of the chip tuneable laser with the squiggle motor was tested showed issues with the laser tuning behaviour. An improved tuning mechanism is proposed using penny motor to provide smoother and continuous operation of thin film rotation.

The absolute distance measurement instrument was demonstrated which could sucessfully measure tens of microns to several millimetres with very good repeatability. Measurements were perfromed to measure glass slides of different thicknesses and surface profile of a standard step height sample by scanning the sample.

Further the lateral scanning probe was developed and investigated for surface profile measurement application. The beam scanning was performed by the use of a dispersive grating which made probe configuration very simple compared to the mechanical scanners. Initial Probe design and simulation were performed using Zemax optical design software. Further

characterization of the lateral scanning probe was performed emperically. A bench top prototype was developed using a suitable optical cage mounting system. Experimental investigations were performed to evaluate the actual capability of the optical probe system for surface measurement applications.

Publications and Awards

Refereed Journal Papers

Martin, H., Kumar, P. and Jiang, X. (2014) 'A hybrid photonics based sensor for surface measurement' CIRP Annals - Manufacturing Technology , 63 (1), pp. 549-552. ISSN 0007-8506

Refereed Conference Papers

Kumar, P., Martin, H., Maxwell, G. and Jiang, X. (2014) 'Hybrid photonic chip interferometer for embedded metrology'. In: Proceedings of SPIE: Integrated Optics: Devices, Materials, and Technologies XVIII. California, USA: SPIE. p. 89880N.

Non-refereed Conference Papers

Kumar, P., Martin, H., Maxwell, G. and Jiang, X. (2013) 'Design of a dispersive lateral scanning surface profilometer'. In: Proceedings of Computing and Engineering Annual Researchers' Conference 2013 : CEARC'13. Huddersfield: University of Huddersfield. pp. 159-164. ISBN 9781862181212

Kumar, P., Martin, H., Maxwell, G. and Jiang, X. (2012) 'Design and development of a self calibrated optical chip interferometer for high precision on-line surface measurement'. In: Proceedings of The Queen's Diamond Jubilee Computing and Engineering Annual Researchers' Conference 2012: CEARC'12. Huddersfield: University of Huddersfield. p. 152. ISBN 978-1-86218-106-9

Awards

Kumar, P., 1st prize winner at 'Computing and Engineering Annual Researchers Conference' 2013, University of Huddersfield.

Kumar, P., 3rd prize winner at 'Research Festival 2012' poster competition, University of Huddersfield.

Bibliography

Alferov, Z. (2000). Double heterostructure lasers: early days and future perspectives. *IEEE Journal of Selected Topics in Quantum Electronics, 6*(6), 832-840.

Alferov, Z. I. (2000). The double heterostructure: concept and its applications in physics, electronics and technology. *Nobel Lecture, 413*.

Ali, S. H. (2012). Advanced nanomeasuring techniques for surface characterization. *ISRN Optics, 2012*.

Alvarez, I., Enguita, J. M., Marina, J., & Fraga, C. (2008). On-line submicron profile measurements from safe distances with conoscopic holography: feasibility and potential problems. *Optical Engineering, 47*(2), 023602-023602-023608.

Armiento, C. A., Negri, A., Tabasky, M., Boudreau, R., Rothman, M., Fitzgerald, T., & Haugsjaa, P. (1992). Gigabit transmitter array modules on silicon waferboard. *Components, Hybrids, and Manufacturing Technology, IEEE Transactions on, 15*(6), 1072-1080.

Bagley, M., Sherlock, G., Cooper, D. M., Westbrook, L. D., Elton, D. J., Wickes, H. J., . . . Devlin, W. J. (1990). Broadband operation of InGaAsP-InGaAs GRIN-SC-MQW BH amplifiers with 115 mW output power. *Electronics Letters, 26*(8), 512-513. doi: 10.1049/el:19900333

Baillard, X., Gauguet, A., Bize, S., Lemonde, P., Laurent, P., Clairon, A., & Rosenbusch, P. (2006). Interference-filter-stabilized external-cavity diode lasers. *Optics Communications, 266*(2), 609-613.

Balasubramanian, N. (1982). Optical system for surface topography measurement: Google Patents.

Basov, N., Eliseev, P., & Popov, Y. M. (1986). Semiconductor lasers. *Physics-Uspekhi, 29*(1), 20-30.

Bassous, E. (1978). Fabrication of novel three-dimensional microstructures by the anisotropic etching of (100) and (110) silicon. *IEEE Trans. Electron Devices, 25*(10), 1178-1185.

Bauters, J. F., Davenport, M. L., Heck, M. J., Doylend, J., Chen, A., Fang, A. W., & Bowers, J. E. (2013). Silicon on ultra-low-loss waveguide photonic integration platform. *Optics Express, 21*(1), 544-555.

Beling, A., & Campbell, J. C. (2009). InP-based high-speed photodetectors. *Journal of lightwave technology, 27*(3), 343-355.

Bendat, J. S., & Piersol, A. G. (2011). *Random data: analysis and measurement procedures* (Vol. 729): John Wiley & Sons.

Benisty, H., Sotomayor-Torres, C., & Weisbuch, C. (1991). Intrinsic mechanism for the poor luminescence properties of quantum-box systems. *Physical Review B, 44*(19), 10945.

Bennett, J. M. (1992a). *Overview: sensitive techniques for surface measurement and characterization.* Paper presented at the Commercial Applications of Precision Manufacturing at the Sub-Micron Level.

Bennett, J. M. (1992b). Recent developments in surface roughness characterization. *Measurement Science and Technology, 3*(12), 1119.

Bhattacharya, P., & Hall, P. (1994). *Semiconductor optoelectronic devices* (Vol. 2): Prentice Hall Upper Saddle River, NJ, USA:.

Bhattacharya, P., Kamath, K. K., Singh, J., Klotzkin, D., Phillips, J., Jiang, H.-T., . . . Laskar, J. (1999). In (Ga) As/GaAs self-organized quantum dot lasers: DC and small-signal modulation properties. *Electron Devices, IEEE Transactions on, 46*(5), 871-883.

Binh, L. N. (2008). *Photonic signal processing: techniques and applications*: CRC Press.
Blunt, L., & Jiang, X. (2003). *Advanced Techniques for Assessment Surface Topography*: Kogan Page Ltd, London, UK.
Boudoux, C., Yun, S., Oh, W., White, W., Iftimia, N., Shishkov, M., . . . Tearney, G. (2005). Rapid wavelength-swept spectrally encoded confocal microscopy. *Optics Express, 13*(20), 8214-8221.
Bowers, J. E., & Burrus Jr, C. A. (1987). Ultrawide-band long-wavelength pin photodetectors. *Lightwave Technology, Journal of, 5*(10), 1339-1350.
Boyd, J., & Sriram, S. (1978). Optical coupling from fibers to channel waveguides formed on silicon. *Applied Optics, 17*(6), 895-898.
Bruzzone, A., Costa, H., Lonardo, P., & Lucca, D. (2008). Advances in engineered surfaces for functional performance. *CIRP Annals-Manufacturing Technology, 57*(2), 750-769.
Bryzek, J., Peterson, K., & McCulley, W. (1994). Micromachines on the march. *Spectrum, IEEE, 31*(5), 20-31.
Bunshah, R. F. (1990). Critical issues in plasma-assisted vapor deposition processes. *Plasma Science, IEEE Transactions on, 18*(6), 846-854.
Carré, P. (1966). Installation et utilisation du comparateur photoélectrique et interférentiel du Bureau International des Poids et Mesures. *Metrologia, 2*(1), 13.
Cha, I., Kitamura, M., Honmou, H., & Mito, I. (1989). 1.5 μm band travelling-wave semiconductor optical amplifiers with window facet structure. *Electronics Letters, 25*(18), 1241-1242.
Chen, R. T., Li, B., Foshee, J. J., Hartman, W. B., & Tang, S. (2000). Polymer-based optical waveguide devices speed connections. *Laser focus world, 36*(8), 139-176.
Cheng, Y.-Y., & Wyant, J. C. (1984). Two-wavelength phase shifting interferometry. *Appl. Opt., 23*(24), 4539-4543.
Chow, W. W., & Koch, S. W. (1999). *Semiconductor-Laser Fundamentals: Physics of the Gain Materials*: Springer Science & Business Media.
Cohen, M., Cina, M., Bassous, E., Oprysko, M., & Speidell, J. (1991). Passive laser-fiber alignment by index method. *Photonics Technology Letters, IEEE, 3*(11), 985-987.
Coleman, J. J., Young, J. D., & Garg, A. (2011). Semiconductor quantum dot lasers: a tutorial. *Lightwave Technology, Journal of, 29*(4), 499-510.
Conroy, M., & Armstrong, J. (2005). *A comparison of surface metrology techniques.* Paper presented at the Journal of Physics: Conference Series.
Coquin, G., & Cheung, K. (1988). Electronically tunable external-cavity semiconductor laser. *Electronics Letters, 24*(10), 599-600.
Creath, K. (1987). Step height measurement using two-wavelength phase-shifting interferometry. *Applied Optics, 26*(14), 2810-2816.
Creath, K. (1988). Phase-measurement interferometry techniques. *Progress in optics, 26*(26), 349-393.
Crookes, C. (1994). *Silica waveguide to photodiode interface for hybrid integration.* Paper presented at the Planar Silicon Hybrid Optoelectronics (Digest No. 1994/198), IEE Colloquium on.
Dabbs, T., & Glass, M. (1992). Fiber-optic confocal microscope: FOCON. *Applied Optics, 31*(16), 3030-3035. doi: 10.1364/ao.31.003030
Davidson, M., Kaufman, K., & Mazor, I. (1987). The coherence probe microscope. *Solid State Technology, 30*(9), 57-59.

de Araújo, M. A., Silva, R., de Lima, E., Pereira, D. P., & de Oliveira, P. C. (2009). Measurement of Gaussian laser beam radius using the knife-edge technique: improvement on data analysis. *Applied Optics, 48*(2), 393-396.

De Chiffre, L., Kunzmann, H., Peggs, G. N., & Lucca, D. A. (2003). Surfaces in Precision Engineering, Microengineering and Nanotechnology. *CIRP Annals - Manufacturing Technology, 52*(2), 561-577. doi: 10.1016/s0007-8506(07)60204-2

De Merlier, J., Mizutani, K., Sudo, S., Naniwae, K., Furushima, Y., Sato, S., . . . Kudo, K. (2005). Full C-band external cavity wavelength tunable laser using a liquid-crystal-based tunable mirror. *Photonics Technology Letters, IEEE, 17*(3), 681-683.

Delaney, P. M., Harris, M. R., & King, R. G. (1994). Fiber-optic laser scanning confocal microscope suitable for fluorescence imaging. *Applied Optics, 33*(4), 573-577.

Deri, R. J., & Kapon, E. (1991). Low-loss III-V semiconductor optical waveguides. *Quantum Electronics, IEEE Journal of, 27*(3), 626-640.

Dickensheets, D., & Kino, G. (1996). Micromachined scanning confocal optical microscope. *Optics Letters, 21*(10), 764-766.

Ding, Y., Kan, Q., Wang, J.-l., Pan, J.-q., Zhou, F., Chen, W.-x., & Wang, W. (2007). Broad-band semiconductor optical amplifiers. *Journal of Luminescence, 122-123*, 208-211. doi: 10.1016/j.jlumin.2006.01.094

Doerr, C. R. (2013). *Highly integrated monolithic photonic integrated circuits.* Paper presented at the Optical Communication (ECOC 2013), 39th European Conference and Exhibition on, vol., no.

Dong, P., Xie, C., & Buhl, L. L. (2014). Monolithic polarization diversity coherent receiver based on 120-degree optical hybrids on silicon. *Optics Express, 22*(2), 2119-2125.

Duan, L. N., & Zhao, J. (2014). Design of Control System of Brushless DC Motor Based on DSP. *Applied Mechanics and Materials, 496*, 1417-1421.

Dupuis, R. D. (1987). Special issue papers: An introduction to the development of the semiconductor laser. *IEEE Journal of Quantum Electronics, 23*(6).

Edge, C., Ash, R., Jones, C., & Goodwin, M. (1991). Flip-chip solder bond mounting of laser diodes. *Electronics Letters, 27*(6), 499-501.

Eliseev, P. G., & Van Luc, V. (1995). Semiconductor optical amplifiers: Multifunctional possibilities, photoresponse and phase shift properties. *Pure and Applied Optics: Journal of the European Optical Society Part A, 4*(4), 295.

Enguita, J. M., Álvarez, I., Frade, M., & Marina, J. (2010). Common-path two-wavelength interferometer with submicron precision for profile measurements in on-line applications. *Optical Engineering, 49*(2), 023602-023602-023608.

Estevez, M. C., Alvarez, M., & Lechuga, L. M. (2012). Integrated optical devices for lab-on-a-chip biosensing applications. *Laser & Photonics Reviews, 6*(4), 463-487. doi: 10.1002/lpor.201100025

Fleming, M., & Mooradian, A. (1981). Spectral characteristics of external-cavity controlled semiconductor lasers. *Quantum Electronics, IEEE Journal of, 17*(1), 44-59.

Ghatak, A., & Thyagarajan, K. (1998). *An introduction to fiber optics*: Cambridge university press.

Ghim, Y.-S., Suratkar, A., & Davies, A. (2010). Reflectometry-based wavelength scanning interferometry for thickness measurements of very thin wafers. *Optics Express, 18*(7), 6522-6529.

Glombitza, U., & Brinkmeyer, E. (1993). Coherent frequency-domain reflectometry for characterization of single-mode integrated-optical waveguides. *Lightwave Technology, Journal of, 11*(8), 1377-1384. doi: 10.1109/50.254098

Goronkin, H., Von Allmen, P., Tsui, R. K., & Zhu, T. X. (1999). Functional nanoscale devices *Nanostructure Science and Technology* (pp. 67-91): Springer.

Grattan, K. T., & Meggitt, B. (1995). *Optical fiber sensor technology* (Vol. 1): Springer.

Hail, M. K. Construction of a tunable external cavity diode laser with applications to atmospheric dial measurements.

Hall, R., Fenner, G., Kingsley, J., Soltys, T., & Carlson, R. (1962). Coherent light emission from Ga-As junctions. *Phys. Rev. Lett, 9*, 366.

Hänsch, T. (1972). Repetitively pulsed tunable dye laser for high resolution spectroscopy. *Applied Optics, 11*(4), 895-898.

Hebden, J., Delpy, D., & Arridge, S. (1993). Infrared lasers muscle in on medical imaging. *Physics World, 6*(8), 23-24.

Hellesø, O. G., Benech, P., & Rimet, R. (1995). Interferometric displacement sensor made by integrated optics on glass. *Sensors and Actuators A: Physical, 47*(1), 478-481.

Henry, C. H., Blonder, G., & Kazarinov, R. (1989). Glass waveguides on silicon for hybrid optical packaging. *Lightwave Technology, Journal of, 7*(10), 1530-1539.

Higurashi, E. (2008). Low temperature bonding for optical microsystems applications. *ECS Transactions, 16*(8), 93-103.

Higurashi, E., & Sawada, R. (2002). *An integrated Fizeau-type interferometric displacement sensor for a feedback-controlled actuation system.* Paper presented at the Micro Electro Mechanical Systems, 2002. The Fifteenth IEEE International Conference on.

Himeno, A. (1999). *Silica-based planar lightwave circuits.* Paper presented at the MRS Proceedings.

Hoffmann, M., Kopka, P., & Voges, E. (1997). Low-loss fiber-matched low-temperature PECVD waveguides with small-core dimensions for optical communication systems. *Photonics Technology Letters, IEEE, 9*(9), 1238-1240.

Hu, J., Feng, N.-N., Carlie, N., Petit, L., Wang, J., Agarwal, A., . . . Kimerling, L. (2007). Low-loss high-index-contrast planar waveguides with graded-index cladding layers. *Optics Express, 15*(22), 14566-14572.

Huang, W.-P. (1994). Coupled-mode theory for optical waveguides: an overview. *JOSA A, 11*(3), 963-983.

Hunsperger, R. G. (1984). *Integrated optics: theory and technology* (Vol. 2): Springer.

Hunziker, W., Vogt, W., Melchior, H., Germann, R., & Harder, C. (1996, 28-31 May 1996). *Low cost packaging of semiconductor laser arrays using passive self-aligned flip-chip technique on Si motherboard.* Paper presented at the Electronic Components and Technology Conference, 1996. Proceedings., 46th.

Hunziker, W., Vogt, W., Melchior, H., Leclerc, D., Brosson, P., Pommereau, F., . . . Fillion, T. (1995). Self-aligned flip-chip packaging of tilted semiconductor optical amplifier arrays on Si motherboard. *Electronics Letters, 31*(6), 488-490.

Iiyama, K., Lu-Tang, W., & Hayashi, K. (1996). Linearizing optical frequency-sweep of a laser diode for FMCW reflectometry. *Lightwave Technology, Journal of, 14*(2), 173-178. doi: 10.1109/50.482260

Ilev, I. K., & Waynant, R. W. (2000). A simple submicron confocal microscope with a fiberoptic output. *Review of Scientific Instruments, 71*(11), 4161-4164.

Infinera. (2013). Photonics Integrated Circuits.

Inokuchi, M., Ando, H., Kinosita, M., Akase, K., Higurashi, E., & Sawada, R. (2009). *Development of a micro displacement sensor with monolithic-integrated two-dimensionally distributed photodiodes.* Paper presented at the Optical MEMS and Nanophotonics, 2009 IEEE/LEOS International Conference on.

Ito, T., Sawada, R., & Higurashi, E. (2003). Integrated micro-displacement sensor that uses beam divergence. *Journal of Micromechanics and Microengineering, 13*(6), 942.

Izutsu, M., Enokihara, A., & Sueta, T. (1982). Optical-waveguide microdisplacement sensor. *Electronics Letters, 18*(20), 867-868.

Jackson, K., Flint, E., Cina, M., Lacey, D., Kwark, Y., Trewhella, J., . . . Vettiger, P. (1994). A high-density, four-channel, OEIC transceiver module utilizing planar-processed optical waveguides and flip-chip, solder-bump technology. *Lightwave Technology, Journal of, 12*(7), 1185-1191.

Janocha, H. (2000). *Microactuators-principles, applications, trends.* Paper presented at the Proc. MICRO. tec 2000, VDE World Microtechnology Congress.

Jeong, S.-H., & Morito, K. (2010). Compact optical 90 hybrid employing a tapered 2× 4 MMI coupler serially connected by a 2× 2 MMI coupler. *Optics Express, 18*(5), 4275-4288.

Jiang, X. (2012). *Precision surface measurement* (Vol. 370.1973): Philosophical Transactions of the Royal Society A: Mathematical, Physical and Engineering Sciences.

Jiang, X., Lin, D., Blunt, L., Zhang, W., & Zhang, L. (2006). Investigation of some critical aspects of on-line surface measurement by a wavelength-division-multiplexing technique. *Measurement Science and Technology, 17*(3), 483.

Jiang, X., Scott, P. J., Whitehouse, D. J., & Blunt, L. (2007a). Paradigm shifts in surface metrology. Part I. Historical philosophy. *Proceedings of the Royal Society A: Mathematical, Physical and Engineering Science, 463*(2085), 2049-2070.

Jiang, X., Scott, P. J., Whitehouse, D. J., & Blunt, L. (2007b). Paradigm shifts in surface metrology. Part II. The current shift. *Proceedings of the Royal Society A: Mathematical, Physical and Engineering Science, 463*(2085), 2071-2099.

Jiang, X., Wang, K., Gao, F., & Muhamedsalih, H. (2010a). Fast surface measurement using wavelength scanning interferometry with compensation of environmental noise. *Applied Optics, 49*(15), 2903-2909.

Jiang, X., Wang, K., Gao, F., & Muhamedsalih, H. (2010b). Fast surface measurement using wavelength scanning interferometry with compensation of environmental noise. *Appl. Opt., 49*(15), 2903-2909.

Jiang, X., Wang, K., & Martin, H. (2006). Near common-path optical fiber interferometer for potentially fast on-line microscale-nanoscale surface measurement. *Opt. Lett., 31*(24), 3603-3605.

Jiang, X. J., & Whitehouse, D. J. (2012). Technological shifts in surface metrology. *CIRP Annals - Manufacturing Technology, 61*(2), 815-836. doi: 10.1016/j.cirp.2012.05.009

Jones, C., & Cooper, K. (1996). Hybrid integration onto silicon motherboards with planar silica waveguides. *IEE Proceedings-Optoelectronics, 143*(5), 316-321.

Kapon, E., Simhony, S., Bhat, R., & Hwang, D. (1989). Single quantum wire semiconductor lasers. *Applied Physics Letters, 55*(26), 2715-2717.

Kashyap, R., Ainslie, B. J., & Maxwell, G. D. (1989). Second harmonic generation in GeO₂ ridge waveguide. *Electronics Letters, 25*(3), 206-208. Retrieved from http://digital-library.theiet.org/content/journals/10.1049/el_19890148

Kawachi, M. (1990). Silica waveguides on silicon and their application to integrated-optic components. *Optical and Quantum Electronics, 22*(5), 391-416.

Kazovsky, L. G., Curtis, L., Young, W. C., & Cheung, N. K. (1987). All-fiber 90 optical hybrid for coherent communications. *Applied Optics, 26*(3), 437-439.

Kelly, A., Lealman, I., Rivers, L., Perrin, S., & Silver, M. (1996). Polarisation insensitive, 25 dB gain semiconductor laser amplifier without antireflection coatings. *Electronics Letters, 32*(19), 1835-1836.

Kikuta, H., Iwata, K., & Nagata, R. (1986). Distance measurement by the wavelength shift of laser diode light. *Applied Optics, 25*(17), 2976-2980.

Kim, D.-H., Ilev, I. K., & Kang, J. U. (2008). Fiberoptic Confocal Microscopy Using a 1.55-μm Fiber Laser for Multimodal Biophotonics Applications. *Selected Topics in Quantum Electronics, IEEE Journal of, 14*(1), 82-87.

Kimura, S., & Wilson, T. (1991). Confocal scanning optical microscope using single-mode fiber for signal detection. *Applied Optics, 30*(16), 2143-2150.

Kumar, K., Avritscher, R., Wang, Y., Lane, N., Madoff, D. C., Yu, T.-K., . . . Zhang, X. (2010). Handheld histology-equivalent sectioning laser-scanning confocal optical microscope for interventional imaging. *Biomedical microdevices, 12*(2), 223-233.

Kurata, K., Yamauchi, K., Kawatani, A., Tanaka, E., Honmou, H., & Ishikawa, S. (1996). A surface mount single-mode laser module using passive alignment. *Components, Packaging, and Manufacturing Technology, Part B: Advanced Packaging, IEEE Transactions on, 19*(3), 524-531.

Kuwamura, S., & Yamaguchi, I. (1997). Wavelength scanning profilometry for real-time surface shape measurement. *Appl. Opt., 36*(19), 4473-4482.

Kwon, O. K., Kim, K. H., Sim, E. D., Kim, J. H., & Oh, K. R. (2005). Monolithically integrated multiwavelength grating cavity laser. *Photonics Technology Letters, IEEE, 17*(9), 1788-1790.

Ladouceur, F., & Love, J. D. (1996). *Silica-based buried channel waveguides and devices*: Chapman & Hall.

Lang, T., Genon-Catalot, D., Dandrea, P., Duport, I. S., & Benech, P. (1998). Integrated optical displacement sensor with four quadrature phase-shifted output signals. *Journal of optics, 29*(3), 135.

Last, R. Semiconductor Optical Amplifier Design and Applications.

Lealman, I., Kelly, A., Rivers, L., Perrin, S., & Moore, R. (1998). Improved gain block for long wavelength (1.55 μm) hybrid integrated devices. *Electronics Letters, 34*(23), 2247-2249.

Lee, W. (2005). *Market trends and applications of ultra-precision freeform machining technology.* Paper presented at the Workshop on Design and Fabrication of Freeform Optics for Photonics and Telecommunication Industries, Hong Kong.

Leonhardt, K., Rippert, K.-H., & Tiziani, H. J. (1989). *Optical methods of measuring rough surfaces.* Paper presented at the 1988 Intl Congress on Optical Science and Engineering.

Li, S., Zhu, J., Qin, W., & Chen, Y. (2011). An alignment approach for coupling mounts using a fiber ended micro-lens. *Optoelectronics and Advanced Materials- Rapid Communications, 5*(7), 718-721.

Li, Y. P., & Henry, C. (1996). Silica-based optical integrated circuits. *IEE Proceedings-Optoelectronics, 143*(5), 263-280.

Liang, C., Descour, M., Sung, K.-B., & Richards-Kortum, R. (2001). Fiber confocal reflectance microscope (FCRM) for in-vivo imaging. *Optics Express, 9*(13), 821-830.

Lifante, G. (2003). *Front Matter*: Wiley Online Library.

Lin, L., Lee, S., Pister, K., & Wu, M. (1995). Self-aligned hybrid integration of semiconductor lasers with micromachined micro-optics for optoelectronic packaging. *Applied Physics Letters, 66*(22), 2946-2948.

Littman, M. G. (1978). Single-mode operation of grazing-incidence pulsed dye laser. *Optics Letters, 3*(4), 138-140.

Liu, A., & Zhang, X. (2007). A review of MEMS external-cavity tunable lasers. *Journal of Micromechanics and Microengineering, 17*(1), R1.

Liu, H. (2005). *Packaging of Integrated Optics Devices.* Paper presented at the Integrated Photonics Research and Applications.

Ma, H., Jen, A. K.-Y., & Dalton, L. R. (2002). Polymer-based optical waveguides: materials, processing, and devices. *Advanced materials, 14*(19), 1339-1365.

Ma, S., Quan, C., Zhu, R., Tay, C., Chen, L., & Gao, Z. (2011). Micro-profile measurement based on windowed Fourier transform in white-light scanning interferometry. *Optics Communications, 284*(10), 2488-2493.

Maitland, K. C., Shin, H. J., Ra, H., Lee, D., Solgaard, O., & Richards-Kortum, R. (2006). Single fiber confocal microscope with a two-axis gimbaled MEMS scanner for cellular imaging. *Optics Express, 14*(19), 8604-8612.

Malacara, D. (1990). Phase shifting interferometry. *Chap, 14*, 456-487.

Malacara, D. (2007). *Optical shop testing* (Vol. 59): John Wiley & Sons.

Martin, H., & Jiang, X. (2010). Rapid phase-shifting fiber interferometer with optical stylus. *Opt. Lett., 35*(5), 655-657.

Martin, H. P. (2010). *Investigations into a multiplexed fibre interferometer for on-line, nanoscale, surface metrology.* The University of Huddersfield.

Maxwell, G. (2008). *Hybrid integration technology for high functionality devices in optical communications.* Paper presented at the Optical Fiber Communication Conference.

Maxwell, G., Poustie, A., Ford, C., Harlow, M., Townley, P., Nield, M., . . . Waller, R. (2005). *Hybrid integration of monolithic semiconductor optical amplifier arrays using passive assembly.* Paper presented at the Electronic Components and Technology Conference, 2005. Proceedings. 55th.

McDougall, R. C. (2006). *Hybrid integration for all-optical signal processing devices.* University of Cambridge.

McWhan, D. (2012). *Sand and silicon: science that changed the world*: Oxford University Press.

Ménager, L., Cabaret, L., Lorgeré, I., & Le Gouët, J.-L. (2000). Diode laser extended cavity for broad-range fast ramping. *Optics Letters, 25*(17), 1246-1248.

Miyajima, H., Murakami, K., & Katashiro, M. (2004). MEMS optical scanners for microscopes. *Selected Topics in Quantum Electronics, IEEE Journal of, 10*(3), 514-527.

Moller, B. A., Jensen, L., Laurent-Lund, C., & Thirstrup, C. (1993). Silica-waveguide thermooptic phase shifter with low power consumption and low lateral heat diffusion. *Photonics Technology Letters, IEEE, 5*(12), 1415-1418.

Moore, E. D. (2011). *Advances in swept-wavelength interferometry for precision measurements.* University of Colorado.

Mroziewicz, B. (2008). External cavity wavelength tunable semiconductor lasers - a review. *Opto-Electronics Review, 16*(4), 347-366. doi: 10.2478/s11772-008-0045-9

Muhamedsalih, H. (2013). *Investigation of Wavelength Scanning Interferometry for Embedded Metrology.* University of Huddersfield.

Mulet, J. (2002). Semiconductor laser dynamics: Compound-cavity, polarization and transverse modes.

Nayak, P. R. (1971). Random process model of rough surfaces. *Journal of Tribology, 93*(3), 398-407.

Okamoto, K. (2010). *Fundamentals of optical waveguides*: Academic press.

Okamoto, T., Sudo, S., Tsuruoka, K., Nielsen, M. L., Mizutani, K., Sato, K., & Kudo, K. (2009). A monolithic wideband wavelength-tunable laser diode integrated with a ring/MZI loop filter. *Selected Topics in Quantum Electronics, IEEE Journal of, 15*(3), 488-493.

Okuno, M., Takato, N., Kitoh, T., & Sugita, A. (1995). Silica-based thermo-optic switches. *NTT review, 7*(5), 57-63.

Olsen, G. H. (1981). InGaAsP laser diodes. *Optical Engineering, 20*(3), 203440-203440-.

Pal, B. P. (1992). *Fundamentals of fibre optics in telecommunication and sensor systems*: Bohem press.

Park, S.-J., Jeong, K.-T., Park, S.-H., & Sung, H.-K. (2002). A novel method for fabrication of a PLC platform for hybrid integration of an optical module by passive alignment. *Photonics Technology Letters, IEEE, 14*(4), 486-488.

Pawley, J. (2010). *Handbook of biological confocal microscopy*: Springer Science & Business Media.

Payne, F., Hussey, C., & Yataki, M. (1985). Modelling fused single-mode-fibre couplers. *Electronics Letters, 21*(11), 461-462.

Pernas, P., Piqueras, J., Torchia, G., Climent-Font, A., & Jaque, F. (2005). *Silicon-based waveguide materials for integrated optics.* Paper presented at the Fibres and Optical Passive Components, 2005. Proceedings of 2005 IEEE/LEOS Workshop on.

Petersen, K. E. (1982). Silicon as a mechanical material. *Proceedings of the IEEE, 70*(5), 420-457.

Poustie, A. (2008). *Hybrid integration for advanced photonic devices.* Paper presented at the Asia Pacific Optical Communications.

Rajadhyaksha, M., Anderson, R., & Webb, R. H. (1999). Video-rate confocal scanning laser microscope for imaging human tissues in vivo. *Applied Optics, 38*(10), 2105-2115.

Ramaswami, R., Sivarajan, K., & Sasaki, G. (2009). *Optical networks: a practical perspective*: Morgan Kaufmann.

Righini, G. C. (1988). Passive Integrated Optical Components. *Journal of Modern Optics, 35*(6), 847-848. doi: 10.1080/09500348814550981

Righini, G. C., & Chiappini, A. (2014). Glass optical waveguides: a review of fabrication techniques. *Optical Engineering, 53*(7), 071819-071819.

Roychoudhuri, C. (2008). *Fundamentals of Photonics*: Bellingham, Wash : SPIE Press, 2008.

Sasaki, J., Kaneyama, Y., Honmou, H., Itoh, M., & Uji, T. (1992, 16-19 Nov 1992). *Self-aligned Assembly Technology For Optical Devices Using AuSn Solder Bumps Flip-chip Bonding.* Paper presented at the LEOS '92, Conference Proceedings. IEEE Lasers and Electro-Optics Society, 1992 Annual Meeting.

Sasaki, J. i., Itoh, M., Tamanuki, T., Hatakeyama, H., Kitamura, S., Shimoda, T., & Kato, T. (2001). Multiple-chip precise self-aligned assembly for hybrid integrated optical modules using Au-Sn solder bumps. *Advanced Packaging, IEEE Transactions on, 24*(4), 569-575.

Sasaki, T., Komiya, T., Fujimura, Y., Saito, M., Semura, S., & Nishimura, M. (2001). Multi-channel power level monitor with upward-reflector and sensor-array integrated in planar lightwave circuit. *OFC, WB6.*

Sato, T., Yamaoto, F., Tsuji, K., Takesue, H., & Horiguchi, T. (2002). An uncooled external cavity diode laser for coarse-WDM access network systems. *Photonics Technology Letters, IEEE, 14*(7), 1001-1003.

Schinke, D., Smith, R., & Hartman, A. (1982). Photodetectors *Semiconductor Devices for Optical Communication* (pp. 63-87): Springer.

Schulz, P. (1989). Wavelength independent Faraday isolator. *Applied Optics, 28*(20), 4458-4464.

Schwider, J., Burow, R., Elssner, K.-E., Grzanna, J., Spolaczyk, R., & Merkel, K. (1983). Digital wave-front measuring interferometry: some systematic error sources. *APPLIED OPTICS, 22*(21), 3421-3432.

Seimetz, M., & Weinert, C.-M. (2006). Options, feasibility, and availability of 2× 4 90 hybrids for coherent optical systems. *Journal of lightwave technology, 24*(3), 1317.

Selvarajan, A. (1992). Integrated optics — technology and applications. *Sadhana, 17*(3-4), 391-409. doi: 10.1007/bf02811350

Shakespeare, W. J., Pearson, R. A., Grenestedt, J. L., Hutapea, P., & Gupta, V. (2005). MEMS integrated submount alignment for optoelectronics. *Journal of lightwave technology, 23*(2), 504.

Sherrington, I., & Smith, E. (1988). Modern measurement techniques in surface metrology: part I; stylus instruments, electron microscopy and non-optical comparators. *Wear, 125*(3), 271-288.

Shieh, H.-P. D., Huang, Y.-P., & Chien, K.-W. (2005). Micro-optics for liquid crystal displays applications. *Journal of display technology, 1*(1), 62.

Shin, H.-J., Pierce, M. C., Lee, D., Ra, H., Solgaard, O., & Richards-Kortum, R. (2007). Fiber-optic confocal microscope using a MEMS scanner and miniature objective lens. *Optics Express, 15*(15), 9113-9122.

Shore, P., & Cranfield, B. (2008). Ultra Precision Surfaces. *Diamond, 10*(1), 0.1.

Singleton, L., Leach, R., Lewis, A., & Cui, Z. (2002). Report on the analysis of the MEMSTAND survey on standardisation of microsystems technology. *MEMSTAND Project IST-2001-37682*.

Smith, R., & Personick, S. (1980). Semiconductor devices for optical communication. *Topics in applied physics, 39*.

Snyder, A. W., & Love, J. (1983). *Optical waveguide theory* (Vol. 190): Springer Science & Business Media.

Stubkjær, K., Mikkelsen, B., Djurhuus, T., Storkfelt, N., Jørgensen, C., Jepsen, K. S., . . . Gliese, U. B. (1992). *Recent advances in semiconductor optical amplifiers and their applications.* Paper presented at the Fourth International Conference on Indium Phosphide and Related Materials.

Suematsu, M., & Takeda, M. (1991). Wavelength-shift interferometry for distance measurements using the Fourier transform technique for fringe analysis. *Appl. Opt., 30*(28), 4046-4055.

Suhara, T., Taniguchi, T., Uemukai, M., Nishihara, H., Hirata, T., Iio, S., & Suehiro, M. (1995). Monolithic integrated-optic position/displacement sensor using waveguide gratings and QW-DFB laser. *Photonics Technology Letters, IEEE, 7*(10), 1195-1197.

Sung, I.-H., Lee, H.-S., & Kim, D.-E. (2003). Prediction of asperity contact condition using FFT-based analysis for micro-grooved surface design in tribological applications. *Journal of Physics D: Applied Physics, 36*(7), 939.

Suzuki, T., Yazawa, T., & Sasaki, O. (2002). Two-wavelength laser diode interferometer with time-sharing sinusoidal phase modulation. *Applied Optics, 41*(10), 1972-1976.

Takeda, M., & Yamamoto, H. (1994). Fourier-transform speckle profilometry: three-dimensional shape measurements of diffuse objects with large height steps and/or spatially isolated surfaces. *APPLIED OPTICS, 33*(34), 7829-7837. doi: 10.1364/ao.33.007829

Tersoff, J., & Hamann, D. (1993). Theory of the scanning tunneling microscope *Scanning Tunneling Microscopy* (pp. 59-67): Springer.

Terui, H., Shimokozono, M., Yanagisawa, M., Hashimoto, T., Yamada, Y., & Horiguchi, M. (1996). Hybrid integration of eight channel PD-array on silica-based PLC using micro-mirror fabrication technique. *Electronics Letters, 32*(18), 1662-1664.

Terui, H., Yamada, Y., Kawachi, M., & Kobayashi, M. (1985). Hybrid integration of a laser diode and high-silica multimode optical channel waveguide on silicon. *Electronics Letters, 21*(15), 646-648.

Thiel, J., Pfeifer, T., & Hartmann, M. (1995). Interferometric measurement of absolute distances of up to 40 m. *Measurement, 16*(1), 1-6.

Tiziani, H. J. (1989). Optical methods for precision measurements. *Optical and Quantum Electronics, 21*(4), 253-282.

Ura, S., Suhara, T., & Nishihara, H. (1989). Integrated-optic interferometer position sensor. *Lightwave Technology, Journal of, 7*(2), 270-273.

Valette, S., Renard, S., Jadot, J., Gidon, P., & Erbeia, C. (1990). Silicon-based integrated optics technology for optical sensor applications. *Sensors and Actuators A: Physical, 23*(1), 1087-1091.

Vorburger, T., & Raja, J. (1990). *Surface finish metrology tutorial*: National Inst. of Standards and Technology.

Vorburger, T., & Teague, E. (1981). Optical techniques for on-line measurement of surface topography. *Precision Engineering, 3*(2), 61-83.

Wada, O. (1994). *Optoelectronic Integration: Physics, Technology and Applications: Physics, Technology, and Applications* (Vol. 269): Springer Science & Business Media.

Wale, M. J., & Edge, C. (1990). Self-aligned flip-chip assembly of protonic devices with electrical and optical connections. *Components, Hybrids, and Manufacturing Technology, IEEE Transactions on, 13*(4), 780-786.

Wang, S., Tian, Y., Tay, C. J., & Quan, C. (2003). Development of a laser-scattering-based probe for on-line measurement of surface roughness. *Applied Optics, 42*(7), 1318-1324.

White, I. H. (1991). A multichannel grating cavity laser for wavelength division multiplexing applications. *Lightwave Technology, Journal of, 9*(7), 893-899.

Whitehouse, D. J. (1997). Surface metrology. *Measurement Science and Technology, 8*(9), 955.

Whitney, P. S. (2002, 2002). *Hybrid integration of photonic subsystems.* Paper presented at the Electronic Components and Technology Conference, 2002. Proceedings. 52nd.

Wilson, T., & Carlini, A. (1987). Size of the detector in confocal imaging systems. *Optics Letters, 12*(4), 227-229.

Wooten, E. L., Kissa, K. M., Yi-Yan, A., Murphy, E. J., Lafaw, D. A., Hallemeier, P. F., . . . McBrien, G. J. (2000). A review of lithium niobate modulators for fiber-optic communications systems. *Selected Topics in Quantum Electronics, IEEE Journal of, 6*(1), 69-82.

Wörhoff, K., Roeloffzen, C. G., de Ridder, R. M., Driessen, A., & Lambeck, P. V. (2007). Design and application of compact and highly tolerant polarization-independent waveguides. *Journal of lightwave technology, 25*(5), 1276-1283.

Wright, D., Greve, P., Fleischer, J., & Austin, L. (1992). Laser beam width, divergence and beam propagation factor—an international standardization approach. *Optical and Quantum Electronics, 24*(9), S993-S1000.

Wyant, J. C., Koliopoulos, C. L., Bhushan, B., & George, O. E. (1984). An optical profilometer for surface characterization of magnetic media. *ASLE transactions, 27*(2), 101-113.

Xiao, G., Corle, T. R., & Kino, G. (1988). Real-time confocal scanning optical microscope. *Applied Physics Letters, 53*(8), 716-718.

Yamada, Y., Suzuki, S., Moriwaki, K., Hibino, Y., Tohmori, Y., Akutsu, Y., . . . Yanagisawa, M. (1995). Application of planar lightwave circuit platform to hybrid integrated optical WDM transmitter/receiver module. *Electronics Letters 31*(16), 1366-1367.

Yamada, Y., Takagi, A., Ogawa, I., Kawachi, M., & Kobayashi, M. (1993a). Silica-based optical waveguide on terraced silicon substrate as hybrid integration platform. *Electronics Letters, 29*(5), 444-446.

Yamada, Y., Takagi, A., Ogawa, I., Kawachi, M., & Kobayashi, M. (1993b). Silica-based optical waveguide on terraced silicon substrate as hybrid integration platform. *Electronics Letters, 29*(5), 444-446.

Yamada, Y., Yamada, M., Terui, H., & Kobayashi, M. (1989). Optical interconnections using a silica-based waveguide on a silicon substrate. *Optical Engineering, 28*(12), 281281-281281-.

Yamaguchi, I., Yamamoto, A., & Kuwamura, S. (1998). Speckle decorrelation in surface profilometry by wavelength scanning interferometry. *Applied Optics, 37*(28), 6721-6728.

Yamaguchi, I., Yamamoto, A., & Yano, M. (2000). Surface topography by wavelength scanning interferometry. *Optical Engineering, 39*(1), 40-46.

Yamamoto, A., Kuo, C.-C., Sunouchi, K., Wada, S., Yamaguchi, I., & Tashiro, H. (2001). Surface shape measurement by wavelength scanning interferometry using an electronically tuned Ti: sapphire laser. *Optical Review, 8*(1), 59-63.

Yamamoto, A., & Yamaguchi, I. (2000). Surface profilometry by wavelength scanning Fizeau interferometer. *Optics & Laser Technology, 32*(4), 261-266.

Yamamoto, A., & Yamaguchi, I. (2002). Profilometry of sloped plane surfaces by wavelength scanning interferometry. *Optical Review, 9*(3), 112-121.

Yariv, A. (1989). Quantum electronics, 3rd. *Edn.(John WieLy & Sons, New York, 1988) p, 389*.

Yotter, R. A., & Wilson, D. M. (2003). A review of photodetectors for sensing light-emitting reporters in biological systems. *Sensors Journal, IEEE, 3*(3), 288-303.

Yu, H., Aleksoff, C., & Ni, J. (2013). Thickness measurement of transparent plates by wavelength stepping and a phase unwrapping algorithm. *Measurement Science and Technology, 24*(7), 075201.

Zappe, H. (1996). *Monolithically Integrated Semiconductor Optical Sensors.* Paper presented at the Lasers and Electro-optics Europe, 1996. CLEO/Europe., Conference on.

Zecchino, M. (2005). Enhanced Vertical Scanning Interferometry a Novel Solution for Difficult to Measure Samples. *Veeco, Tucson*.

Zetie, K., Adams, S., & Tocknell, R. (2000). How does a Mach-Zehnder interferometer work? *Physics Education, 35*(1), 46.

Zhang, D., Zhao, J., Yang, Q., Liu, W., Fu, Y., Li, C., . . . Wang, L. (2012). Compact MEMS external cavity tunable laser with ultra-narrow linewidth for coherent detection. *Optics Express, 20*(18), 19670-19682. doi: 10.1364/oe.20.019670

Zhou, Y., Sun, J., Yan, A., Luan, Z., Wang, L., & Liu, L. (2009). *Optical birefringent 90° hybrid for coherent receiver in free-space optical communication system.* Paper presented at the SPIE Optical Engineering+ Applications.

Zimmermann, L., Voigt, K., Winzer, G., Petermann, K., & Weinert, C. M. (2009). C- band optical 90 degree –hybrid based on silicon-on-insulator 4x4 waveguide couplers. *Photonics Technology Letters, IEEE, 21*(3), 143-145. doi: 10.1109/lpt.2008.2009317

Appendices

Appendix 1

Matlab Script for Absulute Distance Measurement

```
%%%%%%%%Code for calculating the absolute distance measurement using the
Fourier transform method%%%%%%%%%%%%

%Reference interferometer%%%%%
clear all
clc
% for num_picture=1:10

result = dlmread ('D:\Prashant\Work\Experiment n Results\Single point
measurements\Samples\Final measurement results\Rubert sample\Rubert sample
full scan\Ref0198mm.csv', ',');   % reading data from the file
time = result(:, 1);
volts = result(:, 2);

time1 = time(400:22900);      %cropped waveform from the original data
volts1 = volts(400:22900);
figure(1);
plot(time1, volts1,'lineWidth',1.5);
set(gca,'FontSize',14);
xlabel('Time (s)')
ylabel('Voltage')
title('Reference Signal ')
axis tight;
grid

Volts1 = volts1 - mean(volts1);
% Volts = volts1;
window = hann(length(Volts1));
Volts = window.* Volts1;
figure(2);
plot(time1,Volts,'lineWidth',1.5);
set(gca,'FontSize',14);
xlabel('Time (s)')
ylabel('Voltage')
title('Reference Signal ')
axis tight;
grid

% fast fourier transform of the sample/data

transform_norm = fft(Volts);
magnitude_fft = abs(transform_norm);
Filter_fft = transform_norm;
Filter_fft(1:10)=0;
Filter_fft(44:length(Volts))= 0 ;       % filtering by rectangular window
magnitude_fft1 = (magnitude_fft (1:length(Volts)/2)); % selecting only the
positive set of values

scan_time = time1(end)-time(1);
step_time = scan_time/length(Volts);
```

```
Fs = (1/step_time);                              %%%%%       Sampling
frequency
f = (Fs/2)*linspace(0,1,length(magnitude_fft1))*1e-6;

figure(3);
plot(f, magnitude_fft1/norm(magnitude_fft1),'lineWidth',1.5);
set(gca,'FontSize',14);
axis([0 0.1 0 0.4]);
xlabel('Frequency (MHz)')
ylabel('Intensity')
title('FFT of Refrence Signal')
grid

invi_transform =ifft (Filter_fft);     % inverse fourier transform
phase_seperate = log(invi_transform);  %  complex logarithm for seperating
the phase from unwanted amplitude
phase_emg = imag(phase_seperate);      % filtering phase value (imaginary
coefficients)
phase = unwrap (phase_emg);            %This introduces contunuity in the
phase by adding 2pi at the discontinuous points
phase_diff = diff(phase);

figure(4);
plot(phase_diff,'lineWidth',1.5)
set(gca,'FontSize',14)
axis([0 22500 -0.05 0.05]);
xlabel('Sample number')
ylabel('Wr(t) Reference Angular Frequency')
title('Reference Angular Frequency ')
grid on

%%%%%%%%%%%%%%%%%%%%%%%%%%%%%%%%%%%%%%%%%%%%%%%%%%%%%%%%%%%%%%%%%%%%%%%%%%%%%%%
%%%%%%%%%%%%%%%%%%%%%%%%%%%%%%%%%%%%%%%%%%%%%%%%%%
%%%%%Measurement interferometer%%%%%%%

Result = dlmread ('D:\Prashant\Work\Experiment n Results\Single point
measurements\Samples\Final measurement results\Rubert sample\Rubert sample
full scan\240.csv', ',');    % reading data from the file
TIME = Result(:, 1);
VOLTS = Result(:, 2);

TIME1 = TIME(400:22900);
VOLTS1 = VOLTS(400:22900);
figure(5);
plot( TIME1, VOLTS1,'lineWidth',1.5)
set(gca,'FontSize',14);
xlabel('Time(s)')
ylabel('Voltage')
title('Measurement Signal')
axis tight;
grid

% VOLTS_F = VOLTS1;
VOLTS1 = VOLTS1 - mean(VOLTS1);
WINDOW = hann(length(VOLTS1));
VOLTS_F = WINDOW.* VOLTS1;
```

```
figure(6);
plot(TIME1, VOLTS_F,'lineWidth',1.5);
set(gca,'FontSize',14);
xlabel('Time (s)')
ylabel('Voltage')
title('Measurement Signal ')
axis tight;
grid

% fast fourier transform of the sample/data
TRANSFORM_norm = fft(VOLTS_F);
MAGNITUDE_fft = abs(TRANSFORM_norm);
FILTER_fft = TRANSFORM_norm;
FILTER_fft(1:10)=0;
FILTER_fft(63:length(VOLTS_F))= 0 ;       % removal of the Dc component from
the obtained fourier transform data
MAGNITUDE_fft1 = MAGNITUDE_fft (1:length(VOLTS_F)/2);      % selecting only
the positive set of values

SCAN_time = TIME1(end)-TIME(1);
STEP_time = SCAN_time/length(VOLTS_F);
FS = (1/STEP_time);                                        %%%%%     Sampling
frequency
F = (FS/2)*linspace(0,1,length(MAGNITUDE_fft1))*1e-6;

figure(7);
plot(F, MAGNITUDE_fft1/norm(MAGNITUDE_fft1),'lineWidth',1.5);
set(gca,'FontSize',14);
axis([0 0.1 0 0.4]);
xlabel('Frequency (MHz)')
ylabel('Intensity')
title('FFT of Measurement Signal')
grid


INVI_transform =ifft (FILTER_fft);% inverse fourier transform
PHASE_seperate = log(INVI_transform);  %  complex logarithm for seperating
the phase from unwanted amplitude
PHASE_emg = imag(PHASE_seperate);      % filtering phase value (imaginary
coefficients)
PHASE = unwrap (PHASE_emg);%This introduces contunuity in the phase by adding
2pi at the discontinuous points
PHASE_diff = diff(PHASE);

figure(8);
plot(PHASE_diff,'lineWidth',1.5)
set(gca,'FontSize',14);
axis([0 22500 -0.1 0.1]);
xlabel('Sample number')
ylabel('Ws(t) Signal Angular Frequency')
title('Measurement Signal Angular Frequency')
grid
```

```
%%%%%%%%%%%%%%%%%%%%%%%%%%%%%%%%%%%%ratio of the instantenous angular
frequency%%%%%%%%%%%%%%%%%

INST_ANGFREQ = PHASE_diff./phase_diff;
figure(9)
plot(INST_ANGFREQ,'b','lineWidth',1.5);
set(gca,'FontSize',14);
axis([0 22500 -200 2000]);
xlabel('Sample number')
ylabel('Ws(t) / Wr(t)')
title('Ratio of Measurement Signal & Reference Angular Frequencies')
grid

% x =1001;
% y =15000;
% z= 1:1:14000;
% % yline = yline (x:y);
% % YLINE = YLINE (x:y);
% phase_diff = phase_diff(x:y);
% PHASE_diff = PHASE_diff(x:y);

%%%%%%%%%%%%%%%%%%%%%%%%linear fitting to the angular%%%%%%%%%%%%frequency

INST_ANGFREQ = INST_ANGFREQ(1000:21000);    % cropped data to avoid peaks in
ratio of angular frequency
INSTangfreq_Mean = mean(INST_ANGFREQ);
GlassThickness = (INSTangfreq_Mean*0.198*1.599)    % Absolute distance
calculation

z = 1:1:length(INST_ANGFREQ);
COFFE = polyfit(z', INST_ANGFREQ ,1);
z_matxval = linspace( min(z), max(z), length(z));
Yvalue = COFFE(1)*z_matxval+COFFE(2);              %Linear fit to the cropped
ratio of angular frequencies

figure (10)
plot(z,INST_ANGFREQ,'b', 'lineWidth',2)
hold on
plot(z_matxval,Yvalue,'r','linestyle','--','lineWidth',2)
hold off
set(gca,'FontSize',14);
axis([1500 19000 1 2]);
xlabel('Sample number')
ylabel('Ws(t) / Wr(t)')
title('Ratio of Measurement Signal & Reference Angular Frequencies')
grid
```

Appendix 2

Matlab script for surface profile measuremt

```
clear all
clc

Data1 = dlmread ('C:\Users\u1072708\Desktop\PSI\Data 100nm step\I1.csv',
',');   % reading data from the file
% time1 = Data1(:, 1).*1e3;
I1 = smooth(Data1(:, 2));
% I1 = I1 - mean(I1);
figure(1)
plot(I1, 'lineWidth',1.5)
axis tight; grid
% xlabel('Time (ms)')
ylabel('Voltage (V)')
title('Voltage Vs Time graph')
x1_start = 655;
x1_end = 10570;
I1 = I1(x1_start:x1_end);
I1 = I1 - min(I1);

Data2 = dlmread ('C:\Users\u1072708\Desktop\PSI\Data 100nm step\I2.csv',
',');   % reading data from the file
I2 = smooth(Data2(:, 2));
figure(2)
plot(I2, 'lineWidth',1.5)
axis tight; grid
% xlabel('Time (ms)')
ylabel('Voltage (V)')
title('Voltage Vs Time graph')
x2_start = 655;
x2_end = 10570;
I2 = I2(x2_start:x2_end);
I2 = I2 - min(I2);

Data3 = dlmread ('C:\Users\u1072708\Desktop\PSI\Data 100nm step\I3.csv',
',');   % reading data from the file
I3 = smooth(Data3(:, 2));
figure(3)
plot(I3, 'lineWidth',1.5)
axis tight; grid
% xlabel('Time (ms)')
ylabel('Voltage (V)')
title('Voltage Vs Time graph')
x3_start = 655;
x3_end = 10570;
I3 = I3(x3_start:x3_end);
I3 = I3 - min(I3);

Data4 = dlmread ('C:\Users\u1072708\Desktop\PSI\Data 100nm step\I4.csv',
',');   % reading data from the file
I4 =  smooth(Data4(:, 2));
figure(4)
plot(I4, 'lineWidth',1.5)
axis tight; grid
```

```
% xlabel('Time (ms)')
ylabel('Voltage (V)')
title('Voltage Vs Time graph')

x4_start = 655;
x4_end = 10570;
I4 = I4(x4_start:x4_end);
I4 = I4 - min(I4);

figure(5)
plot(I1,'r','lineWidth',1.5)
set(gca,'FontSize',30)
hold on
plot(I2,'k','lineWidth',1.5)
plot(I3,'g','lineWidth',1.5)
plot(I4,'b','lineWidth',1.5)
axis tight; grid
legend('y = I1','y = I2','y = I3','y = I4');
xlabel('Samples')
ylabel('Voltage (V)')
% title('Voltage Vs Time graph')

%%%%%%%%%%%%%%%%%%%%%%%%%Carre algorithm%%%%%%%%%%%%%%%%%%%%%%%
a = (3*(I2-I3))-(I1-I4);
b = (I2-I3)+(I1-I4);
c = (I2+I3)-(I1+I4);

num1=(a.*b);
den=(c);
phase = atan((sqrt(abs(num1))./(abs(den))));
num = (I2-I3);

%%%%%%%%%%%%%%%%%%%%%%%%%%%%%%%%%%%%%%%Phase Corrections%%%%%%%%%%%%%%%%%%
Phase = zeros(length(num),1)';
for j = 1:length(num)

if ((num (j) > 0) && (den(j) > 0))
    Phase(j) = phase(j);

elseif ((num(j) > 0) && (den(j) < 0))
    Phase(j) = pi - phase(j);

elseif ((num(j)  < 0) && (den(j) < 0))
    Phase (j) = pi + phase(j);

elseif ((num(j) < 0) && (den(j) > 0))
    Phase (j) = 2*pi- phase(j);

% elseif ((num(j) == 0)&& (den(j) > 0))
%     Phase (j) = 0;

% elseif (num(j) == 0)
%     Phase (j) = pi;

elseif (den(j) == 0)
```

```
    Phase (j) = pi;
% elseif ((num(j) == 0)&& (den(j) < 0))
%     Phase (j) = pi;

elseif ((num(j) > 0) && (den(j)==0))
    Phase (j) = 0.5*pi;

elseif ((num(j) < 0) && (den(j)==0))
    Phase (j) = 1.5*pi;
end
end

Phase = unwrap (Phase);
figure(6)
plot(Phase,'lineWidth',1.5)
set(gca,'FontSize',30)
% xlabel('Wavelengths (m)')
ylabel('Phase')
% title('Phase ')
axis tight
grid on

% Describe wavelength range incident upon detector using TFF tuning function
Points = length(I1);
N_sample=Points; % Sampling point
start_lambda=1.605e-6;
stop_lambda= zeros(N_sample,1);
n_effective=1.622;
for i=1:N_sample
    scan_angle(i)=34.29-((34.29-10.38)/N_sample).*i;
    value(i)=sind(scan_angle(i))/n_effective;
    stop_lambda(i)=start_lambda.*sqrt(1-value(i).*value(i));
    i=i+1;
end

WLength = stop_lambda*1e+6;
WLength1 = WLength(1) ;                                    % Lower end of source
wavelength
WLength2 = WLength(end);

wlength = WLength(1700:3400);
CorrPhase = Phase(1700:3400);
step_height = (CorrPhase'.*wlength*1e-6/(4*pi))*1e+9;

figure(7)
plot(wlength, step_height,'lineWidth',1.5)
set(gca,'FontSize',30)
xlabel('Wavelengths (um)')
ylabel('Step height (nm)')
title('Step height Vs Wavelengths')
axis tight
grid on
```

Appendix 3

Zemax Simulation Data

Lens Data Editor

Edit Solves View Help

	Surf:Type	Thickness	Glass		Semi-Diameter		Par 1 (unused)	Par 2 (unused)	Par 3 (unused)
OBJ	Standard	Infinity			0.000				
STO	Standard	20.000			0.600				
2	Coordinat..	0.000	-		0.000		0.000	0.000	-63.000
3	Diffracti..	0.000	MIRROR		1.322		0.830	1.000	
4	Standard	-17.185			1.322				
5#	Standard	-3.500	N-LAK22		4.000	U			
6*	Standard	-1.300	N-SF6HT		4.000	U			
7*	Standard	-53.511			4.000	U			
8#	Standard	-1.800	N-SF6HT		12.700	U			
9*	Standard	-9.000	N-LAK22		12.700	U			
10*	Standard	-50.000			12.700	U			
11*	Standard	-1.959	SK14		3.500	U			
12*	Standard	-0.482			3.318	U			
13*	Standard	-2.985	LAKN7		2.968	U			
14*	Standard	-0.465			2.092	U			
15*	Standard	-1.830	SF6		1.959	U			
16*	Standard	-5.617			1.463	U			
17*	Standard	-1.477	LAK9		1.309	U			
18*	Standard	-0.393			1.315	U			
19*	Standard	-1.316	LAK9		1.245	U			
20*	Standard	-2.099		V	0.999	U			
*	Standard	-			0.200	U			

System/Prescription Data

GENERAL LENS DATA:

Surfaces	: 21
Stop	: 1
System Aperture	: Entrance Pupil Diameter = 1.2
Glass Catalogs	: SCHOTT
Ray Aiming	: Off
Apodization	: Gaussian, factor = 1.00000E+000
Temperature (C)	: 2.00000E+001
Pressure (ATM)	: 1.00000E+000
Adjust Index Data To Environment	: Off
Effective Focal Length	: -4.498981 (in air at system temperature and pressure)
Effective Focal Length	: -4.498981 (in image space)
Back Focal Length	: 2.089551
Total Track	: 154.919
Image Space F/#	: 3.749151
Paraxial Working F/#	: 3.749151
Working F/#	: 2.349824
Image Space NA	: 0.1321931
Object Space NA	: 6e-011
Stop Radius	: 0.6
Paraxial Image Height	: 0
Paraxial Magnification	: 0
Entrance Pupil Diameter	:1.2
Entrance Pupil Position	:0
Exit Pupil Diameter	:0.1305232
Exit Pupil Position	:-0.2513187
Field Type	: Angle in degrees
Maximum Radial Field	: 0
Primary Wavelength	: 1.55 µm
Lens Units	: Millimeters

Angular Magnification : 0

Fields : 1

Field Type : Angle in degrees

#	X-Value	Y-Value	Weight
1	0.000000	0.000000	1.000000

Vignetting Factors

#	VDX	VDY	VCX	VCY	VAN
1	0.000000	0.000000	0.000000	0.000000	0.000000

Wavelengths : 3

Units: µm

#	Value	Weight
1	1.505000	1.000000
2	1.550000	1.000000
3	1.580000	1.000000